Higher Order Compact Explicit Jump Immersed Interface Methods for Incompressible Viscous Flows: Application and Development

Ph.D. Thesis

Raghav Singhal

DEPARTMENT OF MATHEMATICS
INDIAN INSTITUTE OF TECHNOLOGY GUWAHATI
GUWAHATI- 781039, INDIA
April, 2023

Higher Order Compact Explicit Jump Immersed Interface Methods for Incompressible Viscous Flows: Application and Development

A thesis submitted
in partial fulfillment of the requirements
for the degree of

DOCTOR OF PHILOSOPHY

by

Raghav Singhal

(Roll Number: 186123012)

(Under the supervision of Prof. Jiten C. Kalita)

Department of Mathematics
INDIAN INSTITUTE OF TECHNOLOGY GUWAHATI
GUWAHATI- 781039, INDIA
April, 2023

Dedicated

To

My Parents

DECLARATION

I hereby declare that the work presented in this thesis entitled "**Higher Order Compact Explicit Jump Immersed Interface Methods for Incompressible Viscous Flows: Application and Development**", has been done by me under the supervision of **Prof. Jiten C. Kalita** for the award of the degree of Doctor of Philosophy and this work has not been previously submitted by for a degree or diploma at this institute or any tertiary educational institution.

Guwahati
April, 2023

Raghav Singhal
Roll No. 186123012
Department of Mathematics
Indian Institute of Technology Guwahati
Guwahati- 781039, Assam, India

CERTIFICATE

It is certified that the work contained in this thesis entitled **"Higher Order Compact Explicit Jump Immersed Interface Methods for Incompressible Viscous Flows: Application and Development"** by **Raghav Singhal**, a student of Department of Matheamtics, Indian Institute of Technology Guwahati, for the award of the degree of Doctor of Philosophy has been carried out under my supervision and this work has not been submitted elsewhere for a degree.

Guwahati
April, 2023

Prof. Jiten C. Kalita
Department of Mathematics
Indian Institute of Technology Guwahati
Guwahati- 781039, Assam, India

Acknowledgement

First and primarily, I would like to express my gratitude to my thesis supervisor, **Prof. Jiten C. Kalita**, who made this work possible and whom I am indebted to. I sincerely thank him for all of his help, encouragement, patience, constructive criticism, and scholarly contributions throughout the course of my research. He took the greatest care of me and helped me feel free to express my opinions, for which I am eternally grateful. His unwavering support and cooperation motivated me to carry out and finish this research and made it possible. His knowledge and wealth of experience influenced the study's direction and sharpened its conclusions. I will always be appreciative of his encouraging words in all facets of my life. Once more, Sir, I would like to express my sincere gratitude.

Mrs. Deepshikha Choudhory showered me with her motherly love and affection, for which I am eternally grateful. It is actually very challenging to convey my appreciation for her in just a few words. I will always be thankful to her.

I would like to special thanks to the members of my doctoral committee, Prof. Rajen Kumar Sinha, Prof. Amaresh Dalal, and Dr. Sweta Tiwari, for their support, perceptive observations, and helpful suggestions. I would like to express my deepest gratitude to Prof. Swaroop Nandan Bora and Dr. Anjan K. Chakrabarty for there support and priceless advice and enormous help during M.Sc and PhD. I sincerely appreciate all of the faculty in Department of Mathematics, Indian Institute of Technology Guwahati for their assistance and cooperation. I appreciate all of the staff at for their help with official and technical matters. I would like to thank Dr. Hari Vansh Rai Mittal (Department of Mathematics, IIT Palakkad) for his help and fruitful discussion. Additionally, I would like to express the deepest appreciation to all of the teachers who inspired and supported me throughout my time in school and college.

I started writing this thesis while I was a student at Department of Mathematics, Indian Institute of Technology Guwahati. I truly appreciate the Indian Institute of Technology Guwahati for providing a wonderful learning environment and a range of resources for me to conduct my research there. I am very appreciative of the Ministry of Human Resource Development's financial assistance with my research during that time.

I would like to express my heartfelt thanks to research colleagues at this time. I want to

extend my gratitude to my close friends Sunny Mehrotra, Monu Kadyan, Abhinay Verma, Eti Goel, Aashna Chauhan, Raghvendra Kumar, Mukul Dwivedi, Atul Kumar Rai, Sumit Kumar and Pratham Singh for their prompt assistance, support, and encouragement. I would like to give thanks to my senior doctor, Dr. Sougata Biswas, as well as Drs. Devanand, Pankaj Kumar, Sailen Dutta, Ram Manohar for their support, friendship, and brotherly love throughout this work.

I would really like to special thanks to my parents, Mrs. Madhuri Singhal and Mr. Manish Kumar Singhal, for their unending support, love, and prayers. I am truly appreciative of everything they have done for me. I want to thank my younger sister Ms. Radhika Singhal in particular for her undying support, constant belief in me, and prodding me to pursue my goals. I also appreciate my uncle, Mr. Rajesh Aggarwal, for providing his medication.

Finally, I would like to thank everyone who contributed to the successful completion of the thesis and apologise for not mentioning each of you by name.

And above all, I thank the Gods for their blessings.

Place: IIT Guwahati | With regards
April, 2023 | Raghav Singhal

Abstract

This study is primarily focused on the development of explicit jump high-order compact finite difference immersed interface approaches for the purpose of solving incompressible viscous flows that are governed by the Navier-Stokes (N-S) equation on uniform and non-uniform grids on a Cartesian mesh. In all, three basic schemes have been developed in the process: one for elliptic problems and the steady state of N-S equations with discontinuities in the solutions, source terms, and coefficients across the interface; the next one is the transient counterpart of the previously developed one uniform grids; and lastly, a discrete level-set approach on non-uniform grids with complex interfaces. The overall accuracy of the scheme is four in space and two in time. Throughout the whole physical domain, a nine-point compact stencil is maintained by incorporating the jump conditions into the right-hand side of the matrix equation $Ax = b$ resulting from discretization of the concerned equations. We use the streamfunction- vorticity (ψ-ζ) formulation of the N-S equation, and the jump conditions for ψ and ζ at the irregular point across the interface are taken into account by using a new method based on Lagrangian interpolation.

The main emphasis of the work is the simulation of flow around bluff bodies by employing the above mentioned schemes, which has many applications in industries and day to day life. During the process, both the grid independence of the computed solutions and the numerical rate of convergence of the schemes are determined on a circular and star-shaped interface. High-quality simulations are carried out over a wide range of Reynolds numbers (Re) between 10 and 3000 for the stationary bluff bodies. Detailed analyses of the fluid flow are performed for flow past stationary circular, ellipse and cactus-shaped cylinders, NACA 0012 airfoil, a swimming fish and oscillating circular cylinders. Furthermore, more specifically, the proposed approaches have been applied to comprehensively investigate heat transfer owing to forced convection from a heated elliptical cylinder in a uniform free stream with angle of inclination.

In all the cases, the proposed schemes were seen to very efficiently capture all the flow and heat characteristics associated with the problems under consideration. Apart from aptly resolving the flow separation leading to secondary and tertiary vortex phenomena, the von *Kármán* vortex's streets, a typical feature of periodic flows under different flow situations have also been accurately captured by our simulation. Computations were performed for not only flow past single bodies, but also those involving multiple and moving bodies, thus exemplifying the robustness of the proposed approaches. For the selected test cases where numerical and experimental results are already available, our computational results were extremely close to all of them.

Contents

List of Figures

List of Tables

1

Introduction

1.1 The backdrop

There is no disputing the fact that the Navier-Stokes[1] (N-S) equations are the most well-known and frequently used fluid flow prediction model. Through momentum balance, Newton's second law of motion provides the backbone of these equations that describes the movement of incompressible viscous flows. By exploiting its power to aptly capture the flow field associated with Newtonian fluids, it may be used to analyse a plethora of fascinating scientific and engineering phenomena. These equations are highly nonlinear coupled partial differential equations (PDEs), and except for a few instances where analytic solutions may be obtained in the most simplified conditions, they are challenging to solve analytically. Therefore, in the majority of physical situations, scientists are left only with the option of using numerical methods in order to solve the N-S equations. This has led to the advent of the field of Computational Fluid Dynamics, also known as CFD, which refers to the use of solving fluid flow problems and their subsequent analysis by means of numerical methods and algorithms. The very first step in this direction is to convert the concerned partial derivatives appearing in the N-S equations in a continuous domain into equivalent algebraic expressions in a discrete domain. The most popular strategies for obtaining such discrete representations are the finite difference (FD), finite element (FE), and finite volume (FV) methods. The finite difference approach, which includes putting up a grid (preferably structured) and using finite difference approximations to approximate the derivatives occurring in the governing equations, is the easiest and historically the oldest method. This leads to an enormous but acceptable algebraic system of equations that can be resolved only by a computer.

---

[1] Some part of this chapter is published in [164].

The Taylor series expansion of the variables at the grid points provides a framework for the most widely used finite difference form of partial derivatives. The leading term in the truncation error (TE) of the Taylor series expansion determines the order of accuracy of the scheme. If the TE is asymptotically proportional to h^p, a scheme is said to be of order of accuracy p, or simply $O(h^p)$, where h is the distance between the two succeeding grid points. Due to their simplicity, central difference methods, which are $O(h^2)$ accurate, have been widely used to solve linear PDEs. It is well known that such methods can produce reasonably good results on appropriate meshes provided that the solution is well behaved. Nevertheless, unless the grid is sufficiently finely tuned, such methods result in false oscillations in the solution when used to compute fluid-flow problems governed by the N-S equations. On the other hand, grid refining necessarily results in an increase in computing expense and time. Similarly, the band-width of the coefficient matrix resulting from the discretization process is again increased by discretization on a non-compact stencil, which is typically associated with higher-order accurate techniques. In the end, more arithmetic operations result from mesh refinement and wider matrices. So neither a higher-order accurate approach on a non-compact stencil nor a lower-order accurate one on a fine mesh may be computationally efficient. These limitations prompted the development of higher order compact (HOC) systems, which have successfully been used in the area of CFD throughout time.

One way of identifying a compact stencil is that neighbouring grid points of the node about which the differences are being sought, are only one step length away from it, either in horizontal, vertical or diagonal direction. Compact FD schemes are defined as finite difference schemes which use these grid points, and higher order schemes are defined as finite difference schemes with orders of accuracy more than two. Compared it to non-compact systems, it yields significant computational economy with a system of linear algebraic equations as a result of compact discretization leading to a coefficient matrix with a lower bandwidth.

There are several approaches that can be adopted in order for FD schemes to accomplish higher-order compactness. Applying series expansion to the differential equations is what Gupta et al. [62] propose in order to achieve higher order compactness. Dennis and Hudson [40] use a transformation that entails increasing the exponential of a defined integral of the convective coefficient of the PDE. The series expansion is part of such transformation. In order to obtain higher order compactness, Gartland [56] applies the discrete weighted mean approximation approach, whereas Noye and Tan [123] employ the weighted modified PDE method. Using the original differential equation as a substitute for the leading truncation error (TE) components of the traditional central difference approximation is another approach to achieving higher-order compactness. Lax and Wendroff [94] were the ones who initially proposed this concept for the time-dependent hyperbolic PDEs. Later on, Sptoz and Carey [168], and, Kalita and his group [74–78] extended this idea to equations of convection-diffusion type. This particular mechanism is the one that has been used for the entirety of the present study. Being designed for equations of the convection-diffusion type, they were ideally suited to model incompressible viscous flows that were governed by the Navier-Stokes equations.

For computing viscous incompressible fluid flows, the primitive variable and stream function-vorticity (ψ-ζ) formulations of the N-S equations have historically been the most frequently used methods. An account of the issues involved with these formulation in the context of incompressible fluid dynamics can be found in [60]. Due to its computing efficiency for flows in two dimensions (2D), the ψ-ζ formulation is more often used since it only involves the handling of two unknowns as compared to three in the case of primitive variables. Additionally, it guarantees the mass conservation equation's perfect fulfilment. But, the primitive variable formulation is recommended in the case of flows in three dimensions. There is also a three-dimensional version of the stream function vorticity formulation in the literature [31], however it involves solving six equations with six unknowns. The N-S equations govern incompressible viscous flows, and the CFD community has witnessed considerable application of both the primitive variable and ψ-ζ formulations over time. Both of these formulations have comparative benefits and drawbacks over one another. Over the years, researchers have designed HOC schemes for the ψ-ζ version of the N-S equations and applied them successfully for simulating fluid flow problems with varied levels of complexity, both on uniform [61, 74–76, 111, 169, 186] and non-uniform [17, 22, 77, 78, 140, 147] grids.

1.2 Immersed Interface Method

Interface problems have been of great interest amongst researchers primarily because of their multi-faceted applications, such as two-fluid interactions, multiphase flows with fixed or moving interface at which states (Solid/Liquid/Gas) are different across the interface, but allows the same material. For Example, water or air, water or ice, bubble formation, free-surface flow, relaxation of an elastic membrane, Rayleigh-Taylor instability of binary flows. In the framework of unstable solidification, the governing equations are combined with interfacial dynamics. Likewise, for resolving high tip curvatures and interdendritic phenomena, simulation of dendrite development during solidification needs very precise interface capture approaches. Recent advancements in composite manufacturing technologies focus on preform densification, which apart from using combined bulk phase, also uses interfacial chemistry.

1.2.1 The need

The main difficulty in simulating multiphase flow lie in handling the interface owing to the fact that generating an excellent body-fitted grid is non-trivial and more time-consuming. Computationally it is quite challenging to regenerate a good body-fitted mesh in moving boundaries since it can undergo modification, merge and separation throughout the course of simulation. In contrast, the construction of a Cartesian mesh is trivial where the interface can get cut by the grid lines, with no additional computational cost. Numerically the interface can be computed by, amongst others, the following techniques: the boundary element method, the front tracking method (Lagrangian approach), the volume-of-fluid method and the level set method (Eulerian approach). From the point of view of Calculus, for those problems governed by N-S equations, such as flow past bluff bodies, discontinuities occur in the coefficients and the source term across the interface may become singular, which leads to the discontinuous or non-smooth solution. As a result, standard FD methods break down when applied to interface problems as continuity is a pre-requisite for the Taylor series expansions that they rely upon. Therefore, such problems pose great challenge to the Mathematicians and Engineers alike. This is where the role of Immersed Interface Methods become crucial.

1.2.2 The method

Immersed Interface Method (IIM) was originally formulated as a sharp interface technique that can precisely capture discontinuities in the flux and the solution. If a numerical approach possesses the properties mentioned below, we refer to it as an IIM [12, 20, 96, 179].

1. Instead of a body-fitted grid, a uniform or adaptive grid or triangulation in Cartesian, polar, or spherical coordinates is employed.

2. Physical reasoning or the governing differential equations provide prior knowledge about jump conditions. More interface relations must frequently be developed from the stated jump conditions and controlling PDEs.

3. Standard finite difference or finite element methods are utilized in the discretization away from the interface. Only at grid points or elements close or on the

interface, numerical techniques updated specially based on the jump conditions are used.

4. Emphasis is given on pointwise convergence, which means that we are more concerned with errors in the infinity norm L^∞ rather than an average norm such as L^1 and L^2. This is due to the fact that an average norm cannot accurately reflect errors at the interface. For moving interface and free boundary problems, the precision of solutions at or at interfaces is of primary concern.

5. If the discontinuities in the coefficients, solution, and flux disappear, the approach becomes the standard one.

1.2.3 Literature review

The origin of IIM lies in the early work of Peskin [133], who developed the Immersed Boundary Method (IBM) in 1972 primarily to handle interface discontinuity to solve Navier-Stokes equations for simulating cardiac mechanics and associated blood flow problems. Here, the geometry is handled as a set of Lagrangian fluid particles and these particles constitute a force function in the fluid, which shows the effect of the boundary and the main feature of IBM in modelling an interface was to add a source term in the form of the Dirac delta function to the N-S equations. Standard FD discretization is used on Cartesian grid that approximates the singular delta function in the interface's nearby region. The major disadvantage of Peskin's approach has been its first order accuracy despite using higher-order approximation to the delta function, and being restricted to problems having continuous solutions only. Subsequently, several researchers endeavoured to improve upon IBM by using the front tracking and level set methods in combination with Peskin's approach for tackling interface discontinuities. Depending upon the type of the forcing function, IBM approach is further characterized as discrete or continuous. In 1984 [112], Mayo developed a Cartesian mesh method to solve biharmonic and Laplace problems on the irregular region where second-order accuracy was reported in maximum norm. In this formulation, Fredholm integral equation of second kind was used to extend the piecewise solution of the remaining part of the domain.

In 1994, Leveque and Li [96] achieved vital success in this area, and developed the Immersed Interface Method for solving the elliptic equations with discontinuous coefficients and singular sources. This method, which is a successor to the Immersed Boundary Method of Peskin [133], improved upon both in dealing with the order of accuracy as well with discontinuous coefficients and singular source function simultaneously. IIM resolves irregularities by modifying numerical schemes in the neighbourhood or on the interfaces. As interfaces are of dimensions one less than that of the solution domain, such additions usually do not increase computing costs significantly. At an irregular point, they accounted for the jump conditions in the solution and in the normal derivative by using Taylor expansions of the discretization on both sides of the interface with first-order accuracy and standard second-order central finite difference were used on regular points. Note that, for 2D or 3D interface problems, the jump conditions are available in the normal direction to the interface, which necessitates the use of a local coordinate system to approximate it. Over the years, the IIM has emerged as a very powerful and effective tool in numerically solving problems involving interfaces. They have been extended to the polar coordinate system [104], and successfully implemented to moving [45] and 3D interface problems [38] as well. Apart from FD, they can also be accommodated into finite volume [20] and the finite element [100] approaches.

IIM generally leads to a non-symmetric coefficients matrix; however, the problems are strictly elliptic and self-adjoint. As such, traditional iterative solvers like Gauss-Seidel may diverge or converge very slowly. In 1999, Huang and Li [67] exhibited that the method in [96] is stable for one-dimensional problems and in two-dimensions, only for problems having piecewise-constant coefficients. In order to improve convergence, Li et al. [102] constructed a new IIM approach where they implemented a maximum principle preserving immersed interface method (MIIM) to achieve a diagonally dominant linear system which allows the use of specially designed multigrid techniques to speed up convergence. In 1997, the same group developed a second-order accurate method for elliptic interface problems by roping in a Fast IIM (FIIM) algorithm [99]. They devised a mechanism which uses auxiliary unknowns revealing the normal derivative at the interface for problems having piecewise constant coefficients. This generates a correction term and experts feel that the success of the fast IIM lies in modelling the jump conditions for the dependent variable and its normal derivative using the standard finite difference (FD) scheme along with this correction term. It enabled the application of various standard fast Poisson solvers. Around the same time, in 1998, Fedkiw et al. [48] introduced a non-oscillatory sharp interface approach GFM (Ghost Fluid Method) to capture discontinuities in the hyperbolic equations. The methodology involves developing the function across the interface using fictitious points. Later on, they generalized the GFM [49] to solve viscous N-S equations by imposing the jump conditions implicitly. In 2000, Liu et al. [107] extended this GFM for solving elliptic equations with variable coefficients having discontinuous across the interface where order of accuracy is reduced to one while handling mutiphase flows.

In 2004, Berthelsen [12] constructed a second-order accurate decomposed immersed interface method (DIIM) on a Cartesian grid which includes more jump conditions to improve accuracy. This method interpolates the jump conditions component-wise iteratively on a nine-point stencil and adds them to the right-hand side of the difference scheme near an interfacial node. It uses the level-set function to capture the interface and maintains the symmetry and diagonal dominance of the coefficient matrix. In 2005, Zhou et al. [193] introduced a new higher-order Matched Interface Boundary (MIB) method for 2D and 3D elliptic problems which is based on the use of fictitious points. In order to accomplish higher-order accuracy, the MIB method compensates the bypassing of the implementation of higher-order jump conditions by repeatedly enforcing the lowest order jump conditions. While MIB demonstrated accuracy up to sixth order in dealing with elliptic curves on irregular interfaces, for straight, regular interfaces, it could go as high as 16th order. In 2007, Zhong [191] proposed an explicit higher-order finite difference method by approximating the derivative in jump condition using Lagrange polynomial with a larger stencil at an irregular node and achieved the accuracy up to $O(h^4)$. One of the drawbacks of the method is that it did not retain the original finite difference expression in the absence of the interface's jump. However, it was equivalent to a local higher-order spline approximation at the interface. Although Zhou's and Zhong's methods are higher-order, Zhou's method uses fictitious points and not explicitly derived, while Zhong's approach is explicit and doesn't use any auxiliary points. In 2012, Cistemino [32] presented a second-order Parallel Cartesian Method (PCM) based on finite-difference to solve the elliptic problems with the irregular interface. In addition, new unknowns were carried out on the interface and parallelized with the PETSc (Portable, Extensible Toolkit for Scientific Computation) library.

Employing a higher-order compact approach [75] at the regular points, Mittal et al. [114] developed an at least a second-order accurate method to solve elliptic and parabolic equations in 1D and 2D on circular interfaces with an HOC approach in both Cartesian and polar grids in 2016. The scheme was on non-uniform grids and employed clustering near the interfaces. In 2018 [115], they introduced a new second-order interfacial points-based approach for solving 2D and 3D elliptic equations. They modified Zhong's [191] idea in considering interfacial points to be one of the grid points in approximating the derivative in jump conditions by a Lagrange polynomial. However, at the irregular points, their stencil failed to maintain its compactness.

Recent advancement in IIM also includes Balam et al. [10], who introduced a fourth-order compact immersed interface approach. This novel method is built from a few adjustments to the central finite difference close to the interface and is based on an implicit formulation gained from generalised Taylor series expansions. The linear system produced by the discretization has matrix coefficients that are identical to those for smooth solutions, and the right-hand side system is modified by the addition of components referred to as jump contributions. Only the points where the nine-point stencil cuts the interface are taken into account for calculating these contributions. The contribution formulas, however, call for an understanding of fourth-order Cartesian jumps. The jumps from the known right-hand function of the Poisson equation and the principal jump conditions were the primary jump sources used to derive them in their study. Feng et al. [51] developed a Fast Fourier Transform (FFT) based method which is a natural generalization of a Augmented Matched Interface and Boundary method (AMIB) for non-staggered boundaries and obtained convergence of orders four, six and eight for 2D and 3D problems. However, the validation of the above methods is performed only on analytical problems, being restricted to the Poisson equation with singular source only.

1.3 Motivation

A close look at the works documented above reveals a broad range of problems pertaining to numerical algorithms that were developed for the purpose of resolving a variety of fluid interface problems. They include problems involving material interface, free surface, fluid structure interaction, multiphase material and so on. For differential equations with discontinuous coefficients and singular source terms in domains involving arbitrary shaped and fixed or moving interfaces, there are still ample avenues of using the HOC finite difference approaches, which have not been explored previously. While working with problems of this form, tackling geometrical complexity at high numerical order and computational efficiency become indispensable, concurrently achieving both of which is quite challenging due to the characteristics of the problem. Till date, to the best of our knowledge, the HOC method mentioned earlier has not been applied to complex flow problems like flow over arbitrarily shaped bluff bodies in grids that use the cartesian coordinate system. Furthermore, some of the difficulties which can still arise during simulations include the depiction of fluid interfaces, the management of discontinuous physical variables, and the maintenance of reliable calculations etc. These are the primary factors of motivation behind the endeavour encompassed in the present PhD work.

1.4 Objectives

The work presented in the dissertation aims to provide novel numerical methodologies that can be applied to a variety of complicated multi-phase fluid interface and heat transfer problems on uniform and non-uniform grid. The following are the objectives of the work:

1. Developing novel higher order accurate finite difference explicit jump immersed interface approaches to solve elliptic and parabolic interface problems on a compact stencil in general.

2. Specifically, investigating the flow and forced convection heat transfer characteristics of an elliptical cylinder placed in a uniform free stream. In addition, exploring the flow characteristics for both steady and unsteady states when the angle of attack of the incoming fluid is varied from 0 to 180 degree, including the drag and lift forces.

1.5 The work

Broadly speaking, the work presented in the dissertation can be divided into two parts. Part one pertains to the development of some novel immersed interface approaches in conjunction with HOC finite difference scheme and the level set formulation. The second part deals with applying them to simulate fluid flows and other real life problems.

As a part of developing immersed interface approaches, firstly, we propose a new higher-order accurate finite difference explicit jump Immersed Interface Method for solving two-dimensional elliptic problems with singular source and discontinuous coefficients in the irregular region on a compact Cartesian mesh. We propose a new strategy for discretizing the solution at irregular points on a nine-point compact stencil such that the higher-order compactness is maintained throughout the whole computational domain. Since the basic elliptic equation considered here is of convection-diffusion type, it can also be extended to incompressible viscous fluid flow problems governed by the steady-state N-S equations.

As a natural follow-up, subsequently, we extend the above scheme to develop a novel hybrid explicit jump immersed interface approach in conjunction with a higher-order compact scheme for simulating transient complex flows governed by the streamfunction-vorticity (ψ-ζ) formulation of the N-S equations. A new strategy has been adopted for the jump conditions at the irregular points across the interface using Lagrangian interpolation on a Cartesian grid. This approach, which starts with the discretization of parabolic equations with discontinuities in the solutions, source terms, and the coefficients across the interface, can easily be accommodated into simulating flow past bluff bodies immersed in the flow. The superiority of the approach is reflected by the reduced magnitude and faster decay of the errors in comparison to other existing methods. Note that, both the above mentioned schemes were designed for uniform Cartesian grids for geometries possessing parametric representation only. Therefore, our next endeavour is to develop a discrete Level Set approach on nonuniform Cartesian grids to tackle geometries which cannot be expressed analytically. Apart from enabling to tackle complicated geometries, this approach is seen to be computationally more economical than the earlier approaches.

For the application part, the steady-state scheme is employed to solve four problems embedded with circular and star-shaped interfaces in a rectangular region having analytical solutions and varied discontinuities across the interface in source and the coefficient terms. We also simulate a plethora of fluid flow problems past bluff bodies in complex flow situations which are governed by the N-S equations; they include problems involving multiple bodies immersed in the flow as well. In the process, we show the superiority of the proposed strategy over the explicit jump finite difference immersed interface method and other existing immersed interface methods by establishing the rate of convergence and grid independence of the computed solutions. In all the cases, our computed results are extremely close to the available numerical and experimental results.

On the other hand, the approaches developed for the unsteady N-S equations are seen to handle several fluid flow problems having practical implications in the real world very efficiently, including flows involving multiple and moving bodies. This includes the flow past a stationary circular and a twenty-four edge cactus cylinder, flows past two tandem cylinders, where in one situation both are fixed and in another, one of them is oscillating transversely with variable amplitude in time. We also simulate flow around hydraulic airfoils mimicking swimming fishes. To the best of our knowledge, the last three examples have been tackled for the first time by such an approach employing the ψ-ζ formulation in finite difference set-up on compact stencil. The extreme closeness of our computed solutions with the existing numerical and experimental results exemplifies the accuracy and the robustness of the proposed approach. As our last endeavour of applying the proposed approaches to real life fluid flow problems, we document the simulation heat and fluid flow resulting from the forced convection of a heated elliptic cylinder over a wide range of angles of incidences.

1.6 Organization of dissertation

The present dissertation is organized into seven chapters. Chapter 2 briefly describes the development of the HOC explicit jump immersed interface method (HEJIIM) for the elliptic interface problems on a Cartesian mesh. In Chapter 3, we validate and check the robustness of the formulation by applying HEJIIM to seven test cases. Chapter 4 explores the development of the transient version of HEJIIM to incompressible viscous flows involving multiple and moving bodies as well. Chapter 5 deals with discrete level set approach for the incompressible viscous flows on non-uniform grid. In Chapter 6, we simulate heat and fluid flow resulting from the forced convection over a heated elliptical cylinder with an angle of incidence in a uniform flow. Finally, chapter 7 concludes the entire work and provides the outlines the scope of future work.

2

A novel Higher Order Compact-immersed interface approach for elliptic problems

In this chapter[1], we propose a new higher-order compact, explicit jump finite difference Immersed Interface Method (HEJIIM) for solving two-dimensional elliptic problems with singular source and discontinuous coefficients in the irregular region on Cartesian mesh. Contrary to the schemes in [114, 115], the proposed scheme maintains its compactness on a nine point stencil at both the regular and irregular points. In order to treat the jump across the interface, we modified the explicit jump immersed interface strategy of Wiegmann and Bube [179] in such a way that fourth order accuracy is retained throughout the whole computational domain.

2.1 Mathematical formulation

The conservative form of an elliptic equation in two dimensions is given by

$$(\beta u_x)_x+(\beta u_y)_y+\kappa(x,y)u = f(x,y)+\sigma\delta\{(x-x^*)(y-y^*)\}(x,y)\in\Omega\,,\quad (x^*,y^*)\in\Gamma. \tag{2.1}$$

where Γ is an interface embedded in a rectangular domain $\Omega=[x_0,x_f]\times[y_0,y_f]$ with defined boundary conditions. The coefficients $\beta(x,y)$, $\kappa(x,y)$ and $f(x,y)$ may be non smooth functions or may have discontinuities across the interface Γ leading to discontinuities in the solution and its derivatives at the interface. To solve an interface problem we generally require two physical jump conditions in the solution u and in the normal

---

[1] Published in [164].

direction to the interface which is defined by:

$$[u] = \lim_{(x,y)\to\Gamma^+} u(x,y) - \lim_{(x,y)\to\Gamma^-} u(x,y) = u^+ - u^- = \hat{S}, \tag{2.2}$$

$$[\beta u_n] = \lim_{(x,y)\to\Gamma^+} \beta u_n(x,y) - \lim_{(x,y)\to\Gamma^-} \beta u_n(x,y) = \beta^+ \frac{\partial u^+}{\partial n} - \beta^- \frac{\partial u^-}{\partial n} = \sigma \tag{2.3}$$

where $\hat{S}$ and σ are strength and flux of the variable u respectively. Here $(x, y) \to \Gamma^+$ represents that interface is approaching from Ω^+ and vice versa for $(x, y) \to \Gamma^-$.

In order to capture the interface Γ, Osher and Sethian [125] conceived a function, widely known as the **Level-Set function**. The interface divides Ω into two sub-domains Ω^- and Ω^+ and therefore $\Omega = \Omega^- \cup \Gamma \cup \Omega^+$. We use zero level set for a two dimensional function $\phi(x, y)$ to represent the interface, i.e

$$\begin{cases} \phi(x,y) < 0 & \text{if } (x,y) \in \Omega^-, \\ \phi(x,y) = 0 & \text{if } (x,y) \in \Gamma, \\ \phi(x,y) > 0 & \text{if } (x,y) \in \Omega^+. \end{cases} \tag{2.4}$$

The schematic of the level-set function representing the interface and the sub-domains in the computational plane can be seen in figure 2.1(a). Here (η, ξ) represents the local coordinate system at an interfacial point $(x^\star, y^\star)$ with each of them representing the tangent and normal direction respectively at the point along the interface. For approximating the jump conditions eq(2.3) on a Cartesian mesh at the point $(x^\star, y^\star)$,

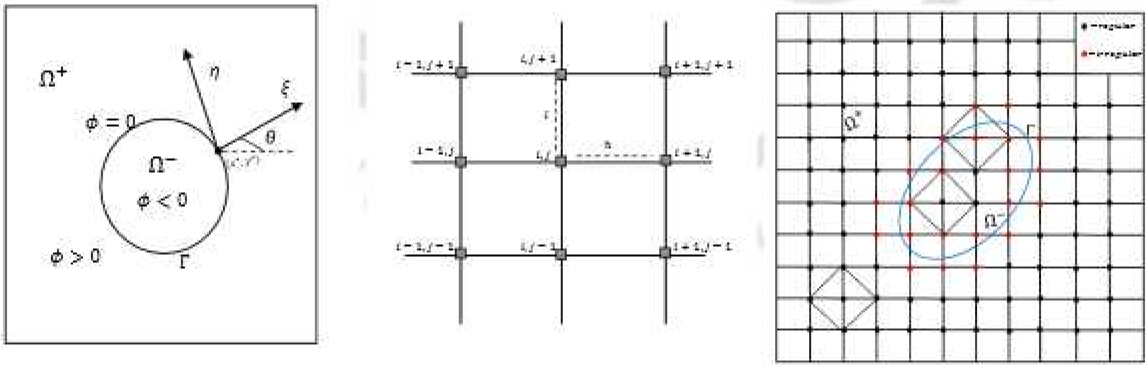

(a) (b) (c)

Figure 2.1: *(a) Schematic of the level-set function along with the local coordinates on an interfacial point, (b) the compact HOC nine point stencil and, (c) regular and irregular points.*

we have

$$\begin{aligned} \xi = &\quad (x - x^\star)cos(\theta) + (y - y^\star)sin(\theta), \qquad (2.5) \\ \eta = &\quad -(x - x^\star)sin(\theta) + (y - y^\star)cos(\theta). \qquad (2.6) \end{aligned}$$

where θ is the angle between x-axis and ξ-direction. The jump conditions for the derivatives up to third order can be calculated by the following formulas.

$$\begin{pmatrix} [u_x] \\ [u_y] \end{pmatrix} = \begin{pmatrix} c & -s \\ s & c \end{pmatrix} \begin{pmatrix} [u_\xi] \\ [u_\eta] \end{pmatrix},$$

$$\begin{pmatrix} [u_{xx}] \\ [u_{xy}] \\ [u_{yy}] \end{pmatrix} = \begin{pmatrix} c^2 & -2cs & s^2 \\ cs & c^2 - s^2 & -cs \\ s^2 & 2cs & c^2 \end{pmatrix} \begin{pmatrix} [u_{\xi\xi}] \\ [u_{\xi\eta}] \\ [u_{\eta\eta}] \end{pmatrix},$$

$$\begin{pmatrix} [u_{xxx}] \\ [u_{xxy}] \\ [u_{xyy}] \\ [u_{yyy}] \end{pmatrix} = \begin{pmatrix} c^3 & -3c^2s & 3cs^2 & -s^3 \\ c^2s & c^3 - 2cs^2 & s^3 - 2c^2s & cs^2 \\ cs^2 & 2c^2s - s^3 & c^3 - 2cs^2 & -cs^2 \\ s^3 & 3s^2c & 3c^2s & c^3 \end{pmatrix} \begin{pmatrix} [u_{\xi\xi\xi}] \\ [u_{\xi\xi\eta}] \\ [u_{\xi\eta\eta}] \\ [u_{\eta\eta\eta}] \end{pmatrix}.$$

where $c = cos(\theta)$ and $s = sin(\theta)$. The non conservative form of equation (2.1) can be written as

$$\beta(u_{xx} + u_{yy}) + c(x, y)u_x + d(x, y)u_y + \kappa(x, y)u = f(x, y). \qquad (2.7)$$

where $c(x, y) = \frac{\partial\beta(x,y)}{\partial x}$ and $d(x, y) = \frac{\partial\beta(x,y)}{\partial y}$. We discretize the domain Ω by vertical and horizontal lines passing through the points (x_i, y_j) given by

$$x_i = x_0 + ih, \quad y_j = y_0 + jl, \quad i = 0, 1, 2, ..., M \quad \text{and} \quad j = 0, 1, 2, ..., N \qquad (2.8)$$

The mesh length along x- and y-directions are defined as $h = \dfrac{x_f - x_0}{M - 1}$ and $l = \dfrac{y_f - y_0}{N - 1}$ respectively (see figure 2.1(a)). In order to a derive a higher-order finite difference scheme on a compact stencil, we divide the grid points into the two following categories : regular and irregular points. A point (i, j) in the computational grid is said to be a regular point if the interface Γ does not cross the standard five point stencil centered at

(i,j). In other words, if the grid points of the five point stencil share the same side of the interface either in Ω^- or Ω^+ then it is called a regular point, and if it shares both sides, then it is an irregular point. We show the regular and irregular points in figure 2.1(c), where the grid points marked red are irregular points and all the other points (marked black) are regular points. Mathematically, $\phi_{ij}^{max}\phi_{ij}^{min} \leq 0$, where

$$\phi_{ij}^{min} = min\{\phi_{i+1}, \phi_{i-1}, \phi_{j+1}, \phi_{j-1}\}, \tag{2.9}$$

$$\phi_{ij}^{max} = max\{\phi_{i+1}, \phi_{i-1}, \phi_{j+1}, \phi_{j-1}\}. \tag{2.10}$$

As mentioned earlier, a compact finite difference scheme [62, 63, 75–77] utilizes grid points located only one step length away from the point about which the finite difference is considered. Additionally, if the order of accuracy is more than two the scheme is termed as a HOC scheme. For discretizing equation (2.7) at regular points, we have reconstructed the HOC formulation developed by Kalita et al. [75] on uniform grids on a nine point stencil shown in figure 2.1(b), which is $O(h^4, l^4)$. At the point (x_i, y_j) on the computational domain, this scheme is given by

$$\left[A_{ij}\delta_x^2 + B_{ij}\delta_y^2 + C_{ij}\delta_x + D_{ij}\delta_y + E_{ij}\delta_x^2\delta_y^2 + H_{ij}\delta_x\delta_y^2 + K_{ij}\delta_x^2\delta_y + L_{ij}\delta_x\delta_y + M_{ij}\right]u_{ij} = F_{ij}. \tag{2.11}$$

where δ_x^2, δ_y^2 , δ_x , δ_y, $\delta_x\delta_y$, $\delta_x\delta_y^2$, $\delta_x^2\delta_y$ and $\delta_x^2\delta_y^2$ are second order accurate central difference operators along x- and y- directions and,

$$A_{ij} =\beta_{ij} + \frac{h^2}{12}\left(2c_x + \kappa_{ij} + \beta_{xx} - \frac{c_{ij}}{\beta_{ij}}(c_{ij} + \beta_x)\right) + \frac{l^2}{12}\left(\beta_{yy} + \frac{d_{ij}}{\beta_{ij}}\beta_y\right), \tag{2.12}$$

$$B_{ij} =\beta_{ij} + \frac{h^2}{12}\left(\beta_{xx} + \frac{c_{ij}}{\beta_{ij}}\beta_c\right) + \frac{l^2}{12}\left(2d_y + \kappa_{ij} + \beta_{yy} - \frac{d_{ij}}{\beta_{ij}}(d_{ij} + \beta_y)\right), \tag{2.13}$$

$$C_{ij} =c_{ij} + \frac{h^2}{12}\left(c_{xx} + 2\kappa_x - \frac{c_{ij}}{\beta_{ij}}(c_x + \kappa_{ij})\right) + \frac{l^2}{12}\left(c_{yy} - \frac{d_{ij}}{\beta_{ij}}c_y\right), \tag{2.14}$$

$$D_{ij} =d_{ij} + \frac{h^2}{12}\left(d_{xx} - \frac{c_{ij}}{\beta_{ij}}d_x\right) + \frac{l^2}{12}\left(d_{yy} + 2\kappa_y - \frac{d_{ij}}{\beta_{ij}}(d_y + \kappa_{ij})\right), \tag{2.15}$$

$$E_{ij} =\beta_{ij}\left(\frac{h^2}{12} + \frac{l^2}{12}\right), \tag{2.16}$$

$$H_{ij} =\frac{h^2}{12}(2\beta_x - c_{ij}) + \frac{l^2}{12}c_{ij}, \tag{2.17}$$

$$K_{ij} =\frac{h^2}{12}d_{ij} + \frac{l^2}{12}(2\beta_y - d_{ij}), \tag{2.18}$$

$$L_{ij} = \frac{h^2}{12}\left(2d_x - \frac{c_{ij}d_{ij}}{\beta_{ij}}\right) + \frac{l^2}{12}\left(2c_y - \frac{c_{ij}d_{ij}}{\beta_{ij}}\right), \tag{2.19}$$

$$M_{ij} = \kappa_{ij} + \frac{h^2}{12\beta_{ij}}(\beta_{ij}\kappa_{xx} - c_{ij}\kappa_x) + \frac{l^2}{12\beta_{ij}}(\beta_{ij}\kappa_{yy} - d_{ij}\kappa_y), \tag{2.20}$$

$$F_{ij} = f_{ij} + \frac{h^2}{12}f_{xx} + \frac{l^2}{12}f_{yy} - \frac{h^2}{12\beta_{ij}}f_x c_{ij} - \frac{l^2}{12\beta_{ij}}f_y d_{ij}. \tag{2.21}$$

On expanding, (2.11) reduces to

$$c_1u_{i-1,j-1} + c_2u_{i,j-1} + c_3u_{i+1,j-1} + c_4u_{i-1,j} + c_5u_{i,j} + c_6u_{i+1,j} + c_7u_{i-1,j+1} + c_8u_{i,j+1} + c_9u_{i+1,j+1} = G_{ij}. \tag{2.22}$$

where $G_{ij} = F_{ij}$ and others coefficients are given by,

$$c_1 = \frac{E_{ij}}{h^2l^2} - \frac{H_{ij}}{2hl^2} - \frac{K_{ij}}{2h^2l} + \frac{L_{ij}}{4hl}, \tag{2.23}$$

$$c_2 = \frac{B_{ij}}{l^2} - \frac{D_{ij}}{2l} - \frac{2E_{ij}}{h^2l^2} + \frac{K_{ij}}{h^2l}, \tag{2.24}$$

$$c_3 = \frac{E_{ij}}{h^2l^2} + \frac{H_{ij}}{2hl^2} - \frac{K_{ij}}{2h^2l} - \frac{L_{ij}}{4hl}, \tag{2.25}$$

$$c_4 = \frac{A_{ij}}{h^2} - \frac{C_{ij}}{2h} - \frac{2E_{ij}}{h^2l^2} + \frac{H_{ij}}{hl^2}, \tag{2.26}$$

$$c_5 = M_{ij} - \frac{2A_{ij}}{h^2} - \frac{2B_{ij}}{l^2} + \frac{4E_{ij}}{h^2l^2}, \tag{2.27}$$

$$c_6 = \frac{A_{ij}}{h^2} + \frac{C_{ij}}{2h} - \frac{2E_{ij}}{h^2l^2} - \frac{H_{ij}}{hl^2}, \tag{2.28}$$

$$c_7 = \frac{E_{ij}}{h^2l^2} + \frac{H_{ij}}{2hl^2} + \frac{K_{ij}}{2h^2l} + \frac{L_{ij}}{4hl}, \tag{2.29}$$

$$c_8 = \frac{B_{ij}}{l^2} + \frac{D_{ij}}{2l} + \frac{2E_{ij}}{h^2l^2} - \frac{K_{ij}}{h^2l}, \tag{2.30}$$

$$c_9 = \frac{E_{ij}}{h^2l^2} - \frac{H_{ij}}{2hl^2} + \frac{K_{ij}}{2h^2l} - \frac{L_{ij}}{4hl}. \tag{2.31}$$

Because of the discontinuity in the solution u at the interface, such an approximation doesn't work at irregular points. Therefore modification is required at these points. At the irregular points, we can have irregularity either in the x- or in y-directions alone, or both x- as well in y-directions at the same time. We modify the above HOC scheme at the irregular points if the interface crosses the finite difference grid in the x- or and y-direction alone, and if it crosses in both the directions simultaneously, we adopt the mechanisms described in the following sections.

2.1.1 Irregular points lying on grid lines parallel to x-axis only

Consider the situation when the irregular point lies only on grid lines parallel to $x-$axis. Suppose we have the interface between (i,j) and $(i+1,j)$ but there can be three possibilities (see Figure 2.2) the interface cut by the grid lines on three interfacial points in the compact stencil i.e $(x_1^\star, y_{j+1})$ lies between (x_i, y_{j+1}) and (x_{i+1}, y_{j+1}) , $(x_2^\star, y_j)$ lies between (x_i, y_j), (x_{i+1}, y_j) and $(x_3^\star, y_{j-1})$ lies between (x_i, y_{j-1}), (x_{i+1}, y_{j-1}). Since all six points lie on left of the interface (refer to case 1 of figure 2.2) having same sign of ϕ function, we need to approximate $u(x_{i+1}, y_{j+1})$, $u(x_{i+1}, y_j)$ and $u(x_{i+1}, y_{j-1})$ to the point (x_i, y_j) using Taylor series expansions. We prove the following lemma, which will allow us to approximate higher-order derivatives including mixed derivatives resulting from discretization.

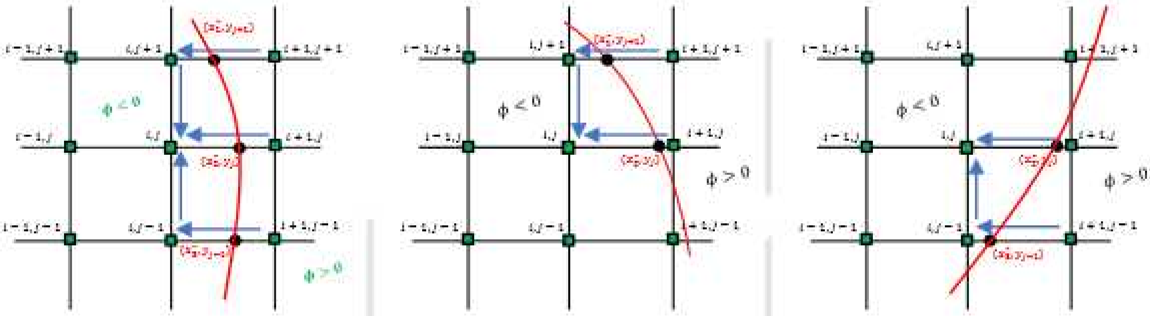

Case 1 Case 2 Case 3

Figure 2.2: *Stencils for irregular points lying on grid lines parallel to x-axis only.*

Lemma 2.1.1. *Consider the interface lie between (i,j) and $(i+1,j)$. Assume $u^- \in C^{k+1}[x_0, x_1^\star] \times [y_0, y_f]$, $u^+ \in C^{k+1}[x_1^\star, x_f] \times [y_0, y_f]$, $h_1^+ = x_{i+1} - x_1^\star$ and $h_1^- = x_i - x_1^\star$ then we have the following inequality*

$$\left\| u(x_{i+1}, y_{j+1}) - \sum_{p=0}^{k} \sum_{q=0}^{k-p} \frac{h^p l^q}{p!\, q!} \frac{\partial^{p+q} u}{\partial x^p \partial y^q}(x_i, y_j) - \sum_{n=0}^{k} \frac{(h_1^+)^n}{n!} \left[\frac{\partial^n u}{\partial x^n}(x_1^\star, y_{j+1}) \right] \right\| \leq K \frac{h^{k+1}}{(k+1)!} + \frac{M_b}{(k+1)!} (|h|+|l|)^{k+1}. \quad (2.32)$$

where $K = \max(\max_{x\in[x_i,x_1^\star)} \mid u^{k+1}(x_1^\star, y_{j+1}) \mid \, , \, \max_{x\in(x_1^\star,x_{i+1}]} \mid u^{k+1}(x_1^\star, y_{j+1}) \mid)$.

Proof. Using Taylor expansions for u^+ at $(x_1^\star, y_{j+1})$ in x- direction

$$u(x_{i+1}, y_{j+1}) = \sum_{n=0}^{k} \frac{(h_1^+)^n}{n!} \frac{\partial^n u^+}{\partial x^n}(x_1^\star, y_{j+1}) + \frac{\partial^{k+1} u^+}{\partial x^{k+1}}(\xi_{k+1}, y_{j+1}) \frac{(h_1^+)^{k+1}}{(k+1)!} \tag{2.33}$$

for some $\xi_{k+1} \in ((x_1^\star, x_{i+1}), y_{j+1})$. Also, we know that

$$\frac{\partial^n u^+}{\partial x^n}(x_1^\star, y_{j+1}) = \frac{\partial^n u^-}{\partial x^n}(x_1^\star, y_{j+1}) + \left[\frac{\partial^n u}{\partial x^n}(x_1^\star, y_{j+1})\right]. \tag{2.34}$$

substituting (2.34) in (2.33), we have

$$\begin{aligned} u(x_{i+1}, y_{j+1}) = \sum_{n=0}^{k} \frac{(h_1^+)^n}{n!} &\left(\frac{\partial^n u^-}{\partial x^n}(x_1^\star, y_{j+1}) + \left[\frac{\partial^n u}{\partial x^n}(x_1^\star, y_{j+1})\right] \right) \\ &+ \frac{\partial^{k+1} u^+}{\partial x^{k+1}}(\xi_{k+1}, y_{j+1}) \frac{(h_1^+)^{k+1}}{(k+1)!}, \end{aligned} \tag{2.35}$$

Taylor expansions of u^- at (x_i, y_{j+1}) yields for $n = 0, 1, 2, ...k$

$$\frac{\partial^n u^-}{\partial x^n}(x_1^\star, y_{j+1}) = \sum_{i=n}^{k} \frac{(-h_1^-)^{i-n}}{(i-n)!} \frac{\partial^i u^-}{\partial x^i}(x_i, y_{j+1}) + \frac{(-h_1^-)^{k-n+1}}{(k-n+1)!} \frac{\partial^{k+1} u^-}{\partial x^{k+1}}(\xi_m, y_{j+1}), \tag{2.36}$$

for some $\xi_m \in ((x_i, x_1^\star), y_{j+1})$. Since this point lies on the left side of the interface, we can replace u^- simply by u. Making use of relation (2.36) in (2.35), therefore

$$\begin{aligned} u(x_{i+1}, y_{j+1}) = &\sum_{n=0}^{k} \frac{(h_1^+)^n}{n!} \left(\sum_{i=n}^{k} \frac{(-h_1^-)^{i-n}}{(i-n)!} \frac{\partial^i u}{\partial x^i}(x_i, y_{j+1}) \right) + \sum_{n=0}^{k} \frac{(h_1^+)^n}{n!} \left[\frac{\partial^n u}{\partial x^n}(x_1^\star, y_{j+1})\right] \\ &+ \sum_{n=0}^{k} \frac{(h_1^+)^n}{n!} \frac{(-h_1^-)^{k-n+1}}{(k-n+1)!} \frac{\partial^{k+1} u^-}{\partial x^{k+1}}(\xi_m, y_{j+1}) + \frac{(h_1^+)^{k+1}}{(k+1)!} \frac{\partial^{k+1} u}{\partial x^{k+1}}(\xi_{k+1}, y_{j+1}). \end{aligned} \tag{2.37}$$

Now

$$\sum_{n=0}^{k} \frac{(h_1^+)^n}{n!} \left(\sum_{i=n}^{k} \frac{(-h_1^-)^{i-n}}{(i-n)!} \frac{\partial^i u}{\partial x^i}(x_i, y_{j+1}) \right) = u^{(0)}(x_i, y_{j+1}) + \left(\frac{h_1^+}{1!} + \frac{(-h_1^-)}{1!} \right) \frac{\partial u}{\partial x}(x_i, y_{j+1})$$

$$+\left(\frac{(h_1^+)^2}{2!}+\frac{h_1^+(-h_1^-)}{1!\,1!}+\frac{(h_1^-)^2}{2!}\right)\frac{\partial^2 u}{\partial x^2}(x_i,y_{j+1})+\dots$$
$$+\frac{\partial^k u}{\partial x^k}(x_i,y_{j+1})\left(\frac{(-h_1^-)^k}{k!}+\frac{h_1^+(-h_1^-)^{k-1}}{1!\,(k-1)!}+\frac{(h_1^+)^2(-h_1^-)^{k-2}}{2!\,(k-2)!}+\dots\frac{(h_1^+)^{k-1}(-h_1^-)}{(k-1)!}+\frac{(h_1^+)^k}{k!}\right), \tag{2.38}$$

$$=u^{(0)}(x_i,y_{j+1})+\frac{h^1}{1!}\frac{\partial u}{\partial x}(x_i,y_{j+1})+\dots\quad+\frac{h^k}{k!}\frac{\partial^k u}{\partial x^k}(x_i,y_{j+1}), \tag{2.39}$$

on applying the Binomial expansion, it becomes

$$\sum_{n=0}^{k}\frac{(h_1^+)^n}{n!}\left(\sum_{i=n}^{k}\frac{(-h_1^-)^{i-n}}{(i-n)!}\frac{\partial^i u}{\partial x^i}(x_i,y_{j+1})\right)=\sum_{p=0}^{k}\frac{h^p}{p!}\frac{\partial^p u}{\partial x^p}(x_i,y_{j+1}). \tag{2.40}$$

using (2.40) in (2.37)

$$u(x_{i+1},y_{j+1})=\sum_{p=0}^{k}\frac{h^p}{p!}\frac{\partial^p u}{\partial x^p}(x_i,y_{j+1})+\sum_{n=0}^{k}\frac{(h_1^+)^n}{n!}\left[\frac{\partial^n u}{\partial x^n}(x_1^\star,y_{j+1})\right]$$
$$+\sum_{n=0}^{k}\frac{(h_1^+)^n(-h_1^-)^{k-n+1}}{n!\,(k-n+1)!}\frac{\partial^{k+1}u^-}{\partial x^{k+1}}(\xi_m,y_{j+1})+\frac{(h_1^+)^{k+1}}{(k+1)!}\frac{\partial^{k+1}u}{\partial x^{k+1}}(\xi_{k+1},y_{j+1}). \tag{2.41}$$

Now we apply the Taylor series expansion for the first part of the above equation in y-direction and $p+q\leq n$ i.e

$$\sum_{p=0}^{k}\frac{h^p}{p!}\frac{\partial^p u}{\partial x^p}(x_i,y_{j+1})=\sum_{p=0}^{k}\sum_{q=0}^{k-p}\frac{h^p l^q}{p!\,q!}\frac{\partial^{p+q}u}{\partial x^p\partial y^q}(x_i,y_j)+\frac{1}{(k+1)!}U^{k+1}(\eta). \tag{2.42}$$

Suppose that all the partial derivative of u of order $(k+1)$ is bounded by M_b,

$$|U^{k+1}(\eta)|=\left|\sum_{r=0}^{k+1}\binom{k+1}{r}h^r l^{k+1-r}\frac{\partial^{(k+1)}u}{\partial x^r\partial y^{k+1-r}}(\eta)\right|\leq M_b(|h|+|l|)^{k+1}. \tag{2.43}$$

Substituting (2.43) into (2.42) and (2.42) into (2.41)

$$u(x_{i+1},y_{j+1})=\sum_{p=0}^{k}\sum_{q=0}^{k-p}\frac{h^p l^q}{p!\,q!}\frac{\partial^{p+q}u}{\partial x^p\partial y^q}(x_i,y_j)$$

$$+\frac{M_b}{(k+1)!}(|h|+|l|)^{k+1}+\sum_{n=0}^{k}\frac{(h_1^+)^n}{n!}\left[\frac{\partial^n u}{\partial x^n}(x_1^\star,y_{j+1})\right]$$
$$+\sum_{n=0}^{k}\frac{\partial^{k+1}u}{\partial x^{k+1}}(\xi_m,y_{j+1})\frac{(h_1^+)^n(-h_1^-)^{k-n+1}}{n!\,(k-n+1)!}+\frac{\partial^{k+1}u}{\partial x^{k+1}}(\xi_{k+1},y_{j+1})\frac{(h_1^+)^{k+1}}{(k+1)!}, \tag{2.44}$$

Letting $K{=}max(max_{x\epsilon[x_i,x_1^\star)}\mid u^{k+1}(x_1^\star,y_{j+1})\mid,\ max_{x\epsilon(x_1^\star,x_{i+1}]}\mid u^{k+1}(x_1^\star,y_{j+1})\mid)$

$$\sum_{n=0}^{k}\frac{\partial^{k+1}u}{\partial x^{k+1}}(\xi_m,y_{j+1})\frac{(h_1^+)^n(-h_1^-)^{k-n+1}}{n!\,(k-n+1)!}+\frac{\partial^{k+1}u}{\partial x^{k+1}}(\xi_{k+1},y_{j+1})\frac{(h_1^+)^{k+1}}{(k+1)!}\leq$$
$$K\sum_{n=0}^{k+1}\frac{(h_1^+)^n(-h_1^-)^{k-n+1}}{n!\,(k-n+1)!}\leq K\frac{h^{k+1}}{(k+1)!}. \tag{2.45}$$

Substituting (2.45) into (2.44) and get the desired result. ☐

Remark 2.1.1. *Let* $h_3^+=x_{i+1}-x_3^\star$ *and* $h_3^-{=}x_i-x_3^\star$ *then we have the following inequality*

$$\left\|u(x_{i+1},y_{j-1})-\sum_{p=0}^{k}\sum_{q=0}^{k-p}\frac{h^p(-l)^q}{p!\,q!}\frac{\partial^{p+q}u}{\partial x^p\partial y^q}(x_i,y_j)-\sum_{n=0}^{k}\frac{(h_3^+)^n}{n!}\left[\frac{\partial^n u}{\partial x^n}(x_3^\star,y_{j-1})\right]\right\|\leq O(h^{k+1},l^{k+1}).$$

Remark 2.1.2. *Similarly, for the other side of the interface.*

$$\left\|u(x_{i-1},y_{j+1})-\sum_{p=0}^{k}\sum_{q=0}^{k-p}\frac{(-h)^p l^q}{p!\,q!}\frac{\partial^{p+q}u}{\partial x^p\partial y^q}(x_i,y_j)+\sum_{n=0}^{k}\frac{(h_1^-)^n}{n!}\left[\frac{\partial^n u}{\partial x^n}(x_1^\star,y_{j+1})\right]\right\|\leq O(h^{k+1},l^{k+1}).$$

$$\left\|u(x_{i-1},y_{j-1})-\sum_{p=0}^{k}\sum_{q=0}^{k-p}\frac{(-h)^p(-l)^q}{p!\,q!}\frac{\partial^{p+q}u}{\partial x^p\partial y^q}(x_i,y_j)+\sum_{n=0}^{k}\frac{(h_3^-)^n}{n!}\left[\frac{\partial^n u}{\partial x^n}(x_3^\star,y_{j-1})\right]\right\|\leq O(h^{k+1},l^{k+1}).$$

Now, we approximate the mixed derivative u_{xy} at the point (x_i, y_j) using the Lemma (2.1.1) and Remark (4.2.1)

$$u_{xy}(x_i, y_j) = \frac{u_{i+1,j+1} - u_{i+1,j-1} - u_{i-1,j+1} + u_{i-1,j-1}}{4hl} - \frac{1}{4hl}\left(C_1x - C_3x\right) + O(h^2, l^2), \tag{2.46}$$

$$\begin{aligned} u_{xxy}(x_i, y_j) =& \frac{u_{i,j-1} - u_{i,j+1}}{h^2 l} + \frac{u_{i+1,j+1} - u_{i+1,j-1} + u_{i-1,j+1} - u_{i-1,j-1}}{2h^2 l} \\ &- \frac{1}{2h^2 l}\left(C_1x - C_3x\right) + O(h^2, l^2), \end{aligned} \tag{2.47}$$

$$\begin{aligned} u_{xyy}(x_i, y_j) =& \frac{u_{i-1,j} - u_{i+1,j}}{hl^2} + \frac{u_{i+1,j+1} + u_{i+1,j-1} - u_{i-1,j+1} - u_{i-1,j-1}}{2hl^2} \\ &- \frac{1}{2hl^2}\left(C_1x - 2C_2x + C_3x\right) + O(h^2, l^2), \end{aligned} \tag{2.48}$$

$$\begin{aligned} u_{xxyy}(x_i, y_j) =& \frac{4u_{i,j} - 2(u_{i-1,j} + u_{i+1,j} + u_{i,j-1} + u_{i,j+1})}{h^2 l^2} \\ &+ \frac{u_{i+1,j+1} + u_{i+1,j-1} + u_{i-1,j+1} + u_{i-1,j-1}}{h^2 l^2} \\ &- \frac{1}{h^2 l^2}\left(C_1x - 2C_2x + C_3x\right) + O(h^2, l^2). \end{aligned} \tag{2.49}$$

Similarly, other operators in equation (2.11) can also be approximated. Depending on how the interface crosses the grid-lines as depicted in figure 2.2, the right hand side of equation (2.22) can be rewritten.
Case 1: $G_{ij} = F_{ij} + c_9C_1x + c_6C_2x + c_3C_3x$,
Case 2: $G_{ij} = F_{ij} + c_9C_1x + c_6C_2x$, and
Case 3: $G_{ij} = F_{ij} + c_6C_2x + c_3C_3x$.
which shows that the jumps can be obtained explicitly at the irregular points, where the jump corrections are given by

$$C_1x = \sum_{n=0}^{k} \frac{(h_1^+)^n}{n!}\left[\frac{\partial^n u}{\partial x^n}(x_1^\star, y_{j+1})\right], \tag{2.50}$$

$$C_2x = \sum_{n=0}^{k} \frac{(h_2^+)^n}{n!}\left[\frac{\partial^n u}{\partial x^n}(x_2^\star, y_j)\right], \tag{2.51}$$

$$C_3x = \sum_{n=0}^{k} \frac{(h_3^+)^n}{n!}\left[\frac{\partial^n u}{\partial x^n}(x_3^\star, y_{j-1})\right]. \tag{2.52}$$

with $h_2^+ = x_{i+1} - x_2^\star$. A close look at the equations (2.1.1)-(2.49) along with the above jump correction would reveal that by choosing $k = 3$ in those expressions, equation (2.11) yields an $O(h^4, l^4)$ approximation at the irregular points as well. The same conclusions can be drawn from the irregular points across the other side of the interface as well as would be seen in sections 2.1.2 and 2.1.3.

2.1.2 Irregular points lying on grid lines parallel to y-axis only

In this section we discuss the scenarios when the irregularity lies only on points lying on grid lines parallel to y-axis. Let the interface cut between (i, j) and $(i, j+1)$ points. Similar to the cases related to x-axis, one can have three possibilities here also: the interface being cut by the grid lines on three interfacial points in the compact stencil i.e $(x_{i-1}, y_1^\star)$ lying between (x_{i-1}, y_j) and (x_{i-1}, y_{j+1}), $(x_i, y_2^\star)$ lying between (x_i, y_j), (x_i, y_{j+1}) and $(x_{i+1}, y_3^\star)$ lies between (x_{i+1}, y_j), (x_{i+1}, y_{j+1}). We approximate $u(x_{i-1}, y_{j+1})$, $u(x_i, y_{j+1})$ and $u(x_{i+1}, y_{j+1})$ to the point (x_i, y_j) by using following lemma:

Lemma 2.1.2. *Consider the interface lie between (i, j) and $(i, j+1)$. Assume $u^- \in C^{k+1}[x_0, x_f] \times [y_0, y_1^\star]$, $u^+ \in C^{k+1}[x_0, x_f] \times [y_1^\star, d]$, $k_1^+ = y_{j+1} - y_1^\star$ and $k_1^- = y_j - y_1^\star$ then we have the following inequality*

$$\left\| u(x_{i-1}, y_{j+1}) - \sum_{p=0}^{k} \sum_{q=0}^{k-p} \frac{(-h)^p l^q}{p!\,q!} \frac{\partial^{p+q} u}{\partial x^p \partial y^q}(x_i, y_j) + \sum_{n=0}^{k} \frac{(k_1^-)^n}{n!} \left[\frac{\partial^n u}{\partial y^n}(x_{i-1}, y_1^\star) \right] \right\| \leq K \frac{l^{k+1}}{(k+1)!} + \frac{M_b}{(k+1)!} (|h| + |l|)^{k+1}$$

where $K = \max(\max_{y \in [y_j, y_1^\star)} \mid u^{k+1}(x_{i-1}, y_1^\star) \mid , \max_{y \in (y_1^\star, y_{j+1}]} \mid u^{k+1}(x_{i-1}, y_1^\star) \mid)$

Proof. Similar to the proof of Lemma 2.1.1; firstly one has to apply Taylor series expansion in the y-direction followed by an expansion along x-direction. □

Other approximation can be derived in same way as in the previous section. With these, the right hand side of equation (2.22) can be written as
Case 4: $G_{ij} = F_{ij} - c_9 C_3 y - c_8 C_2 y - c_7 C_1 y$,
Case 5: $G_{ij} = F_{ij} - c_7 C_1 y - c_8 C_2 y$, and
Case 6: $G_{ij} = F_{ij} - c_9 C_3 y - c_8 C_2 y$.

$$C_1 y = \sum_{n=0}^{k} \frac{(k_1^-)^n}{n!} \left[\frac{\partial^n u}{\partial y^n}(x_{i-1}, y_1^\star) \right], \tag{2.53}$$

$$C_2y = \sum_{n=0}^{k} \frac{(k_2^-)^n}{n!} \left[\frac{\partial^n u}{\partial y^n}(x_i, y_2^\star) \right], \tag{2.54}$$

$$C_3y = \sum_{n=0}^{k} \frac{(k_3^-)^n}{n!} \left[\frac{\partial^n u}{\partial y^n}(x_{i+1}, y_3^\star) \right]. \tag{2.55}$$

where $k_2^- = y_j - y_2^\star$, $k_3^- = y_j - y_3^\star$.

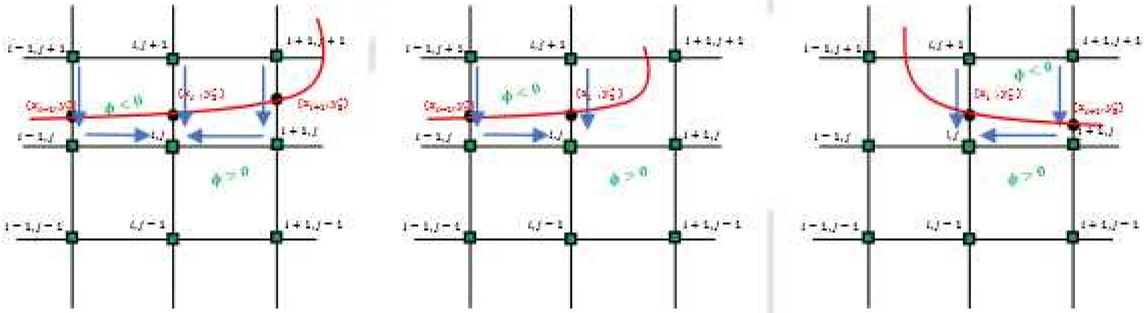

Case 4 Case 5 Case 6

Figure 2.3: *Stencils for irregular points lying on grid lines parallel to y-axis only.*

A close look at equation (2.46)-(2.49) and the expressions for C_1x, C_2x and C_3x would reveal that the jump conditions involve partial derivatives at the three interfacial points on different y-levels with respect to x only. Likewise, the jump conditions C_1y, C_2y and C_3y above involve partial derivatives on different x-levels with respect to y only. On the other hand, the formula for the approximation of mixed derivatives for jump conditions proposed in the EJIIM of Bube and Weigmann [179] used partial derivatives in both x and y-directions simultaneously. However in actual computations, they used only a five point central difference stencil. This is probably the first time that a nine point compact stencil has been used for the jump conditions at the irregular points across the interface, unlike the SJIIM approach of Colnago *et al.* [33]. As a result, our proposed scheme maintains its compactness over a nine point stencil throughout the whole computational domain. Additionally, it also maintains its fourth order accuracy at both the regular and irregular points.

2.1.3 Irregular points lying simultaneously on grid lines parallel to both x-axis and y-axis

Here we have implemented the higher-order approximation at those points where irregularity lies in x-axis as well in y-axis. We have used above lemma in both the axes simultaneously and followed it by taking the average of the correction terms. The two different cases as depicted in figure 2.4 have the followings in the right hand side of (2.22):

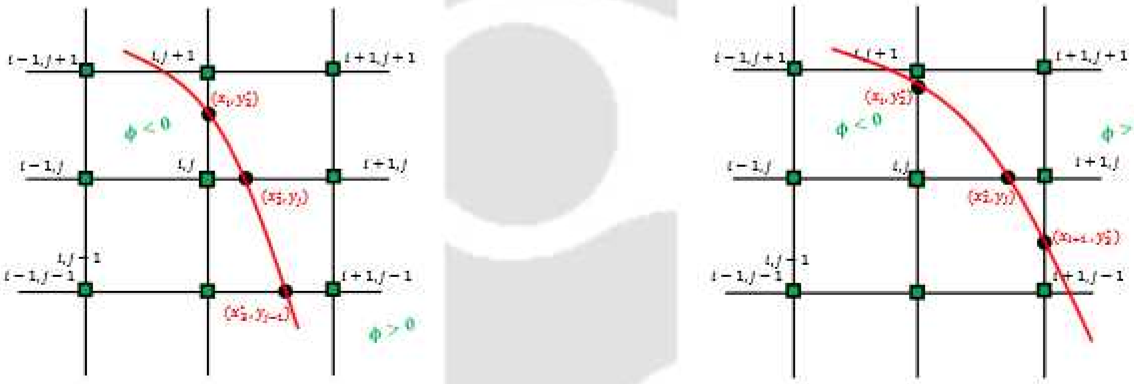

Case 7 Case 8

Figure 2.4: *Stencils for irregular points lying on grid lines parallel to both x-axis and y-axis.*

$$\text{Case7}: \quad \mathrm{G_{ij}} = F_{ij} + c_9(C_2y + C_2x)/2 + c_8C_2y + c_6C_2x + c_3(C_2x + C_3x)/2,$$

$$\text{Case8}: \quad \mathrm{G_{ij}} = F_{ij} + c_9(C_2y + C_2x)/2 + c_8C_2y + c_6C_2x.$$

where C_2x, C_3x are same as defined in Section 2.1.1, and $C_2y = \sum_{n=0}^{k} \frac{(k_2^+)^n}{n!}\left[\frac{\partial^n u}{\partial y^n}(x_i, y_2^\star)\right]$ with $k_2^+ = y_{j+1} - y_2^\star$. In a similar manner, it is easy to derive it for the other cases concerning the interface.

2.2 Solution of algebraic system

The matrix equation resulting from equation (2.22) can be written in the form

$$A\mathbf{u} = \mathbf{b} \tag{2.56}$$

where A is a nona-diagonal matrix whose structure as follows.

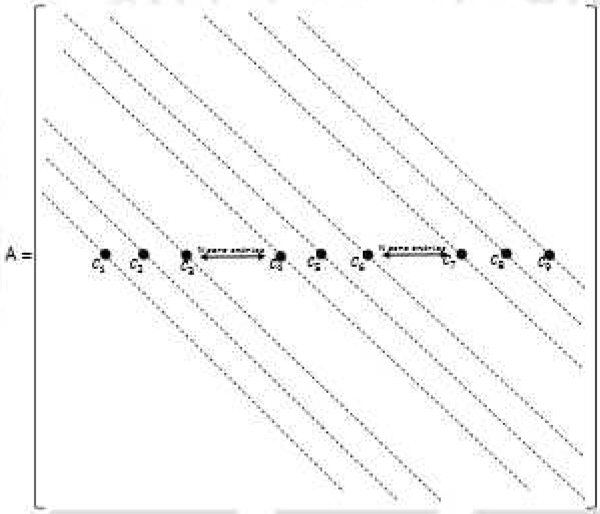

Here one can see that nine non-zero coefficients corresponding to equation (2.22) defined on the stencils shown in figures 2.1(b)-2.4. For a grid of size MN, the coefficient matrix A is of order MN and $\mathbf{u}$ and $\mathbf{b}$ are column matrices of order $MN \times 1$. Equation eq(2.56) can be further decomposed as

$$\begin{bmatrix} A_R & 0 \\ 0 & A_{IR} \end{bmatrix} \begin{bmatrix} \mathbf{u_R} \\ \mathbf{u_{IR}} \end{bmatrix} = \begin{bmatrix} \mathbf{b_R} \\ \mathbf{b_R} + \mathbf{b_C} \end{bmatrix}.$$

The structures of A_R and A_{IR} are similar to A, and $\mathbf{u_R}$ and $\mathbf{u_{IR}}$ are $MN - N_{IR}$ and N_{IR} component vectors, where N_{IR} is the number of irregular points inside the computational domain. Likewise the length of the vectors on the right hand side. Here $\mathbf{b_R}$ corresponds to the term F_{ij} appearing in the list of coefficients following equation (2.22) and $\mathbf{b_C}$ corresponds to the correction terms C_1x, C_2x, C_3x, C_1y, C_2y, and C_3y described in sections 2.1.1, 2.1.2 and 2.1.3. The matrix equation (2.22) is solved by the iterative solver biconjugate gradient stabilized (BiCGStab) [82], where the iterations are stopped when the Euclidean norm of the residual vector $\mathbf{r} = \mathbf{b} - A\mathbf{u}$ arising out of equation (2.22) falls below 10^{-13}.

2.3 Conclusion

In this chapter, we propose a new fourth-order accurate explicit jump Immersed Interface method on a nine point compact stencil for solving two-dimensional elliptic problems with singular source and discontinuous coefficients in the irregular region on a Cartesian mesh. A novel approach for discretizing the solution at irregular places that can be applied to any and all types of irregularities. i.e. irregularities lying along grid lines only parallel to the x-axis or only to the y-axis, or only when it lies on both the axes simultaneously. The second order mix derivatives can also be derived in a manner that is contingent on the nature of the irregularities. The matrix equation $A\mathbf{u} = \mathbf{b}$ resulting from the discretization is such that if the nature of irregularities changes following a change in the shape of the interface, only the vector $\mathbf{b}$ is needed to be modified to accommodate the new scenario, while the matrix A remains the same as presented in the previous section. In the next chapter, we shall examine the efficiency of the proposed scheme by applying it to a wide variety of problems of different complexities.

3

HOC simulation to steady state problems

In this chapter[1], we validate our algorithm resulting from the scheme proposed in Chapter 2, and in the process, apply it to seven test cases. Four of them have analytical solutions while the remaining problems are governed by the highly non-linear Navier-Stokes (N-S) equations, viz., flow past bluff bodies including problems having multiple bodies in the flow domain. The problems have been chosen in such a way that they not only check the robustness of the proposed scheme in terms of tackling the varied nature of the interface geometry, but also in terms of possible discontinuities in the coefficients and the source terms. As the first four problems have analytical solutions, Dirichlet boundary conditions are used for them, whereas for the ones governed by the N-S equations, both Dirichlet and Neumann boundary conditions are applied.

3.1 Numerical examples

3.1.1 Test case 1

We consider the Poisson equation

$$u_{xx} + u_{yy} = 2\int_{\Gamma} \delta(\overrightarrow{x} - \overrightarrow{X}(s))ds \tag{3.1}$$

where the source term has a discontinuity in the form of Dirac delta function along the interface, Γ={(x, y), $x^2 + y^2$=$1/4$}, which is a circle of radius 0.5. The jump conditions are given by $[u]$=0, $[u_n]$=2 and boundary conditions are derived from the analytical

---

[1] Published in [164].

solution

$$u(x,y) = \begin{cases} 1, & \phi \leq 0, \\ 1 + log(2\sqrt{x^2+y^2}), & \phi > 0. \end{cases} \tag{3.2}$$

The level set function ϕ is defined as $\phi(x,y)=x^2+y^2-1/4$.

The surface plots of the computed solution on a grid of size 80×80 is shown in figure 3.1(a). This figure clearly demonstrates the ability of the proposed scheme in resolving the sharp interface. While Berthelsen's decomposed immersed interface method (DIIM) [12] found the use of higher-order differences at the interface complicating the computation owing to more grid points being roped in, our approach, despite using a nine point stencil was seen to capture the solution very efficiently. In table 3.1, we present the results from our computation on grids of sizes $N \times N$ with increasing values of N and compare them with the numerical results of [12, 96, 114, 179]. The maximum error defined as $||E_N||_\infty$, where $||E_N||_\infty = u_{\text{ex}} - u_{\text{num}}$ is a function of the grid size h and rate of convergence (**ROC**) is defined as

$$\text{Order} = \frac{log(\| E_N \|_\infty / \| E_{(N/2)} \|_\infty)}{log(2)}. \tag{3.3}$$

Here $\| E_{N/2} \|_\infty$ is the maximum error of the previous coarser grid having half the number of points in either direction than the current grid size. One can clearly see a much reduced error, decaying at a convergence rate close to four, which is much higher than the ones reported in the existing literature. A graphical representation of the convergence rates of the current scheme along with that of the EJIIM [179] is provided in figure 3.1(b), where the slope of the least square fit line shows the order of accuracy of the respective schemes.

Table 3.1: Grid refinement analysis of maximum error for Test Case 1.

N	Present	ROC	DIIM [12]	ROC	EJIIM [179]	ROC	CIM [29]	ROC
20	7.15×10^{-4}	–	7.88×10^{-4}	–	1.4×10^{-3}	–	7.60×10^{-4}	–
40	7.54×10^{-5}	3.24	2.01×10^{-4}	1.97	1.8×10^{-4}	2.95	2.56×10^{-4}	1.56
80	5.82×10^{-6}	3.69	5.03×10^{-5}	1.99	6.6×10^{-5}	1.44	5.21×10^{-5}	2.29
160	4.17×10^{-7}	3.80	1.26×10^{-5}	2.01	1.9×10^{-5}	1.79	1.14×10^{-5}	2.19
320	2.96×10^{-8}	3.81	3.18×10^{-6}	1.99	3.4×10^{-6}	2.48	2.72×10^{-6}	2.06

In figure 3.2, we exhibit the surface plots of the errors resulting from the current computation on a grid of size 80×80 along with the ones resulting from the EJIIM [179].

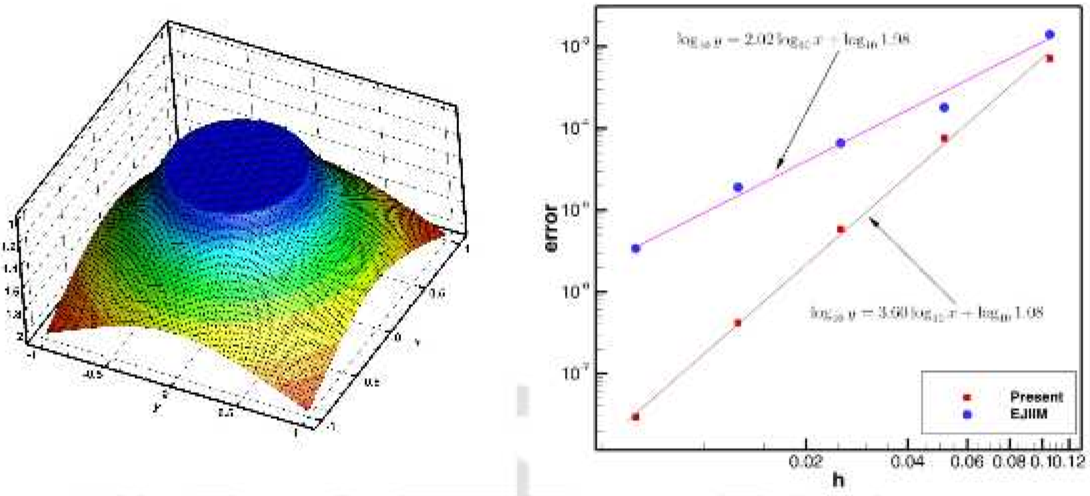

(a) (b)

Figure 3.1: *(a) Surface plots of the numerical solution and the error on grid size* 80×80 *and (b) the convergence results for Test Case 1.*

The relative smoothness of the error in the neighbourhood of the interface along with the drastic reduction of the error clearly demonstrates the efficiency of the current approach over [179]. Further in table 3.2 we have compared the CPU times consumed by the current scheme with EJIIM [179] on different grid sizes for test problem 1. As one can see, the CPU time loss because of the higher-order accuracy of the proposed scheme is minimal. However, in terms of the accuracy of the results, our scheme scores huge gain over EJIIM as the error resulting from our computation decays much faster, which can be seen from figure 3.2 and table 3.1.

Table 3.2: CPU time (in seconds) comparison with EJIIM [179] for Test Case 1.

N	Present	EJIIM [179]
20	0.002	0.002
40	0.004	0.004
80	0.018	0.016
160	0.134	0.115
320	1.523	1.142

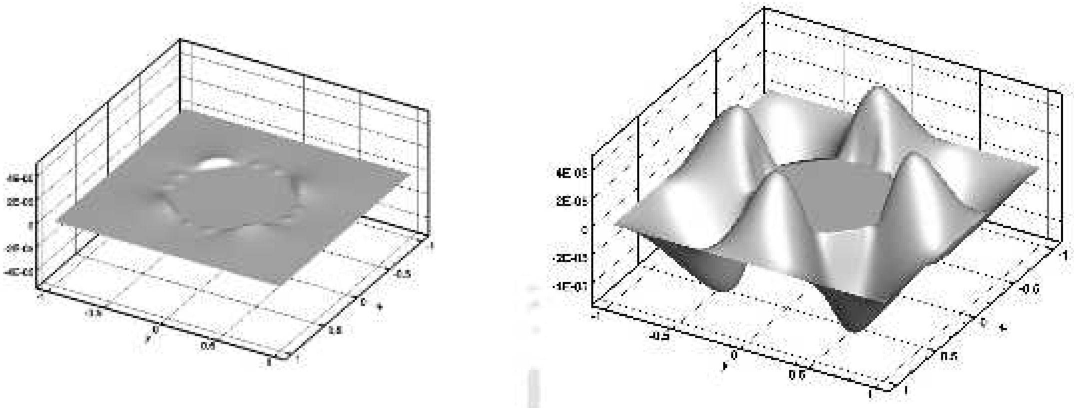

(a) (b)

Figure 3.2: *Error plots on a 80×80 grid by (a) The current approach and (b) EJIIM [179] for Test Case 1.*

3.1.2 Test case 2

Here the differential equation considered is

$$(\beta u_x)_x + (\beta u_y)_y = f(x,y) + S\int_\Gamma \delta(\overrightarrow{x} - \overrightarrow{X}(s))ds \tag{3.4}$$

with $f(x,y) = 8(x^2+y^2)+4$ defined on Ω. δ is the Dirac delta function, S is the strength of the point source at Γ and coefficient β is given by

$$\beta(x,y) = \begin{cases} x^2+y^2+1, & \phi \leq 0, \\ b, & \phi > 0. \end{cases} \tag{3.5}$$

From the above, one can clearly see that the coefficient β is discontinuous across the interface $x^2+y^2=r^2$ with $r=1/2$. The analytical solution to this problem is given by

$$u(x,y) = \begin{cases} r^2, & \phi \leq 0, \\ (1-\frac{1}{8b}-\frac{1}{b})/4 + (\frac{r^4}{2}+r^2)/b + S\log(2r/b), & \phi > 0. \end{cases} \tag{3.6}$$

We show our numerical results for $\beta = 0.001$, 10 and 1000 in tables 3.3-3.5 and figures 3.3-3.4. As in test case 1, when compared with established numerical results

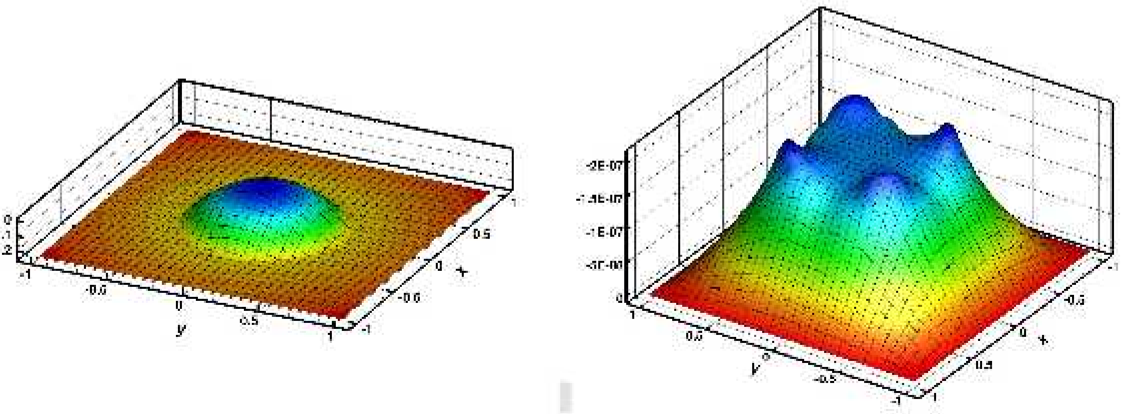

Figure 3.3: *Surface plots of the numerical solution and the error on a grid size* 32×32 *for* $b = 1000$ *for Test Case 2.*

[12, 29, 32, 96, 102, 179], our results fare much better as the tabulated errors on different grid sizes suggest.

Table 3.3: Grid refinement analysis of maximum error for Test Case 2 for $b = 1000$.

N	Present	[115]	CIM [29]	PCM [32]	DIIM [12]	MIM [102]
32	2.10×10^{-7}	1.98×10^{-5}	2.73×10^{-4}	1.82×10^{-4}	2.08×10^{-4}	5.14×10^{-4}
64	2.65×10^{-8}	3.69×10^{-6}	3.88×10^{-5}	4.96×10^{-5}	5.30×10^{-5}	8.24×10^{-5}
128	3.17×10^{-9}	6.72×10^{-7}	5.34×10^{-6}	1.30×10^{-5}	1.33×10^{-5}	1.87×10^{-5}
256	4.32×10^{-10}	1.12×10^{-7}	7.24×10^{-7}	3.33×10^{-6}	3.33×10^{-6}	4.03×10^{-6}

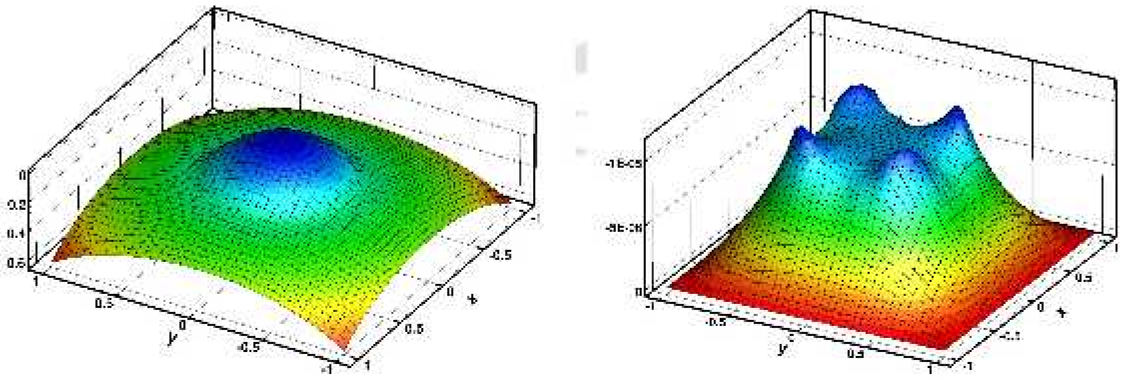

Figure 3.4: *Numerical solution and contour plot of error on grid size* 40×40 *for* $b = 10$ *for Test Case 2.*

Table 3.4: Grid refinement analysis of maximum error for Test Case 2 with $b = 0.001$.

N	Present	[115]	CIM [29]	PCM [32]	DIIM [12]	MIM [102]
32	2.10×10^{-1}	1.26×10^{-1}	4.28×10^{-1}	2.03×10^{0}	4.97×10^{0}	9.35×10^{0}
64	1.95×10^{-2}	2.12×10^{-2}	1.26×10^{-1}	3.52×10^{-1}	1.18×10^{0}	2.01×10^{0}
128	3.11×10^{-3}	3.85×10^{-3}	3.77×10^{-2}	7.25×10^{-2}	2.90×10^{-1}	5.80×10^{-1}
256	4.32×10^{-4}	6.42×10^{-4}	1.36×10^{-2}	1.80×10^{-2}	7.08×10^{-2}	1.37×10^{-1}

Table 3.5: Grid refinement analysis of maximum error for Test Case 2 with $b = 10$ and $S = 0.1$.

N	Present	ROC	PCM [32]	ROC	DIIM [12]	ROC	EJIIM [179]	ROC
20	1.07×10^{-4}	–	4.20×10^{-4}	–	5.36×10^{-4}	–	7.6×10^{-4}	–
40	1.11×10^{-5}	3.26	1.16×10^{-4}	1.85	1.38×10^{-4}	1.95	2.4×10^{-4}	1.66
80	1.30×10^{-6}	3.09	3.75×10^{-5}	1.62	3.47×10^{-5}	1.99	7.90×10^{-5}	1.60
160	1.62×10^{-7}	3.00	5.33×10^{-6}	2.81	8.70×10^{-6}	1.99	2.2×10^{-5}	1.84
320	2.05×10^{-8}	2.98	1.58×10^{-6}	1.75	2.17×10^{-6}	2.01	5.3×10^{-6}	2.05

Table 3.6: Comparison of maximum error for Test Case 2 with Feng et al [50] for $\beta^+ = 10$, $\beta^- = 2$.

N	Present	AMIB [50]
32	2.09×10^{-5}	1.05×10^{-4}
64	2.65×10^{-6}	2.02×10^{-5}
128	3.17×10^{-7}	5.90×10^{-6}
256	5.31×10^{-8}	1.04×10^{-6}

Note that Feng et al. [50] had also solved the above problem with a combination of the MIB [193], Augmented IIM [103] and EJIIM [179] and claimed to have produced faster results. However, apart from the gain in CPU times, they could not improve the order of accuracy and the error as can be seen from table 3.6.

3.1.3 Test case 3

This test case is an example where there are discontinuities both in the diffusion coefficients as well as the source function simultaneously. The equation is given by

$$(\beta u_x)_x + (\beta u_y)_y = f(x, y) \tag{3.7}$$

where the diffusion coefficient β is given by

$$\beta(x,y) = \begin{cases} \beta^-, & \phi \leq 0, \\ \beta^+, & \phi > 0. \end{cases} \tag{3.8}$$

and

$$f(x,y) = \begin{cases} 4/\beta^-, & \phi \leq 0, \\ 16r^2/\beta^+, & \phi > 0. \end{cases} \tag{3.9}$$

The problem has the analytical solution

$$u(x,y) = \begin{cases} \frac{x^2+y^2}{\beta^-}, & \phi \leq 0, \\ \frac{(x^2+y^2)^2+S_0\log(2\sqrt{x^2+y^2})}{\beta^+} + S_1\left(\frac{r_0^2}{\beta^-} - \frac{(x^2+y^2)^2+S_0\log(2r_0)}{\beta^+}\right), & \phi > 0. \end{cases} \tag{3.10}$$

The interface is a star shaped closed curve as shown in figure 3.5 and can be described by the level set function $\phi\,(r,\theta) = r - r_0 - 0.2\sin(w\theta)$, where $r = \sqrt{(x-x_c)^2+(y-y_c)^2}$, $\theta = arctan((y-y_c)/(x-x_c))$, and $x_c = y_c = 0.2/\sqrt{20}$. We study this problem for $r_0 =$ 0.5 and $w =$ 5, 9 and 12. The boundary conditions are derived from analytical solution.

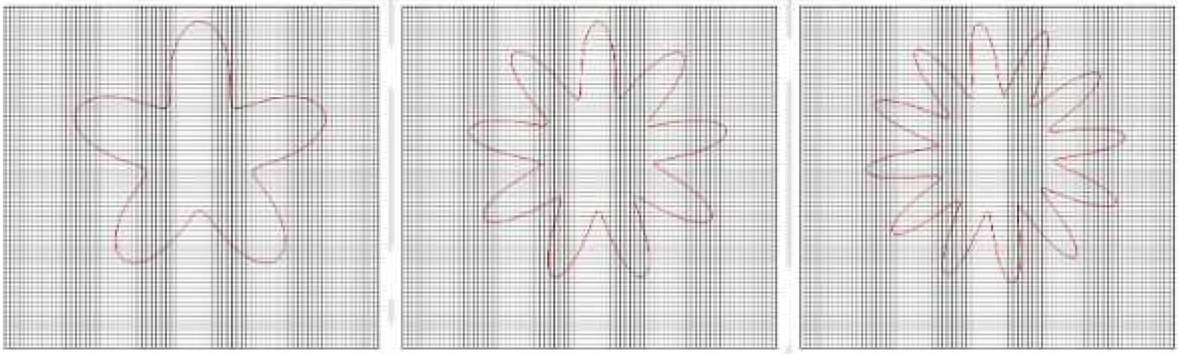

Figure 3.5: *The star shaped five, nine and twelve petal interface of Test Case 3 on a grid of size* 80 × 80.

We compute the solution for different values of $\beta^+ = 2,\ 5,\ 10$ and 10000 with $\beta^- = 1$ such that the robustness of the scheme can be tested for cases with low as well as extremely high jump in the diffusion coefficients β. Our computed solutions are shown in figures 3.6-3.8 along with the surface error plots for the three combinations of

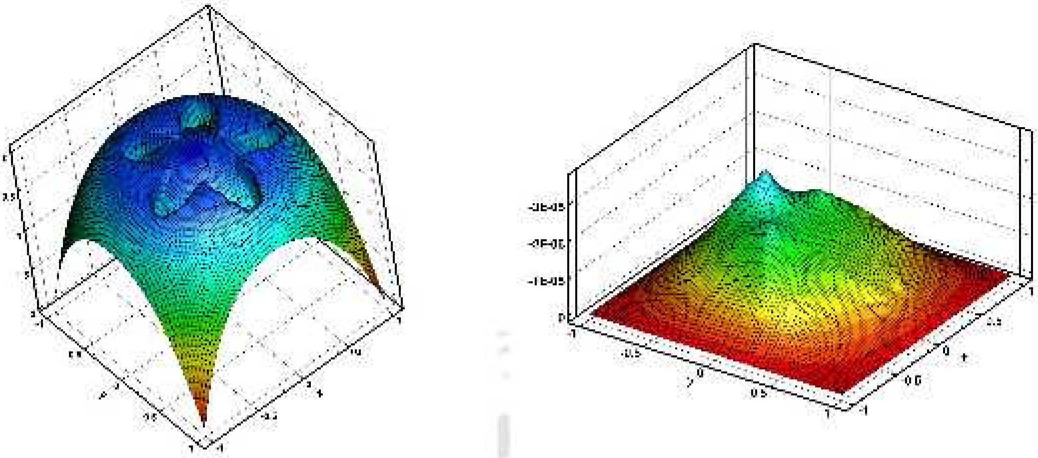

Figure 3.6: *Surface plots of the numerical solution (left) and the error (right) for Test Case 3 with* $\beta^+ = 2$ *on grid size* 80×80.

Table 3.7: Grid refinement analysis of maximum error for Test Case 3 with $\beta^+ = 2$, $\beta^- = 1$, $S_0 = -0.1$, $S_1 = 0$, $r_0 = 0.5$ and $w = 5$.

N	Present	ROC	FIIM [99]	ROC
40	1.82×10^{-4}	–	2.28×10^{-3}	–
80	3.01×10^{-5}	2.59	5.22×10^{-4}	2.12
160	2.87×10^{-6}	3.38	1.26×10^{-4}	2.05
320	4.22×10^{-7}	2.76	2.98×10^{-5}	2.08

Table 3.8: Grid refinement analysis of maximum error for Test Case 3 with $\beta^+ = 10000$, $\beta^- = 1$, $S_0 = -0.1$, $S_1 = 0$, $r_0 = 0.5$ and $w = 5$.

N	Present	FIIM [99]
40	3.64×10^{-7}	6.55×10^{-5}
80	5.57×10^{-8}	7.84×10^{-6}
160	2.16×10^{-8}	5.98×10^{-7}
320	2.51×10^{-9}	5.85×10^{-7}

β^+ and β^- mentioned above. The effect of the jump in β can be clearly observed from these figures. We also compare the maximum error norm on different grid sizes with $N = 40, 80, 160, 320$ for these combinations with those of [49, 99, 115] in tables 3.7-3.9. Once again, one can clearly see that our scheme fare much better than them not only for small jump in β but also for high jumps as well. The effect of the parameter w determining the number of petals can also be seen in figure 3.7.

Table 3.9: Grid refinement analysis of maximum error for Test Case 3 with $\beta^+ = 10$, $\beta^- = 1$, $S_0 = -0.1$, $S_1 = 0$, $r_0 = 0.5$ and $w = 5$.

N	Present	ROC	[115]	ROC	[107]	ROC
40	3.62×10^{-5}	–	7.20×10^{-5}	–	1.67×10^{-4}	–
80	6.01×10^{-6}	2.59	1.75×10^{-5}	2.04	7.35×10^{-5}	1.18
160	5.91×10^{-7}	3.34	4.21×10^{-6}	2.51	–	–
320	1.08×10^{-7}	2.45	8.35×10^{-7}	2.33	–	–

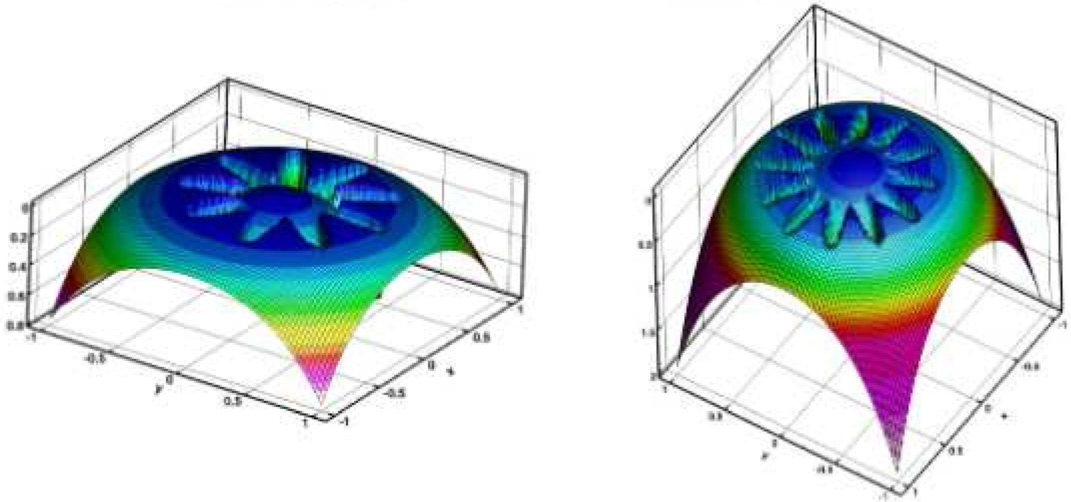

Figure 3.7: *Numerical solution on grid size* 80×80 *for Test Case* 3 *for the combinations* $w = 9$, $\beta^+ = 5$ *and* $w = 12$, $\beta^+ = 2$.

3.1.4 Test case 4

This is an example of a composite material problem with piecewise constant coefficients. This problem is of specific interest in checking the effectiveness of newly developed numerical schemes because of the challenge posed by large differences in material properties. Let

$$u(x, y) = \begin{cases} \frac{2x}{\rho+1+s^2(\rho-1)}, & \phi \leq 0, \\ \frac{x(\rho+1)-s^2(\rho-1)x/(x^2+y^2)}{\rho+1+s^2(\rho-1)}, & \phi > 0. \end{cases} \tag{3.11}$$

where s=0.5, the radius of the same circular interface as described in Test Case 1, and ρ=β^-/β^+. The above is the solution to the Laplace equation $\nabla^2 = 0$ with $[u] = 0$ and $[\beta u_n] = 0$ at the interface and exterior boundary as given in the analytical solution.

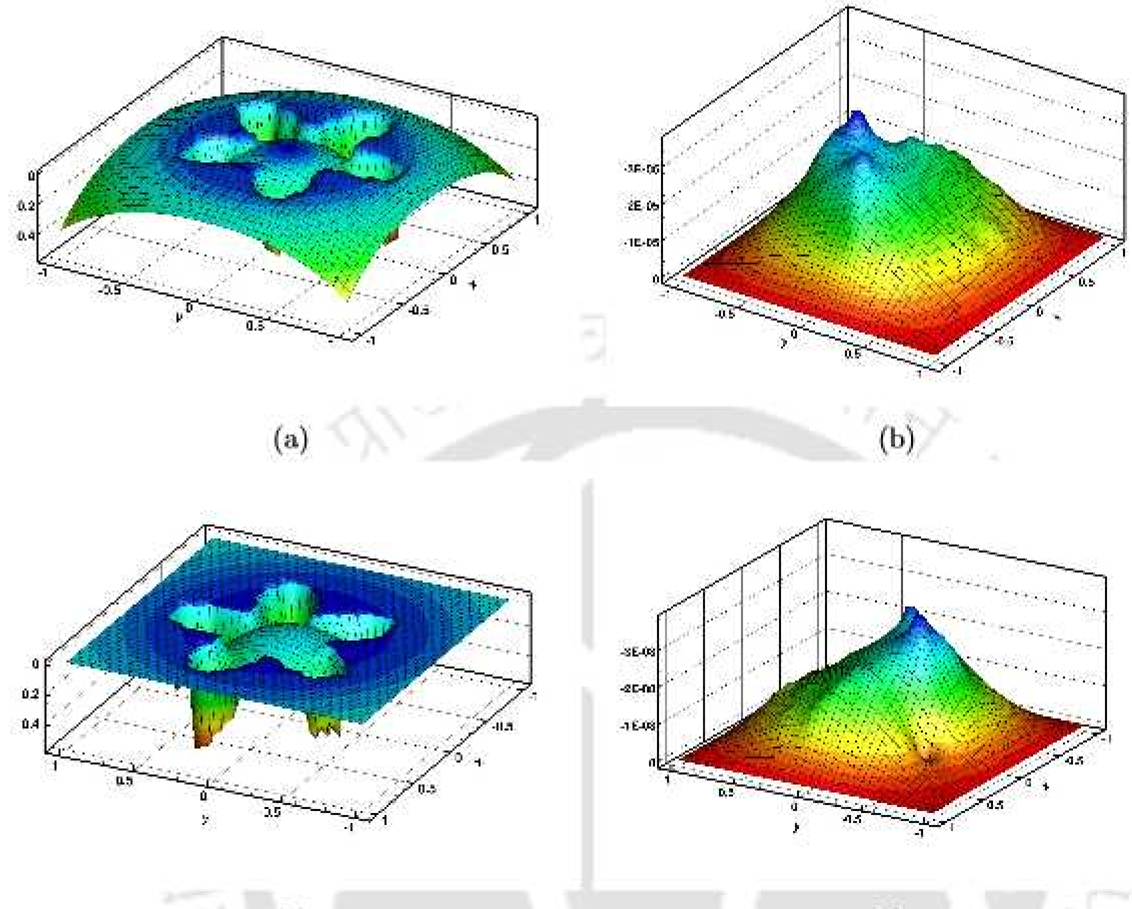

(a) (b)

(c) (d)

Figure 3.8: *Surface plots of the numerical solution (left) and the error (right) for Test Case 3 with (a)-(b) $\beta^+ = 10$ and (c)-(d) $\beta^+ = 10000$ on grid size 40×40.*

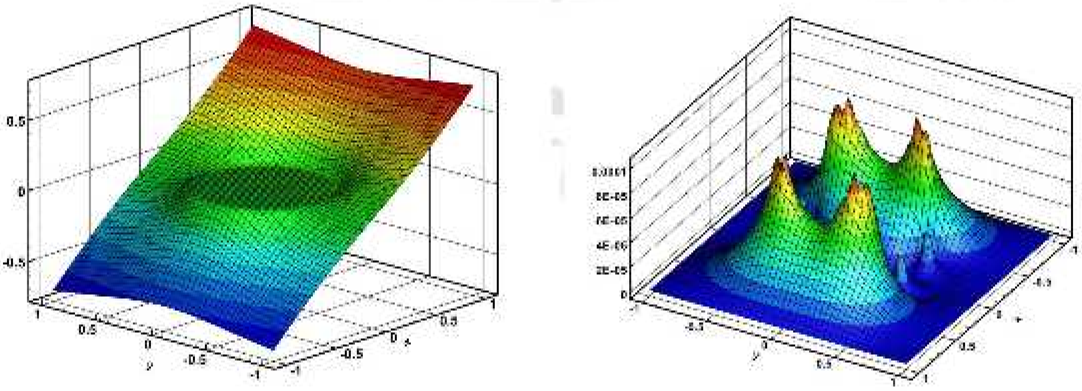

Figure 3.9: *Surface plots of the numerical solution and the error for Test Case 4 for $\rho = 5000$ on grid size 50×50.*

Table 3.10: Grid refinement analysis of maximum error for composite material Test Case 4 with $\rho = 5000$.

N	Present	ROC	DIIM [12]	ROC	FIIM [99]	ROC	EJIIM [179]	ROC
25	1.55×10^{-3}	–	9.80×10^{-4}	–	1.2×10^{-2}	–	1.4×10^{-3}	–
50	1.03×10^{-4}	3.91	2.73×10^{-4}	1.85	9.2×10^{-2}	–	3.5×10^{-4}	2.0
100	1.44×10^{-5}	2.83	4.84×10^{-5}	2.50	5.9×10^{-2}	0.6	9.0×10^{-5}	2.0
200	1.96×10^{-6}	2.87	1.26×10^{-5}	1.94	7.70×10^{-3}	2.9	2.2×10^{-5}	2.0
400	2.57×10^{-7}	2.93	3.49×10^{-6}	1.85	–	–	–	–

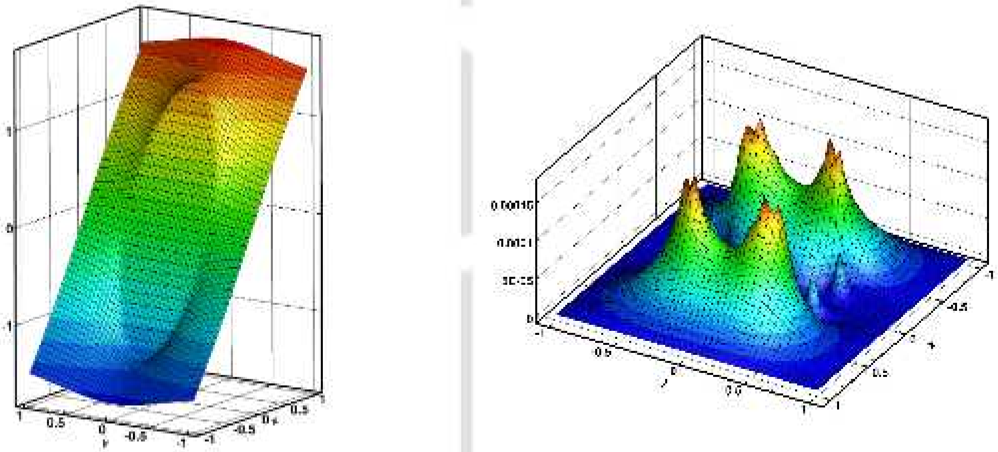

Figure 3.10: *Surface plots of the numerical solution and the error for Test Case 4 for* $\rho = 1/5000$ *on grid size* 50×50.

Table 3.11: Grid refinement analysis of maximum error for composite material Test Case 4 with $\rho = 1/5000$.

N	Present	ROC	DIIM [12]	ROC	FIIM [99]	ROC	EJIIM [179]	ROC
25	3.09×10^{-3}	–	1.63×10^{-3}	–	5.2×10^{-3}	–	1.9×10^{-3}	–
50	1.72×10^{-4}	4.16	4.55×10^{-4}	1.85	1.6×10^{-3}	1.7	5.5×10^{-4}	1.8
100	2.40×10^{-5}	2.84	8.06×10^{-5}	2.50	2.3×10^{-4}	2.8	1.3×10^{-4}	2.1
200	3.27×10^{-6}	2.87	2.10×10^{-5}	1.94	5.0×10^{-5}	2.2	3.2×10^{-5}	2.0
400	4.23×10^{-7}	2.95	5.82×10^{-6}	1.85	–	–	–	–

We tabulate the maximum errors resulting from our computation corresponding to $\rho = 5000$ and $\rho = 1/5000$ in tables 3.10 and 3.11 respectively. We further compare our grid refinement studies with those of [12, 99, 114, 179]. From the tables one can clearly see the errors resulting from our computation decaying at a rate close to three, which is extremely close to the best convergence rate accomplished for this problem by other methods. In figures 3.9 and 3.10, we present the surface plots our computed solutions and errors corresponding to $\rho = 5000$ and $\rho = 1/5000$ respectively . Once again one can see excellent resolution of the sharp interface and relative smoothness of the error near the interface on a grid as coarse as 50×50.

3.1.5 The two-dimensional (2D) steady-state Navier Stokes equation

The next set of problems considered here are concerned with steady-state flows past bluff bodies. The equations governing the flows are the steady-state Navier-Stokes (N-S) equations for incompressible viscous flows which do not possess analytical solutions. The N-S equations provide the mathematical framework for incompressible viscous flows and as such, are the backbones in both theoretical and computational fluid dynamics studies. In particular, the numerical solutions of the N-S equations has played an important role in the recent advances in the flow past bluff bodies in the field of aerospace engineering. We solve the N-S equations in streamfunction-vorticity (ψ-ζ) formulation. Here the vorticity ζ is defined as $\zeta = \dfrac{\partial v}{\partial x} - \dfrac{\partial u}{\partial y}$, where $\mathbf{V} = (u, v)$ is the velocity field with u and v being the horizontal and vertical components of the velocity of the fluid. Defining the velocities in terms of streamfunction ψ as

$$u = \frac{\partial \psi}{\partial y} \quad \text{and} \quad v = -\frac{\partial \psi}{\partial x} \tag{3.12}$$

facilitates the incompressibility condition. The primitive variable formulation of the 2D N-S equations for incompressible viscous flows are given by

$$\begin{aligned} \nabla \cdot \mathbf{V} &= 0 && (3.13) \\ (\mathbf{V} \cdot \nabla)\mathbf{V} &= -\frac{1}{\rho}\nabla p + \frac{\mu}{\rho}\nabla^2 \mathbf{V} && (3.14) \end{aligned}$$

where p, ρ and μ are pressure, density and viscosity respectively. The main interest of this study is to simulate flow fields for the different fixed single and multiple interfaces in two-dimensional laminar flows. Due to the presence of the pressure term, the direct solution of (3.13)-(3.14) has been a costly affair despite representing the fluid phenomena accurately. In order to overcome from this, we define streamfunction-vorticity (ψ-ζ)

formulation. Taking curl of (3.14) yields

$$u\frac{\partial\zeta}{\partial x}+v\frac{\partial\zeta}{\partial y}=\frac{\mu}{\rho}\nabla^2\zeta \tag{3.15}$$

Equation (3.15) is known as the vorticity transport equation. Making use of (3.12) in the definition of vorticity further yields

$$\nabla^2\psi=\frac{\partial^2\psi}{\partial x^2}+\frac{\partial^2\psi}{\partial y^2}=-\zeta \tag{3.16}$$

3.1.6 Non-dimensionalization of the ψ-ζ form of the 2D N-S equations

Defining the non-dimensional variables

$$\text{Let}\quad x^\star=\frac{x}{L},\quad y^\star=\frac{y}{L},\quad u^\star=\frac{u}{U},\quad v^\star=\frac{v}{U},\quad \psi^\star=\frac{\psi L}{U}\quad\text{and}\quad \zeta^\star=\frac{L\zeta}{U},$$

where L is some characteristic length and U the characteristic velocity, equation (3.15) and (3.16) can be rewritten as

$$u^\star\frac{\partial\zeta^\star}{\partial x^\star}+v^\star\frac{\partial\zeta^\star}{\partial y^\star}=\frac{1}{Re}\left(\frac{\partial^2\zeta^\star}{\partial x^{\star2}}+\frac{\partial^2\zeta^\star}{\partial y^{\star2}}\right) \tag{3.17}$$

$$\frac{\partial^2\psi^\star}{\partial x^{\star2}}+\frac{\partial^2\psi^\star}{\partial y^{\star2}}=-\zeta^\star. \tag{3.18}$$

Here Re is the Reynolds number defined by $Re=\dfrac{\rho UL}{\mu}$, which represents the ratio of inertial and viscous forces acting on the fluid. Dropping the asterisks for convenience, the non-dimensional form becomes what is known as the streamfunction-vorticity (ψ-ζ) formulation of the steady-state N-S equations

$$u\frac{\partial\zeta}{\partial x}+v\frac{\partial\zeta}{\partial y}=\frac{1}{Re}\left(\frac{\partial^2\zeta}{\partial x^2}+\frac{\partial^2\zeta}{\partial y^2}\right) \tag{3.19}$$

$$\frac{\partial^2\psi}{\partial x^2}+\frac{\partial^2\psi}{\partial y^2}=-\zeta. \tag{3.20}$$

3.1.7 Test case 5: Flow past a circular cylinder

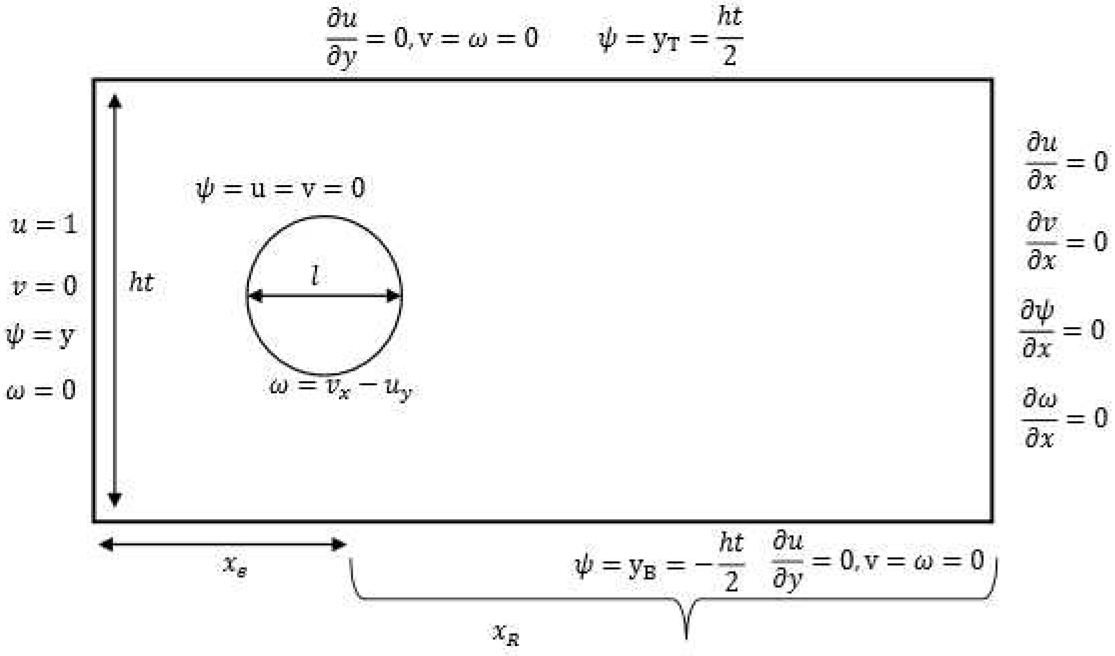

Figure 3.11: *Schematic for the flow past a circular cylinder and the boundary conditions.*

The first problem considered under this category is the 2D steady-state flow past a circular cylinder in uniform stream [9, 20, 27, 73, 81, 89, 95, 156, 170]. The schematic of the problem along with the boundary conditions used is presented in figure 3.11. Here, Reynolds number is defined as $Re = \dfrac{U_{av}l}{\nu}$, where U_{av} is the average inlet velocity, l is the cylinder diameter and ν is the kinematic viscosity of the fluid. In all our computations l was set as 1.0. Note that for the Reynolds numbers under consideration, the flow is always symmetric about the x-axis as the results would suggest.

As depicted in figure 3.11, the computational domain is considered as $-x_e \leq x \leq x_R$, $-\dfrac{ht}{2} \leq y \leq \dfrac{ht}{2}$, where ht and x_R are respectively the height and the length behind the cylinder of the computational domain being considered, and x_e is the entrance length. The cylinder was placed at $(x, y) = (0, 0)$ as its center. On the surface of the cylinder $u = v = \psi = 0$; the same conditions were imposed inside the cylinder as well during computation including that for the vorticity ζ. At the inlet, uniform flow is considered as $u = 1$, $v = 0$ while at the outlet, Neumann boundary conditions are prescribed as $\dfrac{\partial u}{\partial x} = 0 = \dfrac{\partial v}{\partial x} = \dfrac{\partial \psi}{\partial x} = \dfrac{\partial \zeta}{\partial x}$. At the top and bottom $\dfrac{\partial u}{\partial y} = 0$, $v = 0$, and $\psi = \dfrac{ht}{2}$ and

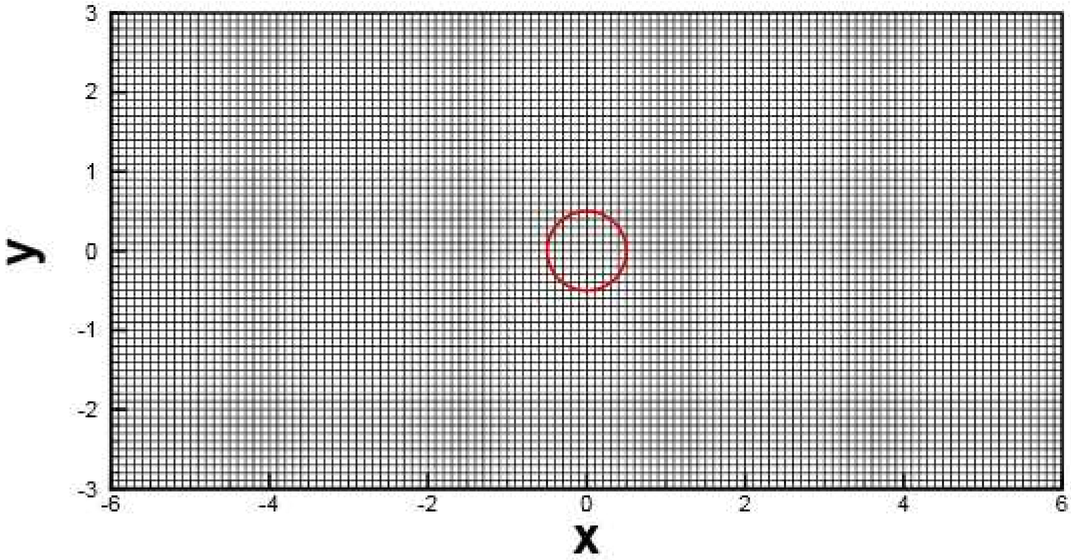

Figure 3.12: *A typical* 121×61 *grid with the circular interface.*

$\psi = -\frac{ht}{2}$ at the upper and lower boundaries respectively. For ζ, at the inlet, top and bottom, a potential flow condition is used, viz., $\zeta = 0$. In figure 3.12 a typical 121×61 grid along with the circular interface is shown.

On the surface of the circular cylinder (or other bluff bodies that would be considered the next examples), which constitutes the interface, jump conditions for ψ is straightforward [183] and hence its discretization thereat. On the other hand, the approximation of the vorticity on the interface is a tricky one, which we have accomplished through a specific interpolation strategy by mapping the ζ values at the irregular and regular points outside the cylinder onto the interface. One can see the schematic for the jump correction of vorticity on the circular interface in figure 3.13(a) for the first quadrant. Here the points 1, 2 and 3, denoted by the red solid circles, correspond to the types of irregular points described in sections 2.1.1, 2.1.2 and 2.1.3 respectively.

For the point 1, firstly a one sided $O(h^2)$ approximation [134] is used to compute ζ by the discretizing $-\nabla^2\psi$, making use of the points to the right and top of this point represented by the triangles as shown in the figure 3.13(a). This is followed by the computation of $-\nabla^2\psi$ employing the regular five point central difference formula at the next point right to 1. Making use of the approximations of $-\nabla^2\psi$ thus found at these points, the value of ζ at the interfacial point to the left of 1 is calculated by fitting a linear Lagrange polynomial. Likewise, the value of ζ at the interfacial point below 2 is calculated by fitting a linear Lagrange polynomial by making use of the values of $-\nabla^2\psi$ at the point 2 and the next point above it.

For point 3, after computing $-\nabla^2\psi$ on it by the same strategy used for 1 and 2, we further compute it at the point 4 diagonally above it by the five point central difference formula; it is then followed the computation of ζ at the point on the surface intercepted by the straight line joining the points 3 and 4 by fitting a linear Lagrange polynomial once again. Setting the ζ values inside the cylinder as zero, the jump condition for vorticity on the interface is simply the interpolated values of ζ thereat. The same approach has been adopted for bluff bodies of other shapes discussed in subsequent sections 3.1.8 and 3.1.9.1 as well. The boundary conditions on the top, bottom, left and right sides of the computational domain for these two problems are as in figure 3.11.

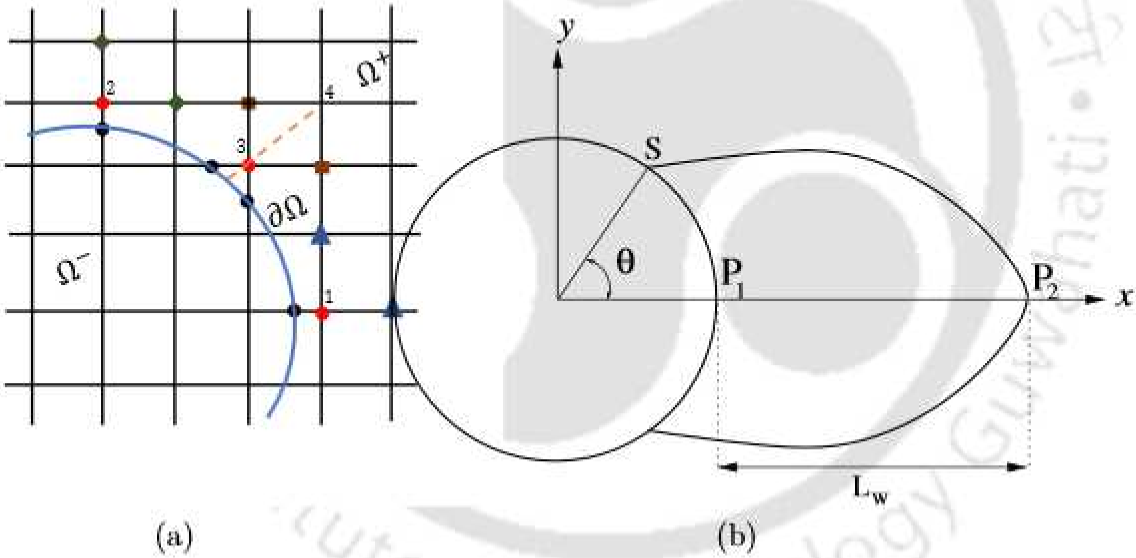

Figure 3.13: *(a) Schematic for the jump correction of vorticity on the circular interface in the first quadrant and (b) flow parameters corresponding to table 3.12 for the flow past an impulsively started circular cylinder:* P_1 *is the rear stagnation point,* P_2*, the wake stagnation point,* L_W*, the wake length, S, the separation point and* θ*, the angle of separation.*

We now discuss the solution procedure of the algebraic systems resulting from the discretization the system of equations (3.19)-(3.20), which reduces to the form $A\Phi = \mathbf{b}$ with Φ representing either ψ or ζ (see section 2.2).

The computation of the steady-state solutions of fluid flow problems governed by coupled equations such as (3.19)-(3.20) involves an outer-inner iteration procedure. After initializing u, v, ψ and ζ with appropriate boundary conditions and interior values (taken from the potential flow conditions), (3.20) is solved for ψ. Once ψ is computed, u and v are computed from equations (3.12) by employing a higher-order compact approximation as given by [77] after which ζ is computed from (3.19). This constitutes one outer iteration. Making use of the updated values of ζ, ψ is computed again. This process is repeated till maximum ζ-error reaches 5×10^{-10}. The inner iterations involve solving the matrix equations at each outer iteration by iterative solvers. We have used biconjugate gradient stabilized method (BiCGStab) [82] with preconditioning, where Incomplete LU decomposition is used as a pre-conditioner. Preconditioning has been particularly useful for high Reynolds numbers on finest grids where we have used the Lis library [1]. The inner iterations were stopped when the Euclidean norm of the residual vector $\mathbf{r} = \mathbf{b} - A\Phi$ arising out of equation (3.19)-(3.20) fell below 10^{-13} as in section 2.2. We have used a relaxation parameter λ for both inner and outer iteration cycles. Larger the value of Reynolds number, smaller is the value of λ.

We have computed solutions for $Re = 10$, 20 and 40 on grid sizes ranging from 121×61 to 549×499. Once the data is available for the lowest Re considered here, the flow is computed for the next Reynolds numbers by using the data from the previous Re as the initial data. In figure 3.14, we present the convergence history of the infinity norm of the ψ and ζ errors against the outer iterations for the Reynolds numbers considered here. Here the error is defined as the difference between the value at the current and the previous outer iteration levels. In all the cases, one can observe a very smooth convergence pattern.

In figure 3.15, we present our computed steady-state streamlines and vorticity contours for Reynolds numbers 10, 20 and 40. One can see two symmetric vortices being formed behind the cylinder, whose size increase with the increase in Reynolds numbers. Once again, our simulations are very close to the well-known numerical results of [20,73,89,95]. A glimpse of this can be seen in the middle column of figure 3.15 where the computed streamlines from [89] for the same Reynolds numbers are presented.

We have also computed the wake length L_w, which is the distance between rear end point P_1 of cylinder and the end of the separation at the point P_2, and the angle θ between the x-axis and the line joining the center of the cylinder and the separation point S on the cylinder (refer to figure 3.13(b)), known as the separation angle. We have further computed the drag coefficient C_D by utilizing the momentum balance along the streamwise direction. All these flow parameters are tabulated in table 3.12 along with some established numerical as well as the path-breaking experimental results of Coutanceau and Bouard [35]. In all the cases, excellent comparison is observed between

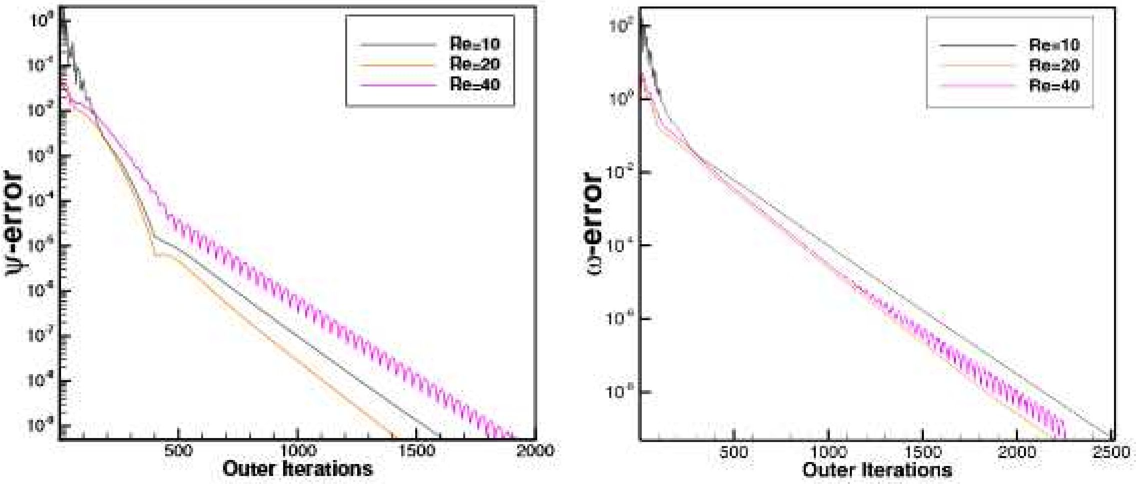

(a) (b)

Figure 3.14: *Effect of Reynolds number on the convergence history on the finest grid (549 × 499) for the flow past circular cylinder problem: (a) ψ-error and (b) ζ-error.*

Table 3.12: Comaprison of wake lengths, separation angles and drag coefficients for different Reynolds numbers..

	Re	[35] (exp)	[39]	[53]	[106]	[183]	[90]	Present
L_w	10	—	0.530	—	—	—	0.531	0.538
	20	1.86	1.880	1.820	1.860	1.840	1.874	1.920
	40	4.38	4.690	4.480	4.56	4.420	4.278	4.540
C_D	10	—	2.846	—	—	—	2.690	2.58
	20	—	2.045	2.001	2.06	2.23	2.160	2.04
	40	—	1.522	1.498	1.54	1.66	1.576	1.64
θ	10	—	29.6	—	—	—	29.69	30.8
	20	44.4	43.7	42.9	43.50	44.20	42.66	45.6
	40	53.4	53.8	51.5	53.60	53.50	53.08	56.3

our computed results and the benchmark solutions.

3.1.8 Test case 6: Flow past two randomly spaced inclined elliptic cylinders

Here, we consider the laminar flow past two randomly spaced elliptic cylinders in uniform stream inclined at different angles to the stream for $Re = 10.0$. The flow configuration is same as in figure 3.11 of the previous example, except that instead of one single cylinder,

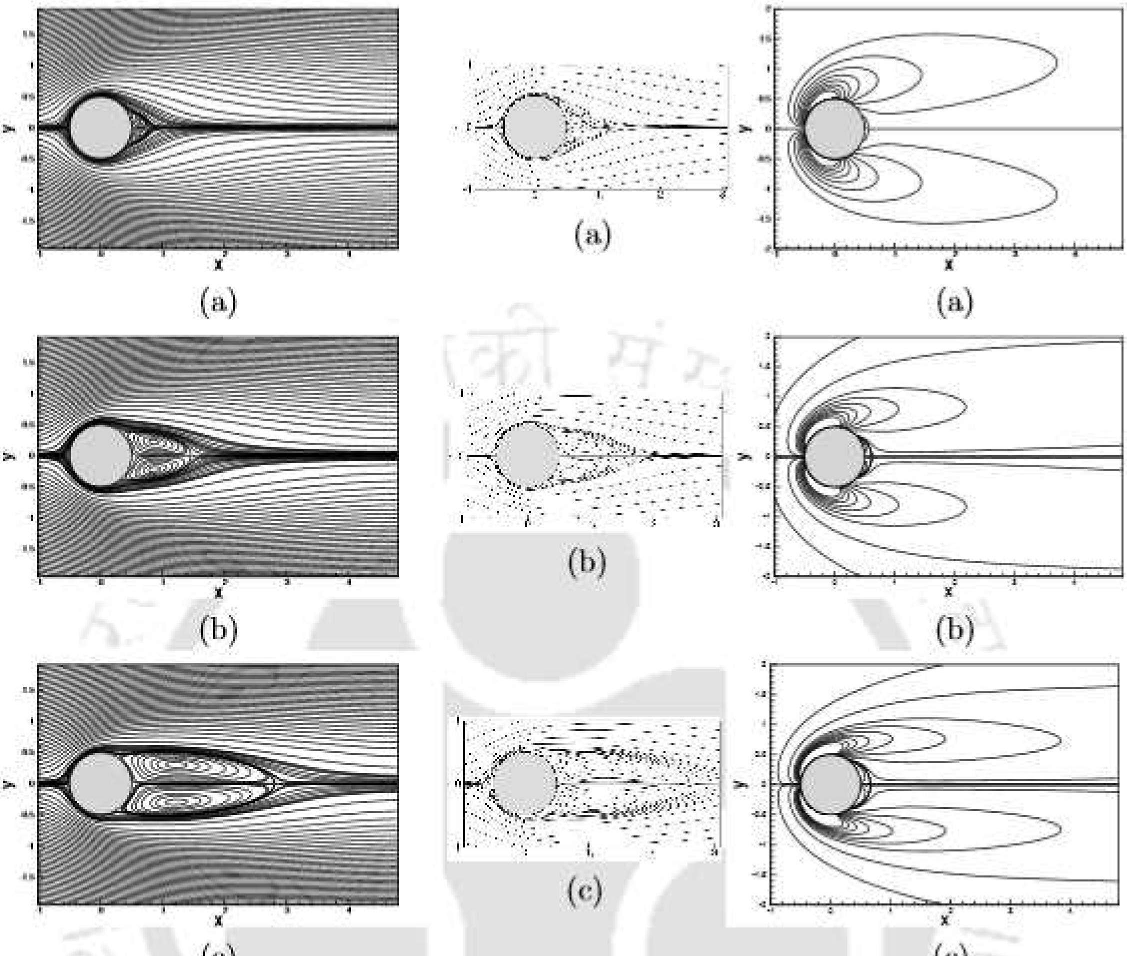

(a) (a) (a)

(b) (b) (b)

(c) (c) (c)

Figure 3.15: *Simulation of flow past circular cylinder problem by present method: Steady-state Streamlines (left) and Vorticity contours (right) for (a) $Re = 10$, (b) $Re = 20$ and (c) $Re = 40$ on grid size 549×499. The simulated streamlines for the corresponding Res from [89] are in the middle column.*

two elliptic cylinders with centres $(0, 0.5)$ and $(4, -0.5)$ with respective eccentricities $\dfrac{\sqrt{15}}{4}$ and $\dfrac{2\sqrt{2}}{3}$ are placed in the uniform stream. The ellipses make angles $\dfrac{3\pi}{4}$ and $\dfrac{\pi}{4}$ respectively with the horizontal line. The rectangular region $[-2.5, 2.5] \times [-3, 7]$ in xy-plane is chosen as the computational domain. In figures 3.16(a)-(b), we show the steady-state streamlines and vorticity contours respectively, where one can see the streamlines separating from the upper sides of the cylinder fronts to form a vortex lying across the imaginary line joining the centres of the ellipses.

In table 3.13, we present the vortex data on three different grids depicting the coordinates of the center of the vortex, the ψ and ζ values thereat and the maximum vorticity value in the domain. For the same grids, we also present the distribution of u

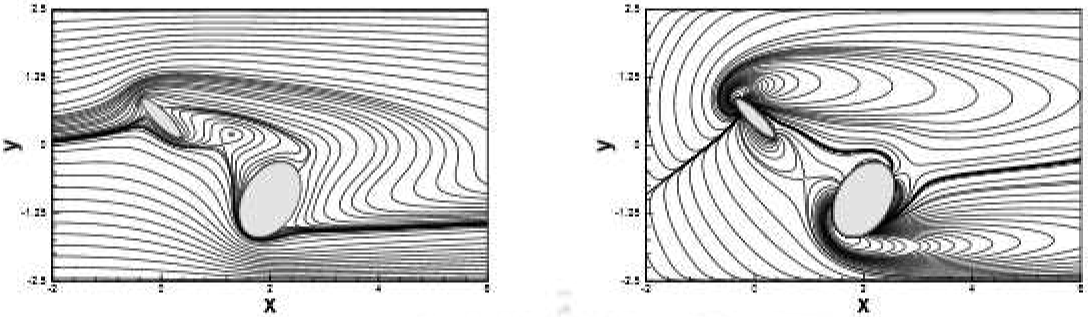

(a) (b)

Figure 3.16: *Simulation of flow past two randomly spaced inclined elliptic cylinders of varied eccentricities in uniform flow for $Re = 10.0$: (a) Streamlines and (b) Vorticity contours on a grid of size 799×399.*

Table 3.13: Grid independence study for Test Case 6.

h	Vortex Centre (x, y)	ψ	ζ	ζ_{max}
$\frac{1}{40}$	$(1.29293, 0.202020)$	-0.028026	-0.154637	21.61155
$\frac{1}{60}$	$(1.27852, 0.201342)$	-0.028087	-0.152500	21.18219
$\frac{1}{80}$	$(1.28392, 0.201005)$	-0.027970	-0.152518	21.23926

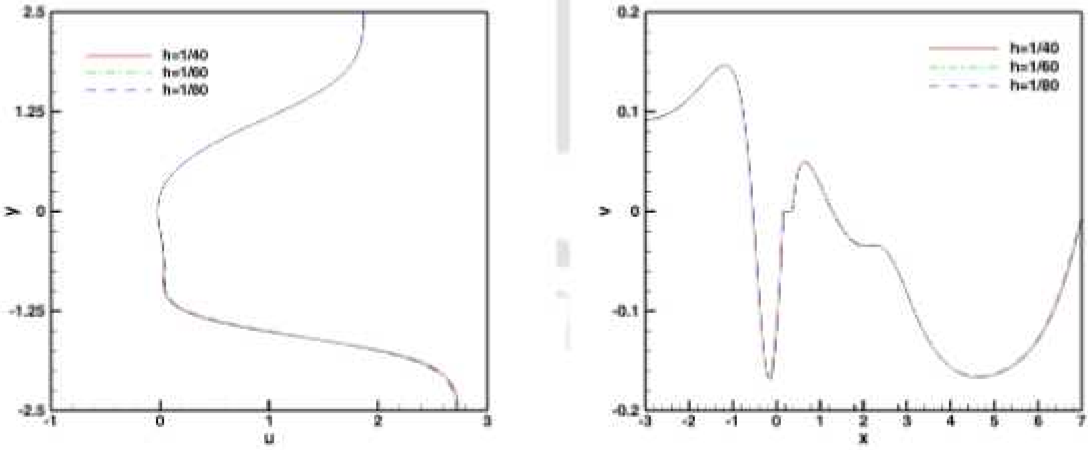

(a) (b)

Figure 3.17: *Grid independence study for the flow past two randomly spaced inclined elliptic cylinders: (a) u-velocity along the vertical line and (b) v-velocity along the horizontal line through the vortex center.*

and v along the vertical and horizontal lines passing through the vortex center in figures 3.17(a)-(b) respectively. Both table 3.13 and the overlapping of the graphs in figure 3.17 clearly establish the grid independence of our computed results.

3.1.9 Test case 7: Simulation of the experimental visualization by Taneda for Stokes flow [174]

In this section, we endeavour to replicate the experimental visualization by Taneda [174], which he had performed in laboratory during the late seventies pertaining to Stokes flows. We consider the following two cases:

3.1.9.1 Case 1

The problem considered here is the flow past two circular cylinders in tandem subjected to uniform flow for $Re = 0.01$. Once again the problem configuration is similar to the one described in test case 5, the only change being, instead of one, two circular cylinders of unit diameters are placed in tandem at a distance ϵd apart, d being the diameter of the cylinder. We have chosen the cases when $\epsilon = 0.5$ and 1.0. In figure 3.18, we present our computed streamlines for these two cases and compare them with the experimental visualization of Taneda [174]. As reported in Taneda's experiment, for $\epsilon = 1.0$, two vortex pairs appear while for $\epsilon = 0.5$, the two vortex pairs merge into one vortex pair. Without resorting to the complicated mathematics that had been adopted in [37] for transforming the physical plane and hence the governing equations, our simulation has very elegantly and accurately captured the flow physics, as is evidenced by the extreme closeness of our numerical results to the experimental ones.

3.1.9.2 Case 2

Here we consider the separation in a linear shear flow past a circular cylinder and a plane [36] for $Re = 0.011$. The problem configuration is shown in figure 3.19 along with the boundary conditions. In the original lab experiment of Taneda [174], coloured glycerine was introduced into the working fluid along a straight line normal to a flat plate and the cylinder was placed above the plate maintaining a gap ϵd, d being the diameter of the cylinder. When the test body was set in motion by slowly moving the plate in the negative x-direction, a linear shear layer flow was seen to establish on the flat plate up to a height of approximately six times the cylinder diameter. As such, we have chosen the computational domain and the boundary conditions as shown in figure

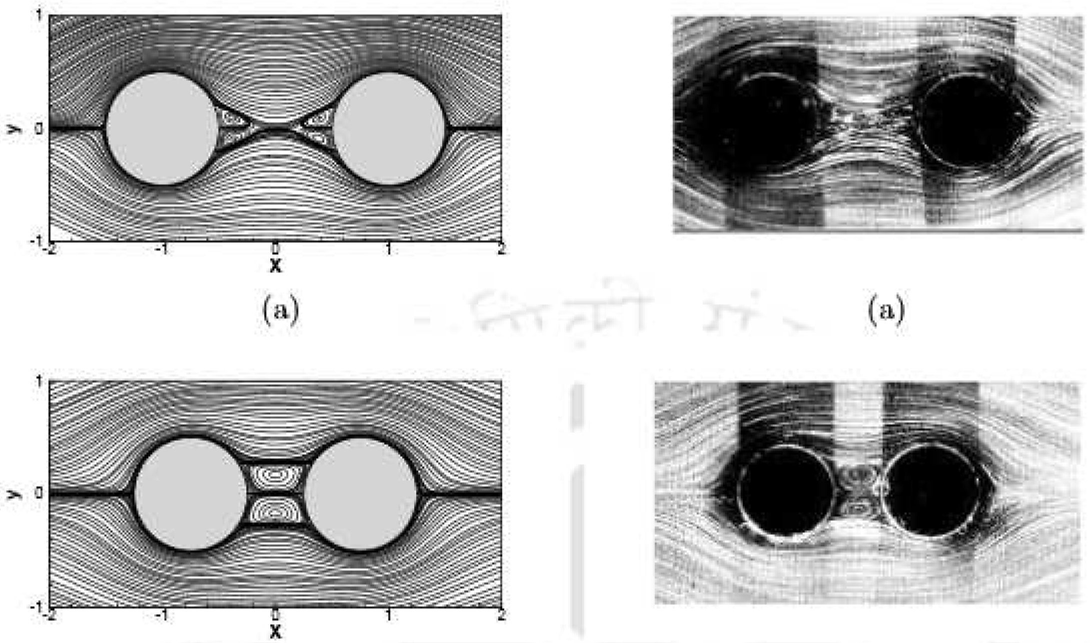

(a) (a)

(b) (b)

Figure 3.18: *Simulation of flow past two circular cylinders in tandem in uniform flow for* $Re = 0.01$*: Computed (left) on a grid of size* 659×479 *and experimental Streamlines from Taneda [174] © [1979] The Physical Society of Japan (J. Phys. Soc. Jpn. [46], [Visualization of Separating Stokes Flows/1935-1942].) (right) when the distance between the cylinders is (a)* $1.0d$ *and (b)* $0.5d$*,* d *being the diameter of the cylinder.*

3.19 so that the same shear layer effect could be accomplished. At the solid boundary at the bottom, an $O(h^3)$ approximation of vorticity $\zeta_{i,0}$ can be obtained by the strategy adopted in [75],

$$\delta_y^+\psi_{i,0} + \frac{h}{2}\zeta_{i,0} + \frac{h^2}{6}\delta_y^+\zeta_{i,0} = 0. \tag{3.21}$$

Making use of the fact that $\psi = 0$ on the bottom boundary, this reduces to

$$2\zeta_{i,0} + \zeta_{i,1} = -\frac{6}{h^2}\psi_{i,1}. \tag{3.22}$$

Although the above is an implicit expression, it could be easily assimilated into the matrix equation for ζ.

In figure 3.20, we present our computed streamlines side by side with the experimental visualization of Taneda [174] for $\epsilon = 0.0$, which corresponds to the scenario when the cylinder touches the plate and $\epsilon = 0.1$ corresponding to a gap of one tenth of the diameter between the cylinder and the plate. As can be seen from the figures,

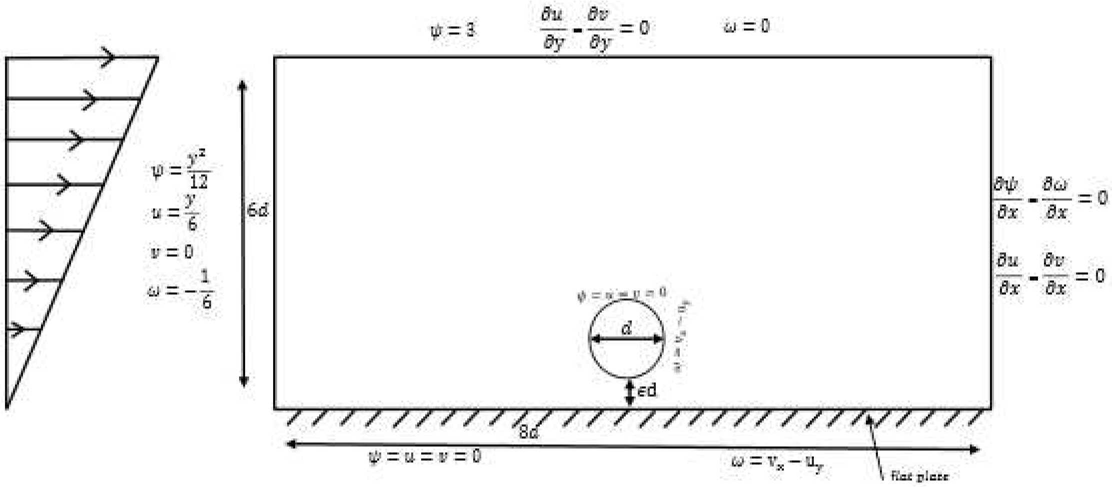

Figure 3.19: *Schematic for the shear flow past a circular cylinder and a plane with the boundary conditions.*

our simulation is extremely close to the experimental results. Note that our findings are in conformity with the theoretical structures of the Stokes flow past a circular cylinder near a plane given by Davis *et al.* [36].

3.2 Conclusion

This chapter is specifically concerned with the application of the HEJIIM developed in Chapter 2 to real life problems. The scheme is employed to solve four problems embedded with circular and star-shaped interfaces in a rectangular region having analytical solutions and varied discontinuities across the interface in source and the coefficient terms. In the process, the order of convergence of the computed solutions is also established. Solutions are compared with numerical results from existing IIMs, and in all the cases, much improved accuracy of the solutions was observed. The robustness of the proposed scheme is, however, better realized when applied to compute the flow in a host of fluid flow problems past bluff bodies governed by the Navier-Stokes equations. They include flows not only past a stationary circular cylinder in uniform and shear flow but also multiple bodies of various shapes immersed in the flow. In the process, we have also established the grid independence of our computed results confirming the accuracy of the simulations performed. Our simulation of the flows was extremely close to well-

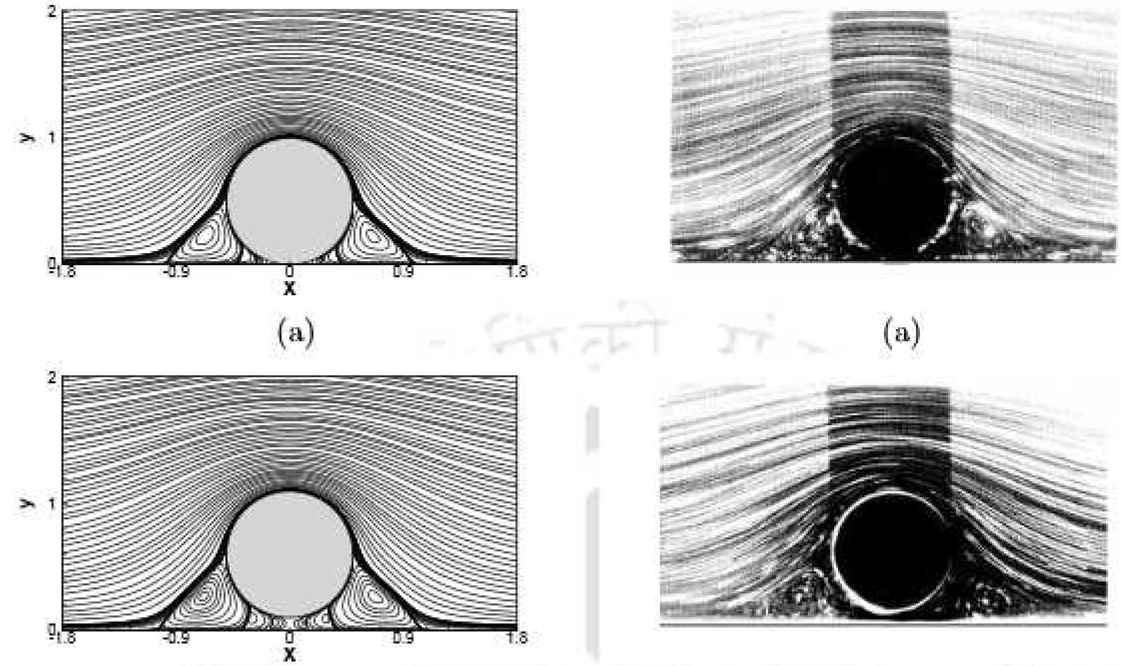

(a) (a)

(b) (b)

Figure 3.20: *Simulation of flow past circular cylinder placed near a plane in shear flow for $Re = 0.011$: Computed (left) on a grid of size 799×299 and experimental Streamlines from Taneda [174] © [1979] The Physical Society of Japan (J. Phys. Soc. Jpn. [46], [Visualization of Separating Stokes Flows/1935-1942].) (right) when the cylinder is (a) $0.0d$ and (b) $0.1d$ above the plane, d being the diameter of the cylinder.*

established numerical results and flows visualization from laboratory experiments. In all, we consider the proposed scheme to be an important addition to the already existing immersed interface methods. In the next chapter, we will present a transient variant of the method developed in Chapter 2.

4

An efficient explicit jump High Order Compact immersed interface approach for transient incompressible viscous flows

4.1 Introduction

Parabolic partial differential equations (pde) with discontinuous coefficients play significant roles in the fields of electrostatics, porous media, multiphase flows, material science, underwater acoustics, biology (blood flow models) and several other fields. For example, one may consider the case of wave propagation in a composite or irregular medium with different material properties, which has numerous engineering applications. Besides, the parabolic equations can be suitably reconstructed in the shape of the unsteady N-S equations that models incompressible viscous flows. As such, devising computationally efficient numerical algorithms and obtaining highly accurate solutions of the N-S equations is one of the primary goals of CFD. In order to deal with bodies of complicated geometries or moving bodies immersed in fluid flows in Cartesian grids, immersed interface methods have been of great efficacy in the past three decades. In chapters 2 and 3, we proposed a new higher-order accurate finite difference explicit jump Immersed Interface Method (HEJIIM) for solving two-dimensional elliptic problems. In the current chapter[1], we extend this idea to transient problems, viz., to parabolic problems with singular source and discontinuous coefficients on a compact Cartesian mesh.

In most of the parabolic problems with discontinuities across some interface, they are mostly expressed in terms of natural jump conditions in the dependent variable given by $[u] = 0$ and its normal derivative $[\beta u_{\mathbf{n}}] = 0$ across the interface. For example,

---

[1] Published in [165].

one may cite the process of conductive heat transfer over mixed media, which has been extensively investigated in the existing literature. Although many of the parabolic equations possess analytical solutions, even for problems having homogeneous jump conditions, the discontinuity present in the diffusion coefficient doesn't allow one to have the analytical solution easily. To overcome these issues, numerical approaches become handy techniques for such types of problems. However, as the solution is not smooth over the whole physical and computational domains, standard numerical algorithms cannot be applied to attain accurate solutions. One must conceive specific numerical procedures in the neighbourhood of these discontinuities to achieve reasonable approximation of the solutions thereat.

Several remarkably designed numerical approaches have already been developed in the literature to solve the parabolic interface problems by incorporating the jump conditions into the discretization process [97, 101, 126, 178, 190]. Notwithstanding, most of these involve finite element and finite volume methods where the interface is captured by body-fitted approach [6, 28, 166], the grid required to be generated could be computationally expensive. In order to avoid this, Li et al. introduced second-order accurate immersed interface method for moving interface problem on Cartesian mesh [98], by using generalized Taylor series expansions to modify the standard FD discretization on the irregular points to recover the loss of accuracy at the interface. Adams et al. [2] introduced the second-order maximum principle immersed interface method to solve the linear parabolic equation. First-order derivatives are approximated by an explicit scheme and the diffusion part by Cranck Nicolson. Bouchon and Peichl [19] presented a method to parabolic equations with mixed boundary conditions, where they applied immersed interface algorithm to discretize Neumann condition and ShortleyWeller approximation for the Dirichlet condition. The most significant and inherent aspect of these approaches lie in their clarity in achieving the solution on Cartesian mesh, which can be generated very speedily and allows users to simulate flows containing moving objects with complex geometries with ease.

In this chapter, we propose a new higher-order compact finite difference Immersed Interface Method for solving two-dimensional parabolic problems, more specifically for transient problems involving bluff bodies immersed in incompressible viscous flows on Cartesian mesh. Such problems are governed by the unsteady N-S equations which are parabolic in nature with singular source and discontinuous coefficients in irregular domains. ψ-ζ form of the N-S equations has been utilized for this purpose as in [20, 106, 144]. Note that Calhoun [20] presented a second-order finite volume approach in an unstable region and imposed no-slip flow condition to find the vorticity sources, while Linnack and Fasel [106] introduced a fourth-order compact difference scheme based on Weigmann [179] approach. Russel and Wang [144] satisfied the no-penetration condition in the streamfucntion by superimposing a homogenous solution to Poisson's equation for moving boundaries and a no-slip condition for the surface vorticity of the objects. In 2008, Wang et al. [177] proposed a higher-order accurate method to solve the 2D incompressible viscous flow in the velocity and vorticity formulation where they added the exerted force function into the primitive variable form, and followed it by by taking its curl to attain a Poisson equation for the velocity. The no-slip condition was assured by the presence of the derivative of the force function in the vorticity equation as the source term. In 2012, Ren et al. [142] introduced IBM based on the ψ-ζ formulation. According to the requirement the velocity at the immersed boundary interpolated from the corrected velocity field accurately satisfies the nonslip boundary condition, the approach performs an implicit velocity correction process. Instead of using the vorticity transport equation, the streamfunction formulation is used to make the vorticity adjustment. It is calculated using the velocity correction's first order derivatives. The approximation of velocity-correction derivatives is provided using two straightforward and effective methods. One is predicated on FD approximation, while the other is dependent on velocity correction & derivative expressions of the Dirac delta function. Recently Ghasemkheli et al. [58] employed an immersed boundary method to solve the ψ-ζ form of the N-S equations through an inverse source problem approach. They converted the vorticity equation into the Helmholtz equation through semi-implicit time discretization, but its order of accuracy was only one. Similar to others IIMs approaches, to ensure the accuracy of the numerical solutions, they adopted special strategies close to the embedded boundary, resulting in the loss of compactness of stencil. In contrast, the proposed scheme maintains its compactness on a nine point stencil at both the regular and irregular points. In order to treat the jump across the interface, we modified the HEJIIM in such a way that at each time step, the scheme maintains fourth order spatial accuracy throughout the whole computational domain.

Using the proposed scheme, firstly we solve one problem with circular interface in a rectangular region having analytical solutions. Then we simulate flow past stationary as well as moving bluff bodies immersed in fluids governed by the N-S equations. Our simulations include flow situations involving multiple and moving bodies as well. For the problem having analytical solution, our results are excellent match with the analytical ones and for the fluid flow problems, our simulations are extremely close to the experimental and available numerical results.

4.2 Mathematical formulation

A two dimensional Parabolic interface problem may be modelled as:

$$\lambda u_t = \nabla \cdot (\beta \nabla u) + \kappa u - f + b\delta\{(x - x^*)(y - y^*)\} \quad \text{in} \quad \Omega \times (0, \infty)\,, \;\; (x^*, y^*) \in \Gamma. \tag{4.1}$$

with specified initial and boundary conditions. Here Ω is an open bounded subset in $\mathbb{R}^2$ and $\mathbf{x} = (x, y)$ is an interior point in the domain having an interface Γ immersed in it, and $(x^*, y^*) \in \Gamma$ is an interfacial point. It is assumed that $\beta(\mathbf{x}, t) \in C^1(\Omega^{\pm}\backslash\Gamma)$ and $\kappa(\mathbf{x}, t)$, $f(\mathbf{x}, t) \in C(\Omega^{\pm}\backslash\Gamma)$ may have finite jump across the interface Γ. Moreover $b(\mathbf{x}, t) \in C(\Gamma)$ and all the parameter β_x and β_y are considered to be bounded, hence the solution $u(\mathbf{x}, t) \in C^2(\Omega^{\pm}\backslash\Gamma)$. If $\hat{n} = (n_1, n_2)^T$ is the unit outward normal vector to the interface at a point $(x^*, y^*) \in \Gamma$ inside Ω^- (see figure 2.1(a)) and $a(\mathbf{x}, t) \in C^2(\Gamma)$, the jump conditions in the solution and the flux across the interface may be expressed as

$$[u]_\Gamma = u^+ - u^- = a(\mathbf{x}, t), \tag{4.2}$$

$$\left[\beta \frac{\partial u}{\partial \hat{n}}\right]_\Gamma = \beta^+ \nabla u^+ - \beta^- \nabla u^- = b(\mathbf{x}, t). \tag{4.3}$$

In other words, the jump conditions in the solution and flux are incorporated in the numerical formulation across the interface to solve such problems, and are defined in (4.2) and (4.3) respectively, where subscripts $+$ and $-$ represents the subdomains Ω^+ and Ω^- respectively.

The domain is considered to be of rectangular shape $\Omega = [x_0, x_f] \times [y_0, y_f]$. The steps for generating a grid with uniform step-lengths h, k in the spatial directions x and y have already been described in section 2.1.

Recall that the level set function $\phi(x, y)$ is a smooth function defined in the two-dimensional domain $\Omega = \Omega^- \cup \Gamma \cup \Omega^+$ as,

$$\begin{cases} \phi(x, y, t) < 0 & \text{if } (x, y) \in \Omega^-, \\ \phi(x, y, t) = 0 & \text{if } (x, y) \in \Gamma, \\ \phi(x, y, t) > 0 & \text{if } (x, y) \in \Omega^+. \end{cases}$$

with the interface lying across $\phi(x, y, t) = 0$.

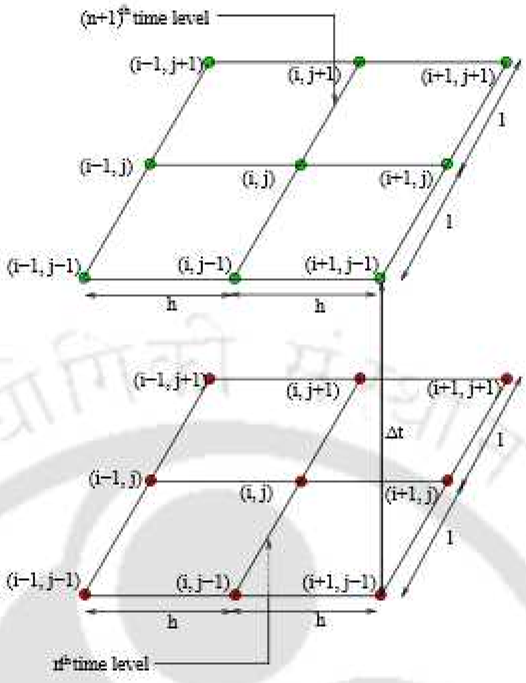

Figure 4.1: *Schematic of the unsteady HOC nine point stencil.*

4.2.1 Discretization on the regular points

We have restructured the HOC finite difference scheme developed by Kalita *et al.* [76] for the two-dimensional transient convection-diffusion equation to discretize equation (4.1) at the regular points. Note that the last term on the right hand of equation (4.1) vanishes at regular points and as such (4.1) may be recast in convection-diffusion-reaction form as

$$\lambda u_t + \beta_x u_x + \beta_y u_y + \beta \nabla^2 u + \kappa u = f \tag{4.4}$$

We use the methodology prescribed in [76] to obtain a high order compact finite difference approximation of (4.4) by using a uniform time step Δt. This is accomplished by first substituting the high order spatial derivatives appearing in the truncation error terms of the central difference approximation of (4.4) by lower order derivatives obtained from successive differentiation of the original differential equation (4.4). Next, the time derivative is approximated numerically by a Crank-Nicolson type of discretization. These result in a spatially fourth and temporally second order accurate finite difference scheme on compact uniform grid requiring nine point stencils both at the $(n)^{\text{th}}$ and $(n+1)^{\text{th}}$ time levels as shown in figure 4.1. As such, it is termed as a $(9, 9)$ scheme [76]. Eventually, the HOC finite difference approximation of (4.4) can be written as

$$\lambda_{ij}\left[1+\frac{h^2}{12}\left(\delta_{xx}+\frac{(c-2\beta_x)}{\beta}\delta_x\right)+\frac{l^2}{12}\left(\delta_{yy}+\frac{(d-2\beta_y)}{\beta}\delta_y\right)\right]\left(u_{ij}^{n+1}-u_{ij}^{n}\right)=$$
$$\frac{\Delta t}{2}(F_{ij}^{n+1}-F_{ij}^{n})+\frac{\Delta t}{2}[A_{ij}\delta_x^2+B_{ij}\delta_y^2+C_{ij}\delta_x+D_{ij}\delta_y+E_{ij}\delta_x^2\delta_y^2+H_{ij}\delta_x\delta_y^2+K_{ij}\delta_x^2\delta_y$$
$$+L_{ij}\delta_x\delta_y+M_{ij}](u_{ij}^{n+1}+u_{ij}^{n})+O((\Delta t)^2,(h^4,l^4)). \tag{4.5}$$

where δ_x^2, δ_y^2 , δ_x , δ_y, $\delta_x\delta_y$, $\delta_x\delta_y^2$, $\delta_x^2\delta_y$ and $\delta_x^2\delta_y^2$ are second order accurate central difference operators along x- and y- directions and,

$$A_{ij}=\beta_{ij}+\frac{h^2}{12}\left(\beta_{xx}+2c_x+\kappa+\frac{(c-2\beta_x)}{\beta}(\beta_x+c)\right)_{ij}+\frac{l^2}{12}\left(\beta_{yy}+\beta_y\frac{(d-2\beta_y)}{\beta}\right)_{ij}, \tag{4.6}$$

$$B_{ij}=\beta_{ij}+\frac{h^2}{12}\left(\beta_{xx}+\beta_x\frac{(c-2\beta_x)}{\beta}\right)_{ij}+\frac{l^2}{12}\left(\beta_{yy}+2d_y+\kappa+\frac{(d-2\beta_y)}{\beta}(\beta_y+d)\right)_{ij}, \tag{4.7}$$

$$C_{ij}=c_{ij}+\frac{h^2}{12}\left(c_{xx}+2\kappa_x+\frac{(c-2\beta_x)}{\beta}(c_x+\kappa)\right)_{ij}+\frac{l^2}{12}\left(c_{yy}+c_y\frac{(d-2\beta_y)}{\beta}\right)_{ij}, \tag{4.8}$$

$$D_{ij}=dij+\frac{h^2}{12}\left(d_{xx}+d_x\frac{(c-2\beta_x)}{\beta}\right)_{ij}+\frac{l^2}{12}\left(d_{yy}+2\kappa_y+\frac{(d-2\beta_y)}{\beta}(d_y+\kappa)\right)_{ij}, \tag{4.9}$$

$$E_{ij}=\beta_{ij}\left(\frac{h^2}{12}+\frac{l^2}{12}\right), \tag{4.10}$$

$$H_{ij}=c_{ij}\left(\frac{h^2}{12}+\frac{l^2}{12}\right), \tag{4.11}$$

$$K_{ij}=d_{ij}\left(\frac{h^2}{12}+\frac{l^2}{12}\right), \tag{4.12}$$

$$L_{ij}=\frac{h^2}{12}\left(2d_x+d\frac{(c-2\beta_x)}{\beta})\right)_{ij}+\frac{l^2}{12}\left(2c_y+c\frac{(d-2\beta_y)}{\beta})\right)_{ij}, \tag{4.13}$$

$$M_{ij}=\kappa_{ij}+\frac{h^2}{12}\left(\kappa_{xx}+\kappa_x\frac{(c-2\beta_x)}{\beta}\right)_{ij}+\frac{l^2}{12}(\beta_{ij}\left(\kappa_{yy}+\kappa_y\frac{(d-2\beta_y)}{\beta}\right)_{ij}, \tag{4.14}$$

$$F_{ij}=f_{ij}+\frac{h^2}{12}\left(f_{xx}+f_x\frac{(c-2\beta_x)}{\beta}\right)_{ij}+\frac{l^2}{12}\left(f_{yy}+f_y\frac{(d-2\beta_y)}{\beta}\right)_{ij}. \tag{4.15}$$

Rewrite the equation (4.5) into

$$\sum_{i=1}^{9} c_i u_i^{n+1} = \sum_{i=1}^{9} c_i^{'} u_i^{n} + \frac{\Delta t}{2}\left(F_{ij}^{n+1} - F_{ij}^{n}\right) \tag{4.16}$$

where $c_i = \lambda m_i - \dfrac{\Delta t}{2} n_i$, $c_i^{'} = \lambda m_i - \dfrac{\Delta t}{2} n_i$, and $m_1 = m_3 = m_7 = m_9 = 0$, $m_5 = \dfrac{8}{12}$,

$$\begin{aligned}
m_2 =& \frac{1}{12}\left(1 - l\frac{(d-2\beta_y)}{\beta}\right), && (4.17)\\
m_8 =& \frac{1}{12}\left(1 + l\frac{(d-2\beta_y)}{\beta}\right), && (4.18)\\
m_4 =& \frac{1}{12}\left(1 - h\frac{(c-2\beta_x)}{\beta}\right), && (4.19)\\
m_6 =& \frac{1}{12}\left(1 + h\frac{(c-2\beta_x)}{\beta}\right), && (4.20)\\
n_1 =& \frac{E_{ij}}{h^2 l^2} - \frac{H_{ij}}{2hl^2} - \frac{K_{ij}}{2h^2 l} + \frac{L_{ij}}{4hl}, && (4.21)\\
n_2 =& \frac{B_{ij}}{l^2} - \frac{D_{ij}}{2l} - \frac{2E_{ij}}{h^2 l^2} + \frac{K_{ij}}{h^2 l}, && (4.22)\\
n_3 =& \frac{E_{ij}}{h^2 l^2} + \frac{H_{ij}}{2hl^2} - \frac{K_{ij}}{2h^2 l} - \frac{L_{ij}}{4hl}, && (4.23)\\
n_4 =& \frac{A_{ij}}{h^2} - \frac{C_{ij}}{2h} - \frac{2E_{ij}}{h^2 l^2} + \frac{H_{ij}}{hl^2}, && (4.24)\\
n_5 =& M_{ij} - \frac{2A_{ij}}{h^2} - \frac{2B_{ij}}{l^2} + \frac{4E_{ij}}{h^2 l^2}, && (4.25)\\
n_6 =& \frac{A_{ij}}{h^2} + \frac{C_{ij}}{2h} - \frac{2E_{ij}}{h^2 l^2} - \frac{H_{ij}}{hl^2}, && (4.26)\\
n_7 =& \frac{E_{ij}}{h^2 l^2} + \frac{H_{ij}}{2hl^2} + \frac{K_{ij}}{2h^2 l} + \frac{L_{ij}}{4hl}, && (4.27)\\
n_8 =& \frac{B_{ij}}{l^2} + \frac{D_{ij}}{2l} + \frac{2E_{ij}}{h^2 l^2} - \frac{K_{ij}}{h^2 l}, && (4.28)\\
n_9 =& \frac{E_{ij}}{h^2 l^2} - \frac{H_{ij}}{2hl^2} + \frac{K_{ij}}{2h^2 l} - \frac{L_{ij}}{4hl}. && (4.29)
\end{aligned}$$

It is worth mentioning that the scheme developed in [76] was devoid of the reaction term present in (4.4) and of any variable diffusion coefficients.

4.2.2 Discretization on the irregular points

In this section, we explore several feasible scenarios for the irregular points and the discretization of the equation thereat.

4.2.2.1 Irregular points lying on grid lines parallel to x-axis only

Here, we describe the case when the irregular point lies only on grid lines parallel to $x-$axis. Let us assume that such a grid line meets the interface between (x_i, y_j) and (x_{i+1}, y_j) (i.e $\phi_{i+1,j} \times \phi_{i,j} < 0$) at the interfacial point (x_2^*, y_j), with the possibility of the interface cutting the grid lines above and below y_j level at the points (x_1^*, y_{j+1}) and (x_3^*, y_{j-1}) respectively on a nine point compact stencil as shown in figure 4.2(a). From this figure, it is clear that $\phi > 0$ on these three points (x_{i+1}, y_{j+1}), (x_{i+1}, y_j) and (x_{i+1}, y_{j-1}), while the remaining six points lie on the other side of the interface where $\phi < 0$.

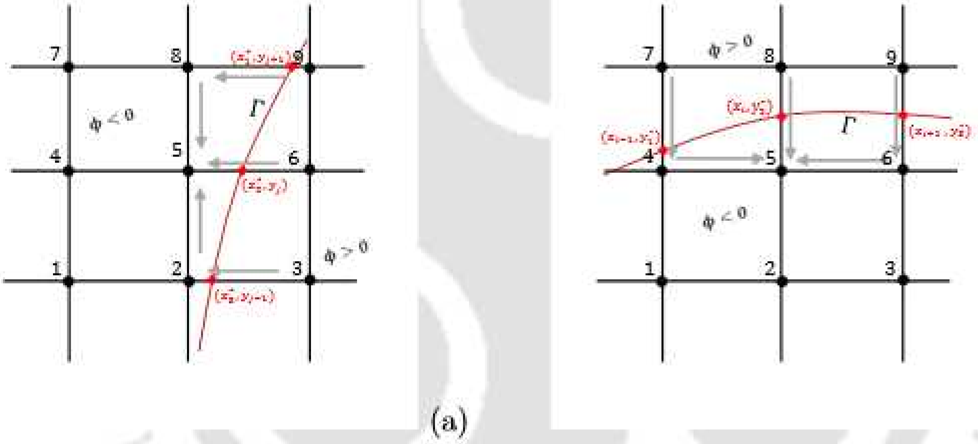

(a) (b)

Figure 4.2: *Stencils around the irregular points lying on grid lines parallel to (a) x-axis only and (b) y-axis only.*

For approximating the mixed derivatives appearing in (4.5), we apply Taylor series expansion to approximate $u(x_{i+1}, y_{j+1})$, $u(x_{i+1}, y_j)$ and $u(x_{i+1}, y_{j-1})$ about the grid point (x_i, y_j) by including the jumps in the solution and the derivatives along the x-direction at the interfacial points. This can be accomplished by firstly expanding the Taylor series in the direction of irregularity i.e. along x- axis as indicated by the arrowheads in figure 4.2(a) and then moving in the other direction along y-axis. The following lemma ensures the high order accuracy of these approximations, detailed proof of which can be found in the subsection 2.1.1 along with other possible scenarios.

Lemma 4.2.1. *Let* $u^- \in C^{k+1}[x_0, x_1^*] \times [y_0, y_f]$, $u^+ \in C^{k+1}[x_1^*, x_f] \times [y_0, y_f]$, $h = x_{i+1} - x_i$,

$h_1^+ = x_{i+1} - x_1^\star$ and $h_1^- = x_i - x_1^\star$ then we have the following inequality

$$\left\| u(x_{i+1}, y_{j+1}) - \sum_{p=0}^{k}\sum_{q=0}^{k-p} \frac{h^p l^q}{p!\,q!}\frac{\partial^{p+q}u}{\partial x^p \partial y^q}(x_i, y_j) - \sum_{r=0}^{k}\frac{(h_1^+)^r}{r!}\left[\frac{\partial^r u}{\partial x^r}(x_1^\star, y_{j+1})\right] \right\| \le K\frac{h^{k+1}}{(k+1)!} + \frac{M}{(k+1)!}(|h|+|l|)^{k+1}$$

where $K = \max(\max_{x\in[x_i, x_1^\star)} \mid u^{k+1}(x_1^\star, y_{j+1}) \mid, \max_{x\in(x_1^\star, x_{i+1}]} \mid u^{k+1}(x_1^\star, y_{j+1}) \mid)$

Remark 4.2.1. *Let $h_3^+ = x_{i+1} - x_3^\star$ and $h_3^- = x_i - x_3^\star$ then we have the following inequality*

$$\left\| u(x_{i+1}, y_{j-1}) - \sum_{p=0}^{k}\sum_{q=0}^{k-p} \frac{h^p (-l)^q}{p!\,q!}\frac{\partial^{p+q}u}{\partial x^p \partial y^q}(x_i, y_j) - \sum_{r=0}^{k}\frac{(h_3^+)^r}{r!}\left[\frac{\partial^r u}{\partial x^r}(x_3^\star, y_{j-1})\right] \right\| \le O(h^{k+1}, l^{k+1}) \tag{4.30}$$

For $k = 3$, the above Lemma and Remarks guarantee that the approximation of (4.4) is fourth order accurate in spatial direction (see table 4.1 for test case 1), yielding

$$\delta_{xy}u_{ij} = \frac{\partial^2 u}{\partial x \partial y} - \frac{1}{4hl}\left(\sum_{r=0}^{k}\frac{(h_1^+)^r}{r!}\left[\frac{\partial^r u}{\partial x^r}(x_1^\star, y_{j+1})\right] - \sum_{r=0}^{k}\frac{(h_3^+)^r}{r!}\left[\frac{\partial^r u}{\partial x^r}(x_3^\star, y_{j-1})\right]\right) + O(h^2, l^2), \tag{4.31}$$

$$\delta_{xx}\delta_y u_{ij} = \frac{\partial^3 u}{\partial x^2 \partial y} + \frac{1}{2h^2 l}\left(\sum_{r=0}^{k}\frac{(h_3^+)^r}{r!}\left[\frac{\partial^r u}{\partial x^r}(x_3^\star, y_{j-1})\right] - \sum_{r=0}^{k}\frac{(h_1^+)^r}{r!}\left[\frac{\partial^r u}{\partial x^r}(x_1^\star, y_{j+1})\right]\right) + O(h^2, l^2), \tag{4.32}$$

$$\delta_x\delta_{yy} u_{ij} = \frac{\partial^3 u}{\partial x \partial y^2} + \frac{1}{2hl^2}\left(2\sum_{r=0}^{k}\frac{(h_2^+)^r}{r!}\left[\frac{\partial^r u}{\partial x^r}(x_2^\star, y_j)\right] - \sum_{r=0}^{k}\frac{(h_1^+)^r}{r!}\left[\frac{\partial^r u}{\partial x^r}(x_1^\star, y_{j+1})\right]\right) - \frac{1}{2hl^2}\sum_{r=0}^{k}\frac{(h_3^+)^r}{r!}\left[\frac{\partial^r u}{\partial x^r}(x_3^\star, y_{j-1})\right] + O(h^2, l^2), \tag{4.33}$$

$$\delta_{xx}\delta_{yy} u_{ij} = \frac{\partial^4 u}{\partial x^2 \partial y^2} + \frac{1}{h^2 l^2}\left(2\sum_{r=0}^{k}\frac{(h_2^+)^r}{r!}\left[\frac{\partial^r u}{\partial x^r}(x_2^\star, y_j)\right] - \sum_{r=0}^{k}\frac{(h_1^+)^r}{r!}\left[\frac{\partial^r u}{\partial x^r}(x_1^\star, y_{j+1})\right]\right) - \frac{1}{h^2 l^2}\sum_{r=0}^{k}\frac{(h_3^+)^r}{r!}\left[\frac{\partial^r u}{\partial x^r}(x_3^\star, y_{j-1})\right] + O(h^2, l^2). \tag{4.34}$$

With these, equation (4.16) at the irregular point (x_i, y_j) reduces to

$$\begin{aligned}
\sum_{i=1}^{9} c_i u_i^{n+1} &- c_3 \sum_{r=0}^{k} \frac{(h_1^+)^r}{r!} \left[\frac{\partial^r u}{\partial x^r}(x_1^\star, y_{j+1})\right]^{(n+1)} - c_6 \sum_{r=0}^{k} \frac{(h_2^+)^r}{r!} \left[\frac{\partial^r u}{\partial x^r}(x_2^\star, y_j)\right]^{(n+1)} \\
&+ c_9 \sum_{r=0}^{k} \frac{(h_3^+)^r}{r!} \left[\frac{\partial^r u}{\partial x^r}(x_3^\star, y_{j-1})\right]^{(n+1)} \\
&= \sum_{i=1}^{9} c_i' u_i^n - c_3' \sum_{r=0}^{k} \frac{(h_1^+)^r}{r!} \left[\frac{\partial^r u}{\partial x^r}(x_1^\star, y_{j+1})\right]^{(n)} - c_6' \sum_{r=0}^{k} \frac{(h_2^+)^r}{r!} \left[\frac{\partial^r u}{\partial x^r}(x_2^\star, y_j)\right]^{(n)} \\
&+ c_9' \sum_{r=0}^{k} \frac{(h_3^+)^r}{r!} \left[\frac{\partial^r u}{\partial x^r}(x_3^\star, y_{j-1})\right]^{(n)} + \frac{\Delta t}{2}\left(F_{ij}^{n+1} - F_{ij}^{n}\right) \qquad (4.35)
\end{aligned}$$

It is important to take note that the jump correction terms are introduced here at each of the time levels n and $(n+1)$ in accordance with what the situation demands.

4.2.2.2 Irregular points lying on grid lines parallel to y-axis only

The treatment for irregular points lying only on grid lines parallel to $y-$axis is similar to the cases described in the above section. The details of the spatial discretizations of interfacial points lying between (x_i, y_j) and (x_i, y_{j+1}) as shown in figure 4.2(b) and other possible cases including treatment of irregular points lying simultaneously on grid lines parallel to both x-axis and y-axis can be found in subsection 2.1.3.

4.3 Streamfunction-vorticity formulation for transient flows

The streamfunction vorticity formulation of the 2D steady state Navier-Stokes equation was presented in section 3.1.5. The primitive variable formulation of the momentum equation for transient flows is given by

$$\frac{\partial \mathbf{V}}{\partial t} + (\mathbf{V} \cdot \nabla)\mathbf{V} = -\nabla p + \frac{1}{Re}\nabla^2 \mathbf{V}, \qquad (4.36)$$

Following the same procedure in chapter 3, the horizontal and the vertical components of the velocity $\mathbf{V}$ is defined as

$$u = \frac{\partial \psi}{\partial y} \quad \text{and} \quad v = -\frac{\partial \psi}{\partial x}. \qquad (4.37)$$

which allows the preservation of the incompressibility condition of the continuity equation (3.13). Taking curl of (4.36) reduces it into the vorticity transport equation

$$\frac{\partial \zeta}{\partial t} = \frac{1}{Re}\nabla^2 \zeta - \mathbf{V}.\nabla \zeta \tag{4.38}$$

where t the time. In the 2D flow field the vorticity vector $\vec{\omega}$ is given by $\nabla \times \mathbf{V} = \vec{\omega} = \zeta \hat{k} = \left(\frac{\partial v}{\partial x} - \frac{\partial u}{\partial y}\right)\hat{k}$, $\hat{k}$ being the unit vector normal to the xy-plane. From the definition of streamfunction ψ and the scalar vorticity ζ above, one can get the following Poisson equation for the streamfunction

$$\nabla^2 \psi = -\zeta \tag{4.39}$$

Let the surface of the bluff body be represented by S_b with curvilinear coordinates s along it and $\hat{n}$, $\hat{\boldsymbol{\phi}}$ be the outward unit normal and tangent vectors respectively (see figure 4.4a). If $\mathbf{V}_S(s,t)$ is the velocity of the fluid on the surface S_b, the corresponding boundary conditions for ψ is

$$\left.\frac{\partial \psi}{\partial n}\right|_{S_b} = \hat{n} \cdot \mathbf{V}_S(s,t), \quad \left.\frac{\partial \psi}{\partial \tau}\right|_{S_b} = -\hat{\boldsymbol{\phi}} \cdot \mathbf{V}_S(s,t). \tag{4.40}$$

The system of equations (4.37)-(4.40) completely describes what is known as the unsteady Streamfunction-Vorticity (ψ-ζ) formulation of the N-S equations. Note that, being parabolic in nature, equation (4.38) can be discretized using (4.16) and (4.35), while (4.39) being elliptic, one may use the approach developed in chapter 2. Over the past few decades, this formulation has been employed for 2D fluid flow computations with great success because of its ease of implementation. In particular, large number of researchers have utilized it in order to check the efficiency of newly developed methods by numerical solving a variety of challenging fluid flow problems. However, owing to the non-specification of vorticity values at the no-slip boundaries, one needs to devise specific approach to approximate the vorticity values thereat. This task becomes more trickier in the immersed interface framework over Cartesian grids for curved boundaries, which is detailed in the next section.

4.3.1 Treatment of irregular points for ψ and ζ

A quick look at equation (4.35) reveals that evaluation of the solution at the $(n+1)^{\text{th}}$ level requires the correction terms on the interfacial points across the interface both at

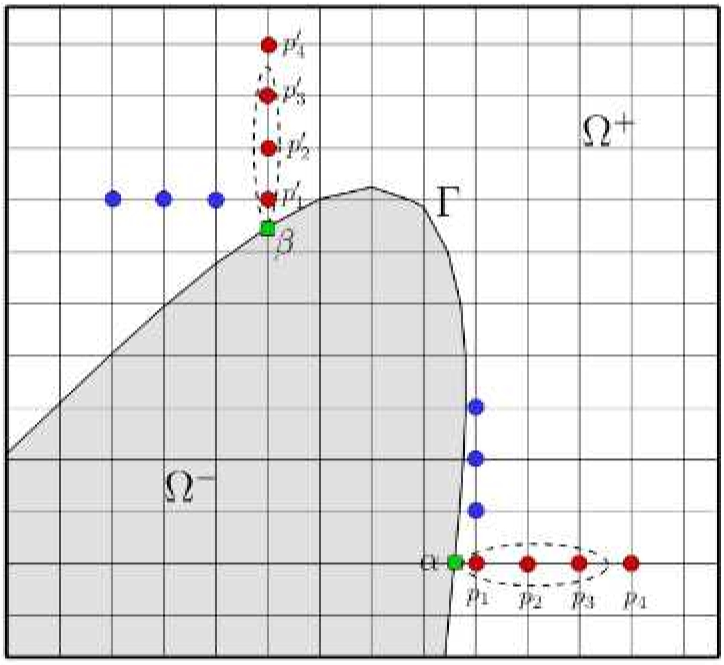

Figure 4.3: *Schematic of the neighbourhood of the interface for the evaluation of correction terms.*

$(n+1)^{\text{th}}$ and $(n)^{\text{th}}$ levels. However, such evaluation for the streamfunction and vorticity across the irregular points is not that straightforward. Therefore, a specific interpolation strategy is adopted to calculate the jumps by mapping the values of u and its derivatives at the regular and irregular points across the interface. Consider two interfacial points α and β (denoted by the green solid squares) as shown in figure 4.3, which corresponds to the classification of irregular points represented in the section 4.2.2.1 and 4.2.2.2 respectively. If $u^{(n)}(\alpha)$ denotes the n^{th} order partial derivative of u at the point α lying along x-axis, the jump invariably involves $[u]$ and $[u^{(n)}(\alpha)]$ thereat from either sides of the interface. However, for the test cases involving fluid flows under consideration here, the physical constraints allow the solution to be zero inside the immersed boundary.

Note that for such cases, all these derivatives must be calculated via evaluation of the variable $u(\mathbf{x})$ through the one sided finite difference formula at an irregular point. For example, in order to evaluate u at the interfacial point α, we employ a Lagrangian interpolation polynomial by making use of the first irregular node p_1 on its right hand side (One can choose either left or right side depending upon the location of the interfacial point.) and the subsequent regular nodes p_2 and p_3 as shown in figure 4.3. A unique polynomial of degree two is

$$P(x) = \sum_{j=1}^{3} u(p_j) l_j(x) + \frac{u^{(4)}(\xi(\mathbf{x}))}{4!} \prod_{i=1}^{3} (\alpha - p_i), \tag{4.41}$$

where $\xi(\mathbf{x})$ is some number lying in the interval $(min\{p_i\}, max\{p_i\})_{1 \leq i \leq 3}$ and

$$l_j(x) = \prod_{i \neq j} \frac{(x - p_i)}{(p_j - p_i)}. \tag{4.42}$$

In the correction of jumps, the successive one-directional derivatives of the variables are also of utmost importance, which can be approximated by the successive differentiation of (4.41). As can be seen from (4.41), it involves the differentiation of the basis functions l_j at each node p_j. This can be accomplished by taking its logarithm

$$ln\left(l_j(x)\right) = ln\left(\prod_{i \neq j} \frac{(x - p_i)}{(p_j - p_i)}\right) = \sum_{i \neq j} ln\left(\frac{(x - p_i)}{(p_j - p_i)}\right).$$

Differentiating the above equation, we have:

$$\frac{l'_j(x)}{l_j(x)} = \sum_{i \neq j} \frac{1/(p_j - p_i)}{(x - p_i)/(p_j - p_i)} = \sum_{i \neq j} \frac{1}{(x - p_i)},$$

which yields

$$l'_j(x) = l_j(x)\left(\sum_{i \neq j} \frac{1}{(x - p_i)}\right). \tag{4.43}$$

Applying product rule for the derivatives in (4.43)

$$\begin{aligned} l''_j(x) &= l'_j(x)\left(\sum_{i \neq j} \frac{1}{(x - p_i)}\right) + l_j(x)\left(\sum_{i \neq j} \frac{1}{(x - p_i)}\right)', \\ &= l'_j(x)\left(\sum_{i \neq j} \frac{1}{(x - p_i)}\right) + l_j(x)\left(\sum_{i \neq j} \frac{-1}{(x - p_i)^2}\right). \end{aligned} \tag{4.44}$$

Substituting (4.43), (4.44) reduces to

$$l_j''(x) = l_j(x)\left[\left(\sum_{i\neq j}\frac{1}{(x-p_i)}\right)^2 - \left(\sum_{i\neq j}\frac{1}{(x-p_i)^2}\right)\right]. \tag{4.45}$$

On the surface of the bluff bodies, which accounts for the interface, the jump condition for ψ can be computed using

$$[\psi] = 0, \quad \left[\frac{\partial\psi}{\partial x}\right] = -\left[v\right], \quad \left[\frac{\partial\psi}{\partial y}\right] = \left[u\right], \tag{4.46}$$

$$\left[\frac{\partial^2\psi}{\partial x^2}\right] = -\left[\frac{\partial v}{\partial x}\right] \text{and} \tag{4.47}$$

$$\left[\frac{\partial^2\psi}{\partial y^2}\right] = \left[\frac{\partial u}{\partial y}\right]. \tag{4.48}$$

In equation (4.47) which is utilized for interfacial points lying only on x-axis, $\dfrac{\partial v}{\partial x}$ is computed using the one-sided second order approximation

$$\left[\frac{\partial v}{\partial x}\right] = \left.\frac{\partial v}{\partial x}\right|_{\alpha^+} = \frac{1}{h\delta h(\delta h + h)}\left(-h(2\delta h + h)v(\alpha) + (\delta h + h)^2 v(p_1) - (\delta h)^2 v(p_2)\right). \tag{4.49}$$

where $\delta h = |p_1 - \alpha|$ and $v(\alpha)$ is computed using equation (4.41). Likewise in (4.48), which is typical of irregular points lying on y-axis, the roles of α, p_1 and p_2 in equation (4.47) are carried out by β, p_1' and p_2' respectively for computing $\dfrac{\partial u}{\partial y}$. While exact jump conditions are not difficult to find for streamfunction because of the availability of exact boundary conditions on solid surfaces, no such conditions are available for vorticity.

For vorticity, at the point α, $[\zeta] = \zeta(\alpha^+)$ is evaluated at the current time level $(n+1)$ by making use of equation (4.41), which requires the value of $\zeta(p_1)^{(n+1)}$. However, p_1 being an irregular point, $\zeta(p_1)^{(n+1)}$ is not readily available thereat. In order to circumvent this, a one-sided $O(h^3)$ approximation is utilized to compute ζ by a one-sided discretization of $-\nabla^2\psi(p_1)$ in x and y-directions, viz., making use of the nodes next right and above p_1, denoted by blue and red dots respectively as shown in figure 4.3. We use

$$\frac{\partial^2\psi}{\partial x^2}(p_1) = \frac{1}{h^2}\left(2\psi(p_1) - 5\psi(p_2) + 4\psi(p_3) - \psi(p_4)\right) + O(h^3) \tag{4.50}$$

and likewise for $\dfrac{\partial^2\psi}{\partial y^2}(p_1')$. Again $\left[\dfrac{\partial\zeta}{\partial x}\right] = \left.\dfrac{\partial\zeta}{\partial x}\right|_{\alpha+}$ at α and $\left[\dfrac{\partial\zeta}{\partial y}\right] = \left.\dfrac{\partial\zeta}{\partial y}\right|_{\beta+}$ at β, the procedure for approximating which is similar to the ones for finding out the jumps of first order derivatives described in equation (4.49). The approximations for the second order jump condition is

$$\left[\frac{\partial^2\zeta}{\partial x^2}\right] = \left.\frac{\partial^2\zeta}{\partial x^2}\right|_{\alpha^+} = \frac{2}{h\delta h(\delta h + h)}\left(h\psi(\alpha) - (\delta h + h)\psi(p_1) + \delta h\psi(p_2)\right). \tag{4.51}$$

Likewise, jump conditions for higher order derivatives can also be estimated.

4.3.2 Fluid dynamic forces on the body

When a body is immersed into a fluid in relative motion, the fluid exerts a force on the bluff body which can be derived from the equations of motion (3.13) and (4.36). We have utilized the momentum approach adopted by Noca *et al.* [122], who devised a formula that does not require explicit knowledge of the pressure term. Note that Equation (4.36) is nothing but confirmation of Newton's second law, which states that the time rate of change within the control volume is equal to the net force. The momentum balance is written in integral form by considering an arbitrary time-dependent control volume $V(t)$ bounded externally by a control surface $S(t)$ and internally by the body surface $S_b(t)$ as shown in figure 4.4(a). Thus $V(t)$ is a simply connected region. The fluid dynamic force $\vec{F}$ in dimensional form acting on body enclosed by a fixed control volume can be written as

$$\vec{F} = -\frac{d}{dt}\int_{V(t)} \rho\tilde{\mathbf{V}}dV + \oint_{S(t)} \hat{n}.\gamma_{mom}\, ds - \oint_{S_b(t)} \rho\hat{n}.(\tilde{\mathbf{V}} - \vec{u_s})\, ds \tag{4.52}$$

where ρ is the density of the fluid, $\hat{n}$ is a unit normal vector, $\tilde{\mathbf{V}}$ is the flow velocity, u_s is the velocity of the surface of the body. The term γ_{mom} is a tensor accumulating several terms evaluated on fixed control volume given by,

$$\begin{aligned}\gamma_{mom} =& \frac{\rho}{2}|\tilde{\mathbf{V}}|^2\mathbf{I} + \rho\left[(\vec{u_s} - \tilde{\mathbf{V}})\tilde{\mathbf{V}} - \tilde{\mathbf{V}}(\vec{x}\times\vec{\omega}) + \zeta(\vec{x}\times\tilde{\mathbf{V}})\right] - \rho\left[\left(\vec{x}.\frac{\partial\tilde{\mathbf{V}}}{\partial t}\mathbf{I} - \vec{x}\frac{\partial\tilde{\mathbf{V}}}{\partial t}\right)\right] \\ &+ [\vec{x}.(\nabla.\mathbf{T})\mathbf{I} - \vec{x}(\nabla.\mathbf{T})] + \mathbf{T}\end{aligned} \tag{4.53}$$

where $\mathbf{I}$ is the unit tensor and $\mathbf{T}$ is the viscous stress tensor $\mathbf{T} = \mu(\nabla\tilde{\mathbf{V}} + \nabla\tilde{\mathbf{V}}^T)$, μ being the dynamic viscosity of the fluid.

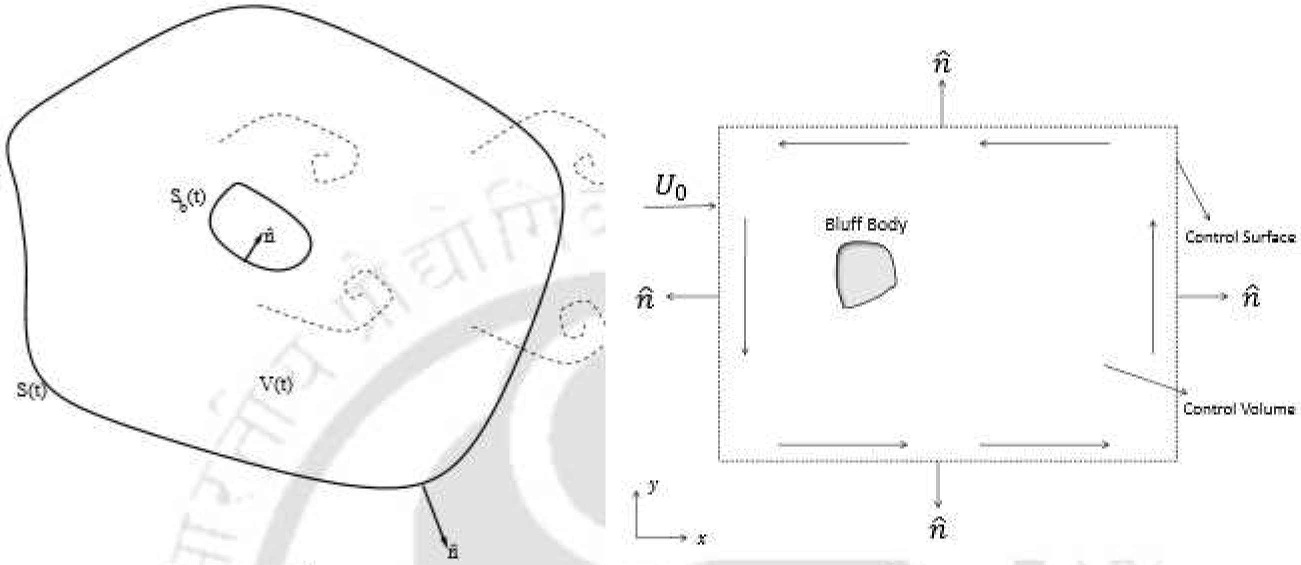

(a) (b)

Figure 4.4: *Schematic of (a) the domain of integration for body force evaluation on a bluff body and (b) rectangular region representing the Control volume.*

We choose V to be a rectangular box of unit depth and net fluxes are calculated across its boundary. For a 2D flow, V reduces to a rectangular region and S reduces to a counter-clockwise rectangular curve (figure 4.4(b)). Under these assumptions, if F_D and F_L are the drag and lift forces and making use of the fact that $\hat{n}ds = dy\hat{i} - dx\hat{j}$, making use of (4.53) in (4.52) and after some complicated vector algebra (see Appendix A), we arrive at

$$\begin{aligned}
\begin{bmatrix} F_D \\ F_L \end{bmatrix} = &- \rho \iint_V \begin{bmatrix} \left(\frac{\partial u}{\partial t} + u\frac{\partial u}{\partial x} + v\frac{\partial u}{\partial y}\right) \\ \left(\frac{\partial v}{\partial t} + u\frac{\partial v}{\partial x} + v\frac{\partial v}{\partial y}\right) \end{bmatrix} dxdy \\
&+ \oint_S \begin{bmatrix} \rho\left(-v(u_s - u) + vy\zeta - y\frac{\partial v}{\partial t}\right) + \nu y \nabla^2 u \\ \rho\left(-\frac{1}{2}(u^2+v^2) - v(v_s - v) - vx\zeta - x\frac{\partial u}{\partial t}\right) - \nu\left(x\nabla^2 u + \frac{\partial u}{\partial y} + \frac{\partial v}{\partial x} + 2\frac{\partial v}{\partial y}\right) \end{bmatrix} dx \\
&+ \oint_S \begin{bmatrix} \rho\left(\frac{1}{2}(u^2+v^2) + u(u_s - u) - uy\zeta - y\frac{\partial v}{\partial t}\right) + \nu\left(y\nabla^2 v + 2\frac{\partial u}{\partial x} + \frac{\partial u}{\partial y} + \frac{\partial v}{\partial x}\right) \\ \rho\left(u(v_s - v) + ux\zeta + x\frac{\partial u}{\partial t}\right) - \nu x \nabla^2 v \end{bmatrix} dy.
\end{aligned} \tag{4.54}$$

Normalizing the drag and lift forces by the characteristic velocity U and characteristic dimension L of the bluff body under consideration, the drag and lift coefficients, viz., C_D and C_L respectively, reduces to

$$\begin{bmatrix} C_D \\ C_L \end{bmatrix} = \begin{bmatrix} F_D/\left(\frac{1}{2}\rho U^2 L\right) \\ F_L/\left(\frac{1}{2}\rho U^2 L\right) \end{bmatrix}. \tag{4.55}$$

Subsequently, under the assumption of a solid bluff body and fixed control volume, and making use of (4.54), equation (4.55) in terms of the non-dimensionalized variables can be written as

$$\begin{aligned} \begin{bmatrix} C_D \\ C_L \end{bmatrix} = & -2 \iint_V \begin{bmatrix} \frac{\partial u}{\partial t} \\ \frac{\partial v}{\partial t} \end{bmatrix} dxdy \\ & + 2 \oint_S \begin{bmatrix} \left(uv + vy\zeta - y\frac{\partial v}{\partial t}\right) + \frac{1}{Re} y \nabla^2 u \\ \left(\frac{1}{2}(v^2 - u^2) - vx\zeta - x\frac{\partial u}{\partial t}\right) - \frac{1}{Re}\left(x\nabla^2 u + \frac{\partial u}{\partial y} + \frac{\partial v}{\partial x} + 2\frac{\partial v}{\partial y}\right) \end{bmatrix} dx \\ & + 2 \oint_S \begin{bmatrix} \left(\frac{1}{2}(v^2 - u^2) - uy\zeta - y\frac{\partial v}{\partial t}\right) + \frac{1}{Re}\left(y\nabla^2 v + 2\frac{\partial u}{\partial x} + \frac{\partial u}{\partial y} + \frac{\partial v}{\partial x}\right) \\ \left(-uv + ux\zeta + x\frac{\partial u}{\partial t}\right) - \frac{1}{Re} x \nabla^2 v \end{bmatrix} dy. \end{aligned} \tag{4.56}$$

Both the line and surface integrals in the above formula are numerically computed by Trapezoidal rule.

4.3.3 Solution of the system of algebraic equation

The N-S equations (4.38)-(4.39) in ψ-ζ formulation can easily be recast into the parabolic equation (4.1). For example, (4.38) can be obtained from (4.1) by setting $\lambda = 1$, $u = \zeta$, $\beta = -1/Re$, $f = 0$, $\beta_x = u$ and $\beta_y = v$. Likewise, (4.39) is nothing but the steady-state version of (4.1) with $u = \psi$, $f = -\zeta$ and $\beta_x = \beta_y = 0$. Equation (4.38) is discretized at regular points by employing (4.5) and at irregular points by the procedure described in sections 4.2.2.1 and 4.2.2.2. (4.39) is discretized by the procedure developed in chapter 2.

Once vorticity ζ and streamfunction ψ have been computed, making use of equation

(4.37), HOC approximation the velocities u and v are given by [75]

$$u_{ij} = \delta_y\psi + \frac{l^2}{6}\left(\delta_y\zeta + \delta_x^2\delta_y\psi\right) + O(h^4, l^4), \tag{4.57}$$

$$v_{ij} = -\delta_x\psi - \frac{h^2}{6}\left(\delta_x\zeta + \delta_x\delta_y^2\psi\right) + O(h^4, l^4). \tag{4.58}$$

In matrix form, the discretized HOC form of the vorticity transport equation (4.38) at the interior nodes is given by

$$\tilde{S}\zeta^{(n+1)} = \tilde{S}'\zeta^{(n)} + \tilde{C}_\zeta^{(n)} + \tilde{C}_\zeta^{(n+1)}, \tag{4.59}$$

where $\tilde{S}$, $\tilde{S}'$ is HOC matrix to the equation (4.38) and $\tilde{C}_\zeta^{(n)}$, $\tilde{C}_\zeta^{(n+1)}$ are the vorticity correction vectors at the irregular points corresponding to the $(n)^{\text{th}}$ and $(n+1)^{\text{th}}$ time levels respectively. Likewise, the HOC matrix representation of equation (4.39) at the interior nodes is

$$\tilde{T}\psi^{(n+1)} + \left[I + \frac{h^2}{12}T\right]\zeta^{(n+1)} = 0, \tag{4.60}$$

where $\tilde{T}$ and T are the HOC and CDS matrices corresponding to the interior nodes. On the other hand, the boundary conditions (4.40) may be expressed

$$N\psi^{(n+1)} + \tilde{B}\zeta^{(n+1)} = \tilde{U}^{(n+1)}, \tag{4.61}$$

$$\psi_B = 0. \tag{4.62}$$

where N is the matrix resulting from normal derivative boundary conditions, $\tilde{B}$ is the vorticity boundary matrix, $\widetilde{U}^{(n+1)}$ is the current velocity vector owing to (4.57)-(4.58), and the subscript I, and B denotes the interior and boundary respectively. The following matrix equations provide a complete picture of the discretized equations at the regular, irregular and the boundary points simultaneously in concise and compact form

$$\begin{bmatrix} \tilde{T}_R & \tilde{T}_{IR} & T_B \\ O & O & I \end{bmatrix} \begin{bmatrix} \psi_R \\ \psi_{IR} \\ \psi_B \end{bmatrix}^{(n+1)} = -\begin{bmatrix} I + \frac{h^2}{12} & \frac{h^2}{12}T_B \\ O & O \end{bmatrix} \begin{bmatrix} \zeta_I \\ \zeta_B \end{bmatrix}^{(n)} + \begin{bmatrix} \tilde{C}_\psi \\ 0 \end{bmatrix}^{(n)}, \tag{4.63}$$

$$\begin{bmatrix} \tilde{S}_R & \tilde{S}_{IR} & \tilde{S}_B \\ \tilde{B}_B & O & \tilde{B}_B \end{bmatrix} \begin{bmatrix} \zeta_R \\ \zeta_{IR} \\ \zeta_B \end{bmatrix}^{(n+1)} = - \begin{bmatrix} O & O \\ N_I & N_B \end{bmatrix} \begin{bmatrix} \psi_I \\ \psi_B \end{bmatrix}^{(n+1)} + \begin{bmatrix} F \\ \tilde{U} \end{bmatrix}^{(n)}, \qquad (4.64)$$

where,

$$F = \begin{bmatrix} \tilde{S}'_R & \tilde{S}'_{IR} & \tilde{S}'_B \end{bmatrix} \begin{bmatrix} \zeta_R \\ \zeta_{IR} \\ \zeta_B \end{bmatrix}^{(n)} + (\tilde{C}_\zeta^{(n+1)} + \tilde{C}_\zeta^{(n)}). \qquad (4.65)$$

and the subscripts R, and IR represent the regular and irregular interior points respectively.

For a grid of size $M \times N$, the matrices $\tilde{S}$, $\tilde{S}'$, $\tilde{T}$ and T are of order MN and $\zeta^{(n)}$, $\zeta^{(n+1)}$, $\psi^{(n)}$, $\psi^{(n+1)}$, $\tilde{C}^{(n)}$, $\tilde{C}^{(n+1)}$ are vectors of length MN in equations (4.59) and (4.60). Apart from the grid size of the computational domain, the size of the block matrices in equations (4.63)-(4.65) depends on the geometry of the immersed body which determines the number of regular and irregular points.

An inner-outer iteration procedure is essential for the time marching solutions of transient fluid flow problems governed by (4.38)-(4.39). Once u, v, ζ and ψ are presented with appropriate initial and boundary conditions, firstly (4.38) and then (4.39) is solved. Once ψ is available, u and v are computed by utilizing (4.57) and (4.58). This completes one outer time iteration.

The inner iterations are composed of solving (4.59) and (4.60) by efficient iterative solvers at each time step. We have accomplished this in our computations by employing the BiCGStab Stabilized [82] iterative solver along with Incomplete LU decomposition as preconditioner with the help of the Lis Library [1]. The inner iterations were stopped when the residual vectors arising out of equations (4.59) and (4.60) fell below 10^{-13}. All our computations were performed on a Intel Xeon processor-based PC with a 32 GB RAM.

4.4 Numerical test cases

In order to demonstrate the effectiveness of the proposed approach, it is applied to several problems. The first of these has analytical solution and the remaining are flow past bluff bodies immersed in fluids, for both the stationary and moving cases. Also considered are flows involving multiple bodies. In all the fluid problems under consideration, the flow is governed by the unsteady N-S equations for incompressible viscous flows.

4.4.1 Test Case 1: Interface problem having analytical solution

As our first test case, we validate our algorithm to solve the parabolic equation given by

$$u_t = \nu \nabla^2 u, \quad (x, y, t) \in \Omega \times (0, T]. \tag{4.66}$$

with initial and boundary conditions

$$u(x, y, 0) = u_0(x, y), \qquad (x, y) \in \Omega,$$

$$u(x, y, t) = u_b(x, y, t), \quad (x, y, t) \in \partial\Omega \times (0, T].$$

The computational domain Ω is the square $[0, 1] \times [0, 1]$ and the solution has a discontinuity across the the circular interface Γ of radius 0.25 centered at the point $(0.5, 0.5)$. The level set function and analytical solution are respectively defined by $\phi = (x - 0.5)^2 + (y - 0.5)^2 - (0.25)^2$ and

$$u(x, y, t) = \begin{cases} e^{-t\nu\pi^2(k_x^2+k_y^2)} cos(k_x \pi x) cos(k_x \pi y), & \phi \geq 0, \\ 0, & \phi < 0. \end{cases} \tag{4.67}$$

respectively, where (k_x, k_y) are wave number and set the values of both are 2. The initial and boundary conditions are obtained from the equation (4.67). We apply a no flux condition on the boundary of the circular interface i.e

$$\frac{\partial u}{\partial n} \equiv \nabla u.\hat{n} = -4\pi e^{-t\nu\pi^2(k_x^2+k_y^2)} (k_x sin(k_x \pi x)(x - 0.5) + k_y sin(k_x \pi y)(y - 0.5)). \tag{4.68}$$

where $\hat{n} = (x - 0.5, y - 0.5)$ is the normal vector to the circle.

In table 4.1, we present the maximum error ($\| E_N \|_\infty = \max|\mathrm{u}_{\mathrm{ex}} - \mathrm{u}_{\mathrm{num}}|$) resulting from our computation on gradually increasing grid sizes $N \times N$ and show the effect of the parameter k described in equation (4.35). Expectedly, a higher value of k yields a better convergence rate (ROC). While the errors resulting from our computation corresponding to $k = 3$ decay at a rate close to four, the ones from the simulation of Calhoun [21] could obtain an ROC close to two only.

We also present the surface plots of our numerical solution on a grid of size 80 ×

Table 4.1: Grid refinement analysis of maximum error for Test Case 1 at $t = 2.5$ for $\nu = 1/200$ with $\triangle t = 10^{-3}$.

N	Present (k=2)	ROC	Present (k=3)	ROC
20	2.57×10^{-4}	–	3.96×10^{-5}	–
40	7.11×10^{-5}	1.85	5.61×10^{-6}	2.81
80	9.82×10^{-6}	2.84	4.59×10^{-7}	3.61
160	1.61×10^{-6}	2.60	3.21×10^{-8}	3.83
320	2.25×10^{-7}	2.83	2.38×10^{-9}	3.75

80 side by side with the surface plots of errors in figures 4.5(a)-(b). Figure 4.5(a) clearly demonstrates that the sharp interface has been resolved very efficiently by our approach. Note that the errors from our computation (see figure 4.5(b)) are much lower in magnitude the ones in [21].

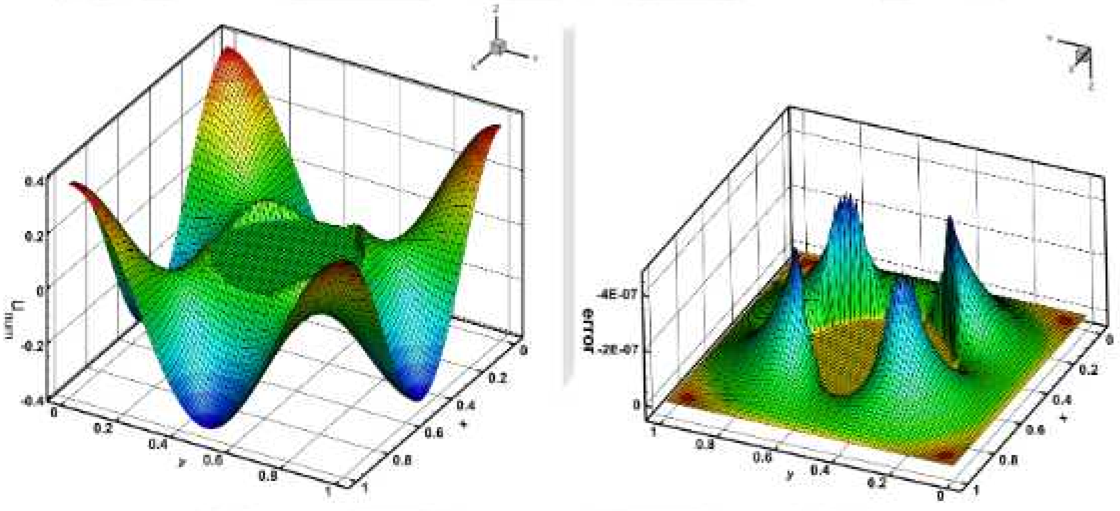

(a) (b)

Figure 4.5: *Surface plots of (a) the numerical solution and (b) error on a grid of size* 80×80 *for Test Case* 1 *for* $k = 3$.

4.4.2 Flow past stationary bluff bodies

The study of the flow past bluff bodies holds an important place in many engineering applications, particularly in the field of naval architecture. Such flows are very complex and are highly characterised by the generation and shedding of vortical structures [30,68, 79,81,90,106,116,128,157,183,194]. Though in practical fields, the Reynolds number

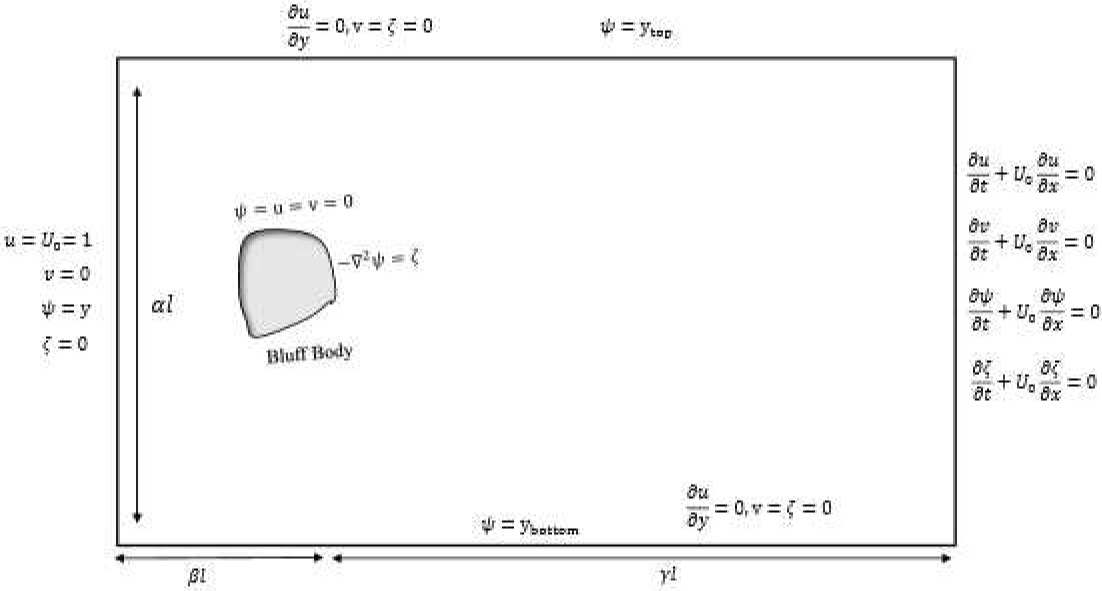

Figure 4.6: *Schematic of the flow past bluff bodies in uniform flow.*

assumes a much higher value, yet our simulation carried out for the laminar regime could provide some insights for further studies. Because of both their theoretical and practical implications, such flows have attracted a lot of attention from the scientific community and been studied for quite a long period of time. Because there is no slip at the boundary conditions, vorticity is created in the region near to the solid surface. This flow phenomenon, along with the structure of the wake, is responsible for greater levels of unsteadiness, pressure fluctuations, structural vibrations, and noise, in addition to increased rates of heat and mass transfer. One of the most exciting topics in computational fluid dynamics is trying to find ways to control or minimize the unwanted behaviour associated with the generation and shedding of these vortices. These attempts continue to be one of the field's primary areas of focus. This in-depth examination was justified by the fact that the vast majority of the cylinder-shaped bluff bodies utilized in engineering and other applications are circular in shape. Simple geometrical configurations have been used in most cases, such as yawed cylinders [141], the usage of end plates [138], elliptic cross section [41], and tandem arrangements [175].

This section is concerned not only with the simulation of flow past stationary bluff bodies, but also with moving ones immersed in fluids. Moreover flow situations involving multiple bodies are also considered. The problems have been chosen in such a way that the ability of the current approach in handling complicated geometry and varied flow situations can be established. As would be seen later on, while most of the previous studies involved computations either by finite volume or finite element approach in extremely finer grids [7, 11, 120, 127, 136, 153, 189] for this kind of flows, our approach accomplishes the same in relatively coarse grids, that too, in FD set-up.

In figure 4.6, we show a schematic of the computational domain along with the boundary conditions used for the simulation. While choosing the dimensions, ample care was taken so that the simulation is free from any entrance effects and there is no hindrance in the smooth shedding of the vortices once the vortices formed on the surface of the bodies start detaching from them. Besides, in all the computations time-steps are chosen in the range $10^{-2} \leq \Delta t \leq 10^{-3}$ according to the flow situation.

4.4.2.1 Test case 2: Flow Past a Stationary Circular Cylinder

In our first test case for flow past stationary bluff bodies, we consider the problem of flow around an impulsively started circular cylinder in a free-stream with uniform velocity. There exists an enormous number of numerical and experimental results for this problem and as such, is a perfect test case for examining the efficiency of the proposed approach by comparing the results obtained from our computations with the benchmark results available in literature. This problem also act as a prelude to tackling problems with moving immersed interfaces.

The schematic for this problem has already been shown in figure 4.6 where the bluff body is now the circular cylinder. Here, Reynolds number is described as $Re = \dfrac{U_0 l}{\nu}$, where l is the cylinder diameter, U_0 is the free stream velocity at the inlet, and ν is the kinematic viscosity of the fluid. For our simulations, we assume l is to be 1.0 with the center of cylinder fixed at $(0,0)$. We have chosen $\beta = 5.0$, $\alpha = 10.0$, and $\gamma = 25.0$ in figure 4.6 such that the corresponding dimensions of the computational domain are $-5.0 \leq x \leq 25.0$ and $-5.0 \leq y \leq 5.0$; as such $y_{top} = 5.0$ and $y_{bottom} = -5.0$. The boundary conditions at the far-field and on the surface of the cylinder are as follows:

- $u = 1$, $v = 0$, $\psi = y$ and $\zeta = 0$ on the left wall $x = -5.0$,
- $\dfrac{\partial u}{\partial y} = 0$, $v = 0$, $\psi = y_{bottom}$ and $\zeta = 0$ on the bottom wall $y = -5.0$,
- $\dfrac{\partial u}{\partial y} = 0$, $v = 0$, $\psi = y_{top}$ and $\zeta = 0$ on the top wall $y = 5.0$,
- $\dfrac{\partial u}{\partial t} + U_0\dfrac{\partial u}{\partial x} = 0$, $\dfrac{\partial v}{\partial t} + U_0\dfrac{\partial v}{\partial x} = 0$, $\dfrac{\partial \psi}{\partial t} + U_0\dfrac{\partial \psi}{\partial x} = 0$ and $\dfrac{\partial \zeta}{\partial t} + U_0\dfrac{\partial \zeta}{\partial x} = 0$ on the right wall $x = 25.0$.

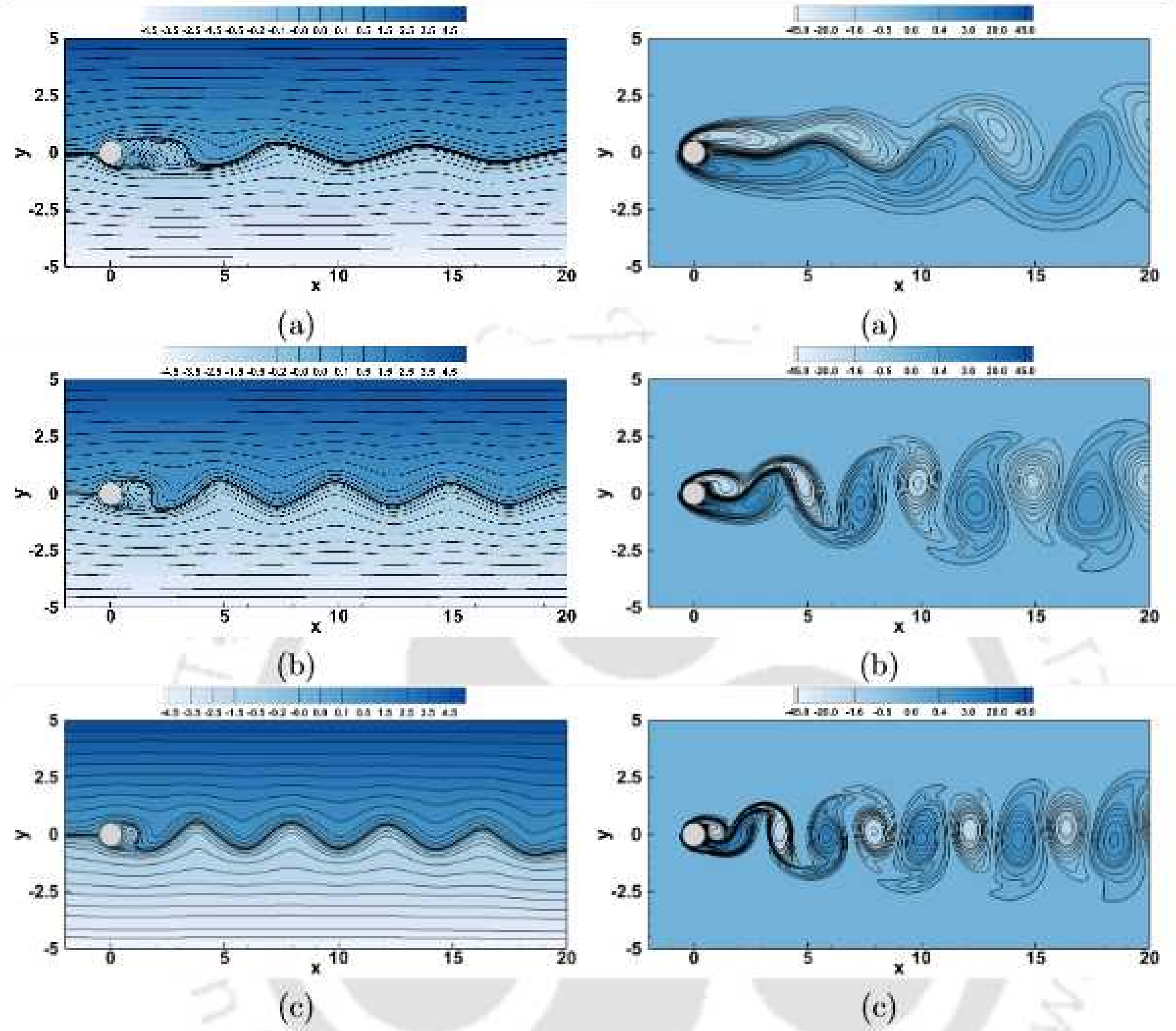

Figure 4.7: *Simulation of flow past circular cylinder problem by present method: Streamlines (left) and Vorticity contours (right) for (a) $Re = 50$, (b) $Re = 100$ and (c) $Re = 200$.*

- $u = v = \psi = 0$, $\zeta = -\nabla^2\psi$ on the surface of the cylinder.

Literature suggests that the flow for an impulsively started stationary cylinder becomes unsteady beyond a critical Reynolds number $45 \leq Re_C \leq 48$. In the following, we present our computational results for Reynolds numbers $Re = 50$, 100 and 200. Note that in many studies, when the Reynolds number under consideration is slightly above R_C as in the case of $Re = 50$, the flow is artificially perturbed [44, 144] in order to break the symmetry of the flow. However, in the computation through our approach, asymmetry sets in naturally without the need of such perturbation. The flow for the range of Re chosen, eventually becomes periodic and is fraught with the vortex shedding phenomenon characterised by the existence of von Kármán vortex street. Once shedding process starts some times after the flow symmetry is broken about $y = 0$ line, vortices

Table 4.2: Comparison of Strouhal number, drag and lift coefficients of the periodic flow for $Re = 100$ and 200.

Re	100			200		
Reference	St	C_D	C_L	St	C_D	C_L
Frank *et al.* [54]	-	-	-	0.194	1.31	± 0.65
Williamson [180]	0.163	-	-	0.190	-	-
Calhoun [20]	0.175	1.330 ± 0.014	± 0.298	0.202	1.172 ± 0.058	± 0.668
Le *et al.* [95]	0.160	1.37 ± 0.009	± 0.323	0.187	1.34 ± 0.030	± 0.430
Berthelsen *et al.* [13]	0.169	1.38 ± 0.010	± 0.340	0.200	1.37 ± 0.046	-
Russel & Wang [144]	0.169	1.380 ± 0.007	± 0.300	0.195	1.290 ± 0.022	± 0.708
S.Sen [148]	0.165	1.394 ± 0.007	± 0.191	0.197	1.375 ± 0.038	± 0.500
Present Study	0.180	1.402 ± 0.042	± 0.232	0.210	1.288 ± 0.058	± 0.425

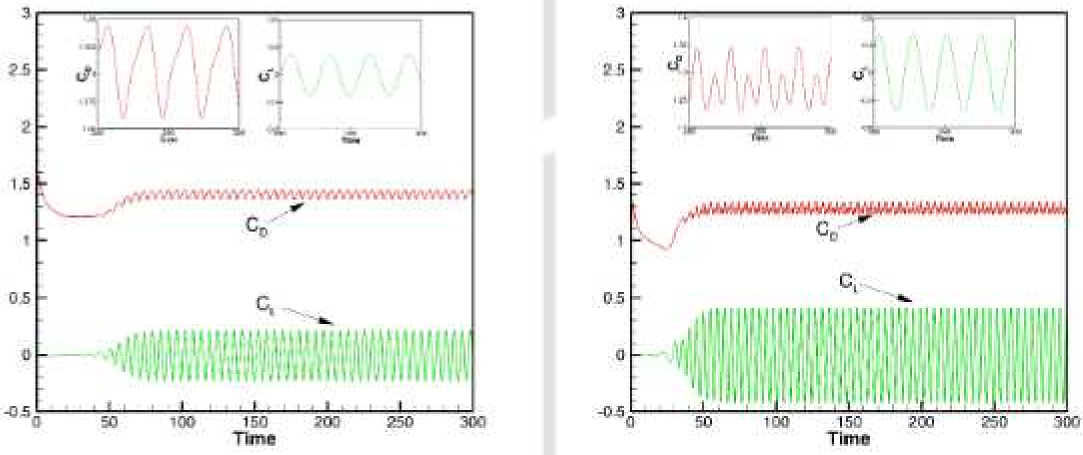

(a) (b)

Figure 4.8: *History of drag and lift coefficients for the flow past an impulsively started stationary cylinder for (a) $Re = 100$ and (b) $Re = 200$.*

are shed alternatively from the either side of the $y = 0$ line in a regular fashion. We depict this process in figure 4.7 where the left panel shows the instantaneous streamlines and the right, the vorticity contours for $Re = 50$ (top), 100 (middle) and 200 (bottom) respectively. As these figures indicate, shedding becomes more prominent with increase in Re value.

We further compute the drag and lift coefficients C_D and C_L respectively by the formulas (4.56) and the Strouhal number St, which describes the mechanism of the oscillatory flow during the shedding process. It is defined as $St = \dfrac{fD}{U_0}$, where f is the dominant frequency of the periodic lift variations, extracted from a time sample of C_Ls. In figures 4.8(a)-(b), we plot the time histories of the drag and lift coefficients for

$Re = 100$ and 200 respectively. We also compare our computed Strouhal numbers, drag and lift coefficients for the same Reynolds numbers with established experimental and numerical results in table 4.2 and obtain excellent comparison. In the next chapter, we will establish the control volume independence of dynamic forces.

4.4.2.2 Test case 3: Flow past a cactus shaped cylinder

The study of flow past cactus shaped cylinder is gradually gaining momentum amongst researchers in the last few years. The saguaro cactus, out of all the numerous species of cactus, is the one that has attracted the most attention from the scientific community, focusing particularly on its aerodynamics. These cacti can reach a height of up to 50 feet [64], yet their root systems are quite shallow and cover an area of less than 1 foot. Saguaro cacti are able to tolerate extremely high wind velocities ($Re \sim 10^6$), despite the fact that their root systems are relatively shallow [57]. Niklas et al. [121] made the observation that the h/D aspect ratio, which is defined as the total height of cacti above ground divided by the largest diameter of the cross section, is proportional to the height of the cactus. Saguaro cacti that are more than 15 feet tall have a h/D ratio that falls somewhere between 12 and 23, while Saguaro cacti that are much more slender have a h/D ratio that is significantly lower (5-12). The diameters of these cacti, on average, are roughly 1.5 feet. Additionally, the trunk of a saguaro has a cross section that is defined by longitudinal cavities, and the spines of the cavities are located at the tips of the cavities. According to Hodge's observations [64], the number of cavities on the surface of the cactus can range anywhere from 10 to 30, depending on how old the plant is and how tall it is. A cactus that is 5 feet tall has an average cavity depth of 0.07 ± 0.0015 [57], assuming that l is the height of the spike. The number of cavities and the cavity depth will alter as the cactus grows, but the average cavity depth will remain the same. Talley and Mungal [173] made the observation that the cavity depth might grow in areas higher up the trunk.

Numerous researchers, like Talley et al. [172], Talley and Mungal [173], Lim et al. [105], Babu et al. [7], and Liu et al. [108], have already conducted numerical and experimental research on the effect that grooves have, yielding fascinating findings. It would appear that the cavities are able to lessen the effect of the fluctuating forces and bring about a reduction in the amount of drag. When the Reynolds number is between 2×10^4 and 2×10^5, a reduction in the drag coefficient is observed to be proportional to the depth of the cavities. Additionally, it was determined through experimentation and measurement that cavities prevent rapid oscillations in the drag coefficient, which results in more stable strains on the structure (Talley and Mungal [173], Talley et al. [172]). However, when the Reynolds number is (≤ 300), the cavities change the wake transition effects that are generally seen at such Reynolds number for a smooth cylinder. This results in a remarkable reduction of the drag and lift forces (Babu and Mahesh [7]). Recently Farhana and Sharif [3] consider triangular V-shaped, the U-shaped, and Rectangular shape valley and observed that the U-grooves result in a significant reduction in the average drag coefficient (by approximately 13% for $Re = 200$ and by 10% for $Re = 300$ in comparison to the case of a smooth cylinder). Therefore, the reduction of the dynamic forces is influenced by the shape of the cactus as well as the total number of its spikes. Additionally, the smoothness of the valley is another aspect that should be considered.

In this part of the flow simulation, we have considered the flow over a more complex geometry, i.e a closed curve in the shape of the cross-section of a cactus shaped cylinder. The flow configuration is similar to the flow past an impulsively started circular cylinder except the fact that the circle is now replaced by a closed curve in the shape of the cross section of a cactus plant. To the best of our knowledge, all the earlier simulations for flows involving cactus shapes were carried out in the finite element framework.

We have used the following level set function for generating the cactus shape centered at (x_c, y_c) is given by

$$\phi(r,\theta) = r - r_0 - L\sin(w\theta) \tag{4.69}$$

where $r = \sqrt{(x-x_c)^2+(y-y_c)^2}$, $\theta = arctan((y-y_c)/(x-x_c))$, r_0, w are parameters determining the base and the number of spikes and L is the maximum height of the spikes. In all our simulations, the center of the cactus shaped region is assumed to be at the origin. The geometry of the cactus along with the mesh around the surface is depicted in figures 4.9(a)-(b) respectively. We have chosen a spike ratio of value 0.105 for a 24 spike cactus which is nothing but the ratio between the maximum height L of the spike and the total diameter D (set as 1 here) of the the cylinder. Note that a spike ratio zero corresponds to a smooth cylinder described in section 4.4.2.1.

Computations were carried out for $Re = 100$ and 300 along with that for the smooth cylinder till periodic vortex shedding stage is reached. Opposed to the smooth cylinder, the flow pattern in the neighbourhood of the surface changes significantly for cactus shaped cylinder. Figure 4.10(a)-(b) shows the instantaneous streamlines and velocity vector plots respectively inside a cactus groove for $Re = 300$. These plots clearly indicate the presence of recirculation zones inside the grooves; one can also see the existence of a secondary zone which is consistent with the findings of [7]. In order

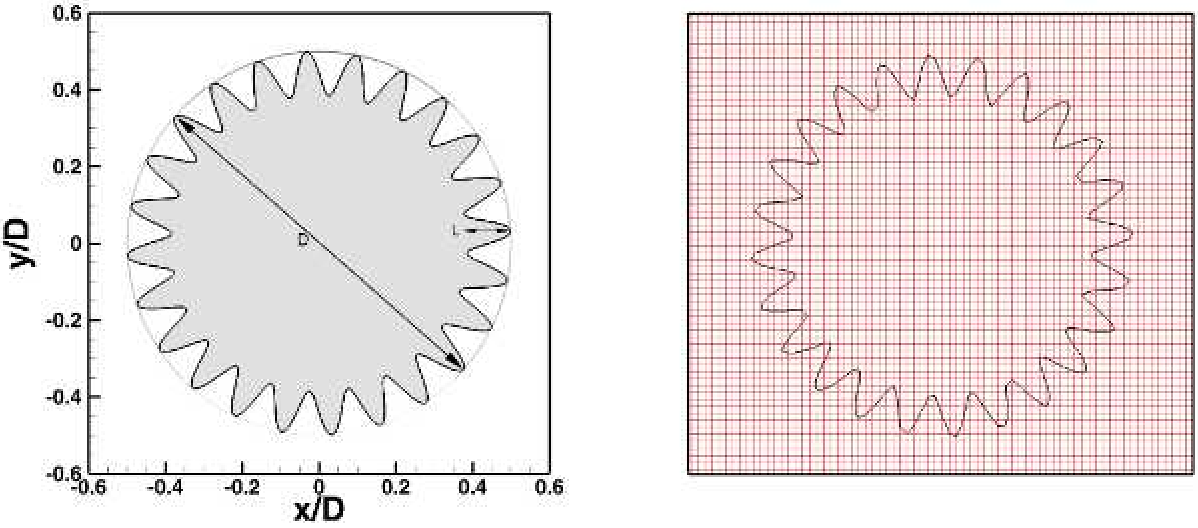

(a) (b)

Figure 4.9: *(a) Schematic of the 24 spike cactus geometry and (b) the mesh around the surface of the immersed cactus on a grid corresponding to step length* $h = l = 0.018D$.

Table 4.3: Comparison of Strouhal number, drag and lift coefficients of the periodic flow for Cactus shaped and Circular Cylinders for $Re = 100$ and 300.

Re	100			300		
Flow parameters	*Cactus*	*Circular*	*%difference*	*Cactus*	*Circular*	*%difference*
St	0.175	0.180	-	0.220	0.251	–
C_D	1.268	1.402	9.56	0.905	1.205	24.89
C_L	±0.151	±0.233	35.19	±0.454	±0.596	23.82

to gain further insight into the flow field variation around the cactus cylinders, we plot the streamfunction (left column) and vorticity contours (right column) in figures 4.11(a)-(e) at five different phases within a shedding cycle. Note that figure 4.11(c) is a mirror image of 4.11(a) and 4.11(e) while figure 4.11(d) is a mirror image of figure 4.11(b). This is because of the fact the shedding of vortices takes place from the upper and the lower parts of the cylinder alternately during a half-cycle period. It further exemplifies the efficiency of our approach in accurately capturing the phenomenon which is obvious from the accompanying video "cycl.avi" depicting one complete cycle of the vorticity contours (Multimedia View: `https://doi.org/10.1063/5.0107308.1`). The time history of drag and lift coefficients for these two Res, depicting the periodic nature of the flow is shown in figure 4.12.

In table 4.3, we compare the force coefficients and Strouhal numbers for the periodic

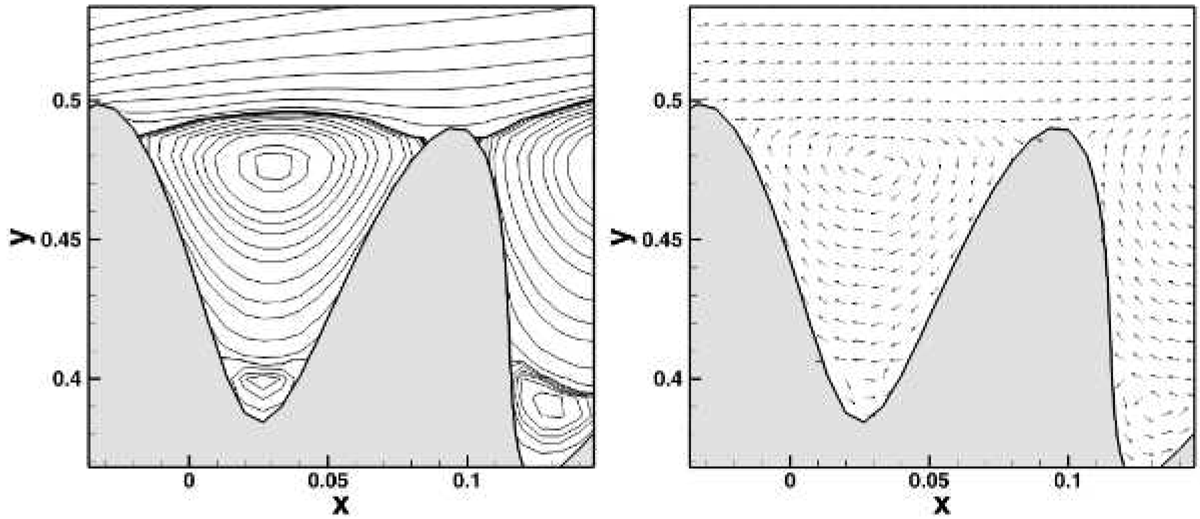

(a) (b)

Figure 4.10: *Instantaneous (a) streamlines and (b) velocity vector plots for flow past a twenty four spike cactus cylinder for $Re = 300$ ($h = l = 0.01D$).*

flows for the cactus shaped and circular cylinders for $Re = 100$ and 300. There seems to be clearly a reduction in the unsteady loads for the cactus shaped cylinder compared to the smooth circular cylinder. With increase in Reynolds number, the drag reduction becomes more prominent. Our observations are consistent with the findings of Babu and Mahesh [7]. The decrement in percentage difference from reference [7] may be attributed to the fact that while their valleys were extremely sharp, the ones employed in our computation are smooth (see figure 4.9(a)). The reduction in the unsteady loads is also evident from the comparison of the power spectra of the cactus shaped and circular cylinder shown in figure 4.13 which reflects the decrease in the higher frequency contents of the loads. It is worth mentioning that while [7] had used 436×10^3 and 7×10^6 hexahedral elements for flow computations for $Re = 100$ and 300 respectively, we have used only 110×10^3 nodes for both the cases. Moreover, while the elements of the grid converged solution were $0.0052D$ in the azimuthal direction and $0.0006D$ radially on the surface of the cylinder in their case, we used a step length $0.018D$ in both the vertical and horizontal directions in our computation (see figure 4.9(b)).

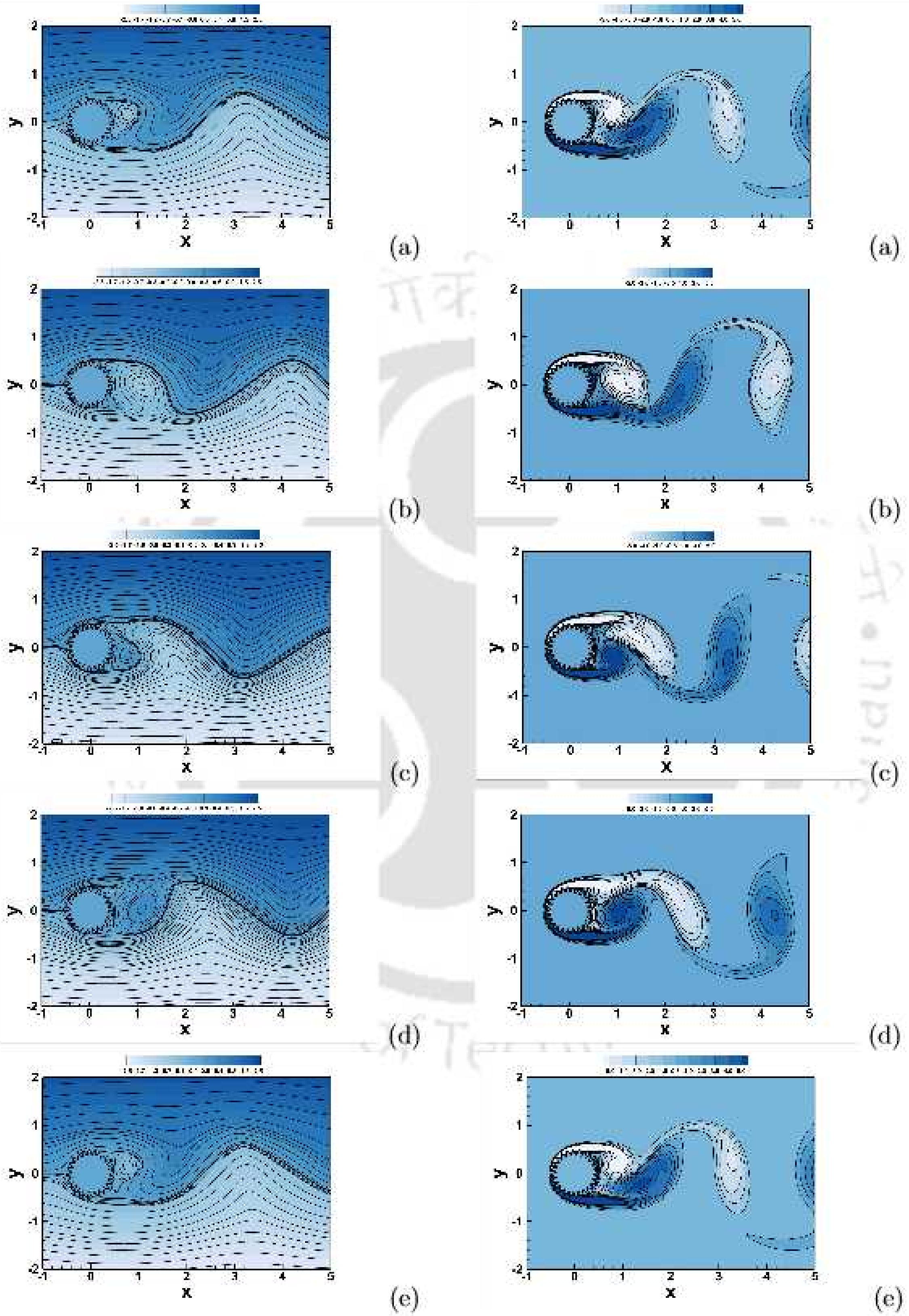

Figure 4.11: *Streamfunction (left) and vorticity (right) contours for the flow past a 24 spike cactus for* $Re = 300$*: (a)* $t = 0$*, (b)* $t = \frac{\pi}{2}$*, (c)* $t = \pi$*, (d)* $t = \frac{3\pi}{2}$ *and (e)* $t = 2\pi$*.*

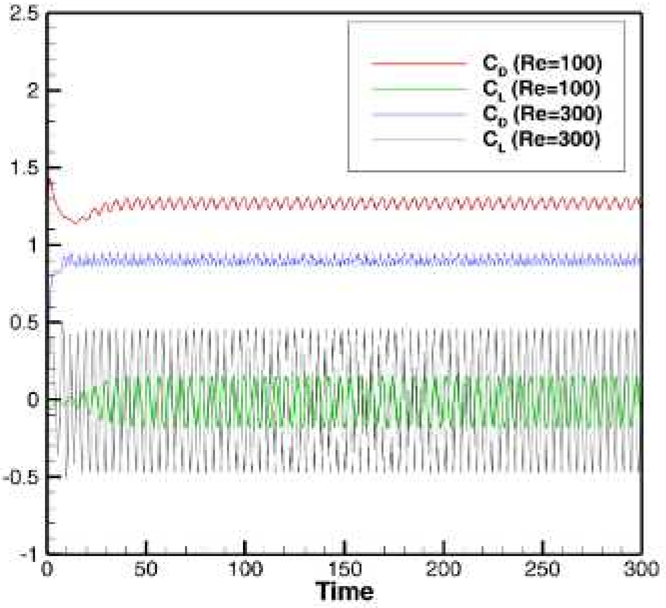

Figure 4.12: *Time histories of drag and lift coefficients for the cactus shaped cylinder for $Re = 100$ and 300.*

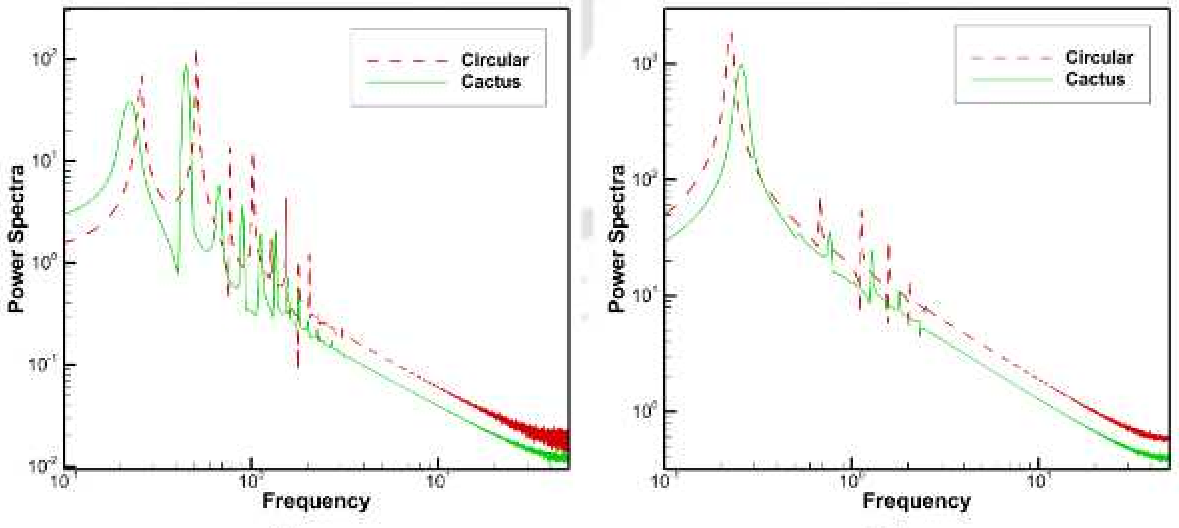

(a) (b)

Figure 4.13: *Comparison of power spectra of the cactus shaped and circular (smooth) cylinders for $Re = 300$ based on the time histories of (a)drag and (b) lift coefficients.*

4.4.3 Flow past two tandem circular cylinders

Flow induced oscillations of multiple circular cylinders is an extremely complex flow problem. It has garnered immense interest over the last few decades owing to its real life applications in the field of off-shore oil drilling rigs and tall chimneys, heat exchanger and riser tubes, cooling of nuclear fuel rods amongst others. In the same vein, the next problems considered here are the flow past two tandem cylinders of equal diameter D separated by a distance PD, where the downstream cylinder is stationary and the upstream cylinder is either kept stationary or oscillating transversely.

4.4.3.1 Test case 4: Stationary upstream cylinder

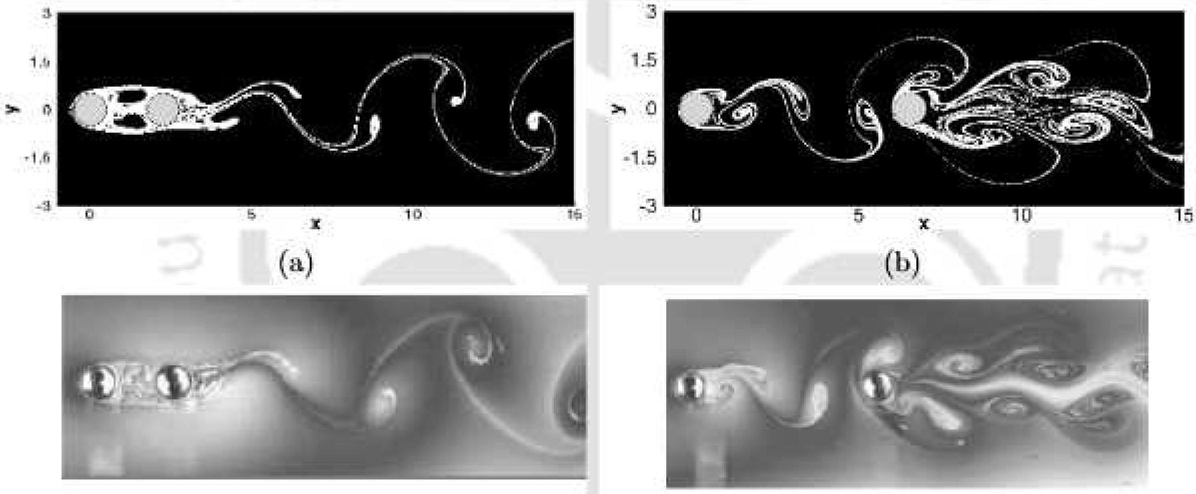

(a) (b)

(c) (d)

Figure 4.14: *Comparison of (a)-(b) computed streaklines for $P = 2.25$ and 6.58 respectively with the (c)-(d) experimental visualization of Yang et al. [184] for Test Case 4.*

Here the flow configuration is similar to the one shown in figure 4.6 except the fact that the single bluff body in the figure is replaced by a stationary circular cylinder at the origin and another cylinder of same dimension is placed to its right at a distance P apart for $Re = 200$. We have considered $P = 2.25$ and 6.58 which characterises the medium pitch and long-pitch regime categorized recently by Hoisseini *et al* [66]. The gap between the cylinders are chosen so as to compare our simulations with the recent experimental visualizations of Yang *et al.* [184] and in the process validate our simulations. The streaklines resulting from our computations are presented top and

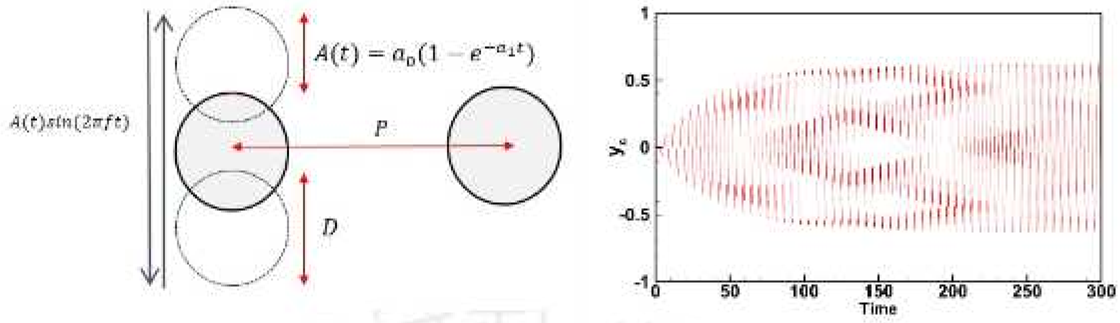

(a) (b)

Figure 4.15: *(a) Schematic of the upstream and downstream cylinders and (b) Displacement of the upstream cylinder center for Test Case 5.*

bottom along with the visualizations of Yang *et al.* [184] in figure 4.14. Our simulations are extremely close to experimental ones exemplifying the efficiency of our immersed interface approach. From figure 4.14(a),(c), one can spot that no shedded vortex is visible in the gap between the cylinders in the medium pitched regime and wake behind the downstream cylinder resembles that of an isolated cylinder. On the other hand, for the long pitch regime, vortex shedding reminiscent of an isolated cylinder is observed in the gap as well as behind the downstream cylinder (see figure 4.14(b),(d)). Our observations are consistent with the experimental results of [184] and the numerical simulations of [66], thus establishing the robustness of the current approach.

4.4.3.2 Test case 5: Oscillating upstream cylinder

Next, we consider the case, where the stationary upstream cylinder in the above example is now replaced by a transversely oscillating one. This study is similar to the third experimental arrangement by Kim *et al.* [86] where a fixed cylinder was placed in the wake of a transversely oscillating cylinder to suppress vortex induced vibration (VIV). However, in our computation, we allow the vibrating amplitude of the upstream cylinder to vary and evolve with time t through the function $A(t) = a_0(1 - e^{-a_1 t})$; for $a_0 = 0.0$, it reduces to a stationary cylinder. Under the imposed oscillation, the displacement of the y-coordinate of the center of this cylinder is given by $A(t)\sin(2\pi f t)$. In our computations, we have chosen $a_0 = 0.626$, $a_1 = 0.025$, $P = 2.95$ and $f = 0.182$. The schematic of the problem is similar to figure 4.6 except the fact that the bluff body shown in that figure is now replaced by the upstream oscillating cylinder with velocity $(u, v) = (0, 2A(t)\pi f \cos(2\pi f t))$ and another stationary cylinder of the same dimension is placed to its right. The schematic of these two cylinders and the time history of the displacement of the upstream cylinder is shown in figures 4.15(a)-(b) respectively.

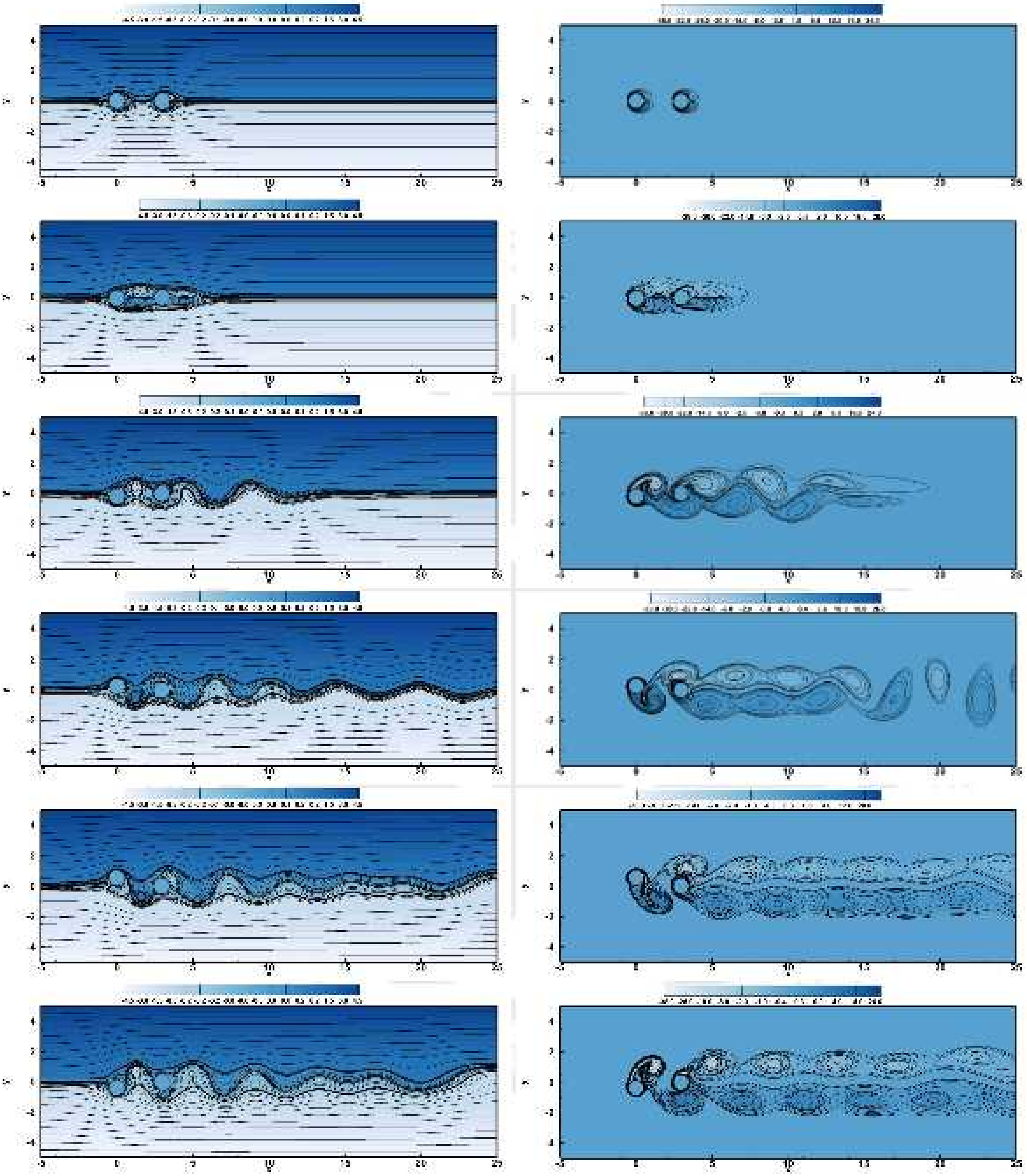

Figure 4.16: *Streamlines (left) and vorticity contours (right) for flow past two tandem circular cylinders from top to bottom at:* $t = 1, 5, 20, 50, 100$*, and* 300 *respectively for Test Case 5.*

In figure 4.16, we show the evolution of the flow by plotting the streamlines and vor-

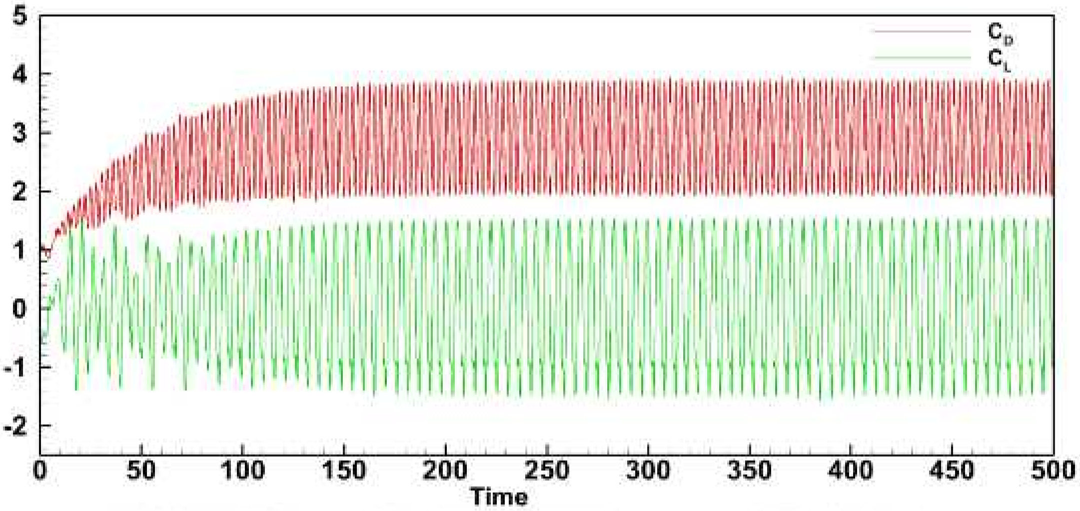

Figure 4.17: *History of drag and lift coefficients of the tandem cylinders for case 5.*

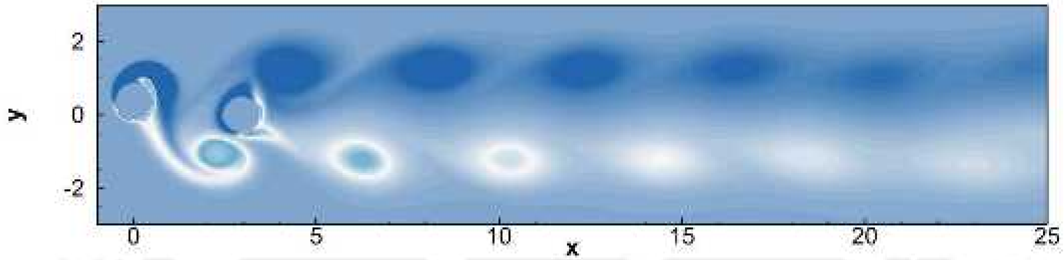

Figure 4.18: *Vorticity contours for the tandem cylinders for case 5 at time $t = 200.0$. The evolution of the same from time $t = 0$ to $t = 200$ can be seen in the accompanying video tandem.avi. Multimedia View:* `https://doi.org/10.1063/5.0107308.2`.

ticity contours for this flow for $Re = 100$ at time stations $t = 1,\ 5,\ 20,\ 50,\ 100$ and 300. It is evident that the wake behind the cylinders settles into a periodic motion eventually, which is also confirmed by figure 4.17, where we show the time history of the drag and lift coefficients of the upstream cylinder. A **2S** shedding mode, typical of this kind of flow [11] is obvious here. This can be further observed in the accompanying video "tandem.avi" where the evolution of the vorticity contours during $0 \leq t \leq 200$ is shown, which is embedded in figure 4.18 at time $t = 200.0$. It is heartening to note that without the inclusion of any external circles embedded into the figures, the interfaces have been captured very smoothly by our immersed interface approach on a relatively coarse grid with step-length $h = l = 0.0295$.

In figure 4.19(a), we show time history of the displacement of the oscillating cylinder side by side with the time history of the corresponding lift coefficient for a very short time range $480 \leq t \leq 500$. These figures demonstrate that the primary vortex shedding

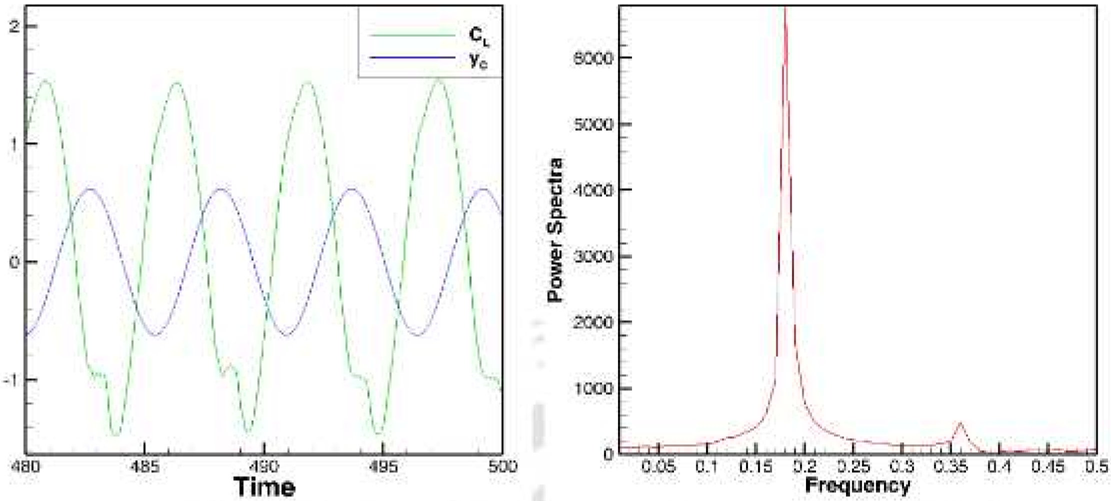

(a) (b)

Figure 4.19: *(a) Time history of the y-coordinate of the oscillating cylinder and lift coefficient, and (b) Power spectra of the lift coefficient displaying the Strouhal number. for Test Case 5.*

frequency and the frequency of vibration of the cylinder is almost equal. Figure 4.19(b) reconfirms the fact as the Strouhal number St (as defined in section 4.4.2.1) computation from the Fast Fourier Transform of the lift coefficient history results in a value of 0.1801, which is extremely close to the frequency 0.182 of the upstream cylinder. Thus we conclude that the flow situation under consideration here exhibits the characteristics of a **lock-on** regime.

4.5 Conclusion

The current chapter is concerned with the development of a hybrid explicit jump immersed interface approach in conjunction with a HOC scheme for simulating transient complex flows on Cartesian grids. Originally developed for parabolic equations with discontinuities in the solutions, source terms and the coefficients across the interface, this approach was seen to easily accommodate the N-S equations for simulating flow past bluff bodies immersed in the flow. ψ-ζ formulation of the N-S equations for incompressible viscous flows has been utilized for this purpose. A novel strategy has been adopted for the jump conditions at the irregular points across the interface using Lagrangian interpolation on a Cartesian grid. A compact and concise form of the matrix equations resulting from the discretization of the ψ and ζ equations have also been provided.

Firstly a parabolic problem having a known analytical solution is solved in order to establish the spatial rate of convergence of the proposed approach. Our approach was seen to reduce magnitude of the error with a much faster decay rate of $O(h^4)$ in comparison to other existing methods, thus establishing the theoretical rate of convergence in the way. Next, it was employed to simulate several complex fluid flow problems past bluff bodies having real life applications, including flows involving multiple and moving bodies. This includes the flow past a stationary circular and a twenty-four edge cactus cylinder, flows past two tandem cylinders, where in one situation both are fixed and in another, one of them is transversely oscillating in the flow. Except for the stationary circular cylinder cases, opposed to most of the earlier computations which were performed by either finite volume or finite element approach in extremely finer grids , our approach accomplishes the same in relatively coarse grids in FD set-up. Moreover, to the best of our knowledge, the tandem cylinder case, where one cylinder is oscillating with variable amplitudes along with the stationary cactus, have been tackled for the first time by such an approach employing the ψ-ζ formulation of the N-S equations against the primitive variable formulation in earlier simulations. Furthermore, in the process, we also provide elaborate description of the steps to compute drag and lift coefficients in multiply connected domains.

In all cases, our computed solutions are extremely close to existing numerical and experimental results. Thus, apart from exemplifying the accuracy and the robustness of the proposed approach, our simulations aptly demonstrate its ability in handling complicated geometries and varied flow situations. In the next chapter, we will extend the current approach to nonuniform grids along with the proposal of a novel discrete level set strategy.

5

A discrete level set approach for transient incompressible viscous flows on nonuniform grids

5.1 Introduction

In the field of computational fluid dynamics, the finite difference method is frequently implemented. The procedure can be summarized as follows: first, a grid is established in the problem domain; then, the governing equations are discretized with reference to the grid; and finally, the equations are solved numerically. The usage of a uniform grid is standard procedure, despite the fact that this particular structure might not be the most effective one for faster computing. Grid points need to be clustered together in areas with significant gradients for the solution to be resolved accurately, but in areas with minor gradients, they need to be spread out for numerous reasons [65, 134]. As a result, a grid that is not uniform is recommended for many different flow configurations. The most common method is to commence by mapping the physical space, which has a nonuniform grid, into a computational space, which contains a uniform grid. Next, a transformed set of equations is solved, and only then is the solution mapped back onto the physical space. Numerous problems may arise owing to the adoption of such an approach. In the transformed version of the governing equation, there is a significant increase in the number of terms that need to be discretized, which results in additional computational work. The modification of the equations frequently leads to the addition of cross-derivative terms, which increases the computational complexity of many of the techniques used to find solutions [65]. In addition, if the transformation is not explicitly known, the grid may have to be created via the numerical solution of some differential equation, which amounts to further error in the solution. In general, the technique for finding a solution becomes more difficult, more expensive, and frequently more prone to errors.

Note that in all the numerical methods mentioned in the previous chapters for tackling interfacial geometry, the shape is known a priori in terms of either as a parametric curve (surface) or the graph of a function. However, in many practical situations, for example, the flow around a NACA airfoil, the geometry of the body may not be expressible this way. In the present study[1], we propose an approach to circumvent this difficulty by defining a discrete level-set function arising out of the coordinates of the discrete points defining the geometry. In the process, we also expand our recently developed HEJIIM approach to transient problems on nonuniform grids. Our new approach is employed on flow past circular and cactus cylinders along with NACA 0012 airfoil and a swimming fish, which involves interfaces of varied complexity.

5.2 Mathematical formulation

Consider a rectangular shape domain given by $\Omega = [x_0, x_f] \times [y_0, y_f]$ in xy-plane.The interval $[x_0, x_f]$ and $[y_0, y_f]$ are partitioned into $(M-1)$ and $(N-1)$ sub-intervals respectively, which are not necessarily of equal lengths. Firstly, a block with a uniform grid is generated where the bluff body is implanted, and in the region surrounding these blocks, a non-uniform grid is created according to the flow situation. For example, in order to construct a centro-symmetric grid with clustering towards the walls, one may make use of the stretching function [78].

$$x_i = \frac{i}{M} - \frac{\lambda_1}{2\pi} sin\left(\frac{2i\pi}{M}\right), \quad 0 \le \lambda_1 < 1 \quad \text{in the } x\text{-direction}, \tag{5.1}$$

$$y_j = \frac{j}{N} - \frac{\lambda_2}{2\pi} sin\left(\frac{2j\pi}{N}\right), \quad 0 \le \lambda_2 < 1 \quad \text{in the } y\text{-direction}. \tag{5.2}$$

Here, M and N are the number of grid points in x and y direction respectively. In all of the computations that have been performed here, the value of $\lambda_1 = \lambda_1 = 0.85$ has been applied. At the grid point (x_i, y_j) in the computational domain, we define the forward and backward step-lengths x_f, x_b in the x-direction as follows:

$$x_f = x_{i+1} - x_i, \quad \text{and} \quad x_b = x_i - x_{i-1}. \tag{5.3}$$

---

[1] Under preparation in [163].

Similarly, in y-direction,

$$y_f = y_{j+1} - y_j, \quad \text{and} \quad y_b = y_j - y_{j-1}. \tag{5.4}$$

Note that the grid is generated in such a way that all the irregular points lie on the block containing the uniform grid, and we use the scheme proposed in chapter 4 thereat. In the remaining region covered by a non-uniform grid, the HOC scheme developed for transient convection-diffusion equations [78] has been used. The 2D unsteady convection-diffusion equation for a flow variable Φ can be expressed as

$$\lambda \frac{\partial \Phi}{\partial t} - \nabla^2 \Phi + c(x,y,t)\frac{\partial \Phi}{\partial x} + +d(x,y,t)\frac{\partial \Phi}{\partial y} = f(x,y,t) \tag{5.5}$$

The numerical approximation of the solution ϕ_{ij}^n at grid point (x_i, y_j) at the $(n)^{\text{th}}$ time level is given by [78]

$$\begin{aligned} &\lambda[1 + (H_1 + cH_2)\delta_x + (K_1 + dK_2)\delta_y + H_2 - 0.5(x_f - x_b)(H_1 + cH_2)\delta_x^2 \\ &+K_2 - 0.5(y_f - y_b)(K_1 + dK_2)\delta_y^2]\delta_t^+ \Phi_{ij}^n + [-A_{ij}\delta_x^2 - B_{ij}\delta_y^2 + C_{ij}\delta_x + D_{ij}\delta_y \\ &+G_{ij}\delta_x\delta_y - H_{ij}\delta_x\delta_y^2 - K_{ij}\delta_x^2\delta_y - L_{ij}\delta_x^2\delta_y^2]\Phi_{ij}^n = F_{ij}. \end{aligned} \tag{5.6}$$

where δ_t^+ represents the forward time operator with uniform time step Δt and n denotes the time level. The coefficients $H_1, H_2, K_1, K_2, A_{ij}, B_{ij}, C_{ij}, D_{ij}, G_{ij}, H_{ij}, K_{ij}, L_{ij}$ and F_{ij} can be found in [78] and the nonuniform compact stencil that has been utilised for the current computation is shown in figure 5.1.

5.3 Discrete Level-Set approach

In the following, we detail the steps for incorporating the discrete level-set approach for complex geometries immersed in transient flows. For rectangular, circular, elliptical, and regular structures, the level set equation is explicitly defined, but not for arbitrarily irregular geometries. As mentioned earlier, almost all the numerical methods tackling interfaces having irregularly shaped geometries in the FD set-up, dealt only with geometries with known parametric representations. As such, finding level set functions for the points enclosing these geometries was straightforward. On the other hand, for arbitrary geometries representing bluff bodies that are defined only by a few points across its boundary, estimating fluid flow around it is extremely challenging.

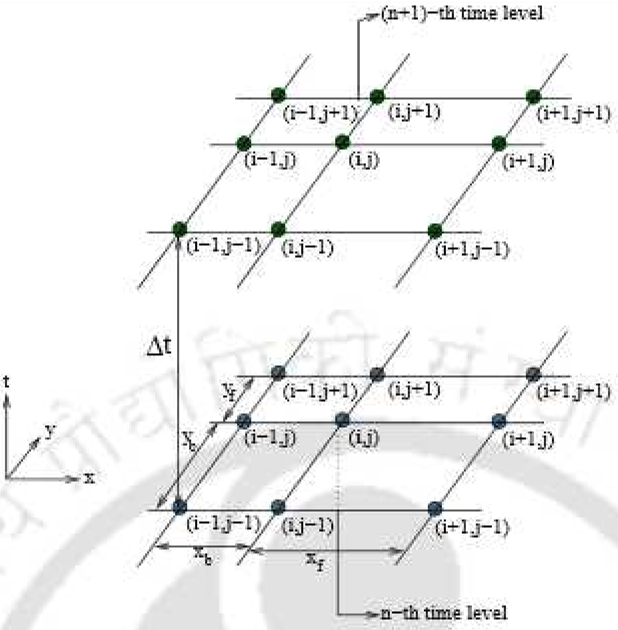

Figure 5.1: *The unsteady* $(9,9)$ *non-uniform compact stencil.*

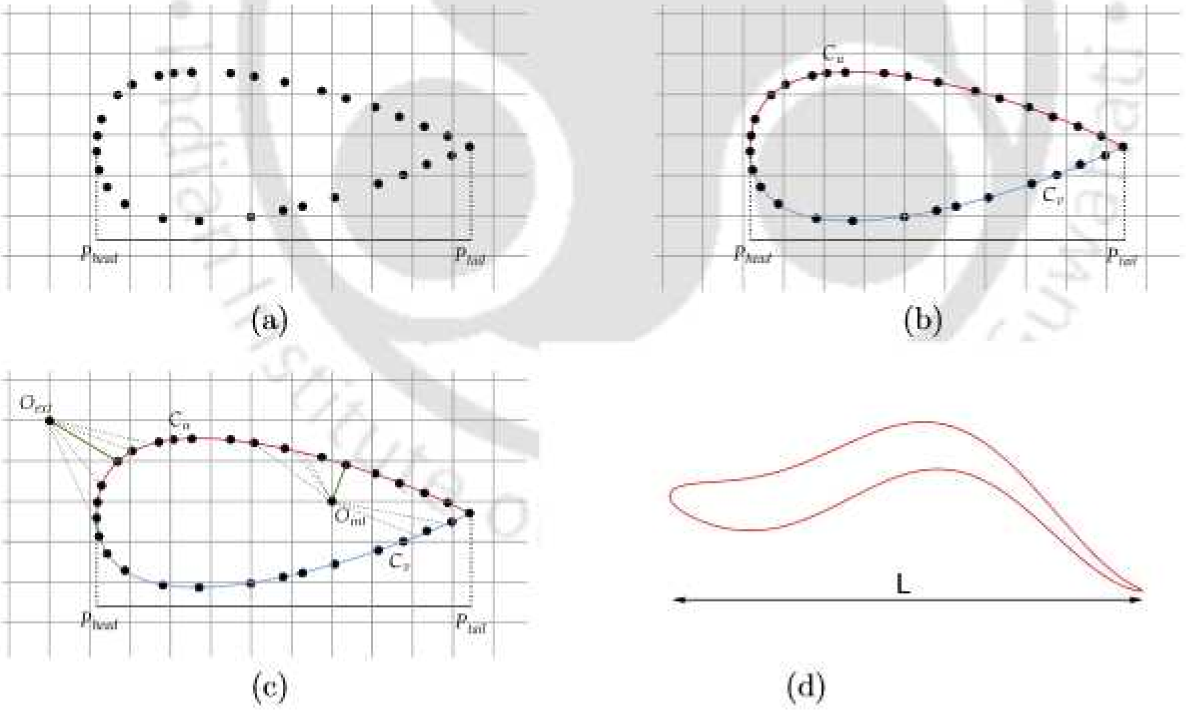

(a) (b)

(c) (d)

Figure 5.2: *(a) Representation of NACA 0012 airfoil through discrete points, (b) joined by two parametric curves, (c) approximate the minimum value from the grid points, and (d) undulation of swimming fish geometry.*

In order to illustrate the procedure, we choose the interface Γ of a NACA 0012 airfoil. Here Γ is a non-intersecting, closed C^1 curve that can be subdivided into many portions, which are locally analytical everywhere (including at the segment endpoints). The coordinates (P, Q) of certain number of points that are good enough to define the boundary of the airfoil can be found in the website `https://turbmodels.larc.nasa.gov/naca0012_val.html`, from where we have extracted them as shown in figure 5.2(a). Firstly, we determine the coordinates of the head and tail of the airfoil along the x- axis, which are denoted as P_{head} and P_{tail} respectively. Next, the points are categorized as upper or lower points across distance $(P_{\text{head}} - P_{\text{tail}})$ depending upon the Q coordinates of the chosen points which represents the upper (Q_u) and lower (Q_v) parts of the interface. Afterwards, two curves denoted C_u (coloured in red) representing the upper surface and C_v (coloured in blue) representing the lower one, are generated by using cubic spline interpolation as shown in figure 5.2(b). We start at the point (P_{head}, Q_{head}), move along the upper surface along the red curve to reach the point (P_{tail}, Q_{tail}) and then move along the blue curve to reach back the point (P_{head}, Q_{head}). This completes the generation of the airfoil boundary.

Once the interface is completely determined, the task of finding whether a grid point in the computational domain lies inside or outside of it is pretty straightforward. So, the most important objective for the discrete level set is to specify the discrete unique function values that should be assigned to each grid point in such a manner that it satisfies the level set function characteristics. If a grid point O_{ext} is situated in Ω^+, then one must determine the distance to the curves C_u and C_v, in that order, and select the value that is the smallest (see figure 5.2(c)), which is the value of the discrete level set function thereat. In a similar manner, for point O_{int} the only modification it undergoes is the change of sign, we simply take the negative of the minimum distance. Figure 5.2(d)) is a demonstration of the generation of a swimming fish from an airfoil by the introduction of undulation as would be seen in section 5.4.4 which is known as swimming fish. In the following, we provide the pseudo-code in algorithm 5.1 for the same, where $I[\mathbf{z}]$ indicates the index of the variable $\mathbf{z}$ inside the computational domain.

5.4 Numerical examples

In order to validate the approach proposed in the previous section, firstly we have implemented it the simulation of flows past impulsively started circular and cactus-shaped cylinders. Although they have been simulated in our previous chapters, we have generated the level set function through the pseudo-code documented above. In the process, it has provided us with an opportunity to compare its computational economy

Algorithm 5.1 Pseudocode of discrete level set approach

```
for $i \leftarrow 1$ to $M$ do
    for $j \leftarrow I[P_{head}]$ to $I[P_{tail}]$ do
        if $P_j \leq x_i$ & $x_i \leq P_{j+1}$ then
            $C_u[j] \leftarrow$ cubicspline ($P_{head}$ to $P_{tail}, Q^u$)
            $C_v[j] \leftarrow$ cubicspline ($P_{head}$ to $P_{tail}, Q^v$)
        end if
    end for
end for
for $k \leftarrow 1$ to $N$ do
    for $j \leftarrow 1$ to $M$ do
        if $I[P_{head}] - 1 < j$ & $j < I[P_{tail}] + 1$ & $C_v[j] \leq y_k$ & $y_k \leq C_u[j]$ then
            $\phi[j,k] \leftarrow -\min\{\min(dist(\mathbf{X}, C_u)), \min(dist(\mathbf{X}, C_v))\}$
        else:
            $\phi[j,k] \leftarrow \min\{\min(dist(\mathbf{X}, C_u)), \min(dist(\mathbf{X}, C_v))\}$
        end if
    end for
end for
return $\phi$
```

with the results obtained on uniform grids. Next, the flows past a NACA0012 airfoil and a swimming fish are taken by where the geometry of the bluff body under consideration is defined only by a handful of discrete points.

5.4.1 Flow past an impulsively started circular cylinder

One of the most well-studied topics in computational fluid dynamics is the vortex dynamics characterised by the secondary and tertiary phenomena coupled with the typical von Karmaan vortex street caused by an impulsively initiated circular cylinder. It has attracted the interest of researchers for nearly a century, owing to the fact that it exhibits practically all of the fluid mechanical phenomena for incompressible viscous flows in the most basic of geometric configurations. The flow structure, on the other hand, is extremely complicated, especially for large Reynolds numbers, making flow calculation much more difficult and exciting. Because of its prominence, this subject has a multitude of experimental, theoretical, and numerical results available in the literature [4, 79, 88, 137, 161, 192]. The schematic and the boundary conditions have already been described in chapter 4.

5.4.1.1 $Re = 200$

Firstly, we utilize this problem to show the distinct advantage of the current formulation on nonuniform Cartesian grids (see figure 5.3) over the formulation over equally spaced grid points [165] in terms efficiency of computation. For this, we simulate the flow for Reynolds number 200, which is fraught with the presence of the so called von Karmann vortex street in the periodic regime. In figure 5.4, we compare the vorticity contours at time $t = 400.0$ computed on uniform and nonuniform grids. The similarity between the simulations on both grids, in which all of the flow characteristics have been captured in a reasonably accurate manner, can be easily seen by everyone. However, it is heartening to note that while the uniform grid required $999 \times 399 = 398601$ nodes for the computation, the same could be achieved by the nonuniform grid using $441 \times 221 = 97461$ nodes and $\Delta t = 10^{-2}$, which is a four fold gain in space as well as in computational time.

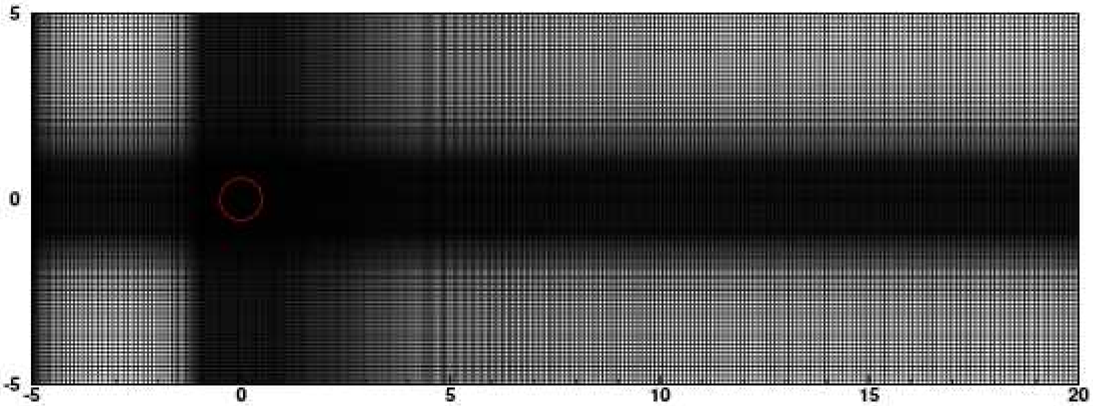

Figure 5.3: *Non-uniform grid for the flow past a circular cylinder.*

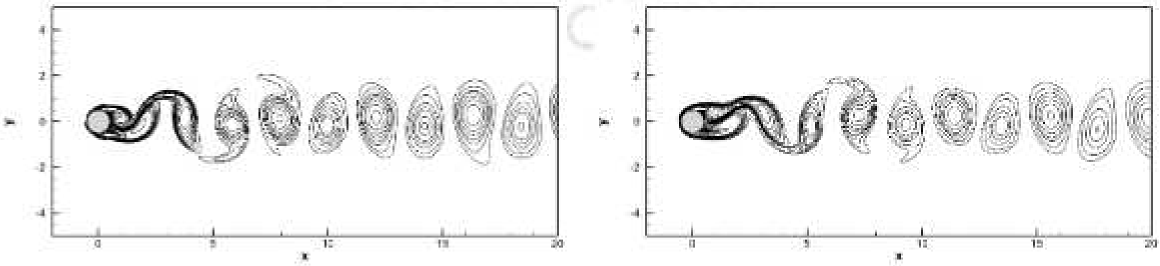

Figure 5.4: *Comparison of the simulation of flow past circular cylinder problem for $Re = 200$ at time $t = 400.0$ by the formulation on a uniform 999×399 grid [165] (left) and the present formulation on a nonuniform 441×221 grid (right): Vorticity contours.*

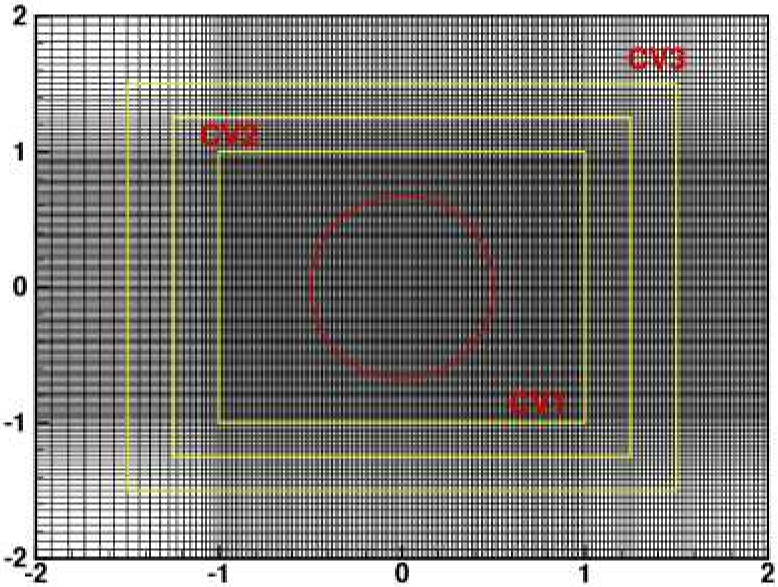

Figure 5.5: *Non-uniform grid enclosed around a circular cylinder along the various control volumes.*

A detailed perspective of the area close to the immersed boundary is presented in the figure 5.5, which also serves to define the various control volumes (CV) used in the calculation of the unsteady loads. In order to establish that the fluid dynamic forces computed by using the approaches developed in chapter 4 are independent of the control volumes chosen, three different CVs are considered. We define CV1 as the square $[-d, d] \times [-d, d]$ with $d = 1$ and its center coinciding with the cylinder's centre, i.e. origin. In a similar manner, CV2 and CV3 are the squares with $d = 1.25$ and $d = 1.5$ respectively. In figure 5.6 and table 5.1, we present the drag and lift coefficients for these various CVs for $Re = 200$ on the same grid. The overlap of the graphs in figure 5.6 and table 5.1 both establish the control volume independence of our computed forces. As a result, all of the computational dynamics force simulations for this work have been performed on CV2.

5.4.1.2 $Re = 1000$ and 3000

At higher Reynolds values, flow around a cylinder becomes three-dimensional and turbulent, and we will not explore that regime. We confine our computation to the early stages of flow development when the two-dimensional laminar assumption is still valid. Another distinguishing feature of this flow range is that it exhibits the so called α phe-

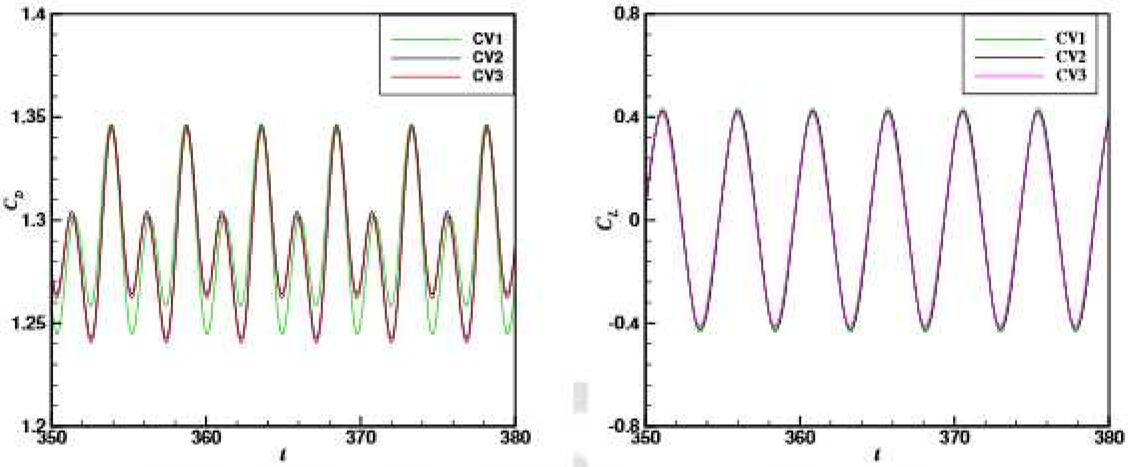

(a) (b)

Figure 5.6: *Control volume independence study for the flow past circular cylinder on (a) drag and (b) lift forces for $Re = 200$.*

Table 5.1: Drag and lift coefficients for the various control volumes for the flow past circular cylinder for $Re = 200$.

CV	C_D	C_L
CV1	1.29535 ± 0.05065	± 0.43401
CV2	1.29412 ± 0.05193	± 0.42320
CV3	1.29193 ± 0.05137	± 0.42019

nomenon. This secondary phenomenon has been reported in the literature at the initial stage of flow [18, 79–81, 90] when the secondary vortex begins to appear from the surface of the cylinder after the formation of two symmetrical primary vortices behind the cylinder. Initially, the streamlines close to the cylinder deviate from the surface giving rise to a bulge pattern and eventually form a secondary eddy. This eddy grows in size to such an extent that it touches the boundary of the primary eddy, thereby splitting the primary one into two parts and isolating the region of the wake next to the separation point where another secondary eddy becomes visible. When these two secondary eddies are equal in size and strength, the flow is said to undergo the α-phenomenon. According to experimental data [18], the α-phenomenon is clearly observable in the region of Reynolds numbers $800 \leq \mathrm{Re} \leq 5000$. For our simulation, we have chosen $Re = 1000$ and 3000 to demonstrate the occurrence of this phenomenon. The computational domain and non-uniform grid of $485 \times 485 = 235225$ nodes with clustering near to the

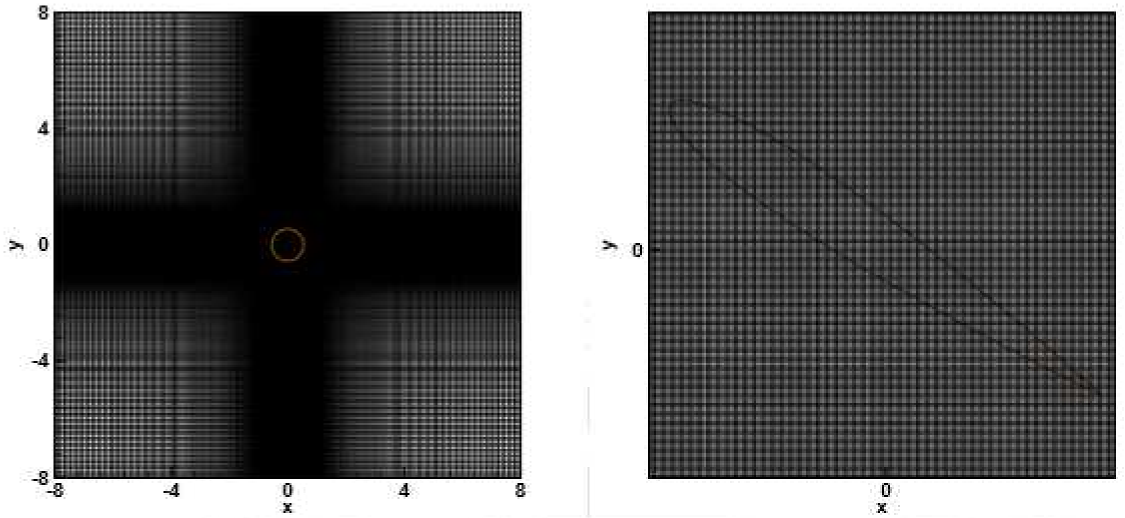

(a) (b)

Figure 5.7: *Cartesian grid for the flow around (a) circular cylinder for $Re = 1000$ and (b) zoomed view of the grid near the an airfoil for $Re = 3000$.*

area of interest are as shown in figure 5.7(a), and time step $\Delta t = 10^{-3}$ is taken for the simulation.

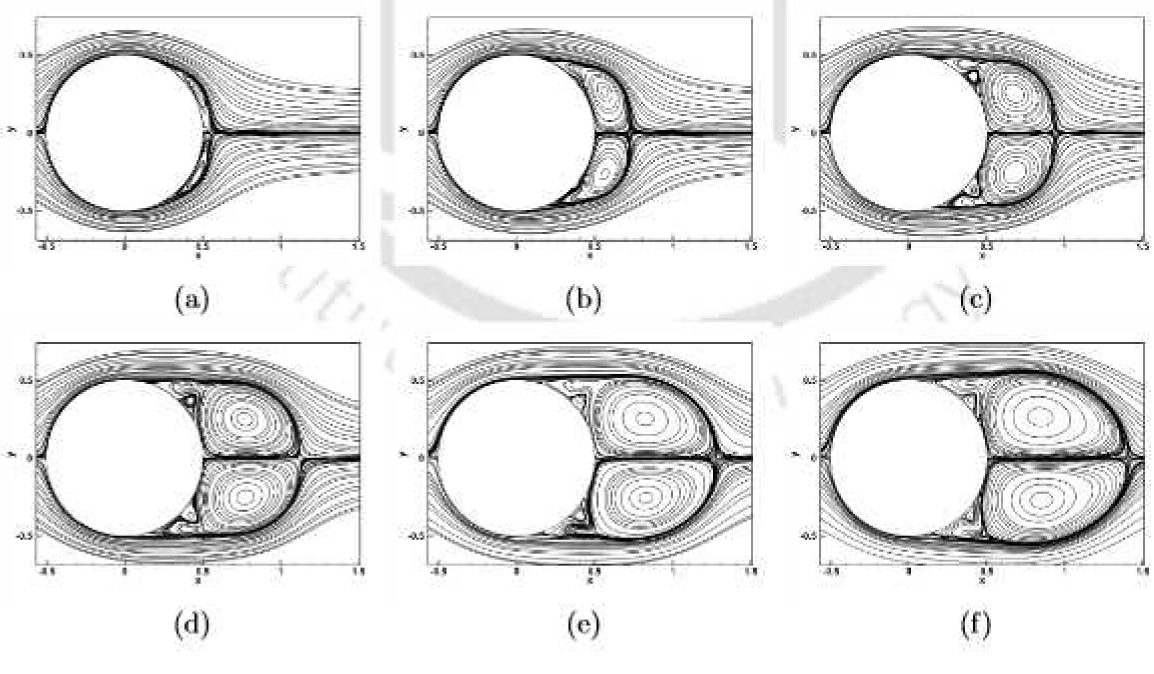

(a) (b) (c)

(d) (e) (f)

Figure 5.8: *Streamlines for $Re = 1000$ at (a) $t = 1.25$, (b) $t = 1.75$, (c) $t = 2.5$, (d) $t = 3.50$, (e) $t = 4.50$ and (f) $t = 6.00$.*

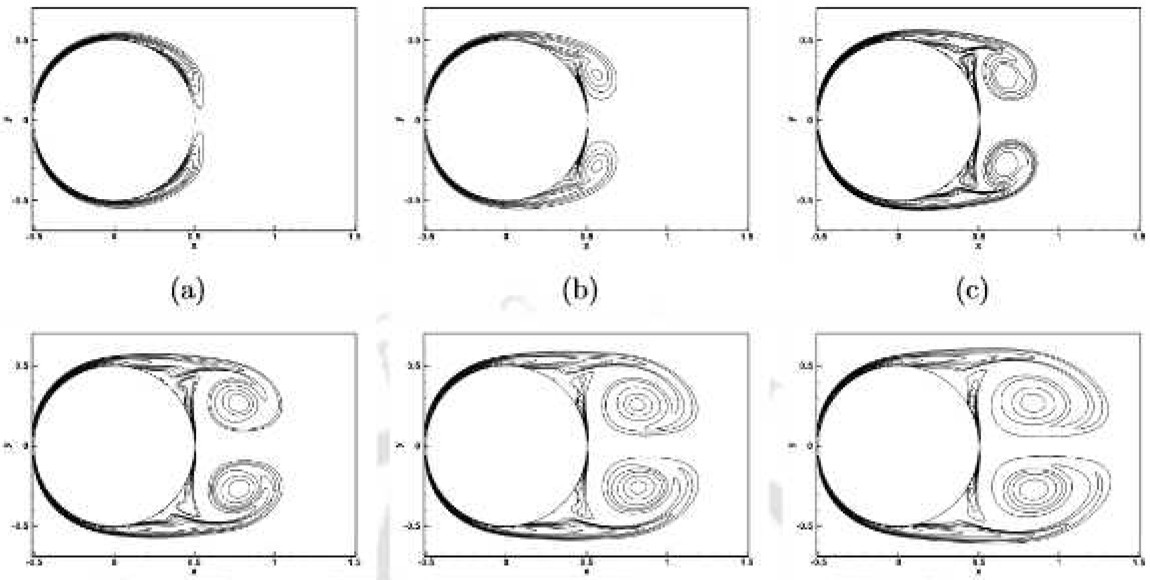

(a) (b) (c)

(d) (e) (f)

Figure 5.9: *Vorticity contours for Re* = 1000 *at (a)* $t = 1.25$, *(b)* $t = 1.75$, *(c)* $t = 2.5$, *(d)* $t = 3.50$, *(e)* $t = 4.50$ *and (f)* $t = 6.00$.

Figure 5.8(a) reveals that the secondary vortex has yet to develop at $t = 1.25$ and it makes its appearance at $t = 1.75$ (figure 5.8(b)). When the primary vortex remains stable, the secondary vortex expands to the point where its outer surface meets the main recirculating zone boundary (figure 5.8(c) and (d)). As a result, the primary eddy is split into two halves, and the region in the wake around the separation point is isolated, forming another secondary eddy. These two secondary eddies are comparable in strength and size, forming a pair of secondary eddies (figure 5.8(e) and (f)). This is nothing but the α-phenomenon described above. Figure 5.9 (a)-(f) depicts the matching vorticity patterns for the same time period, and they are remarkably similar to those presented in [4, 79, 88, 137, 161].

In figure 5.10, we describe the development of streamlines for $Re = 3000$, and compare the computed solutions with the findings of Bouard and Coutanceau [109] obtained through experimental visualization. Once again, the computational results and the experimental data are extremely close to one another.

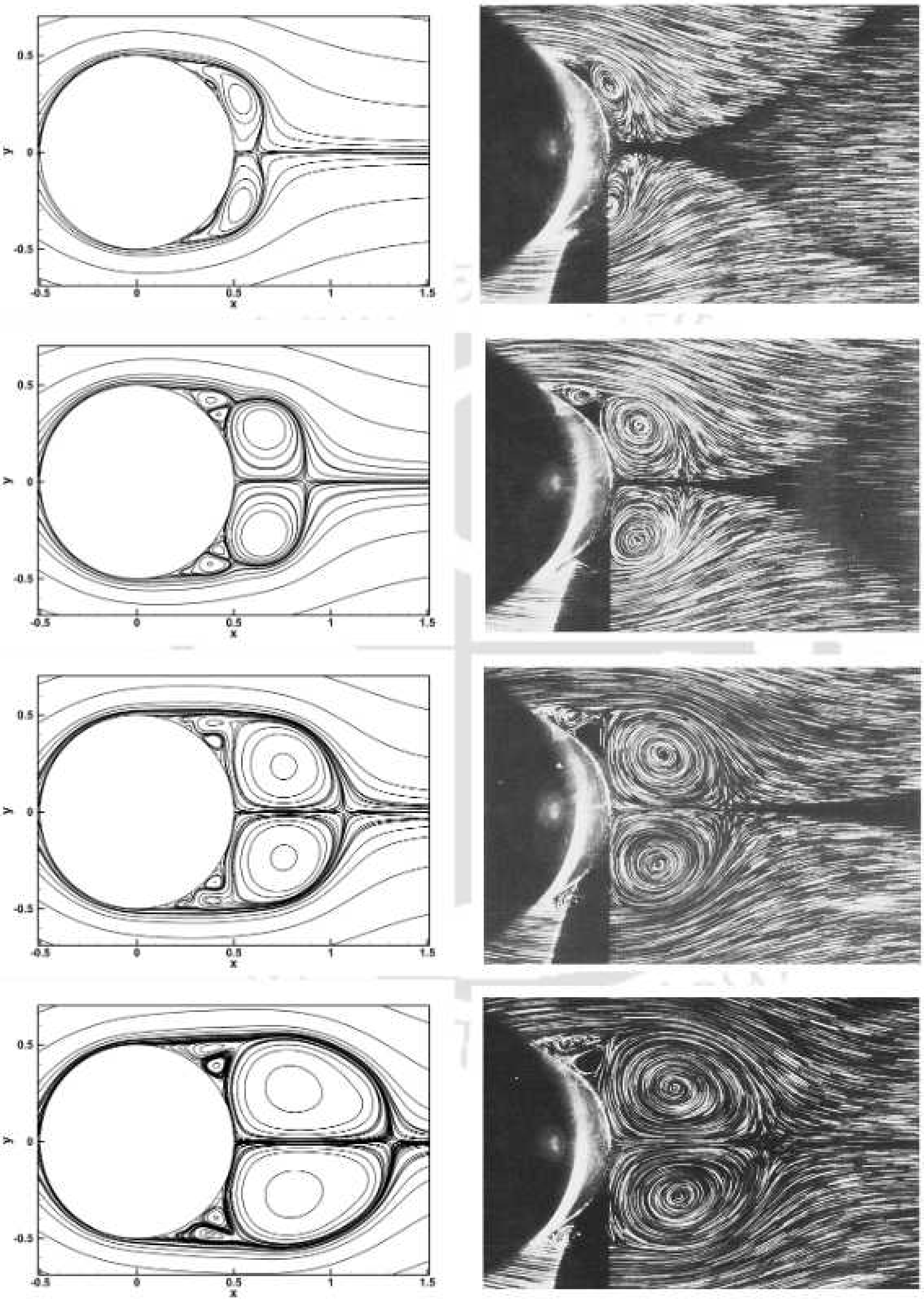

Figure 5.10: *Comparison of numerical (left) and experimental (right) [109] streamlines for* $Re = 3000$ *at* $t = 1$, 1.5, 2, *and* 2.5 *from top to bottom respectively.*

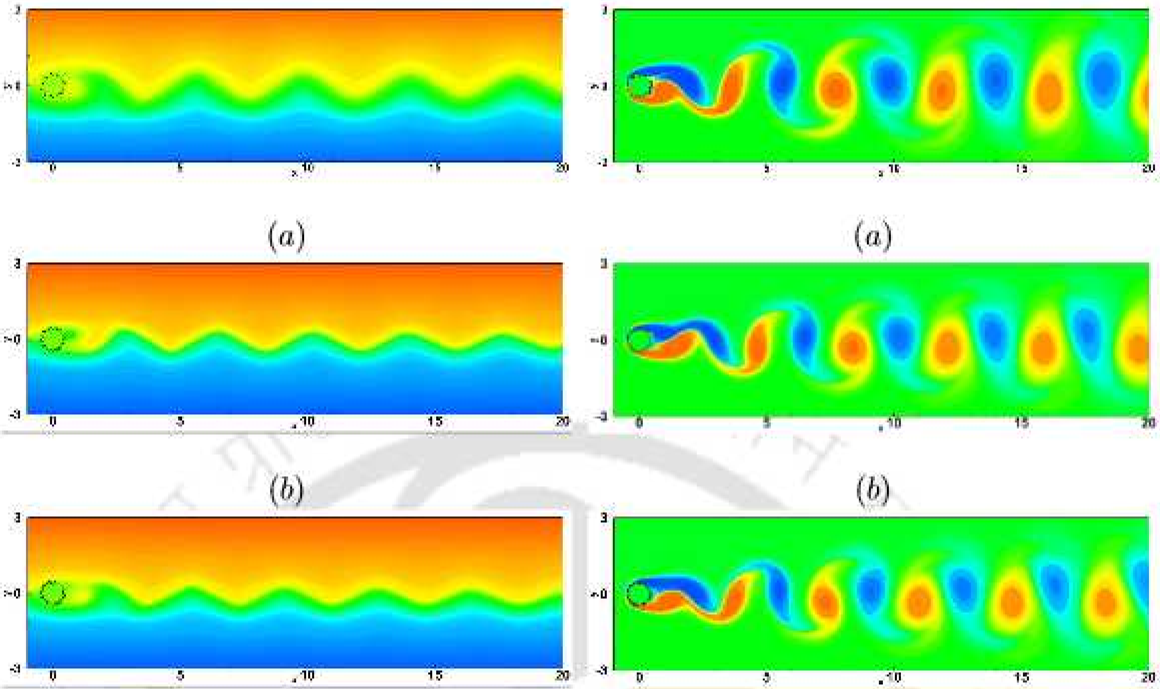

(a) (a)

(b) (b)

(c) (c)

Figure 5.11: *Streamlines (left) and vorticity (right) contours for the flow past cactus shaped cylinder in a uniform flow for $Re = 200$, (a) $w = 8$, (b) $w = 16$ and (c) $w = 24$ spikes.*

5.4.2 Flow past a cactus cylinder

In the previous chapter 4, we simulated the flow over a cactus shape cylinder for $w = 24$ spikes but there we utilized an explicit formula of level set function. Here, we analyze the flow over a cactus for the values of w equal to 8, 16, and 24 in order to demonstrate that the discrete method is effective. The computational domain is the same as the one shown in the figure 5.3, with the exception of the circle being replaced by a cactus cylinder with a grid of 501×401 with $\Delta t = 10^{-2}$. We depict instantaneous streamline and vorticity contours in figure 5.11 for $Re = 200$. As can be observed, the number of Von-Karman vortices increases as the number of spikes increases. We plot the time histories of the drag and lift coefficients in figure 5.12. The following table 5.2 presents a comparison of the force coefficients and Strouhal numbers for periodic flows involving cactus-shaped and circular cylinder. As the spikes on the cactus continue to grow, it appears that there is a clear reduction in the unsteady loads for the cactus-shaped

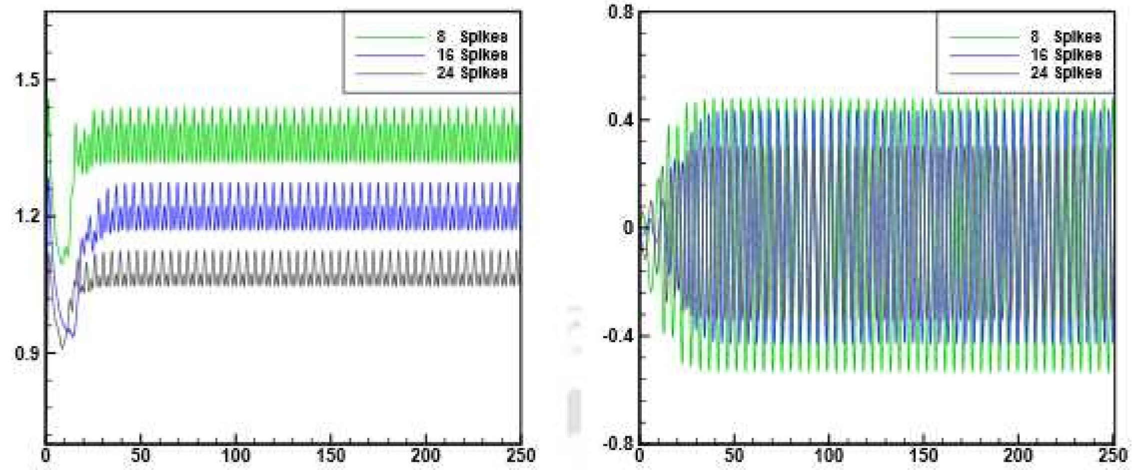

(a) (b)

Figure 5.12: *Time histories of (a) drag and (b) lift coefficients for the cactus shaped cylinder for* $Re = 200$.

Table 5.2: Comparison of Strouhal number, drag and lift coefficients of the periodic flow for Cactus shaped and Circular Cylinders for $w = 16$ and $w = 24$ spikes at $Re = 200$.

Flow Parameters	Circle	16 Spikes	% Difference	24 Spikes	% Difference
St	0.210	0.218	–	0.225	–
C_D	1.295	1.220	6.64	1.08	16.60
C_L	±0.430	±0.420	2.32	±0.304	29.30

cylinder in comparison to the smooth circular cylinder. Once again, the findings of Babu and Mahesh [7] are in agreement with the observations that we have made.

5.4.3 Flow past an airfoil

The study of unsteady incompressible flow in complicated geometric configurations adopting curvilinear coordinate system is considered to be one of the most important challenges in the field of CFD. This has been done for the flow past a circular cylinder in a great number of investigations, mostly due to the fact that its geometry is so straightforward. Since engineering applications frequently include flows over complicated objects like wings, blades, missiles, and so on, it would be worthwhile to explore other bluff bodies like airfoils in our study. When it comes to these types of flows, the thickness of the flow along with the angle of attack have a significant impact on the nature of separation and the structure of the wake. According to Nair and Sengupta [152], the flow around airfoils that corresponds to a relatively high Reynolds number is characterized by four primary flow phenomena when the angle of attack is high. They are: (a) the instability of unsteady flow, (b) the forming of a bubble over the airfoils, (c) the interaction of vortices in the wake, and (d) the creation of an alleyway, which is the cause of flow accelerating over the lower surface of the airfoil and wrapping around the vortices over the top surface of the wing. Flows around airfoils, in addition to demonstrating the aforementioned physically fascinating phenomena, serve as appropriate test cases for confirming the robustness of numerical techniques.

The investigation of the unstable flow that occurs behind the symmetric airfoils NACA 0012 and NACA 0015 is of particular interest. In this context, "NACA" refers to the National Advisory Committee for Aeronautics, which was the organization that came before the National Aeronautics and Space Administration (NASA). In the published research, results from both traditional [55, 124, 158] and contemporary [152, 167] experiments have been reported in relation to incompressible flow through airfoils. The work of Mehta and Lavan [113] represents one of the earlier instances of a computational approach to flow past an airfoil. In 1975, they investigated the case of laminar flow past an impulsively initiated Joukowski airfoil for a Reynolds number 1000. In the experimental study that Freymuth [55] conducted in 1985, he examined the impact of uniform acceleration on flow via a NACA 0015 airfoil at a variety of Reynolds numbers and angles of attack by using the flow visualization approach. He defined the Reynolds number by referring to the airfoil's chord length in conjunction with the uniform acceleration. Ohmi et al. [124] reported their computational and experimental observations for a NACA 0012 airfoil in 1991. The airfoil was analysed with an angle of attack of 30 degrees and a $Re = 3000$. In 1995, Shen and Loc [158] used a domain decomposition method that coupled a vortex method and a FD method to carry out numerical simulations for external flows around NACA 0012 for $Re = 1000$ and 10000 at angles of attack 200 and 340. In the same year, Morikawa and Gronig [117] examined experimentally as well as computationally the leading edge vortex system around NACA 0015 as a result of both airfoil oscillation and the unsteady motion. The exploratory work of the flow field around an airfoil was resumed in 2003 by Soria et al. [167], who applied the multigrid cross-correlation digital particle image velocimetry (MCCDPIV) approach to determine the flow field around a NACA 0015 airfoil at 30° attack angle, in which the flow is accelerated to a constant velocity from a resting state. In the same manner, numerous studies have been carried out over a long period of time, both experimentally and numerically, for a variety of Reynolds numbers and angles of attack.

Following the completion of a successful validation of the flow over a circular cylinder, a further benchmark case for the flow over a NACA 0012 airfoil is examined here. There is a sharp corner on the trailing edge of the airfoil, in addition to the leading edge of the airfoil having a small radius in comparison to a chord length. This presents quite a challenge for some interpolations that are performed using immersed boundary methods. Researchers have been successful in accomplishing this objective by using body fitting and transformation [87, 135, 149, 182] rather than the approach described here.

We have considered the flow past the NACA 0012 airfoil at an angle of attack of 34° which is generated using a discrete level set approach coupled with a Cartesian technique (see figure 5.7(b)). In the figures 5.13-5.14, we show comparisons of the streamlines demonstrating excellent matches between the computed results and those reported in [159] for $Re = 1000$ at angle attack 34°. Our numerical simulations are able to capture all of the primary and secondary vortices that have been identified by the experimental visualization. In addition, the time progress of the flow structures is accurately reproduced by the simulations. The post-processed vorticity contours that correspond to each of the different times are provided in the figure 5.15.

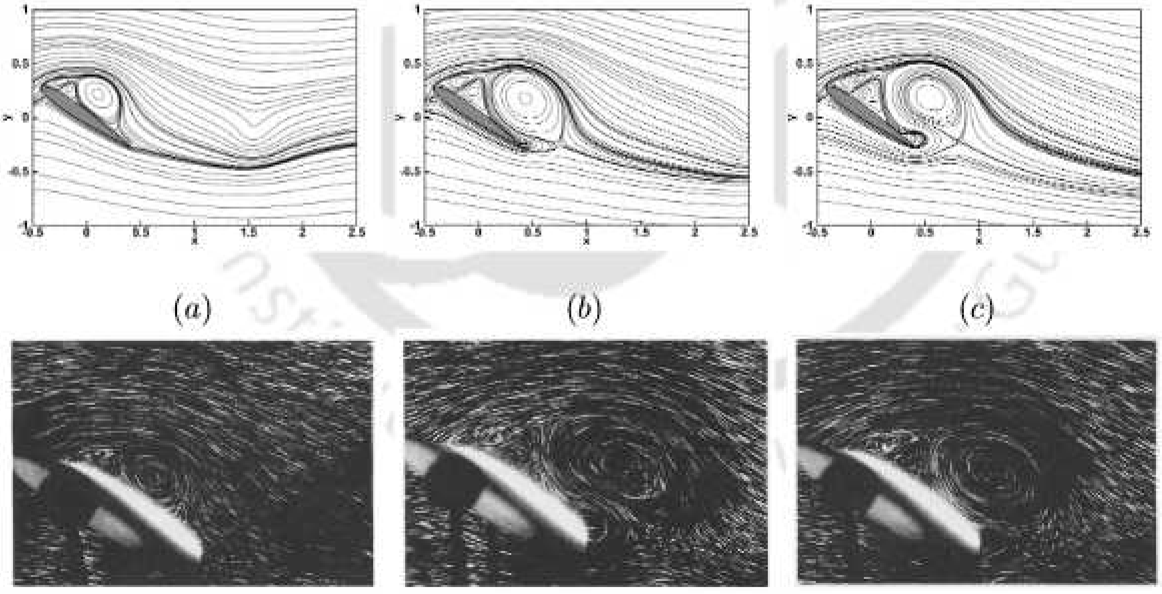

(a) (b) (c)

(a) (b) (c)

Figure 5.13: *Comparison of numerical (top) and experimental visualizations (bottom) [159] streamlines for NACA 0012 airfoil at* 34° *angle for* $Re = 1000$ *at (a)* $t = 1.6$, *(b)* $t = 2.8$, *and (c)* $t = 3.2$.

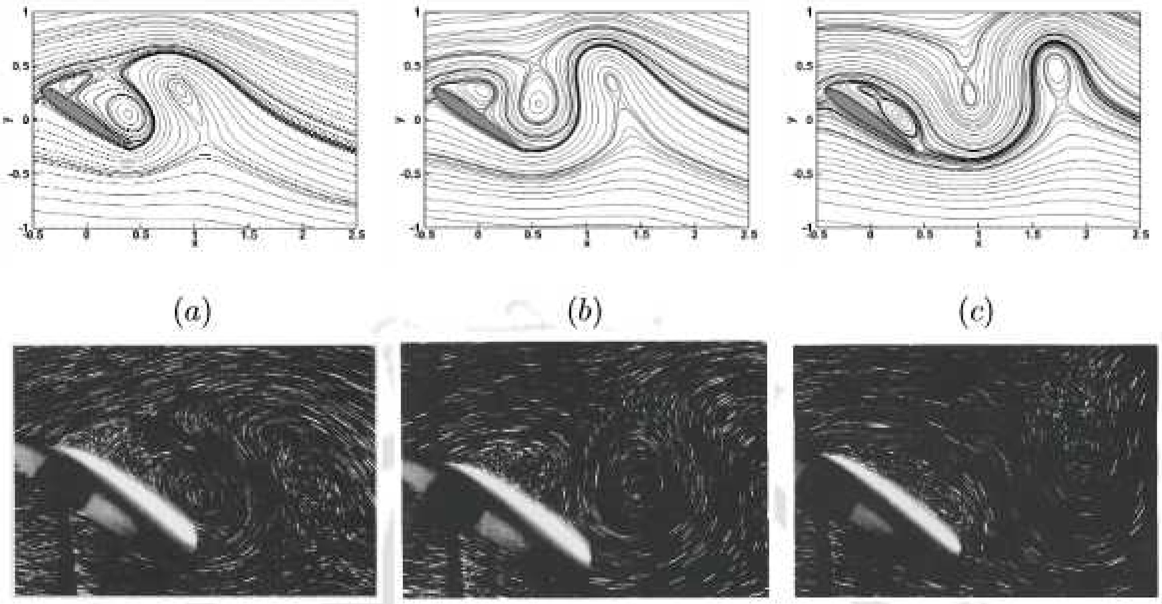

(*a*) (*b*) (*c*)

(*a*) (*b*) (*c*)

Figure 5.14: *Comparison of numerical (top) and experimental visualizations (bottom) [159] streamlines for NACA 0012 airfoil at 34° angle for* $Re = 1000$ *at (a)* $t = 4.0$, *(b)* $t = 4.8$, *and (c)* $t = 5.6$.

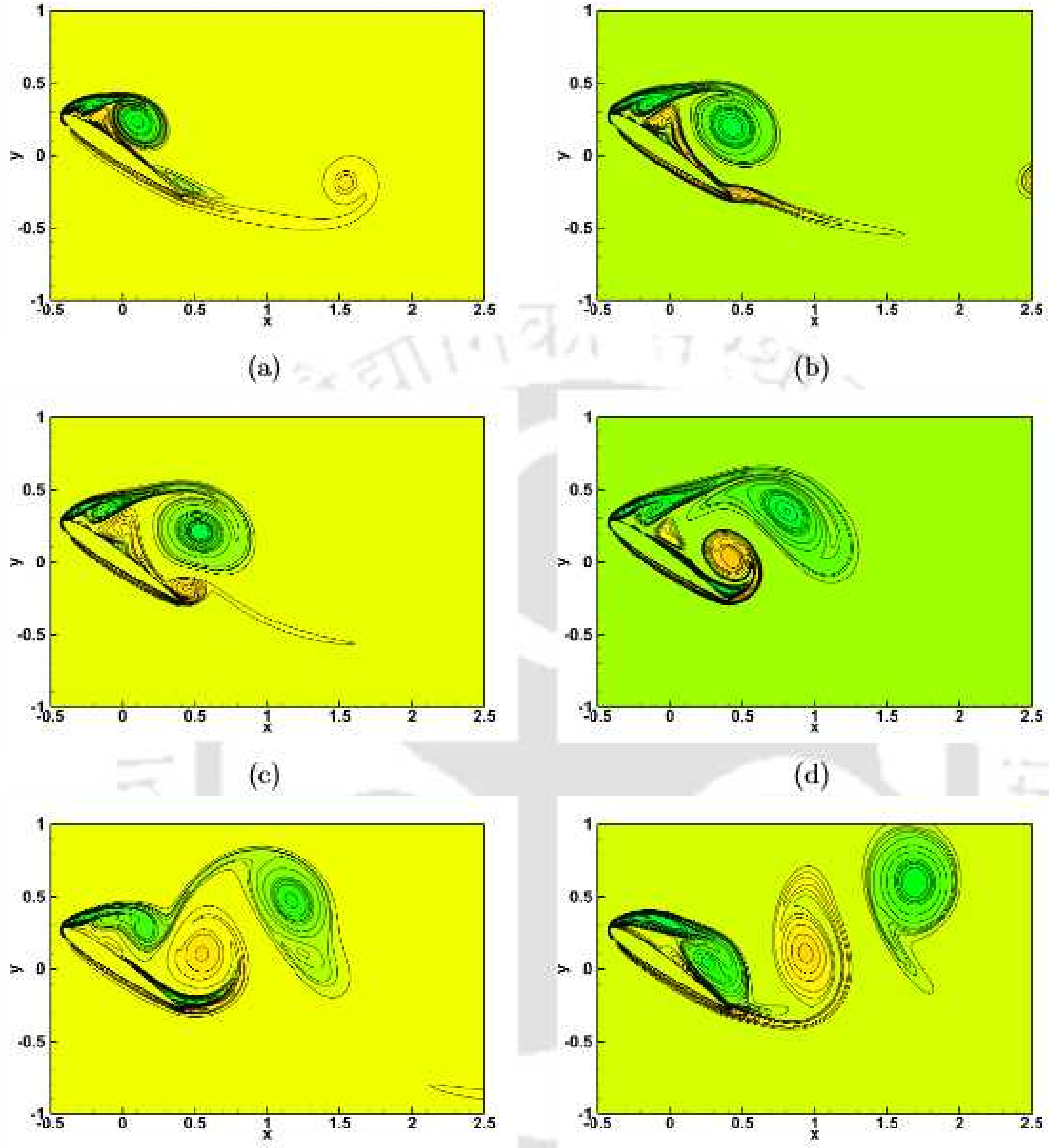

(a) (b)

(c) (d)

(e) (f)

Figure 5.15: *Evolution of vorticity contours for NACA 0012 airfoil at* 34° *angle for* $Re = 1000$ *at (a)* $t = 1.6$*, (b)* $t = 2.8$*, (c)* $t = 3.2$*, (d)* $t = 4.0$*, (e)* $t = 4.8$*, (f)* $t = 5.6$.

5.4.4 Flow past a swimming fish

Researchers are perpetually motivated by nature to examine natural events and make use of the mechanisms uncovered via their investigations in order to create more effective and robust technologies. Since the development of micro-aerial and swimming robots, which have promising future applications in both civilian and military settings, a variety of research efforts have been focused on the creation of methods that can improve the performance of these robots. Utilizing the surroundings around them as a source of effective propulsion is an important part of the swimming process for fish. As a consequence of this feature, many different kinds of fish tend to swim together in groupings that are referred to as schools [59, 83, 84, 119, 154].

5.4.5 Geometry

The undulating motion is utilized to represent the body motion for the fish-like propulsion, which changes to the pitching motion with bigger wavelengths of rearward traveling wave λ, which is employed as a parameter to prescribe the undulation. This motion is prescribed by the undulation. The action of the caudal fin and tail is modelled through the adoption of the pitching motion to create the fish-like propulsion.

NACA 0012 depicts an initial shape of the hydrofoil at the beginning of fish-like locomotion that mimics the undulating shape of a fish's body. This shape allows the hydrofoil to move like a fish. The straight hydrofoil can be converted into the wave-shaped hydrofoil by using a non-dimensional lateral displacement. dY displacement that varies over the length of the body as a function of position i.e.

$$dY = A(\mathbf{X}) sin\left(2\pi\frac{\mathbf{X}}{\lambda}\right) \tag{5.7}$$

where $\mathbf{X}$ is a non-dimensional representation of the distance from the head and λ is a non-dimensional representation of the wavelength of a wave that is moving across the hydrofoil. In addition, $A(\mathbf{X})$ represents the chordwise flexure amplitude of the undulation, which is modelled in this case by a static head linear motion (SHLM) kind of kinematics as

$$A(\mathbf{X}) = A_{max}\mathbf{X} \tag{5.8}$$

with A_{max} denoting the maximum non-dimensional lateral displacement, also referred to as the amplitude of undulation. For the purpose of modelling the periodic undulatory motion, a time-wise variation is added to (5.7).

$$\text{For motion with undulation:} \quad dY = A(\mathbf{X}) sin\left[2\pi\left(\frac{\mathbf{X}}{\lambda} - \frac{tSt}{2A_{max}}\right)\right] \tag{5.9}$$

where t is the non-dimensional time and St denoted the Strouhal number, also known as the non-dimensional frequency of undulation f. The previous equation for the undulating motion corresponds to the pitching motion about the horizontal centre line when the wavelength of the undulation is very large and $\lambda \to \infty$.

$$\text{Pitching motion:} \quad dY = A(\mathbf{X}) sin\left(-2\pi \frac{tSt}{2A_{max}}\right) \tag{5.10}$$

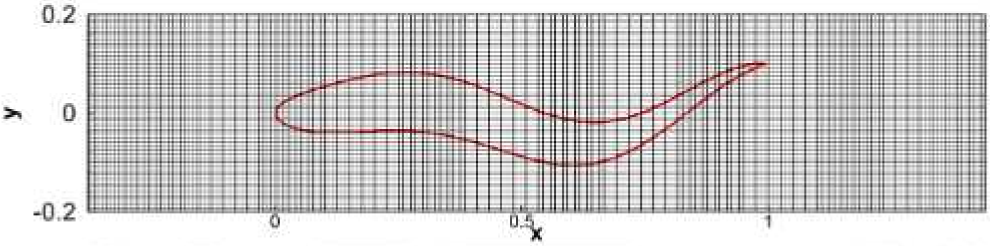

(a)

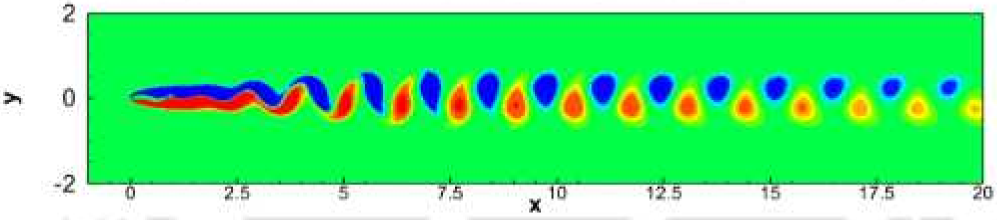

(b)

Figure 5.16: *(a) Close view of the grid near the hydrofoil and (b) vorticity contours for stationary hydrofoil for* $Re = 500$ *at* $\lambda = 0.8$ *and* $A_{max} = 0.1$.

The zoomed-in view of the grid near the stationary hydrofoil is depicted in figure 5.16(a), where parameters $\lambda = 0.8$ and $A_{max} = 0.1$ are considered. The vorticity contours can be seen for a Reynolds number of 500 once the flow settles in the wake behind the hydrofoil as shown in (b). The figure 5.17 (a)-(f) present the temporal variation of vorticity contours for one time period "T" of undulating hydrofoil at $St = 0.4$ and $Re = 500$, where $2S$ shedding mode is obvious in a manner that is similar to prior research [83, 84, 154]. Our contours in this case are not satisfactory; nevertheless, we are working toward enhancing them, and this is our main focus for the future plan.

5.5 Conclusion

We introduce a discrete level set approach for simulating transient incompressible viscous flows on a non-uniform grid based on a Cartesian mesh in streamfunction vortic-

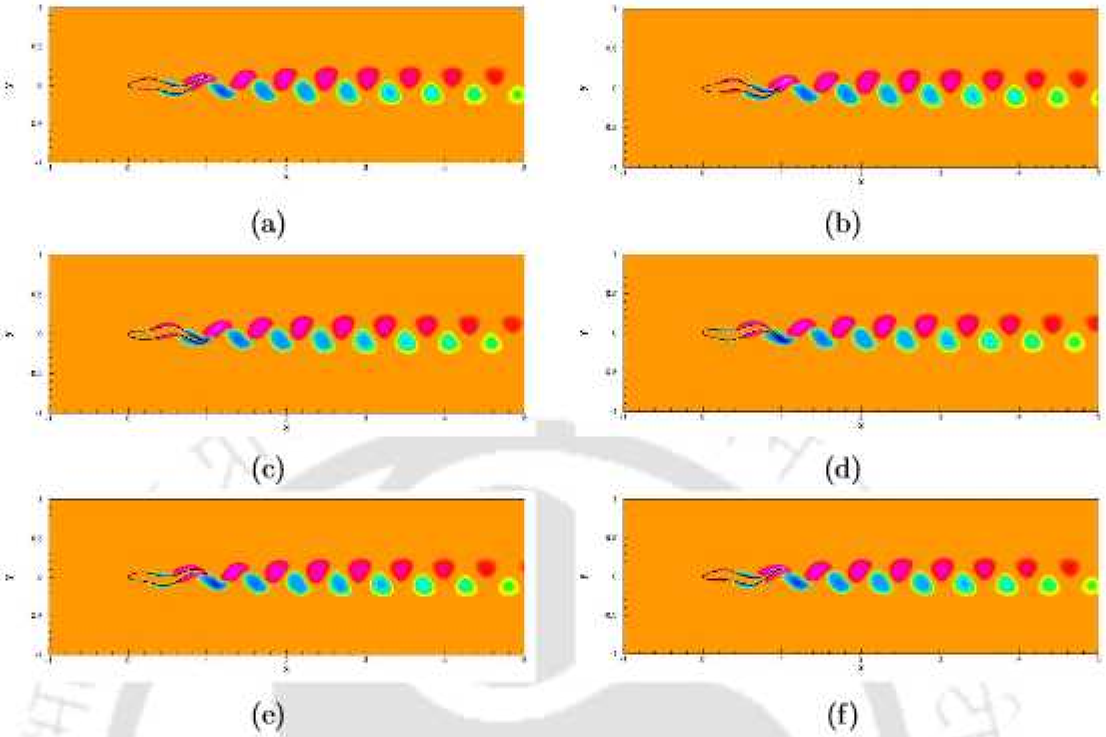

(a) (b) (c) (d) (e) (f)

Figure 5.17: *(a)-(f) Temporal variation of instantaneous vorticity contours, within one time period "T" of undulating hydrofoil at $\lambda = 0.8$, $A_{max} = 0.1$, $St = 0.4$ and $Re = 500$.*

ity formulation. The purpose of this method is to specifically treat irregular geometries in a fluid flow for which an explicit level set function is not available. We present a detailed description of how such a function can be generated on a complicated interface from a set of discrete points. In order to validate our approach, we first investigate the flow over a circular cylinder at moderately high Reynolds numbers (Re) to demonstrate the efficiency over a uniform mesh, and also establish control volume independence for unsteady loads. Moreover, we accurately capture the α phenomena for a high $Re = 3000$ in the laminar regime. We further investigate the effects of the shape of a cactus cylinder for 8, 16, and 24 spikes using our novel discrete technique, yielding the conclusion that Drag is reduced as the number of spikes on the cactus increases. In addition, we generate the boundaries of a the NACA 0012 and stationary fish, and the findings of the simulation are found to be impressively consistent with those obtained from previous numerical and experimental research. The strategy of using nonuniform grid in this chapter has been thoroughly implemented in the next chapter.

6

Comprehensive study of forced convection over a heated elliptical cylinder with varying angle of incidences to uniform free stream

6.1 Introduction

Bodies immersed in fluid flow can be characterized as being streamlined or blunt/bluff, depending on its overall shape and structure. A bluff body can be defined as a body that, as a result of its shape, has separated flow over a substantial part of its surface [34]; any body, which when kept in fluid flow, the fluid does not touch the whole boundary of the object. Roshko [143] defined a bluff body as one that resulted in a wide extent of separated flow and is associated with significant drag force as well as vortex-shedding. Flow past bluff bodies is commonly found in nature and engineering applications, for instance flow past an airplane, a submarine, an automobile, or wind blowing past a high-rise building. Thus, over the years, massive research efforts have been undertaken to gain a comprehensive understanding of the fluid flow and heat transfer phenomena past bluff bodies of various cross-sectional geometries. Although much effort has been devoted to analyzing the complex flow physics and thermo-fluid transport phenomenon for a variety of cross-sections (circular, rectangular, square, and elliptical), most of the literature deals with circular geometry. A thorough review of this topic can be found in the works of Williamson [181], and the books of Zdravkovich [187, 188].

It is well known that, in general, beyond a critical Reynolds number flow around slender cylindrical bodies exhibits periodic vortex shedding as a result of the Bénard-von Kármán instability which then leads to alternate vortex structures known as the von Kármán vortex street. This phenomena is responsible for fluctuating forces on the body that may cause structural vibrations, acoustic noise emissions, and at times, resonance, which would trigger the failure of structures [91]. Examples of such cylindrical structures in engineering applications include skyscrapers, towering structures, long-spanned bridges, and wires. The frequency associated with the periodic wake, the forces and moment acting on the body, as well as the heat transfer parameters, are a strong function of the body shape and size, Reynolds number of the flow, and the angle of attack [139]. Thus, from an engineering point of view, it is crucial to investigate flow around slender bodies with different shapes.

Over the years plethora of studies, both numerical and experimental, have been undertaken to investigate forced convection heat transfer over a circular cylinder. Notable among the early studies are the ones carried out by Dennis et.al. [42], Apelt and Ledwich [5], and Jafroudi and Yang [70]. Subsequent numerical investigations of impact were undertaken by Lange et.al. [93], Kieft et.al. [85], Shi et.al. [160], Bharti et.al. [14], Sarkar et.al. [146]. More recently, Cao et.al. [23] numerically analyzed forced convection heat transfer around a heated circular cylinder in laminar flow regime (Re = 20 - 180, Pr = 0.7) from the Lagrangian viewpoint. They computed the Lagrangian coherent structures and employed them to study the convection features around the cylinder at different Re's. Among the experimental studies, the works of Dumouchel et.al. [46], Wang et.al. [176], Kieft et.al. [85], Nakamura and Igarashi [118] stand out.

The most commonly studied geometry after the circular cylinder is that of a square/ rectangular cylinder. Thus, several studies - mostly numerical - exist for the forced convection heat transfer phenomena over a square geometry as well. Notable among them are the works of Sharma and Eswaran [155], Dhiman et.al. [43], Ranjan et.al. [139], Sahu et.al. [145], Sen et.al. [150], Bai and Alam [8]. Other unusual shapes such as a triangular cylinder (De and Dalal [92]), semi-circular cylinder (Chandra and Chhabra [25], Chatterjee et.al. [26], Bhinder et.al. [15]), cam-shaped cylinder (Chamoli et.al. [24]), blunt-headed cylinder (Pawar et.al. [132]) have also garnered the attention of researchers in recent years.

The bluff body, on which the flow and heat transfer phenomena has been investigated the most over the years is the circular cylinder. Dennis et.al. [42] numerically investigated steady laminar forced convection from a circular cylinder at low Reynolds numbers (Re). They carried out computations for $0.01 \leq Re \leq 40$, and found that the mean and local Nusselt numbers calculated via their numerical approach compared favourably with then available experimental results. Later on, similar studies were also undertaken by Apelt and Ledwich [5], and Jafroudi and Yang [70]. Lange et.al. [93] carried out a numerical investigation of 2D flow around a heated circular cylinder in laminar crossflow.

They presented results, in terms of Nu and C_D variations with Reynolds number for $10^{-4} \leq Re \leq 200$ and temperature loadings of 1.003 - 1.5. Dumouchel et.al. [46] carried out an experimental study of the heated wake downstream of a circular cylinder at low Re's. They found that the flow regime downstream of the cylinder can be characterized by an effective Re calculated at an effective temperature $T_{\text{eff}} = T_\infty + 0.24(T_w - T_\infty)$, where T_w, and T_∞ are temperatures of the cylinder and upstream flow respectively. Wang et.al. [176] experimentally studied the laminar vortex shedding of airflow behind a circular cylinder with different heating temperatures, emphasizing on the relationship of wake frequency and Re. Kieft et.al. [85] studied both numerically and experimentally the effect of heat input on the wake characteristics and vortex structure from a horizontal circular cylinder in cross flow. For $Re = 75$ and a range of Richardson number ($0 \leq Ri \leq 1$) they analyzed the different vortex characteristics and production of baroclinic vorticity production terms. Shi et.al. [160] numerically investigated the effect of cylinder heating on the flow and heat transfer characteristics in a 2D horizontal laminar flow of air past a heated circular cylinder for $0.001 \leq Re \leq 170$, considering the variation of fluid properties with temperature. Nakamura and Igarashi [118] reported that, for a circular cylinder in crossflow, the Nusselt number in the rear stagnation point increases with Reynolds number in the laminar shedding regime ($Re < 150$). Bharti et.a. [14] simulated forced convection heat transfer from an unconfined circular cylinder in the steady cross-flow regime ($10 \leq Re \leq 45$, $0.7 \leq Pr \leq 400$) and presented correlations for Nusselt number as a function of the pertinent dimensionless variables. They reported $15 - 20\%$ increase in the heat transfer coefficient for uniform heat flux condition than the isothermal condition of the cylinder, given the Reynolds and Prandtl numbers remained same for both. Sarkar et.al. [146] used an SUPG based finite element method to numerically investigate the combined effect of Prandtl number ($0.7 \leq Pr \leq 100$) and Richardson number ($0 \leq Ri \leq 2$) on the wake dynamics and heat transfer past a circular cylinder in crossflow. For forced convection, they found that the average Nusselt number ($\overline{Nu}$) increases with increasing Re and Pr. They also proposed a new correlation for $\overline{Nu}$ using least square technique ($\overline{Nu} = 0.459\, Re^{0.548} Pr^{0.373}$ for $80 \leq Re \leq 180$ and $0.7 \leq Pr \leq 100$), and a correlation on Colburn heat transfer factor ($j_c = 0.521\, Re^{0.452}$ for $80 \leq Re \leq 180$). Recently, Cao et.al. [23] numerically analyzed forced convection heat transfer around a heated circular cylinder in laminar flow regime ($Re = 20 - 180$, $Pr = 0.7$) from the Lagrangian viewpoint. They computed the Lagrangian coherent structures and employed them to study the convection features around the cylinder at different Re's.

The investigation of heat transfer phenomena over a square cylinder has also been carried out over the years. Sharma and Eswaran [155] carried out a numerical investigation of the flow and heat transfer characteristics of a square cylinder (isothermal and constant heat flux conditions) in a cross flow for $1 \leq Re \leq 160$ and $Pr = 0.7$. Dhiman et.al. [43] investigated the flow and heat transfer characteristics in the steady flow regime of an isolated square cylinder in crossflow placed symmetrically in a planar slit for the range of conditions as $1 \leq Re \leq 45$, $0.7 \leq Pr \leq 4000$ and blockage ratio $= 1/8$, $1/6$ & $1/4$. Ranjan et.al. [139] carried out a numerical investigation of flow and heat transfer phenomena over a square cylinder at incidence ($\alpha = 0^{\circ} - 45^{\circ}$) for a range of Re's ($60 \leq Re \leq 150$) using a finite volume approach on unstructured grids. They reported and analyzed the dependence of Strouhal number (St), drag and lift coefficients, moment coefficient and average Nusselt number on Reynolds number, and angle of incidence for a fixed blockage ratio. Sahu et.al. [145] carried out a numerical investigation of the effects of Re and Pr on the rate of heat transfer from a square cylinder in the unsteady two-dimensional periodic flow regime, for the range of $60 \leq Re \leq 160$ and $0.7 \leq Pr \leq 50$. They obtained simple heat transfer correlations for the isothermal and constant heat flux conditions on the solid square cylinder, in addition to demonstrating the role of Prandtl number in heat transfer characteristics in the unsteady flow regime. Sen et.al. [150] used a stabilized finite-element formulation to investigate the flow past a square cylinder at zero incidence for $Re \leq 150$. Bai and Alam [8] investigated the wake of a square cylinder for $Re < 10^7$. Two-dimensional (2D) laminar simulation and three-dimensional (3D) large-eddy simulation were conducted at $Re \leq 10^3$, while experiments of hotwire, particle image velocimetry, and force measurements were carried out at a higher Re range of $10^3 < Re < 4.5 \times 10^4$.

A number of studies have been reported on some uncommon shapes of bluff bodies as well. De and Dalal [92] employed a second order accurate finite volume method to simulate 2D laminar flow and heat transfer past a heated triangular cylinder placed in a channel for $80 \leq Re \leq 200$ and blockage ratio $1/12 \leq \beta \leq 1/3$. They reported that overall Nusselt number remains almost unchanged for different blockage ratios, and at lower blockage ratios, flow is found to be similar to the unconfined flow and is more prone to wake instability. Chandra and Chhabra [25] carried out a numerical investigation of momentum and heat transfer characteristics of a semi-circular cylinder immersed in unconfined flowing Newtonian fluids in the steady flow regime. Chatterjee et.al. [26] reported results for numerical simulation of laminar forced convection heat transfer for flow past a semi-circular cylinder in an unconfined medium ($Re = 50 - 150$, $Pr = 0.71$). They observed substantial differences in the in the global flow and heat transfer quantities for the two different configurations of the obstacle chosen in the study. The wake dynamics and forced convective heat transfer characteristics past a semi-circular cylinder at incidence ($0^{\circ} \leq \alpha \leq 180^{\circ}$) were studied by Bhinder et.al. [15] for $80 \leq Re \leq 180$ with air as the working fluid. Chamoli et.al. [24] studied the effect of shape modification on heat transfer and drag for fluid flow past a cam-shaped cylinder for $Re = 100, 200$. They showed that the cam-shaped cylinder alters wake size, controls and suppresses vortex shedding, inhibits shear layer interaction, and enhances convective heat transfer rate. Pawar et.al. [132] studied the forced convective flow and heat transfer characteristics past a blunt-headed cylinder in crossflow. Computations were carried out for $Re = 40-160$ and $\alpha = 0^{\circ}-180^{\circ}$, with air as the working fluid. They observed that a blunt headed cylinder exhibits an enhanced heat transfer rate compared to a rectangular cylinder. They also carried out an entropy generation analysis to study the effects of Re and angle of incidence on the efficiency of thermofluid transport characteristics.

Among the various cross sections/shapes of bluff bodies (cirular, rectangular/square, elliptical) the elliptic geometry has been considered the elementary shape of interest for wings, submarines, rotor blades, and missiles [185]. The problem of flow past an elliptical cylinder has received intermittent attention over the years from scientific community. Lugt and Haussling [110] numerically investigated laminar flow past an elliptic cylinder at 45° angle of incidence. The solutions were shown to approach steady and quasi-steady states at $Re = 15$ and $Re = 30$ respectively, while a Kármán vortex street developed at $Re = 200$. Patel [130] studied the development of Kármán vortex street for flow past an impulsively started elliptic cylinder for $Re = 200$ at different angles of incidence ($\alpha = 0^{\circ}$, 30°, 45°, 90°) and presented semi-analytical solutions in terms of flow characteristics such as surface pressure and vorticity distributions, the transient development of streamlines and equivorticity lines, and drag coefficient. Jackson [69], while investigating the critical Reynolds number for the onset of vortex shedding for 2D laminar flow past bluff bodies of different shapes reported that, for an elliptic cylinder, the values of the critical Re and the corresponding Strouhal number decreased as the angle of incidence increased. Park et.al. [129] studied the effect of angle of incidence on the unsteady laminar flow past an impulsively started, slender elliptic cylinder for $25 \leq Re \leq 600$. They identified five distinct flow regimes - two steady flow regimes which were demarcated by the presence of a steady separation bubble, and three unsteady regimes which were characterized by the frequency and amplitude of the periodic variations of force coefficients. Johnson et.al. [72] investigated the vortex structures behind 2D elliptic cylinders for $30 \leq Re \leq 300$ and aspect ratio (AR) in the range $0.01-1$. They reported that as the AR is decreased, the shedding behind the elliptic cylinder changes from steady Kármán vortex shedding to flow with two distinct regions. The first region is situated directly behind the cylinder and contains two rows of vortices rolling up from the cylinder with a region of relatively dead flow in between. The second region is located further downstream consisting of secondary vortices that results from a strong interaction of the two rows of vortices due to a convective instability. Faruquee et.al. [47] examined the effect of AR on the flow field of an elliptic cylinder for $0.3 \leq AR \leq 1$ at $Re = 40$ with the cylinder placed with the major axis parallel to the free-stream, and reported various wake parameters, drag coefficient, pressure and velocity distributions in terms of AR. They also reported a critical AR of 0.34 below which no vortices form behind the cylinder. Sen et.al [151] calculated the laminar separation Reynolds number (Re_s) for $Re \leq 40$, $0^{\circ} \leq \alpha \leq 90^{\circ}$, and $AR = 0.2$, 0.5, 0.8, and 1. Paul et.al. [131] presented a numerical study on predicting onset of flow separation and vortex shedding in flow past unconfined 2D elliptical cylinders for various AR's and a wide range of Angles of Attack (AOA). They employed a variety of methods to estimate Re_s, critical Reynolds number (Re_{cr}), and critical Strouhal number (St_{cr}), and proposed functional relationships for Re_{cr} and St_{cr} in terms of AR and AOA. Yoon et.al. [185] investigated the flow around an elliptic cylinder for $20 \leq Re \leq 100$, $0^{\circ} \leq \alpha \leq 90^{\circ}$, and $AR = 0.2$. They reported that the Strouhal number decreased as the angle of incidence increased, and the rate of decrease in the values of the Strouhal number was faster when the value of Re increased. While measuring the variation of the stagnation point, they found that it moved downstream along the lower surface of the cylinder as the angle of incidence increased, and the time-averaged stagnation point is strongly dependent on the angle of incidence and weakly dependent on Re. Thus, we see that a number of important studies have been carried out to understand the flow phenomena over an unconfined elliptic cylinder. However, there is a distinct lack of comprehensive studies dealing with heat transfer phenomena w.r.t. to flow past an elliptic cylinder. The current chapter[1] is attempt to address this issue.

6.2 Problem statement and governing equations

Consider a heated elliptical cylinder of aspect ratio $AR(= 2/3)$ placed in a uniform free stream (figure 6.1). The fluid flow is two-dimensional, incompressible and laminar with constant properties. Additionally the effect of gravity is neglected. The free stream velocity is U_0 and the fluid Prandtl number (Pr) is taken to be 0.71. The surface of the cylinder is maintained at a constant temperature of T_s, whereas the free stream has a temperature T_∞. It is assumed that the temperature difference $\Delta T(= T_s - T_\infty)$ has a negligible effect on the fluid properties.

---

[1] Under review in [162].

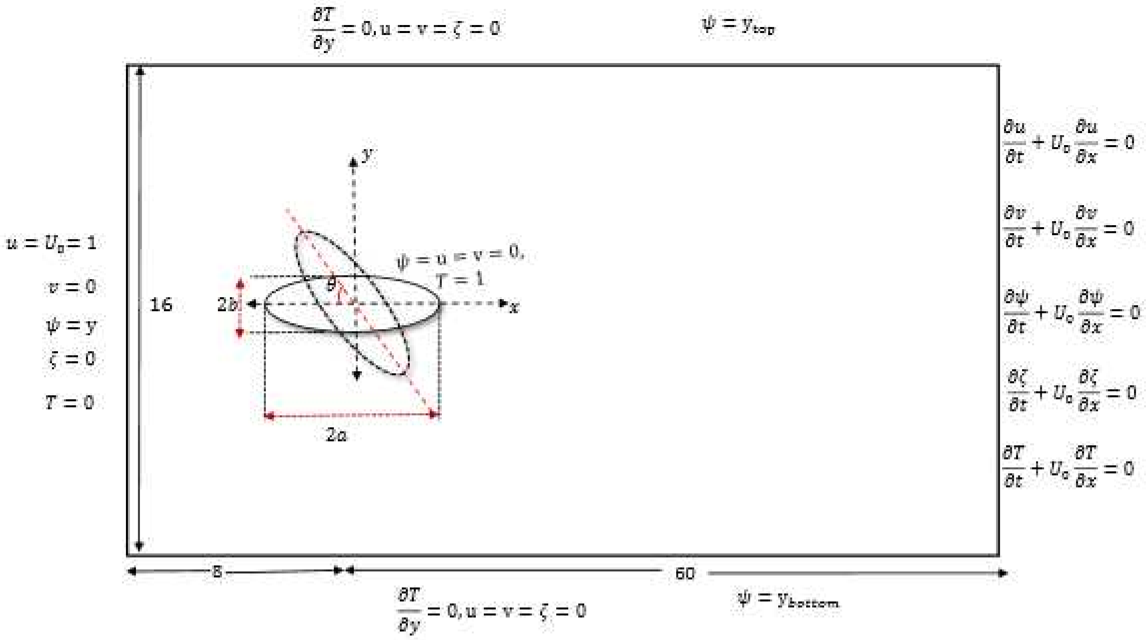

Figure 6.1: Schematic and boundary conditions for forced convection over an inclined elliptic cylinder.

Under these assumptions the 2D incompressible N-S equations, in streamfunction-vorticity (ψ-ζ) form and the energy equation in dimensionless form, are given by

$$\nabla^2 \psi = -\zeta \tag{6.1}$$

$$\frac{\partial \zeta}{\partial t} + u\frac{\partial \zeta}{\partial x} + v\frac{\partial \zeta}{\partial y} = \frac{1}{Re}\nabla^2 \zeta \tag{6.2}$$

$$\frac{\partial T}{\partial t} + u\frac{\partial T}{\partial x} + v\frac{\partial T}{\partial y} = \frac{1}{RePr}\nabla^2 T \tag{6.3}$$

Here $Re = \dfrac{U_0 L}{\nu}$ is the Reynolds number (U_0 and L being characteristic velocity and length respectively), and $Pr = \dfrac{\nu}{\alpha}$ is the Prandtl number, where ν and α are the dynamic viscosity and thermal diffusivity of the fluid respectively.

The streamfunction (ψ) and vorticity (ζ) are defined as follows:

$$u = \frac{\partial \psi}{\partial y}, \quad v = -\frac{\partial \psi}{\partial x} \quad \text{and} \quad \zeta = \frac{\partial v}{\partial x} - \frac{\partial u}{\partial y}. \tag{6.4}$$

For the purpose of determining the immersed boundary, we have employed the level set function developed by Sethian and Osher [125]. The level set function for an inclined ellipse is defined as

$$\phi(x,y,\theta) = \left(\frac{-(x-xc)cos(\theta)+(y-yc)sin(\theta)}{a}\right)^2 + \left(\frac{(x-xc)sin(\theta)+(y-yc)cos(\theta)}{b}\right)^2 - 1 \tag{6.5}$$

where a and b are major and minor axis, and (xc, yc) is the center of the ellipse, and θ is an angle which varies from $0 \leq \theta \leq 2\pi$. The normal vector is defined as

$$\mathbf{n} = (n_1, n_2) = \frac{\nabla\phi}{|\nabla\phi|} = \frac{\phi_x\vec{i} + \phi_y\vec{j}}{\sqrt{\phi_x^2 + \phi_y^2}}. \tag{6.6}$$

6.2.1 Initial and boundary conditions

The following initial and boundary conditions are applied on the non-dimensional variables as follows (figure 6.1)

1. Initial condition: At time $t = 0$, $u = 1$, $v = 0$, and $T = 0$.
2. At the inlet of the domain, the fluid flow is uniform with constant temperature i.e., $u = 1$, $v = 0$, and $T = 0$.
3. Convective boundary conditions are applied on the outlet of the domain, i.e., $\frac{\partial\Phi}{\partial t} + U_0\frac{\partial\Phi}{\partial x} = 0$, where $\Phi = u$, v, ψ, ζ, T.
4. Free slip and adiabatic boundary conditions are applied on the top and bottom wall, i.e., $u = v = \zeta = 0$, $\frac{\partial T}{\partial y} = 0$, $\psi = y_T$ at the top boundary and $\psi = y_B$ at the bottom boundary. Here the subscripts T and B denote "Top' and 'Bottom' respectively.
5. On the surface of the cylinder, no-slip boundary conditions are applied along with constant temperature, i.e., $u = v = \psi = 0$ and $T = 1$.

In order to compute the fluid flow and heat transfer characteristics governed by equations (6.1)- (6.3), We used the methodology described in chapter 4, including the additional equation (6.3), which is again in the convection diffusion form. The discretization is similar to that of the equation (6.2), where the coefficients are adjusted accordingly.

6.2.2 Solution of system of equations

The set of equations that result from discretizing equations (6.1) - (6.3) can be written in matrix form as

$$A_1\psi^{n+1} = f_1(\zeta^n, \tilde{C}_\psi^n) \tag{6.7}$$

$$A_2\zeta^{n+1} = f_2(\zeta^n, u^{n+1}, v^{n+1}, Re, \tilde{C}_\zeta^{n+1}, \tilde{C}_\zeta^n) \tag{6.8}$$

$$A_3T^{n+1} = f_3(T^n, u^{n+1}, v^{n+1}, Re, Pr, \tilde{C}_T^{n+1}, \tilde{C}_T^n) \tag{6.9}$$

In above equations, the coefficient matrices A_1, A_2 and A_3 are asymmetric sparse matrices containing a maximum of nine non-zero values on the diagonals in each row. $\tilde{C}_\psi^n$, $\tilde{C}_\zeta^n$, $\tilde{C}_\zeta^{n+1}$ and $\tilde{C}_T^n$, $\tilde{C}_T^{n+1}$ are the streamfunction, vorticity and temperature correction vectors respectively at the irregular points corresponding to the n^{th} and $(n+1)^{\text{th}}$ time level. For a grid of size $M \times N$, the matrices A_1, A_2 and A_3 are of order MN and ψ^{n+1}, ζ^n, ζ^{n+1}, T^n, T^{n+1}, u^{n+1}, v^{n+1}, $\tilde{C}_\psi^n$, $\tilde{C}_\zeta^n$, $\tilde{C}_\zeta^{n+1}$, $\tilde{C}_T^n$, $\tilde{C}_T^{n+1}$ are vectors of length MN.

Note that the discrete values of the velocities at the $(n+1)^{\text{th}}$ time level are contained in the equations (6.8) and (6.9). However, they are accessible after computing streamfunction from equation (6.7). The fourth order approximation of the velocities u, v are obtained by the method outlined in the work of Kalita et.al. [?]. An outer-inner iteration procedure is used to calculate the solutions to the problems governed by equations (6.1) - (6.3). The following steps describe this computational algorithm:

1. Initialize u, v, ψ, ζ and T and apply the appropriate boundary conditions.
2. Calculate streamfunction jump correction $\tilde{C}_\psi$.
3. Solve equation (6.7) to obtain ψ.
4. Compute u and v by Thomas algorithm from equations (6.4) [71, 78, 89].
5. Calculate vorticity and temperature jump corrections $\tilde{C}_\zeta$, $\tilde{C}_T$.
6. Use (6.8) and (6.9) to determine ζ and T.
   This comprises an outer iteration.
7. Once the discrete values of u, v, ψ, ζ and T are updated, repeat the steps 2-6.

Since A_1, A_2 and A_3 are sparse matrices, solving them requires the use of iterative techniques. Using traditional iterative techniques like Gauss-Seidel is not worthwhile since the coefficient matrices A_1, A_2, A_3 are not diagonally dominant. The inner iterations consist of solving the matrix equations (6.7) - (6.9) at each outer iteration by iterative solvers. The inner iterations are made up of efficient iterative solvers solving equations (6.7)- (6.9) at each time step. In our computations, we employed the Biconjugate gradient stabilized (BiCGStab) [82] iterative solver, along with Incomplete LU decomposition as a preconditioner, with the help of Lis Library [1]. When the residual vectors resulting from equations (6.7)- (6.9) fell below 10^{-9}, the inner iterations were terminated. We performed all of our calculations on a computer with a 32 GB RAM and an Intel Xeon processor.

6.3 Calculation of Nusselt number

The Nusselt number characterises the rate of heat transfer across the fluid around the heated elliptic cylinder. On the other hand, drag and lift coefficients are dimensionless quantities that is related to the drag and lift generated by a bluff body across the fluid in its neighbourhood. As such they are vital parameters yielding useful information about the heat and fluid flow characteristics for the problem under consideration. In this section, we describe in brief the procedure for calculating the Nusselt number.

The quantitative parameter indicating heat transfer, i.e. the local Nusselt number (Nu), is defined as

$$Nu = -\frac{\partial T}{\partial n} \tag{6.10}$$

where n is the direction normal to the cylinder surface.

Contrary to the usual approach of resorting to grid-transformation for calculating Nusselt number of bluff bodies, we have calculated it using the following approach, where merely gathering flow information along the normal direction to the boundary of the bluff body suffices. We have divided the interface, i.e., the surface of the cylinder, into N_P number of interfacial points. Now, in order to identify the interfacial points on the interface, we require the polar coordinates of the inclined ellipse, which is obtained as follows:

Let

$$-(x-xc)cos(\theta) + (y-yc)sin(\theta) = \ acos(\varphi) \tag{6.11}$$

$$(x-xc)sin(\theta) + (y-yc)cos(\theta) = \ bsin(\varphi) \tag{6.12}$$

Add both equations (6.11) and (6.12) after multiplying by $cos(\theta)$ in (6.11) and $(-sin(\theta))$

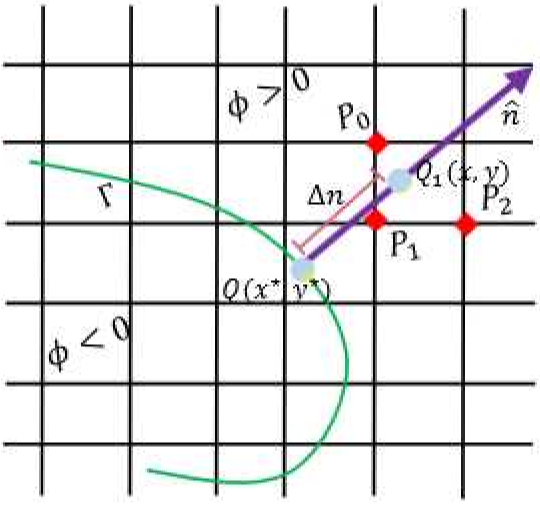

Figure 6.2: Schematic of Nusselt number computation along the boundary an inclined elliptic cylinder.

in (6.12), we get

$$x = xc - acos(\theta)cos(\varphi) + bsin(\theta)sin(\varphi) \tag{6.13}$$

Similarly, add both equations (6.11) and (6.12) after multiplying by $sin(\theta)$ in (6.11) and $cos(\theta)$ in (6.12), we get

$$y = yc + asin(\theta)cos(\varphi) + bcos(\theta)sin(\varphi) \tag{6.14}$$

Let $Q^\star(x^\star, y^\star)$ be an interfacial point on the bluff body's boundary, and $Q_1(x, y)$ be a point in the normal direction of $Q^\star(x^\star, y^\star)$ with $\triangle\mathbf{n}$ being the distance between $Q^\star$ and Q_1 along the direction normal to the interface at $Q^\star$ (see figure 6.2). Then

$$Q_1(x, y) = Q^\star(x^\star, y^\star) + (n_1, n_2)\triangle\mathbf{n}$$

Thus, the local Nu at a point $Q^\star(x^\star, y^\star)$ is given by

$$Nu|_{Q^\star(x^\star,y^\star)} = -\left.\frac{\partial T}{\partial \mathbf{n}}\right|_{Q^\star(x^\star,y^\star)} \tag{6.15}$$

$$= -\frac{T(Q_1(x, y)) - T(Q^\star(x^\star, y^\star))}{\triangle\mathbf{n}} \tag{6.16}$$

Although the approximation of the value of T at the point $Q_1(x,y)$ in the normal direction, it does not have to be a grid point in the computational domain, hence $T(Q_1(x,y))$ is unknown. As such, we compute the value of $T(Q_1(x,y))$ using a linear bivariate interpolating polynomial, which is given as follows:

Let $p(a,b)$ be a linear bivariate interpolation polynomial in two variable is defined by

$$p(a,b) = p_0 + p_1 a + p_2 b \tag{6.17}$$

Given three points $P_0(a_0,b_0)$, $P_1(a_1,b_1)$, $P_2(a_2,b_2)$, the Vandermonde matrix on these three nodes is defined as

$$\mathcal{P} = \begin{bmatrix} 1 & a_0 & b_0 \\ 1 & a_1 & b_1 \\ 1 & a_2 & b_2 \end{bmatrix}$$

Lemma 6.3.1. *Interpolating of T by polynomials $p(a,b)$ on the points P_0, P_1 and P_2 is always possible if and only if $det\mathcal{P} \neq 0$*

Proof. Let us represent the vector of T values at the three points by $\mathcal{F} = [t_0, t_1, t_2]^T$ and define $\mathbb{X} = [p_0, p_1, p_2]^T$. Considering the fact that $p(a,b)$ satisfies $p(a_i,b_i) = t_i$ for $i \in \{0,1,2\}$ can be expressed as $\mathcal{P}\mathbb{X} = \mathcal{F}$ which provides a solution for an arbitrary $\mathbb{X}$ if and only if $det\mathcal{P} \neq 0$. □

Remark 6.3.1. *If P_0, P_1 and P_2 are lies on a same line then interpolation by linear polynomials is not possible on these points.*

In the above linear interpolation, the unknown coefficients p_0, p_1 and p_2 are explicitly provided by

$$\begin{aligned} p_0 &= (t_0a_1b_2 - t_0a_2b_1 - t_1a_0b_2 + t_1a_2b_0 + t_2a_0b_1 - t_2a_1b_0)/A \\ p_1 &= (t_0b_1 - t_1b_0 - t_0b_2 + t_2b_0 + t_1b_2 - t_2b_1)/A \\ p_2 &= -(t_0a_1 - t_1a_0 - t_0a_2 + t_2a_0 + t_1a_2 - t_2a_1)/A \end{aligned}$$

where $A = (a_0b_1 - a_1b_0 - a_0b_2 + a_2b_0 + a_1b_2 - a_2b_1)$.

We determined the local Nusselt number at the point $Q_1(x,y)$ using the above interpolation formula (6.17) by selecting three nearest grid points. Thus, the local Nu is calculated at N_P points. Note that in our computation of local Nu, we have taken $\triangle\mathbf{n} = 0.1$ and $N_P = 201$.

The surface averaged Nusselt number is given by

$$Nu_{\text{av}} = \frac{1}{W} \int_W Nu\, dS \tag{6.18}$$

where W is the surface area of the cylinder. The integral in equation (6.18) is calculated using Simpson's 1/3 rule.

6.4 Code Validation and Grid Independence

6.4.1 Code validation

In order to validate our code, firstly we simulate forced convection over a horizontal circular cylinder at low Reynolds numbers. As will be seen shortly, the results from the present computation are an excellent match with well established results in the literature. Note that the computational domain as well as the boundary conditions for this case is the same as shown in figure 6.1. The only difference is that the elliptical cylinder has been replaced by a circular cylinder of characteristic length (diameter) $D = 1$.

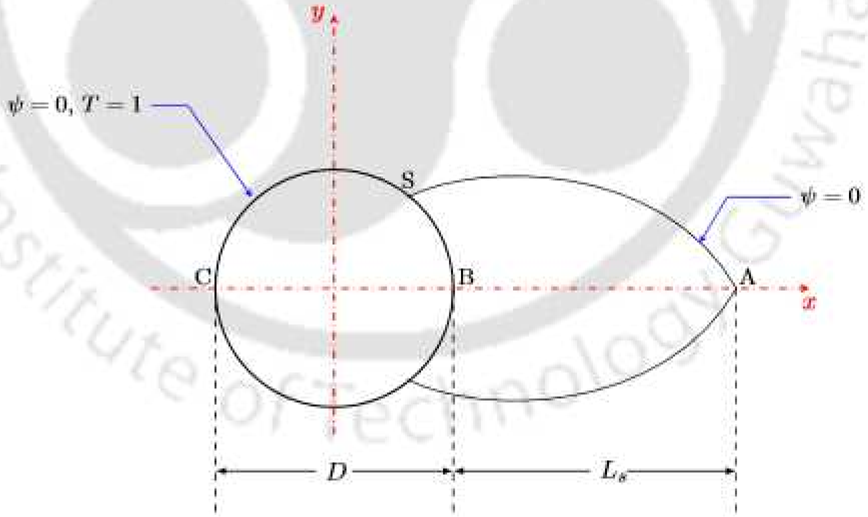

Figure 6.3: Schematic of wake-bubble geometry for the circular cylinder.

Figure 6.3 shows the typical wake-bubble geometry of the flow. Points A, B, and C denote wake stagnation point, back stagnation point, and front stagnation point respectively. The eddy length L_s is the distance from the rear of the cylinder to the wake stagnation point.

Table 6.1: Comparison of eddy length (L_s)

Re	L_s			
	Present	Biswas and Sarkar [16]	Takami and Keller [171]	Dennis and Chang [39]
15	1.224	1.189	1.162	–
20	1.831	1.865	1.844	1.88
30	3.225	3.226	3.223	–
35	3.859	3.793	–	–
40	4.455	4.424	4.650	4.69

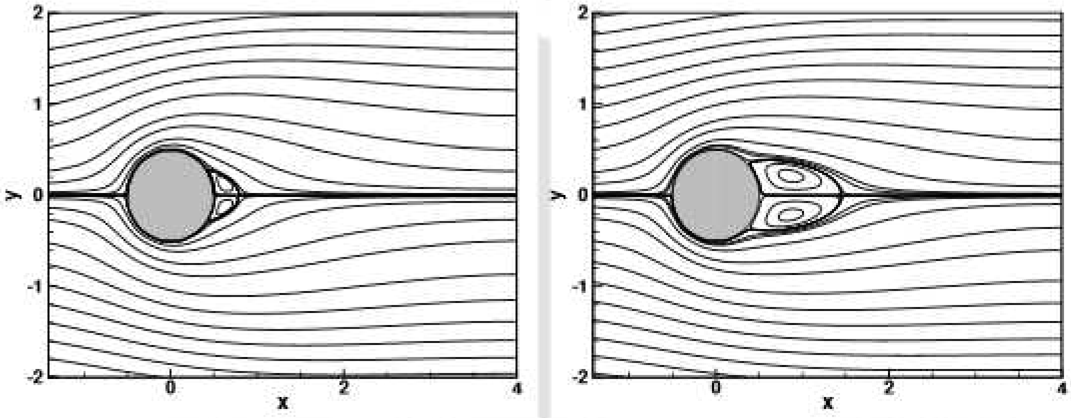

(a) $Re = 10$ (b) $Re = 20$

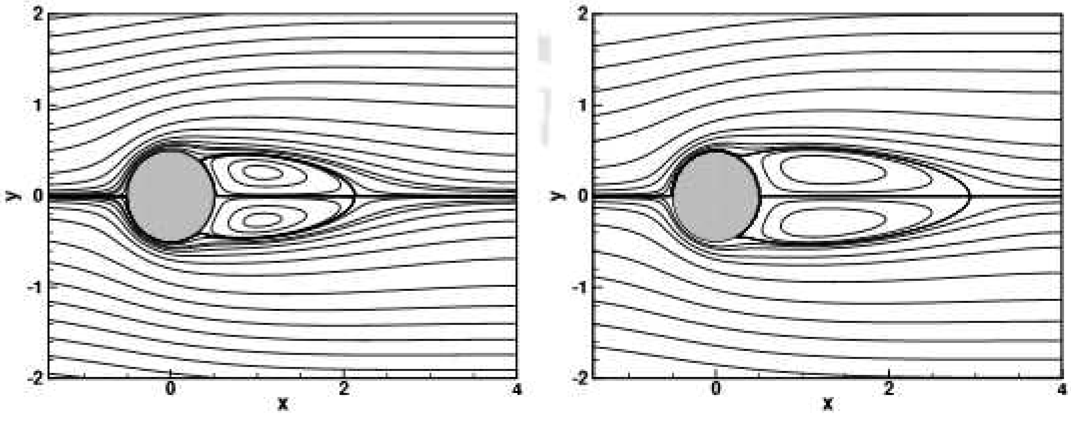

(c) $Re = 30$ (d) $Re = 40$

Figure 6.4: Steady state streamlines for (a)$Re = 10$, (b)$Re = 20$, (c)$Re = 30$, and (d)$Re = 40$.

Table 6.2: Comparison of surface averaged Nusselt number (Nu_{av})

Re	Nu_{av}			
	Present	Biswas and Sarkar [16]	Jafroudi and Yang [70]	Apelt and Ledwich [5]
15	2.2103	2.1809	2.176	2.193
20	2.4617	2.4483	2.433	–
30	2.9287	2.8877	2.850	–
35	3.1281	3.0772	–	–
40	3.2492	3.2351	3.2	3.255

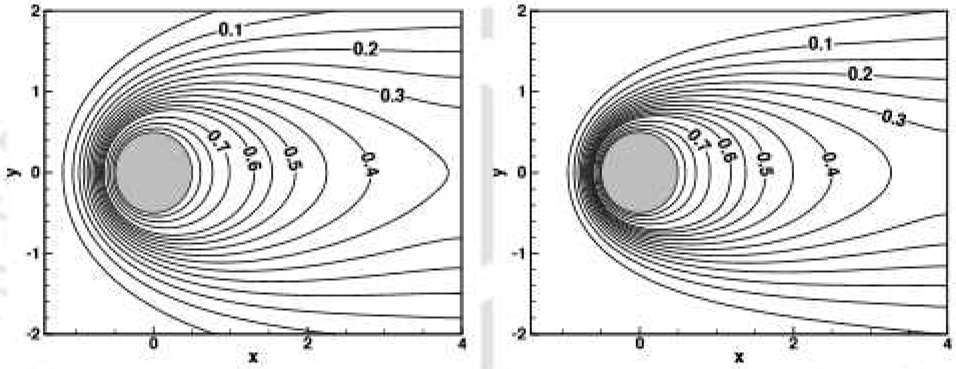

(a) $Re = 10$ (b) $Re = 20$

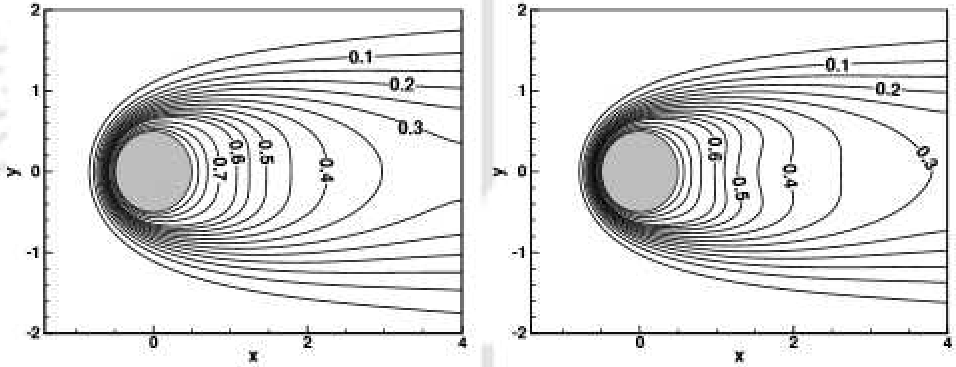

(c) $Re = 30$ (d) $Re = 40$

Figure 6.5: Steady state isotherms for (a)$Re = 10$, (b)$Re = 20$, (c)$Re = 30$, and (d)$Re = 40$..

For this comparison exercise, simulations are carried out for Re = 15, 20, 30, 35, and 40. Previous works (Takami and Keller [171], Dennis and Chang [39], Apelt and Ledwich [5], Jafroudi and Yang [70]) have shown that the flow is steady for these values of Re's. In the present case steady-state has been reached through time marching. The values of eddy length (L_s), and surface averaged Nusselt number (Nu_{av}) from the present computation have been compared with well established results in tables 6.1, and 6.2 respectively. One can see that in all the cases, excellent match has been obtained.

Figures 6.4 and 6.5 (a)-(d) show the streamlines and isotherms for $Re = 10 - 40$. One can clearly see from the figures 6.4 (a)-(d) that the eddy length increases linearly with Re. The isotherms are symmetrical about the x-axis in the wake region. Figures 6.5 (a)-(d) also reveal that the isotherms become steeper with Re in the near wake region. This implies that with an increase in fluid velocity sets a higher temperature gradient resulting in enhanced heat transfer from the cylinder surface. This is evident from the values of Nu_{av} in table 6.2 as well. The streamlines and isotherms resulting from our computation are very similar to the simulations of [16].

The second case of our validation consists of the comparison of the streaklines for the flow past an elliptic cylinder of $AR = 0.67$ at Reynolds number 107 from the experimental visualization of Fonseca et al [52] with the current numerical simulation in figure 6.6. One can clearly see the closeness between them where our simulation has been able to capture all the fluid flow characteristics observed in the experiment.

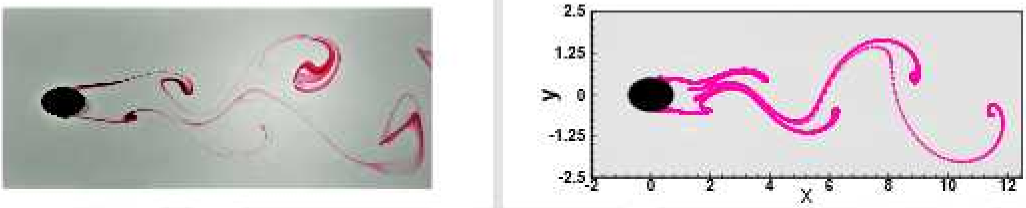

(a) (b)

Figure 6.6: Comparison of the streaklines for the flow past an elliptic cylinder of $AR = 0.67$ at $Re = 107$ from : (a) the experiment of Fonseca et al [52] and (b) present numerical simulation.

6.4.2 Grid independence

In order to establish grid independence of the computed data, we compare the steady state streamlines and isotherms at three different grid sizes for $Re = 40$, and $\theta = 0^{\circ}$. The three different grid sizes used for this exercise are 319×161, 463×265, and 621×353. As seen from figure 6.7, the overlapping of contours for streamlines and isotherms at grid sizes 463×265, and 621×353 clearly indicate grid independence of the computed data. Thus, all our computations in this work have been carried out on a grid of size 463×265.

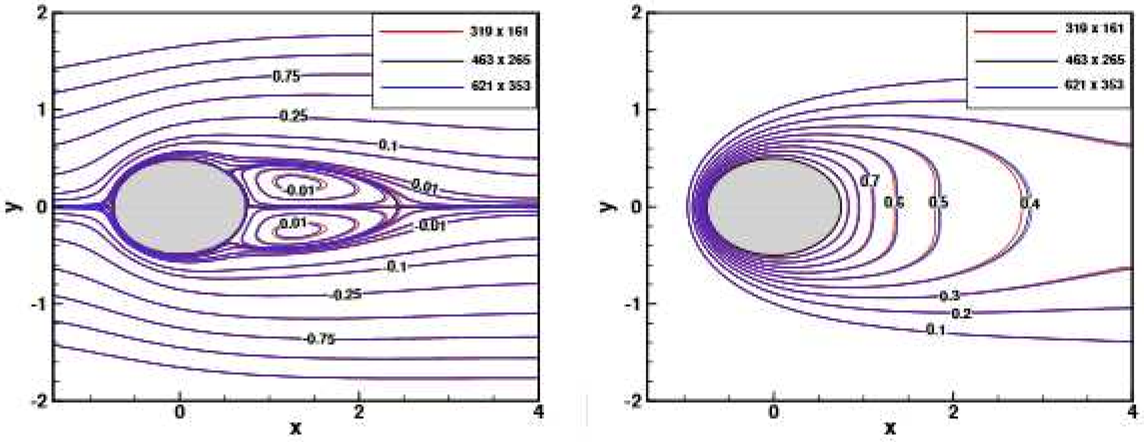

(a) Streamlines (b) Isotherms

Figure 6.7: Steady state (a) streamlines and (b) isotherms for $\theta = 0^\circ$ and $Re = 40$, at three different grids viz. 319×161, 463×265, and 621×353.

6.5 Results and discussion

In this section, we document our results from extensive computations that we have carried out and simultaneously, the analysis of the same. For the problem considered in this work, there are two parameters viz. angle of attack (θ) and Reynolds number (Re), which are crucial for the study. Their values have been varied and the subsequent effects on the flow and heat transfer characteristics have been investigated thoroughly. While the angle of attack is varied in increments of 15° in the range $0^\circ \leq \theta < 180^\circ$, the Reynolds number is varied in increments of 10 in the range $10 \leq Re \leq 130$. Firstly, we present the steady state results, and then the transient ones.

6.5.1 Steady state

Computations are carried out for $0^\circ \leq \theta < 180^0$, and $10 \leq Re \leq Re_c$, where Re_c denotes the critical Re at which the flow transitions from steady to unsteady state. As the angle of attack changes, the value of Re_c also changes.

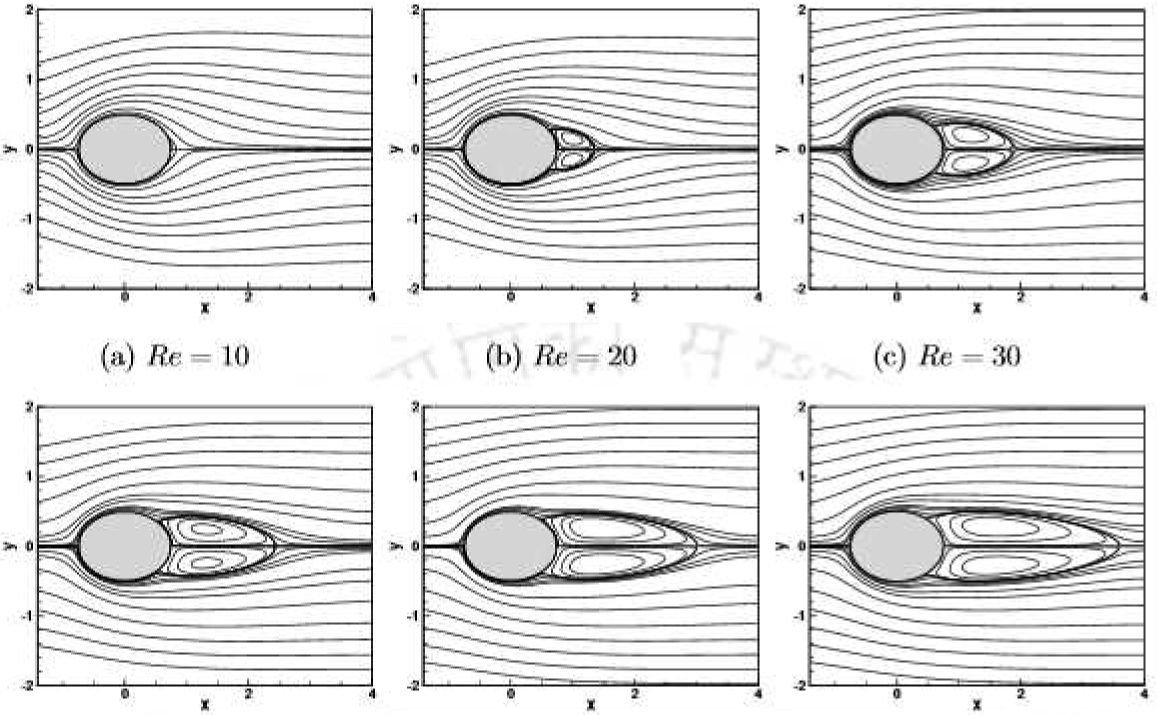

(a) $Re = 10$ (b) $Re = 20$ (c) $Re = 30$

(d) $Re = 40$ (e) $Re = 50$ (f) $Re = 59$

Figure 6.8: Steady state streamlines for $\theta = 0^{\circ}$ and (a)$Re = 10$, (b)$Re = 20$, (c)$Re = 30$, (d)$Re = 40$, and (e)$Re = 50$, and (f) $Re = 59$.

Figures 6.8 and 6.9 show the streamlines and isotherms respectively for $\theta = 0^{\circ}$. Re_c for $\theta = 0^{\circ}$ is in the range $59 \leq Re < 60$. For all the Re's considered in this range, the steady recirculation bubble, consisting of two counter-rotating vortices that elongate as Re is increased, remains symmetric about the x-axis (figures 6.8 (a)-(f)). The upper vortex rotates in clockwise direction, whereas the lower vortex rotates in counter-clockwise direction. The isotherms are more evenly spread out at $Re = 10$ (figure 6.9 (a)) denoting negligible convective heat transfer. As Re increases, the isotherms become more clustered both upstream and downstream of the cylinder, and one can observe the formation of thermal boundary layer on the surface of the cylinder which becomes thinner with increasing Re (figures 6.9 (b) - (f)). The thinning of the thermal boundary layer is most prominent near the leading edge of the cylinder. Finally, a slight distortion in the isotherms can be seen when $Re = 40$ (figure 6.9 (d)), which increases as Re increases (figures 6.9 (e) - (f)). Note that the isotherms also appear symmetric about the x-axis since the flow is symmetric about the line $y = 0$ for $\theta = 0^{\circ}$.

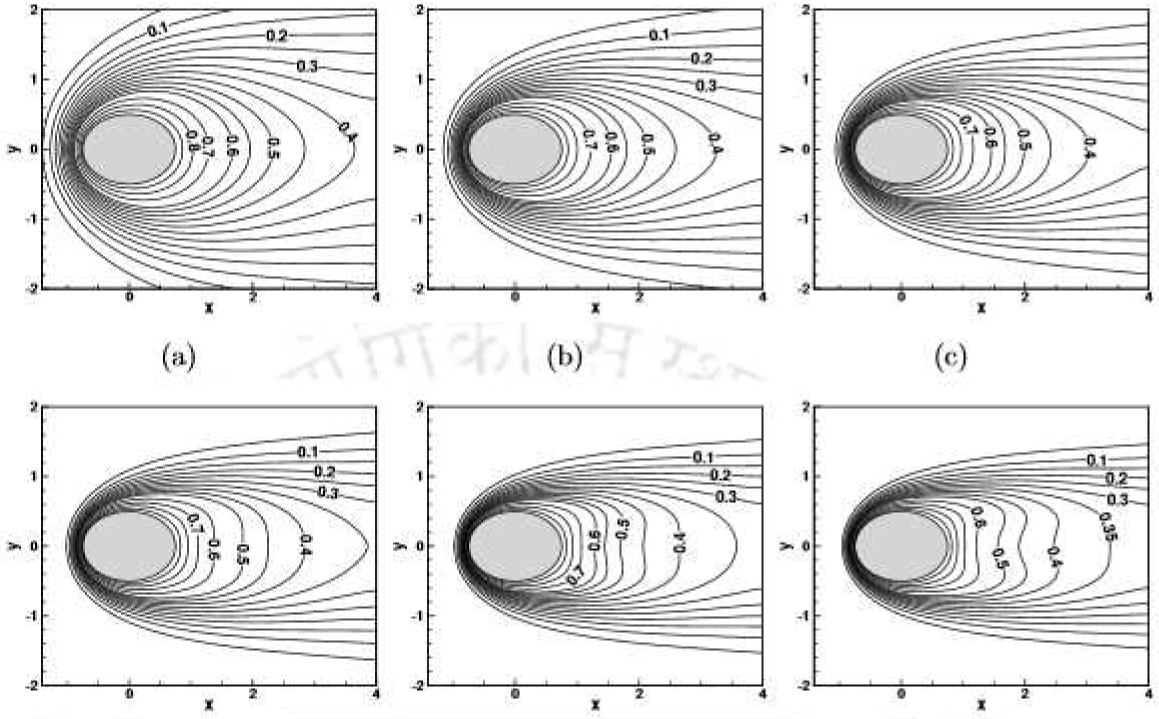

(a) (b) (c)

(d) (e) (f)

Figure 6.9: Steady state isotherms for $\theta = 0^{\circ}$ and (a)$Re = 10$, (b)$Re = 20$, (c)$Re = 30$, (d)$Re = 40$, (e)$Re = 50$, and (f) $Re = 59$.

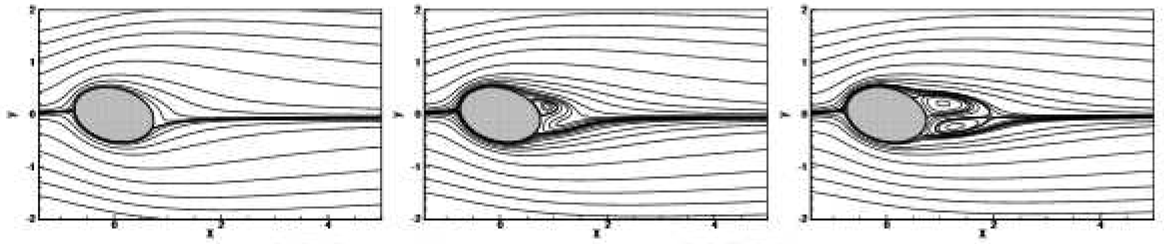

(a) $Re = 10$ (b) $Re = 20$ (c) $Re = 30$

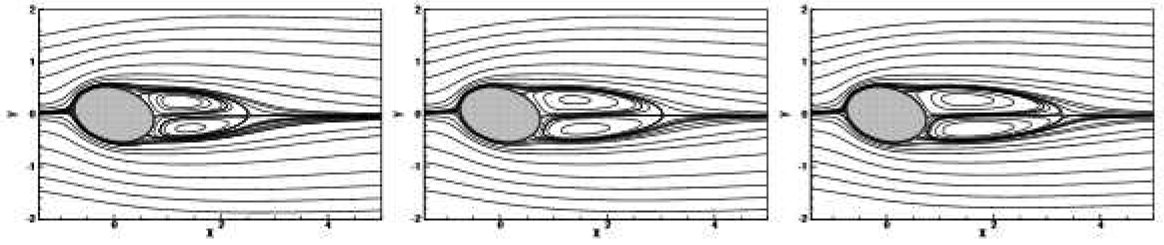

(d) $Re = 40$ (e) $Re = 50$ (f) $Re = 59$

Figure 6.10: Steady state streamlines for $\theta = 15^{\circ}$ and (a)$Re = 10$, (b)$Re = 20$, (c)$Re = 30$, (d)$Re = 40$, (e)$Re = 50$, and (f) $Re = 59$.

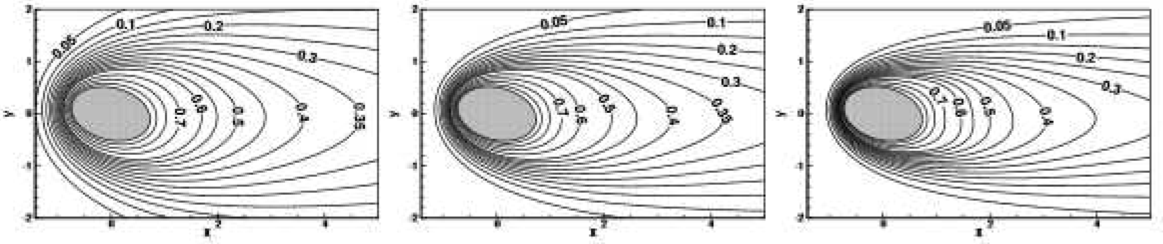

(a) $Re = 10$ (b) $Re = 20$ (c) $Re = 30$

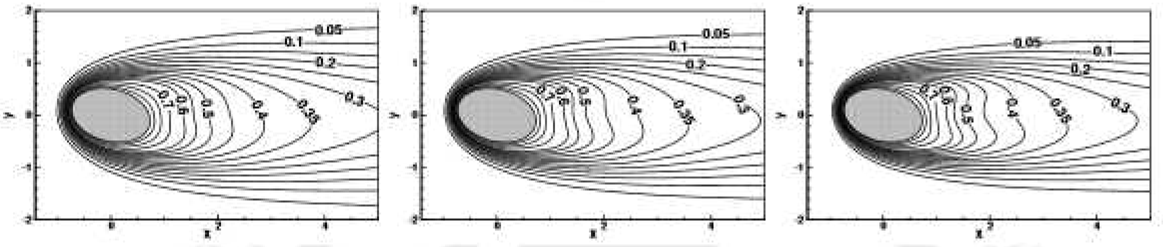

(d) $Re = 40$ (e) $Re = 50$ (f) $Re = 59$

Figure 6.11: Steady state isotherms for $\theta = 15^{\circ}$ and (a)$Re = 10$, (b)$Re = 20$, (c)$Re = 30$, (d)$Re = 40$, (e)$Re = 50$, and (f) $Re = 59$.

Figures 6.10 and 6.11 show the streamlines and isotherms respectively for $\theta = 15^{\circ}$. Re_c for $\theta = 15^{\circ}$ is in the range $59 \leq Re < 60$. Note that as the cylinder now occupies a position asymmetric to the incoming flow, the flow in the wake of the cylinder also loses its symmetry, which is reflected in the streamlines and isotherms. At $Re = 10$ (figure 6.10 (a)), flow separation does not happen and the tiny recirculation bubble seen for $\theta = 0^{\circ}$ (figure 6.8 (a)) vanishes, although a slight bulge in the streamlines can be seen at the rear end of the cylinder. At $Re = 20$ (figure 6.10 (b)), flow separates from the surface of the cylinder and a clockwise rotating recirculation region appears attached on the upper part of the cylinder. A counter-clockwise rotating vortex appears as well on the lower part of the cylinder at $Re = 30$ (figure 6.10 (c)). This vortex, however, remains detached from the cylinder surface. Both vortices grow in size and strength as the Re increases (figures 6.10 (d) - (f)). Due to the asymmetric nature of the flow w.r.t the cylinder, these vortices are also of unequal strengths and sizes. This asymmetry is reflected in the isotherms as well (figures 6.11 (a) - (f)). A better insight into the nature of heat transfer characteristics can be gleaned from the plot of surface Nusselt number, which is presented in a subsequent section.

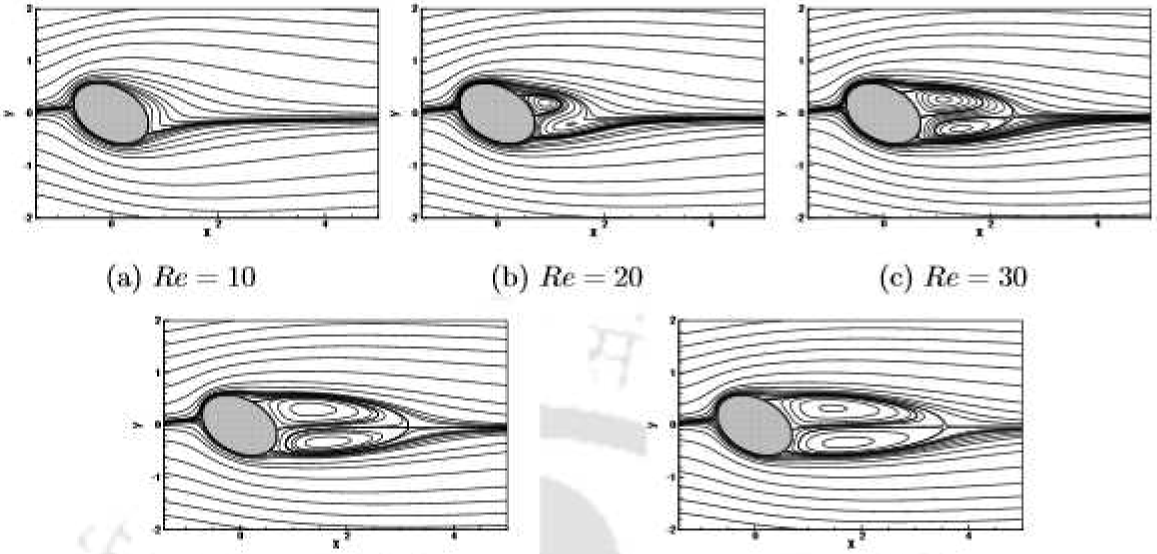

(a) $Re = 10$ (b) $Re = 20$ (c) $Re = 30$

(d) $Re = 40$ (e) $Re = 49$

Figure 6.12: Steady state streamlines for $\theta = 30^{\circ}$ and (a)$Re = 10$, (b)$Re = 20$, (c)$Re = 30$, (d)$Re = 40$, and (e)$Re = 49$.

Figures 6.12 and 6.13 show the streamlines and isotherms respectively for $\theta = 30^{\circ}$, where the Re_c is in the range $49 \leq Re < 50$. The barely discernible bulge when $\theta = 15^{\circ}$ at $Re = 10$ (figure 6.11 (a)) is more noticeable when $\theta = 30^{\circ}$ (figure 6.12 (a)) implying that the flow is on the brink of separating from the cylinder surface. The clockwise rotating vortex attached on the upper surface of the cylinder grows in size at $Re = 20$, and a counterclockwise rotating vortex begins to form near the lower surface of the cylinder (figure 6.12 (b)). Flow pattern for the rest of the Re's follow a similar pattern to the previous configuration. The isotherms also follow a similar pattern, except that the distortions in the isotherms appear at a much lower Re as θ is increased, $Re = 40$ for this case (figure 6.13 (d)) compared to $Re = 50$ for $\theta = 15^{\circ}$ (figure 6.11 (e)). This would indicate that the overall heat transfer rate for the same Re is comparably higher (see section 6.5.1.1).

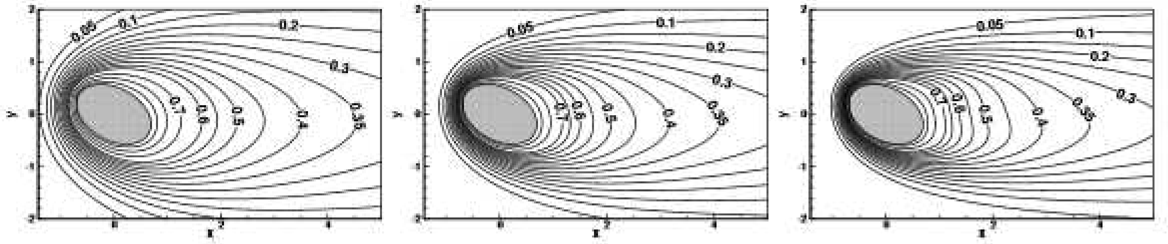

(a) $Re = 10$ (b) $Re = 20$ (c) $Re = 30$

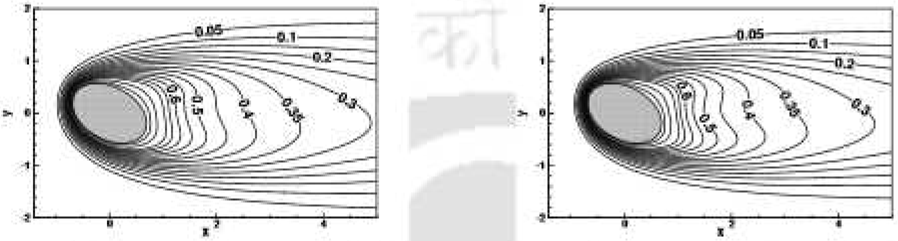

(d) $Re = 40$ (e) $Re = 49$

Figure 6.13: Steady state isotherms for $\theta = 30^{\circ}$ and (a)$Re = 10$, (b)$Re = 20$, (c)$Re = 30$, (d)$Re = 40$, and (e)$Re = 49$.

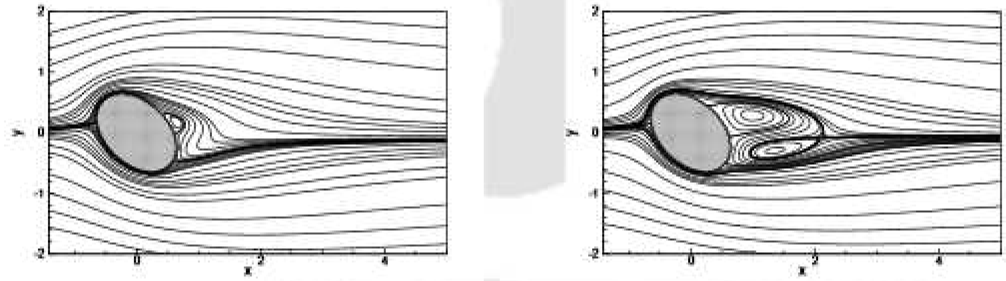

(a) $Re = 10$ (b) $Re = 20$

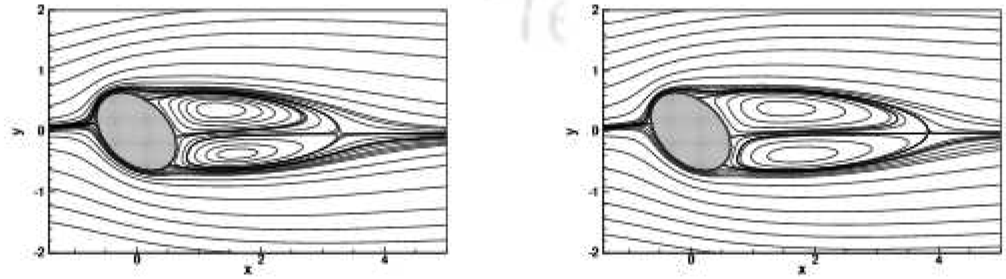

(c) $Re = 30$ (d) $Re = 38$

Figure 6.14: Steady state streamlines for $\theta = 45^{\circ}$ and (a)$Re = 10$, (b)$Re = 20$, (c)$Re = 30$, and (d) $Re = 38$.

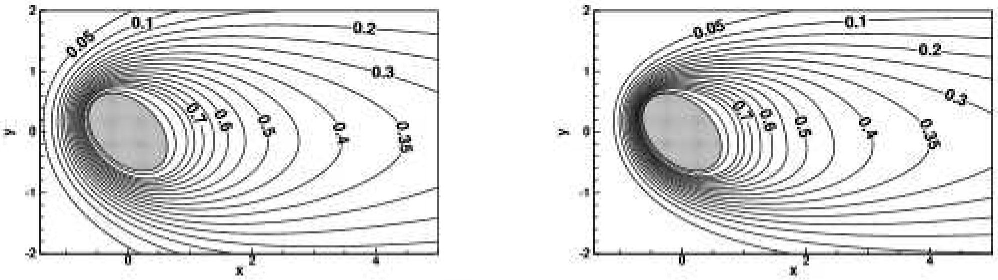

(a) $Re = 10$ (b) $Re = 20$

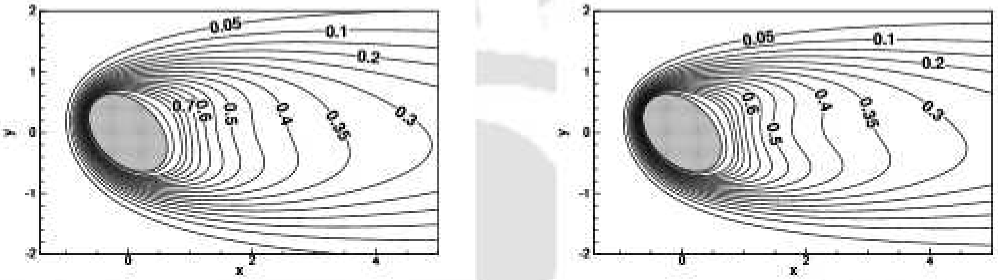

(c) $Re = 30$ (d) $Re = 38$

Figure 6.15: Steady state isotherms for $\theta = 45^{\circ}$ and (a)$Re = 10$, (b)$Re = 20$, (c)$Re = 30$, and (d)$Re = 38$.

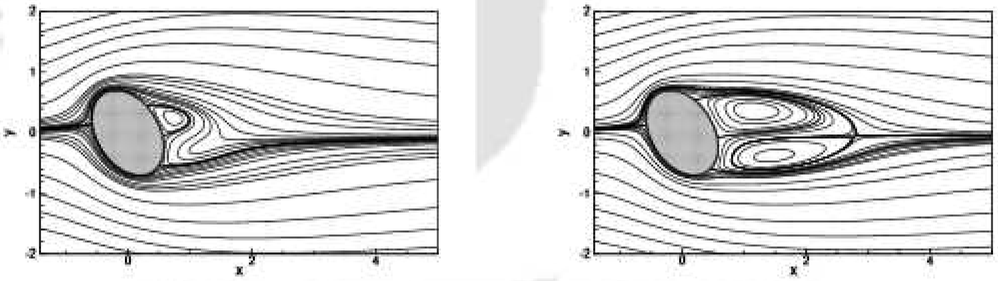

(a) $Re = 10$ (b) $Re = 20$

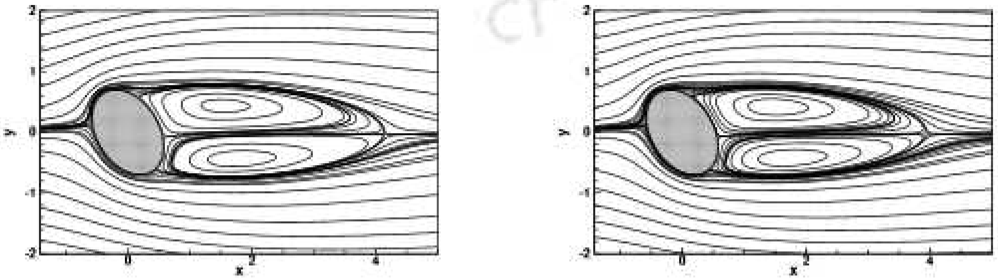

(c) $Re = 30$ (d) $Re = 31$

Figure 6.16: Steady state streamlines for $\theta = 60^{\circ}$ and (a)$Re = 10$, (b)$Re = 20$, (c)$Re = 30$, and (d)$Re = 31$.

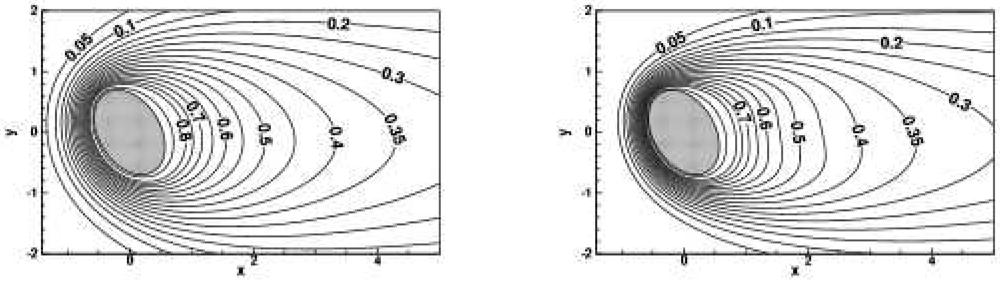

(a) $Re = 10$ (b) $Re = 20$

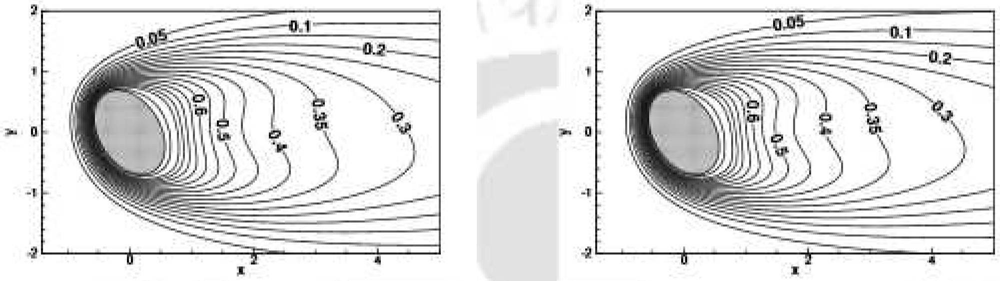

(c) $Re = 30$ (d) $Re = 31$

Figure 6.17: Steady state streamlines for $\theta = 60^{\circ}$ and (a)$Re = 10$, (b)$Re = 20$, (c)$Re = 30$, and (d)$Re = 31$.

Steady state streamlines and isotherms for $\theta = 45^{\circ}$ are shown in figures 6.14 and 6.15 respectively where the Re_c is in the range $38 \leq Re < 39$. Here, in sharp contrast to the previous two cases, flow separation occurs at $Re = 10$ and we see the appearance of a recirculation region on the upper surface of the cylinder (figure 6.14 (a)). Also, distortions in the isotherms appear at a lesser Re (figure 6.15 (c)) compared to the previous two cases. The evolution of streamlines follow a similar pattern - the size and strength of the vortices increase with Re. However, note that the value of Re_c decreases when θ is increased.

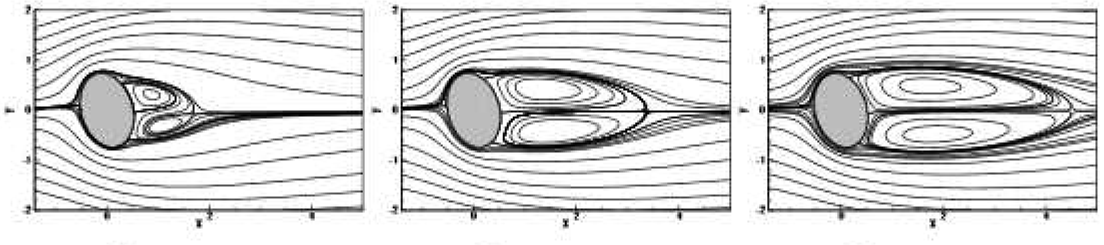

(a) $Re = 10$ (b) $Re = 20$ (c) $Re = 28$

Figure 6.18: Steady state streamlines for $\theta = 75^{\circ}$ and (a)$Re = 10$, (b)$Re = 20$, (c) $Re = 28$.

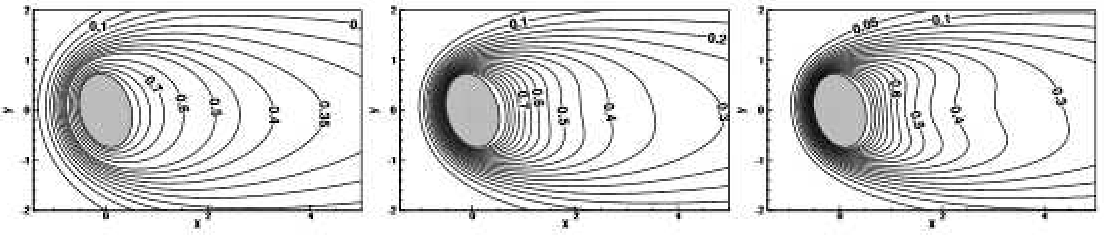

(a) $Re = 10$ (b) $Re = 20$ (c) $Re = 28$

Figure 6.19: Steady state isotherms for $\theta = 75^{\circ}$ and (a)$Re = 10$, (b)$Re = 20$, (c) $Re = 28$.

Figures 6.16 and 6.17 show the steady state streamlines and isotherms respectively for $\theta = 60^{\circ}$. Here, the Re_c is in the range $31 \leq Re < 32$. At $Re = 10$ (figure 6.16 (a)), the recirculation region that formed at $\theta = 45^{\circ}$ increases in size. As seen previously there is a gradual increase in the sizes of the vortices formed on the surfaces of the cylinder as Re is increased, and the value of Re_c also drops to $Re = 31$ at $\theta = 60^{\circ}$. One can also notice that the flow is gradually becoming symmetric as θ is increased. The distortions in the isotherms appear at a much lower Re (figure 6.17 (b)) than for $\theta = 45^{\circ}$.

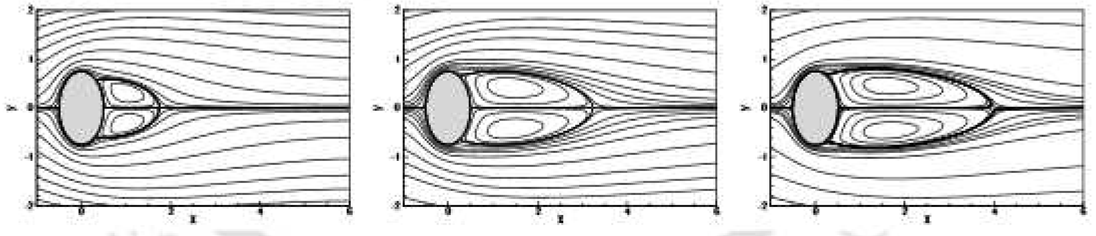

(a) $Re = 10$ (b) $Re = 20$ (c) $Re = 25$

Figure 6.20: Steady state streamlines for $\theta = 90^{\circ}$ and (a)$Re = 10$, (b)$Re = 20$, (c) $Re = 25$.

Steady state streamlines and isotherms for $\theta = 75^{\circ}$ are shown in figures 6.18 and 6.19 respectively. The Re_c in this case is in the range $28 \leq Re < 29$. At $Re = 10$, we observe the formation of two recirculation regions on the surface of the cylinder as opposed to only one for $\theta = 45^{\circ}, 60^{\circ}$ and none for $\theta = 15^{\circ}, 30^{\circ}$. The wake region appears nearly symmetric as θ is increased. This tendency of the flow to approach symmetry is observed in the isotherms as well. Distortions in the isotherms in case appears at $Re = 20$ (figure 6.19 (b)), which is the same as for $\theta = 60^{\circ}$, but a closer look reveals that the distortion seen at $\theta = 75^{\circ}$ is more pronounced than that observed at $\theta = 60^{\circ}$.

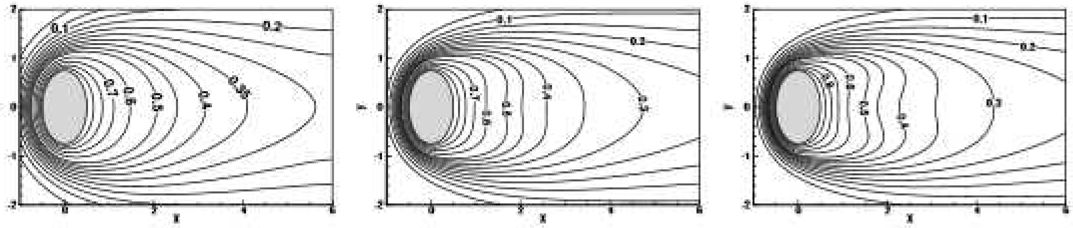
(a) $Re = 10$ (b) $Re = 20$ (c) $Re = 25$

Figure 6.21: Steady state isotherms for $\theta = 90^{\circ}$ and (a)$Re = 10$, (b)$Re = 20$, (c) $Re = 25$.

As θ is increased to 90° and incoming flow is symmetric w.r.t to the cylinder, we observe the flow becoming symmetric again in the cylinder wake, as evident from the streamlines and isotherms in figures 6.20 and 6.21 respectively. The Re_c is in the range $25 \leq Re < 26$. Again, distortion in the isotherms at $Re = 20$ is more pronounced than that observed at $\theta = 75^{\circ}$ (figure 6.21(b)).

The wake lengths for $\theta = 0^{\circ}$, 90° are tabulated in 6.3 for reference. As we can see from the table also the wake lengths at $\theta = 90^{\circ}$ are markedly higher than the wake length at $\theta = 0^{\circ}$.

Table 6.3: Wake length for $\theta = 0^{\circ}$, 90°

Re	θ	
	0°	90°
10	0.085	1.307
20	0.643	2.725
25	0.922	3.457
30	1.141	–
40	1.693	–
50	2.262	–
59	2.848	–

6.5.1.1 Average Nusselt number and Drag coefficient

The local and surface averaged Nusselt numbers are calculated from equations (6.10) and (6.18) respectively. We then plot the variation of the local Nu along the surface of the cylinder. Figure 6.22 shows the schematic for measuring the perimeter of the ellipse. When $\theta = 0^{\circ}$, we start at point P and then move clockwise along the points Q, R, S, W. Note that W coincides with P. Let l_E denote the perimeter of the cylinder measured along $PQRSW$. When $\theta \neq 0^{\circ}$, the perimeter is measured along $P'Q'R'S'W'$.

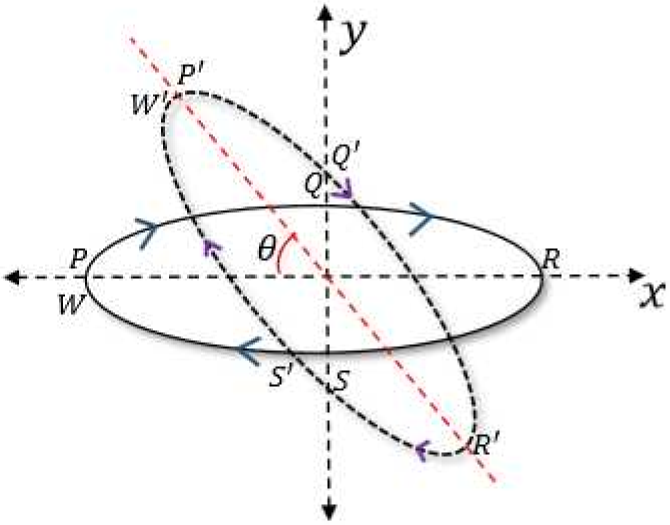

Figure 6.22: Schematic showing the cylinder orientation for Nusselt number computation.

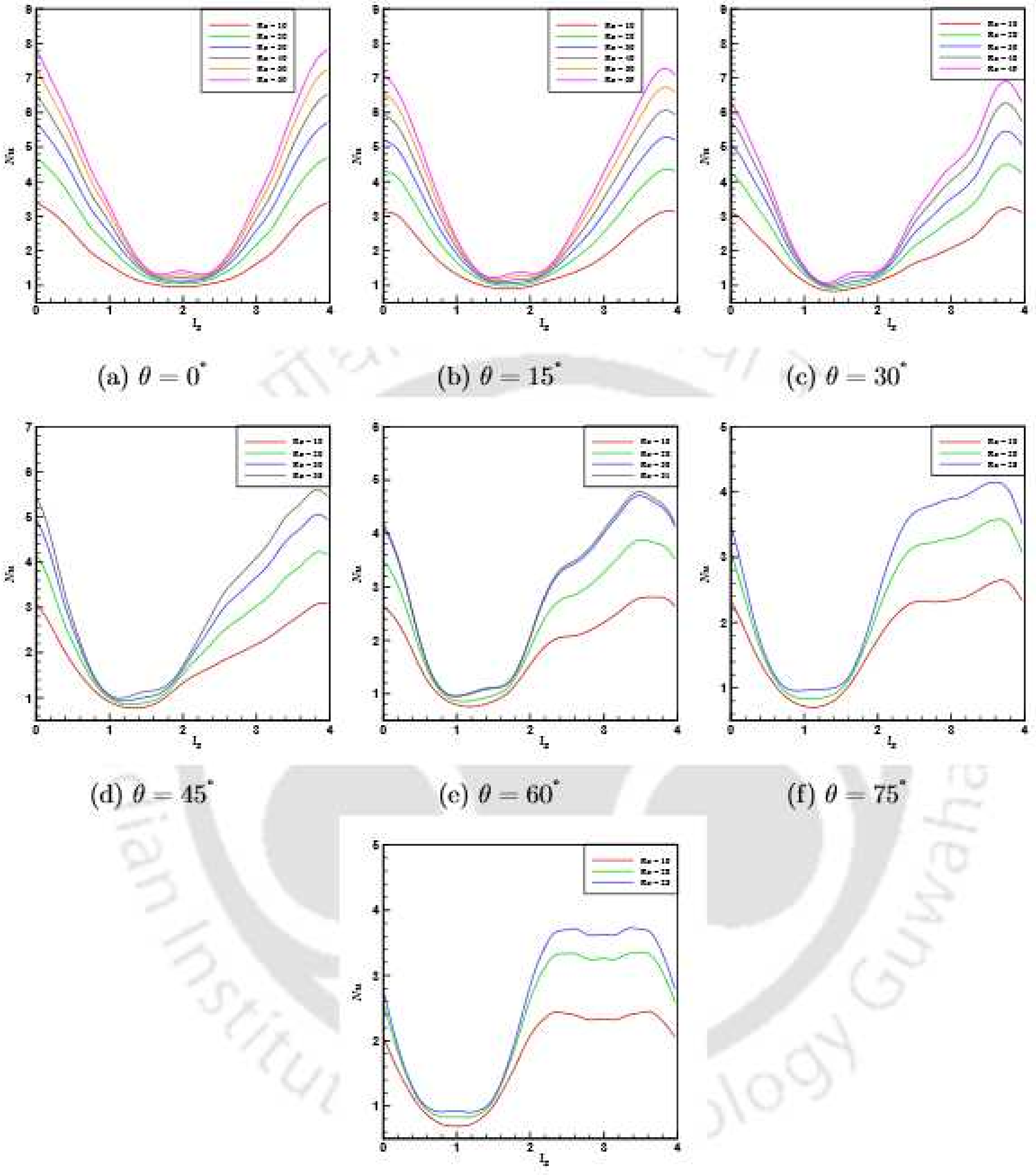

(a) $\theta = 0^{\circ}$ (b) $\theta = 15^{\circ}$ (c) $\theta = 30^{\circ}$

(d) $\theta = 45^{\circ}$ (e) $\theta = 60^{\circ}$ (f) $\theta = 75^{\circ}$

(g) $\theta = 90^{\circ}$

Figure 6.23: Variation of local Nusselt number along the surface of the cylinder for (a) $\theta = 0^{\circ}$, (b) $\theta = 15^{\circ}$, (c) $\theta = 30^{\circ}$, (d) $\theta = 45^{\circ}$, (e) $\theta = 60^{\circ}$, (f) $\theta = 75^{\circ}$, (g) $\theta = 90^{\circ}$.

Figure 6.23 shows the variation of local Nu along the surface of the cylinder for $\theta = 0^{\circ} - 90^{\circ}$. For every value of θ we observe that Nu increases with Re. For $\theta = 0^{\circ}$ (figure 6.23 (a)), the variation in Nu is observed to be symmetric, with the maximum Nu at the leading edge of the cylinder, i.e., at point P shown in the schematic (figure

6.22). At $\theta = 15^{\circ}$ (figure 6.23 (b)), Nu decreases first along the surface $P'Q'R'$. In the vicinity of the point R' we observe a global minima and a local maxima of Nu. As one moves from the point R', i.e., the trailing edge of the cylinder, to the point W' along the surface $R'S'W'$, an increase in Nu is observed. The variation of Nu for $\theta = 30^{\circ}$ (figure 6.23 (c)) follows a similar pattern as that of $\theta = 15^{\circ}$. However, two important differences stand out. First, the maximum value of Nu for any Re at $\theta = 30^{\circ}$ is greater than the maximum value of Nu for the same Re at $\theta = 15^{\circ}$. This is due to the fact that flow separation happens at a lower Re for $\theta = 30^{\circ}$, which leads to greater mixing of the fluid thus increasing the rate of heat transfer. Thus, $\max(Nu)$ at $Re = 40$ for $\theta = 30^{\circ} > \max(Nu)$ at $Re = 40$ for $\theta = 15^{\circ}$, and so on. Secondly, there is slight shift in the locations of the local maxima and minima of Nu in the clockwise direction. For $\theta = 45^{\circ}$ (figure 6.23 (d)) also, the variation in Nu follows the pattern we observed for $\theta = 30^{\circ}$. We also observe that the variation of Nu along the surface $P'Q'R'$ assumes an almost parabolic shape. At $\theta = 60^{\circ}$ (figure 6.23 (e)), similar to the previous two cases, the locations of the local maxima and minima shift in the clockwise direction along the surface of the cylinder. At $\theta = 75^{\circ}$ (figure 6.23 (f)), there is a significant reversal in one of the patterns observed in the previous four cases. Here, one can observe that the maximum value of Nu for a particular Re is less than the maximum value of Nu for the same Re at $\theta = 60^{\circ}$, i.e., max $\max(Nu)$ at $Re = 10$ for $\theta = 75^{\circ} < \max(Nu)$ at $Re = 10$ for $\theta = 60^{\circ}$. Note that, at $\theta = 90^{\circ}$ (figure 6.23 (g)), the maximum value of Nu for a particular Re is again less than the maximum value of Nu for the same Re at $\theta = 75^{\circ}$. Interestingly, the minimum value of Nu keeps on decreasing from $\theta = 15^{\circ} - 90^{\circ}$, and it occurs on the surface $P'Q'R'$. Note that for the variation of Nu is smoother along the surface on the part $P'Q'R'$ for all values of θ.

The variation of surface averaged Nusselt number, Nu_{av}, with the Reynolds number for different values of θ is shown in figure 6.24 (a). Apart from $\theta = 0^{\circ}$, the variation of Nu_{av} follows a similar pattern for all values of θ. For $\theta = 0^{\circ}$, we observe that the value of Nu_{av} for a particular Re is markedly higher than the corresponding Nu_{av} values at other values of θ. For the rest of θ values considered, the average Nusselt number increases with Re due an increase in flow strength as Re is increased. Note that the value of Nu_{av} also increases as θ is increased. Thus, the value of Nu_{av} at $Re = 10$ for $\theta = 30^{\circ}$ is greater than the value of Nu_{av} at $Re = 10$ for $\theta = 15^{\circ}$ and so on. Also, the value of Nu_{av} is minimum at $\theta = 15^{\circ}$.

Figure 6.24 (b) shows the variation of drag coefficient C_D with Re for different values of θ, which is computed by using (4.56). We can see that for a particular θ, C_D decreases with Re, which is on the expected line, as with increase in Re, inertial forces start dominating the viscous ones. Two cases, however, stand out viz. $\theta = 0^{\circ}$ and $\theta = 90^{\circ}$. For a given Re, the values of C_D at $\theta = 0^{\circ}, 90^{\circ}$ are greater than the value of C_D at the rest of θ values. Further, the drag forced experienced by the body at $\theta = 90^{\circ}$ is the highest of all for a given Re. Also, as θ is increased for a particular Re, flow separation occurs, which leads to an increase in the pressure difference between the front and rear half of the cylinder, thereby causing an increase in the pressure drag force. Thus for a fixed Reynolds number, C_D increases as θ is increased.

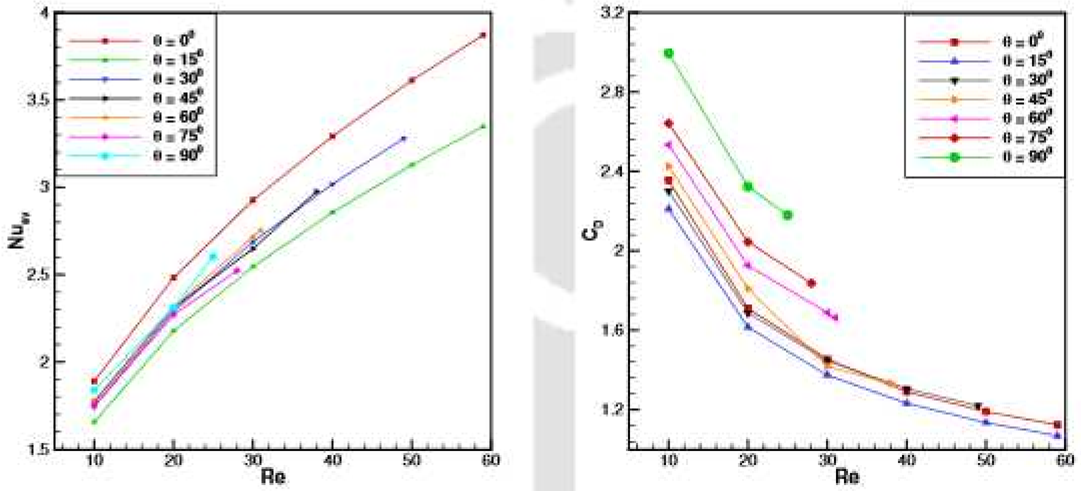

(a) Nu_{av} vs. Re (b) C_D vs. Re

Figure 6.24: Variation of (a) Surface Averaged Nusselt number (Nu_{av}) and (b) Average drag C_D with Re for different values of θ.

6.5.1.2 Heat and fluid flow beyond $\theta = 90^{\circ}$

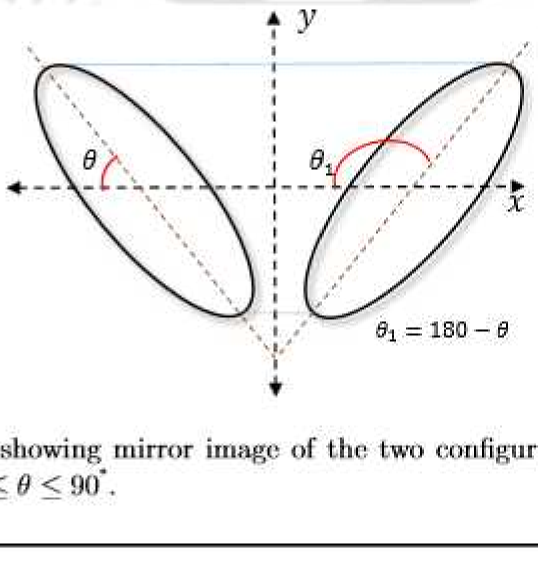

Figure 6.25: Schematic showing mirror image of the two configurations corresponding to θ and $\theta_1 = 180^{\circ} - \theta$ for $0^{\circ} \leq \theta \leq 90^{\circ}$.

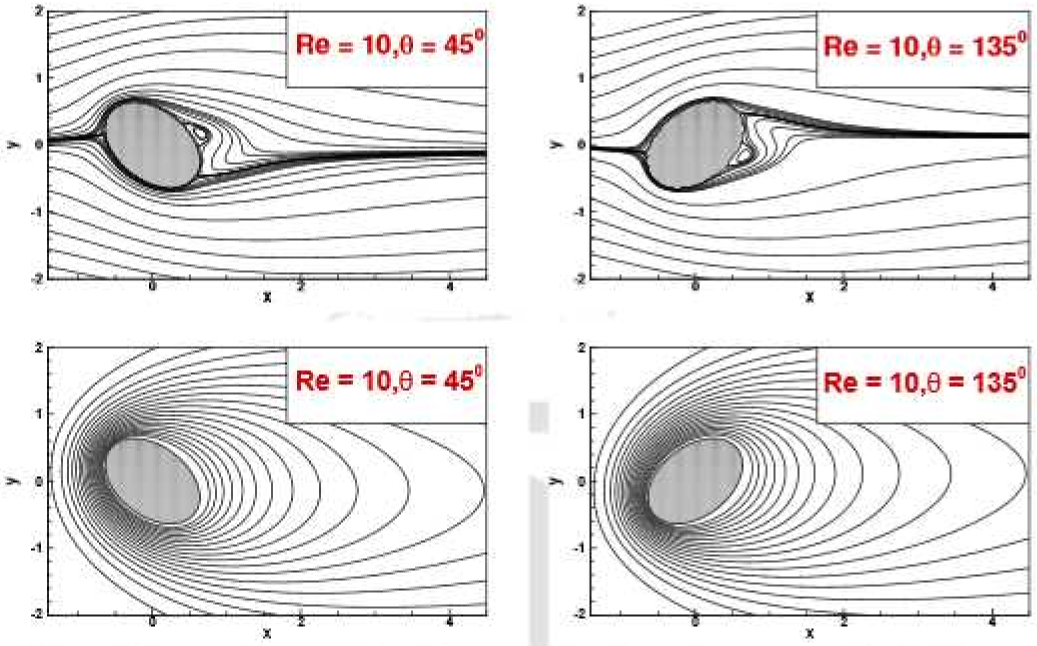

Figure 6.26: Comparison of streamlines (top) and isotherms (bottom) for $Re = 10$ with $\theta = 45^\circ$ (left) and $\theta = 135^\circ$ (right)

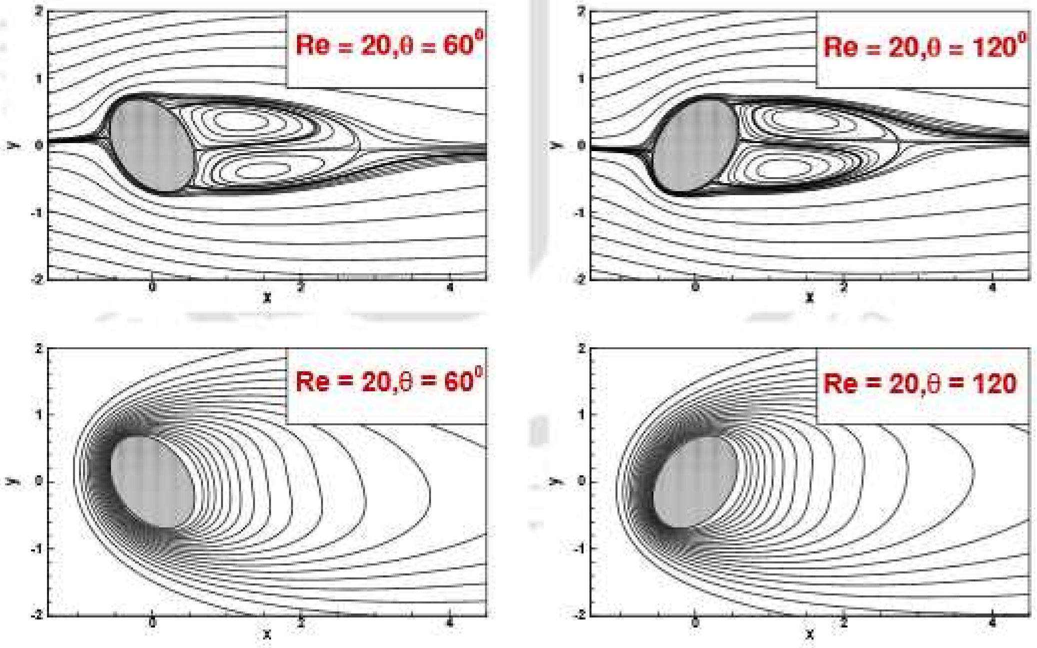

Figure 6.27: Comparison of streamlines (top) and isotherms (bottom) for $Re = 20$ with $\theta = 60^\circ$ (left) and $\theta = 120^\circ$ (right)

We carried out continued our computations for $90^\circ < \theta < 180^\circ$ as well. However, in this range of θ, we observed that, about an $x = constant$ line, the flow in the wake of the cylinder is a mirror image of the flow in range of $0^\circ \leq \theta \leq 90^\circ$, i.e., flow for

θ ($90^\circ < \theta < 180^\circ$) is a mirror image of flow for $180^\circ - \theta$ ($0^\circ \leq \theta \leq 90^\circ$). In other words, flow pattern for $\theta = 105^\circ$ is a mirror image of flow pattern for $\theta = 75^\circ$, that of $\theta = 120^\circ$ is a mirror image of $\theta = 60^\circ$ and so on. In figure 6.25 the schematic on the left represents the configurations in the range $0^\circ < \theta \leq 90^\circ$. On the right, the configuration for the range $90^\circ < \theta < 180^\circ$ is represented. As shown in the figure, the schematic on the right with an angle of attack $\theta_1 (= 180^\circ - \theta)$ is the mirror image about the y- axis of the schematic on the right. To demonstrate this interesting phenomena, we have chosen three flow configurations at different θ and Re, and compared them with their $180^\circ - \theta$ counterparts (see figure 6.27- 6.28). This particular symmetry results from the geometry of the cylinder, as well as the particular assumption of negligible gravity on the flow (see section 6.2). As a result of this particular symmetry there is no marked difference in the quantitative parameters as well. Thus there is no difference in the values of the average Nusselt number (Nu_{av}) as well as the average drag (C_D) for the configuration $\theta = 45^\circ$ and its mirror image $\theta = 135^\circ$, and so on as can be seen from tables 6.4-6.6.

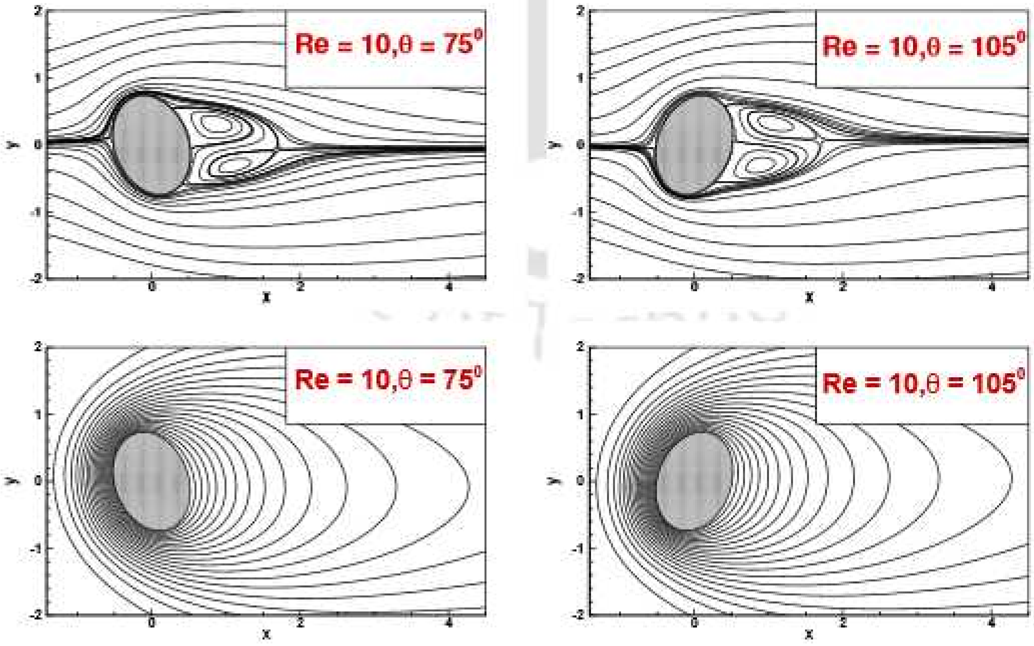

Figure 6.28: Comparison of streamlines (top) and isotherms (bottom) for $Re = 10$ with $\theta = 75^\circ$ (left) and $\theta = 105^\circ$ (right).

Table 6.4: Comparison of surface averaged Nusselt number Nu_{av} and drag coefficients C_D for $\theta = 45^\circ$ and $\theta = 135^\circ$.

	Nu_{av}		C_D	
Re	$\theta = 45^\circ$	$\theta = 135^\circ$	$\theta = 45^\circ$	$\theta = 135^\circ$
10	1.798	1.802	2.913	2.907
20	2.349	2.356	2.173	2.083
30	2.759	2.768	1.702	1.692
38	3.032	3.041	1.598	1.591

Table 6.5: Comparison of surface averaged Nusselt number Nu_{av} and drag coefficients C_D for $\theta = 60^\circ$ and $\theta = 120^\circ$.

	Nu_{av}		C_D	
Re	$\theta = 60^\circ$	$\theta = 120^\circ$	$\theta = 60^\circ$	$\theta = 120^\circ$
10	1.815	1.821	3.017	2.958
20	2.366	2.373	2.311	2.317
30	2.779	2.794	2.027	2.034
31	2.816	2.898	1.996	2.013

Table 6.6: Comparison of surface averaged Nusselt number Nu_{av} and drag coefficients C_D for $\theta = 75^\circ$ and $\theta = 105^\circ$.

	Nu_{av}		C_D	
Re	$\theta = 75^\circ$	$\theta = 105^\circ$	$\theta = 75^\circ$	$\theta = 105^\circ$
10	1.756	1.761	2.961	2.916
20	2.283	2.911	2.454	2.433
28	2.610	2.619	1.965	1.946

6.5.2 Transient state

In this section, we present the results for transient state flow phenomena in terms of streamlines, vorticity contours, isotherms, as well as the force coefficients (C_D, C_L), surface averaged Nusselt numbers, and Strouhal numbers. Computations were carried for $Re_c \leq Re \leq 120$, and $0 \leq \theta \leq 180^\circ$. However, as we noted in section 6.5.1, the flow phenomena for $90^\circ < \theta < 180^\circ$ is a mirror image of the flow phenomena for $0^\circ < \theta < 90^\circ$. Hence, we present results only for $0^\circ \leq \theta \leq 90^\circ$.

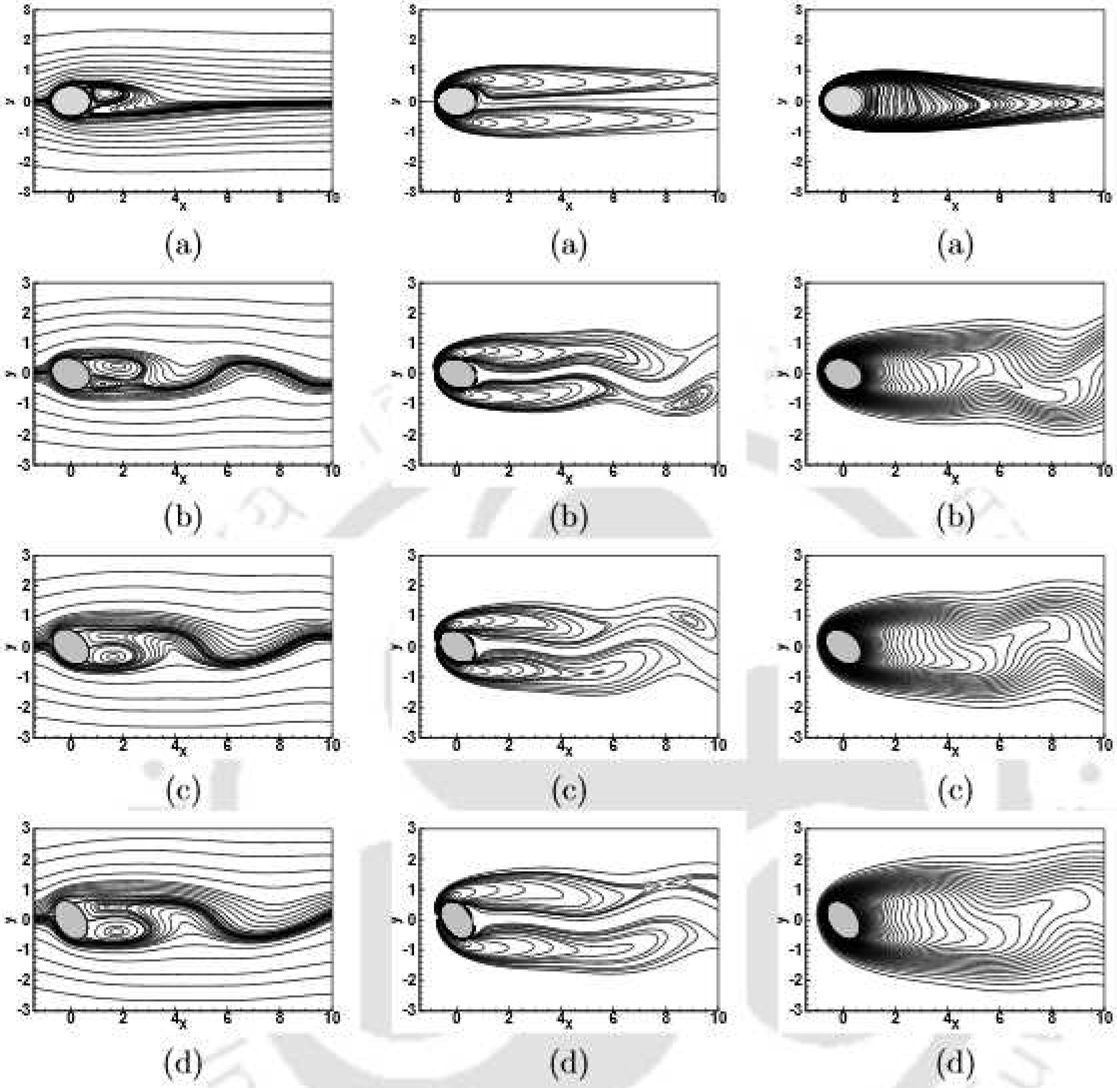

(a) (a) (a)

(b) (b) (b)

(c) (c) (c)

(d) (d) (d)

Figure 6.29: *Transition to unsteadiness, flow in the vicinity of Critical Reynolds number: Streamlines (left), vorticity (middle) and isotherms (right) for the combinations* (θ, Re), $(a) = (0^{\circ}, 60)$, $(b) = (15^{\circ}, 60)$, $(c) = (30^{\circ}, 50)$, *and* $(d) = (45^{\circ}, 39)$, *respectively.*

In general, in the unsteady regime, two rows of well defined vortices are formed with clockwise vortices being shed from the upper side of the cylinder and counterclockwise vortices from the lower side. This is the well known von Karman vortex street that stretches over the entire downstream region in the wake of the cylinder. Since the mechanism of vortex shedding remains same for all values of θ considered, we take $Re = 100$ as the representative Reynolds number for which we present our analysis. Quantitative parameters like Strouhal number, Drag and Lift forces, and Nusselt number will be discussed at length subsequently. Note that the flow becomes unsteady beyond the critical Reynolds number, Re_c. However, it is not necessary that vortex shedding commences immediately after Re_c. Thus, for some cases even though the flow becomes unsteady at Re_c, vortex shedding is seen to commence for Reynolds numbers slightly higher than Re_c. To exactly pinpoint the critical Reynolds number at which vortex shedding commences would require a separate study. Therefore, in order to have a fair enough idea about Re_c for different inclinations of the elliptic cylinder, we plot the streamlines, vorticity contours and the isotherm contours for the (θ, Re) combination in figure 6.29-6.30 such that the flow for $(\theta, Re-1)$ is always steady. These figures clearly demonstrate the unsteady nature of the flow and as such $Re_c \in (Re-1, Re]$, for the Reynolds numbers considered in these figures. Interestingly, the mirror phenomena described above holds true for the critical Reynolds number as well, that is, Re_c is same for θ and $180^{\circ} - \theta$ for all $0^{\circ} \leq \theta \leq 90^{\circ}$.

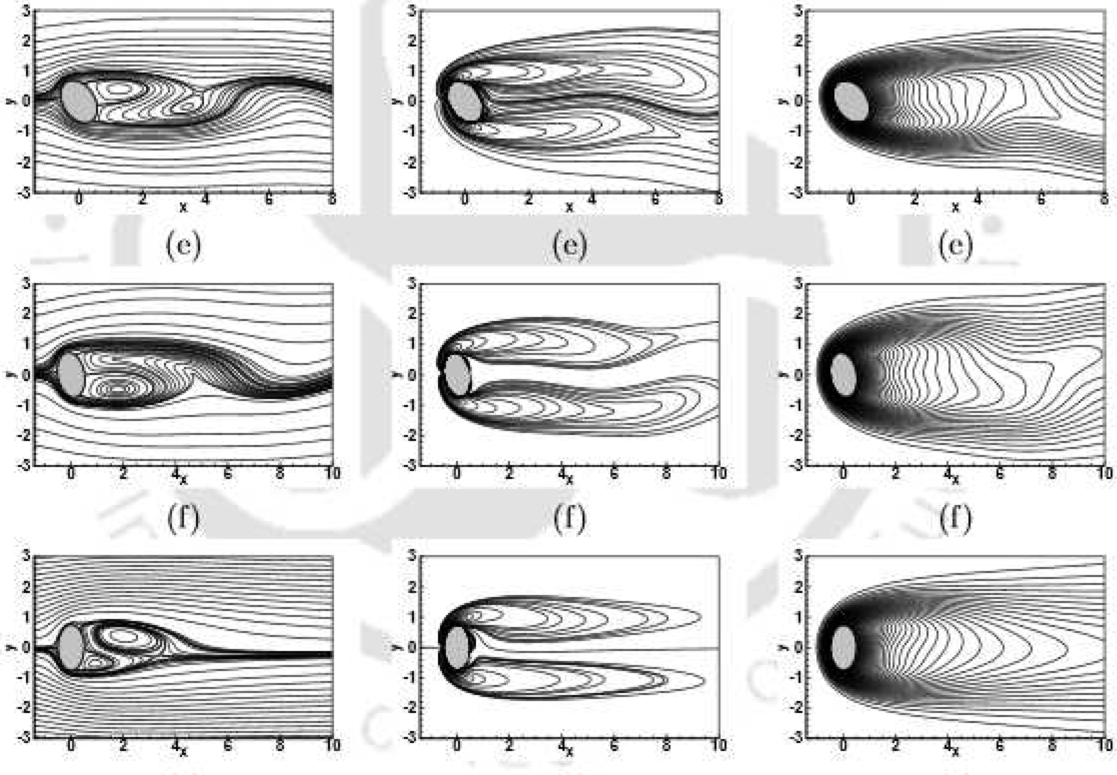

Figure 6.30: *Transition to unsteadiness, flow in the vicinity of Critical Reynolds number: Streamlines (left), vorticity (middle) and isotherms (right) for the combinations* (θ, Re), $(e) = (60^{\circ}, 32)$, $(f) = (75^{\circ}, 29)$, *and* $(g) = (90^{\circ}, 26)$, *respectively.*

6.5.2.1 Flow field and isotherms

Figure 6.31 shows the instantaneous streamlines, vorticity contours, and isotherms for $Re = 100$ and $\theta = 0^{\circ}$ at different instants of time in a complete vortex shedding cycle.

Here T represents the time period of vortex shedding, and the flow patterns are shown at equal intervals of $T/4$ within a vortex shedding cycle. We can see that the growth of the upper vortex is accompanied by the formation of a lower vortex in the flow field (figure 6.31 (a)). While the upper vortex begins to decay, the lower vortex grows and attaches itself to the trailing edge (figure 6.31 (b)). Subsequently, the upper vortex reappears around the leading edge and grows in such a way that it suppresses the lower vortex, which starts to get smaller (figure 6.31 (c), 6.31 (d)). This process is repeated for the shedding cycle.

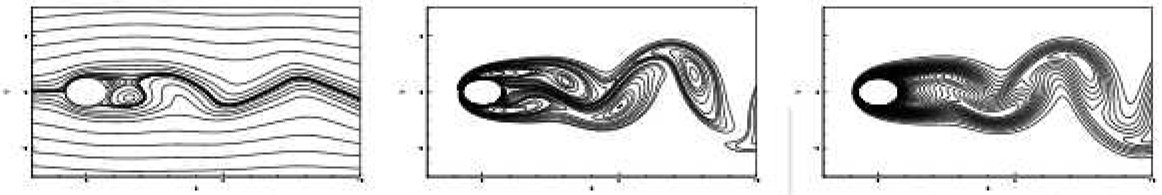

(a) $t + T/4$

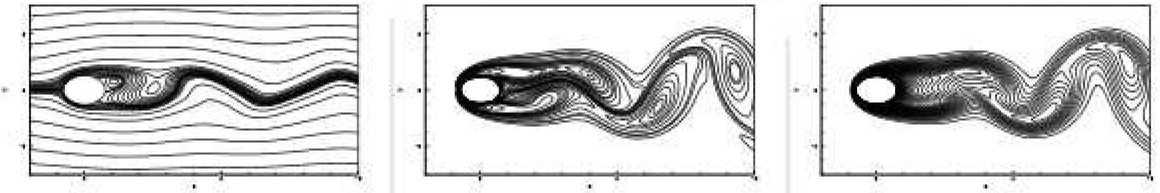

(b) $t + T/2$

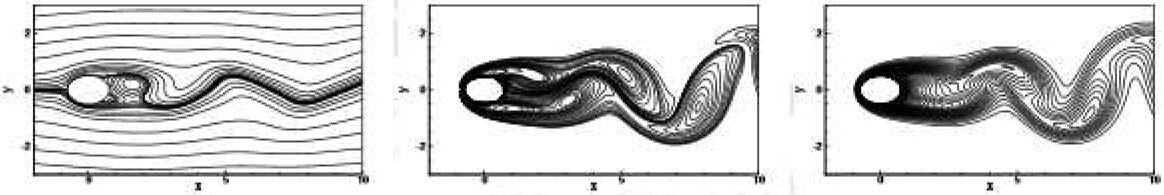

(c) $t + 3T/4$

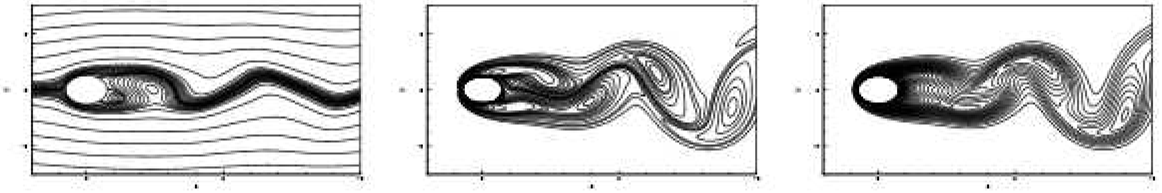

(d) $t + T$

Figure 6.31: Instantaneous streamlines (left), vorticity contours (middle) and isotherms (right) within a vortex shedding period for $Re = 100$ and $\theta = 0^{\circ}$.

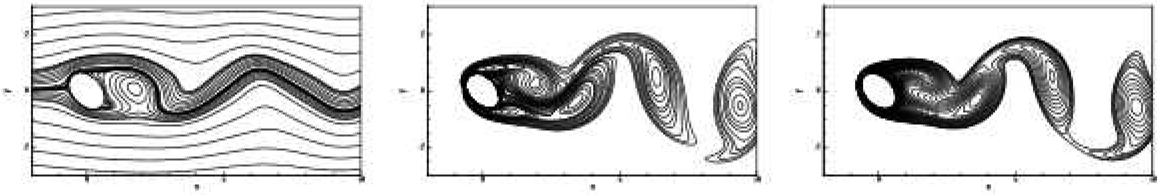

(a) $t + T/4$

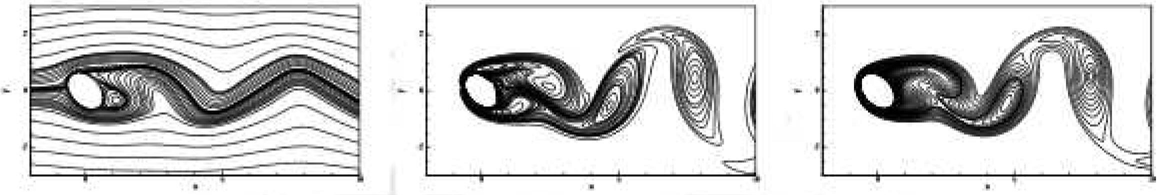

(b) $t + T/2$

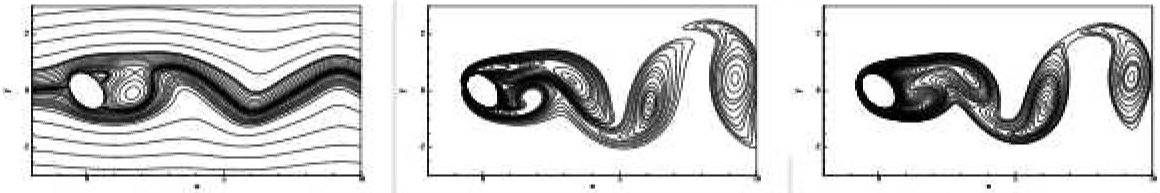

(c) $t + 3T/4$

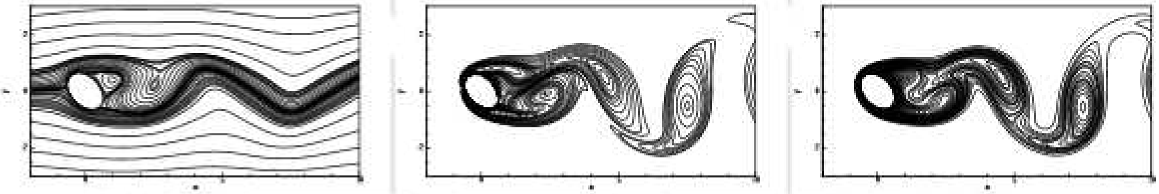

(d) $t + T$

Figure 6.32: Instantaneous streamlines (left), vorticity contours (middle) and isotherms (right) within a vortex shedding period for $Re = 100$ and $\theta = 45^{\circ}$.

Figures 6.32 and 6.33 show the instantaneous streamlines, vorticity contours and isotherms for $Re = 100$, and $\theta = 45^{\circ}$, 75° respectively. We see that as the angle of incidence is increased, the undulations in the streamlines become progressively complex. Also, vortex shedding occurs at a shorter distance from the trailing edge of the cylinder, becoming considerably wider as θ is increased.

The instantaneous isotherms also depict vortex shedding (figures 6.31 - 6.33). Figure 6.34 shows the instantaneous vorticity contours and isotherms for $Re = 100$ and $0 \leq \theta \leq 90^{\circ}$. Note that the vorticity contours are structurally similar to the corresponding isotherms, which implies that the shedding vortices carry the heat away with them from the heated cylinder. The core of the vortex contains most of the heat, and the heat gets diffused into the free stream as the vortices are convected away from the cylinder. One can observe that the hot fluid is captured in the core of the shed vortices, as can be seen from the existence of local maxima of the contour values at the vortex centers. Also, one can see the heat being diffused into the free stream in the far wake. One of the other ways to demonstrate the diffusion of heat into the free stream is to carry out a FFT of the transverse component of velocity and temperature at different locations downstream of the cylinder. Figure 6.35 shows the FFT of the y-velocity v at six different locations viz. $x = 10$, $x = 20$, $x = 30$, $x = 40$, $x = 50$, and $x = 60$ for $Re = 100$ and $\theta = 15^{\circ}$. The primary frequency f_P is the vortex shedding frequency. One can observe that the value of f_P remains same in all the locations. However the amplitude decreases as one moves from $x = 10$ to $x = 60$. This shows the diffusion of energy downstream of the cylinder.

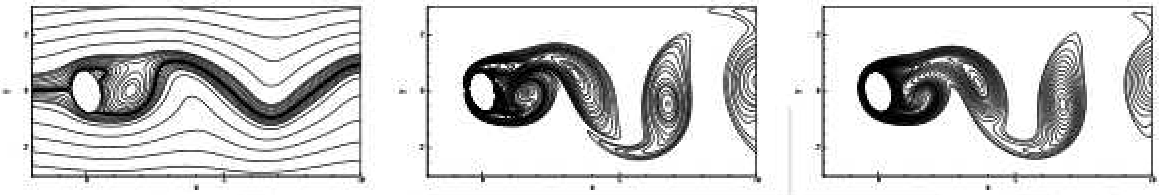

(a) $t + T/4$

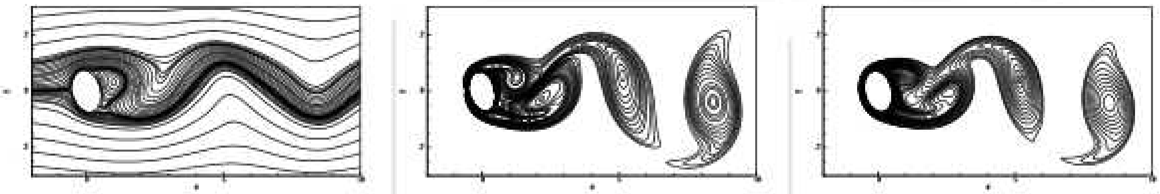

(b) $t + T/2$

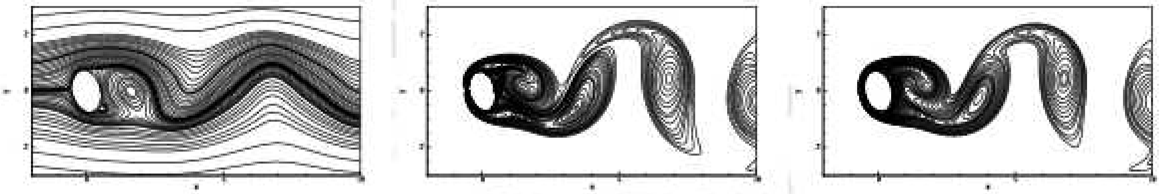

(c) $t + 3T/4$

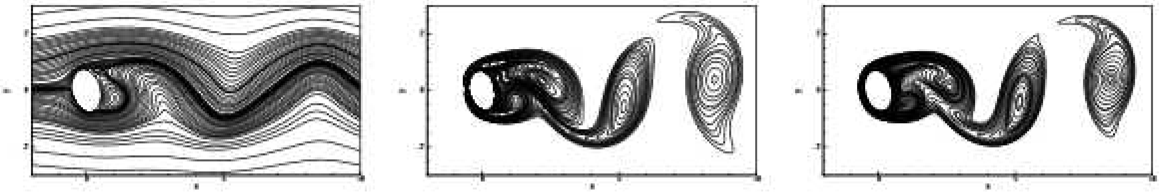

(d) $t + T$

Figure 6.33: Instantaneous streamlines (left), vorticity contours (middle) and isotherms (right) within a vortex shedding period for $Re = 100$ and $\theta = 75^{\circ}$.

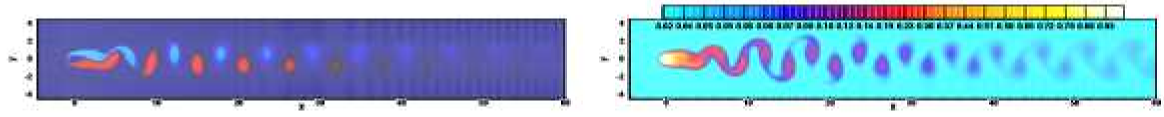

(a) $\theta = 0^\circ$

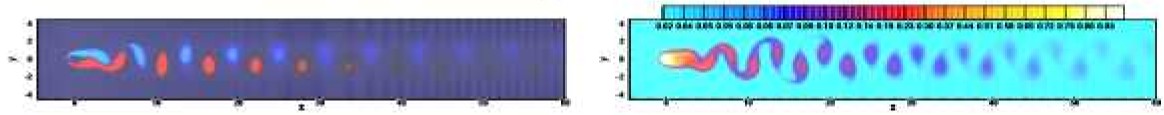

(b) $\theta = 15^\circ$

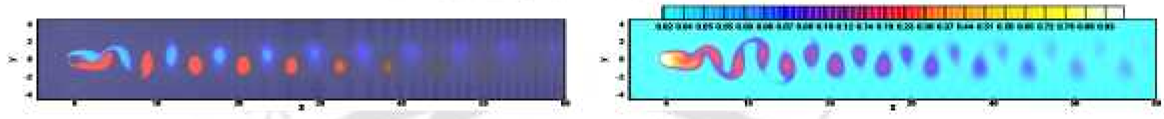

(c) $\theta = 30^\circ$

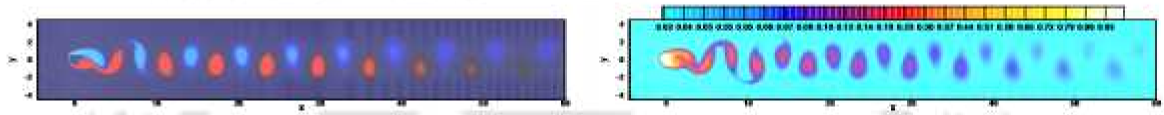

(d) $\theta = 45^\circ$

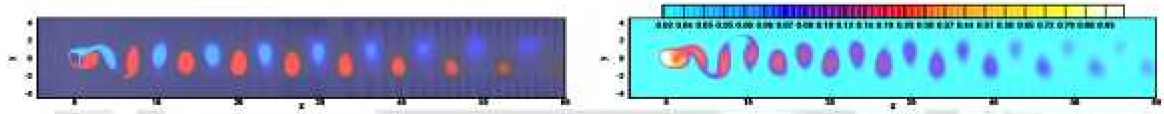

(e) $\theta = 60^\circ$

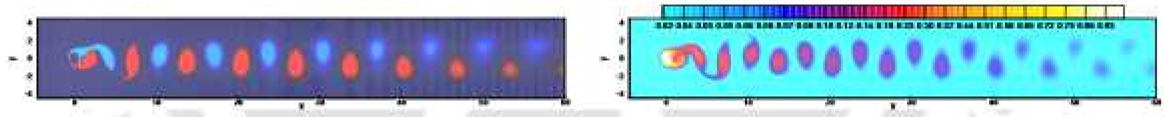

(f) $\theta = 75^\circ$

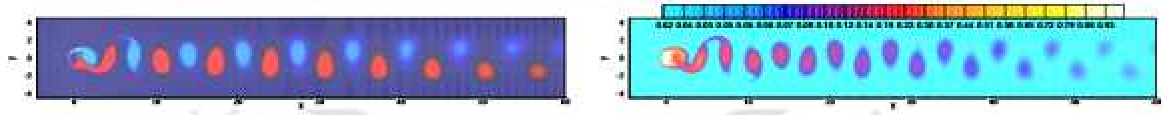

(g) $\theta = 90^\circ$

Figure 6.34: Instantaneous vorticity contours (left) and isotherms (right) for $Re = 100$ and (a) $\theta = 0^\circ$, (b) $\theta = 15^\circ$, (c) $\theta = 30^\circ$, (d) $\theta = 45^\circ$, (e) $\theta = 60^\circ$, (f) $\theta = 75^\circ$, and (g) $\theta = 90^\circ$.

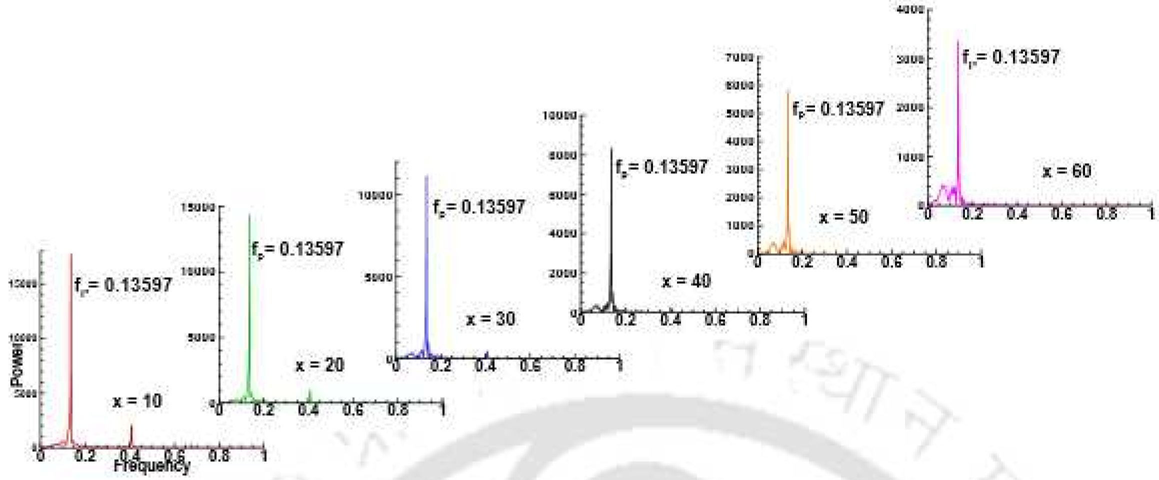

Figure 6.35: Power spectra of the time history of v-velocity at six spatial locations.

Another interesting characteristic of the flow field is that the vortices shed from the cylinder are not of equal and opposite strength (and size) as the angle of incidence is increased. At $\theta = 0^{\circ}$ (figure 6.34 (a)), counter-rotating vortices of equal and opposite strengths are shed from the cylinder. As θ increases, the upper vortex is stronger and more dominant than the lower vortex. For $0^{\circ} < \theta \leq 45^{\circ}$ (figures 6.34 (a)-(d)) the lower vortex is not strong enough to overcome the suppression induced by the upper one. Thus, the growth of the lower vortex is suppressed by the upper vortex, which pushes the lower one to move slightly downstream of the flow. For $\theta \geq 60^{\circ}$ (figures 6.34 (e)-(f)), the lower vortex gradually gains enough strength to balance the upper vortex, until at $\theta = 90^{\circ}$ (figure 6.34 (g)) when the lower vortex balances the upper one completely, and vortices of equal sizes are shed from the cylinder.

6.5.2.2 Drag and Lift coefficients

The drag and lift coefficients, C_D and C_L, are calculated from equation (4.56). Figure 6.36 shows the time history of C_D, C_L for $Re = 100$ and $0^{\circ} \leq \theta \leq 90^{\circ}$. Since the flow field is oscillatory in nature at this value of Re, the force coefficients also exhibit an oscillatory behaviour. C_D and C_L can written as $C_D = \overline{C_D} + C'_D(t)$, $C_L = \overline{C_L} + C'_L(t)$, where $\overline{C_D}$ and $\overline{C_L}$ are mean values that remain constant with time, and $C'_D(t)$, $C'_L(t)$ are the fluctuating components. It can be observed from figures 6.36 (a), 6.36 (b) that the drag force first decreases as θ changes from 0° to 15°. Note that a magnified view of C_D is provided in the inset of figure 6.36 (a) for clarity. The value of C_D then increases for $\theta = 15^{\circ} - 45^{\circ}$ (figures 6.36 (b) - 6.36 (d)). It again drops as θ is increased to 60°, after which it increases till $\theta = 90^{\circ}$. The value of C_L is positive only for $\theta = 0^{\circ}$, 45°. For the rest of the values of θ, we witness negative lift values.

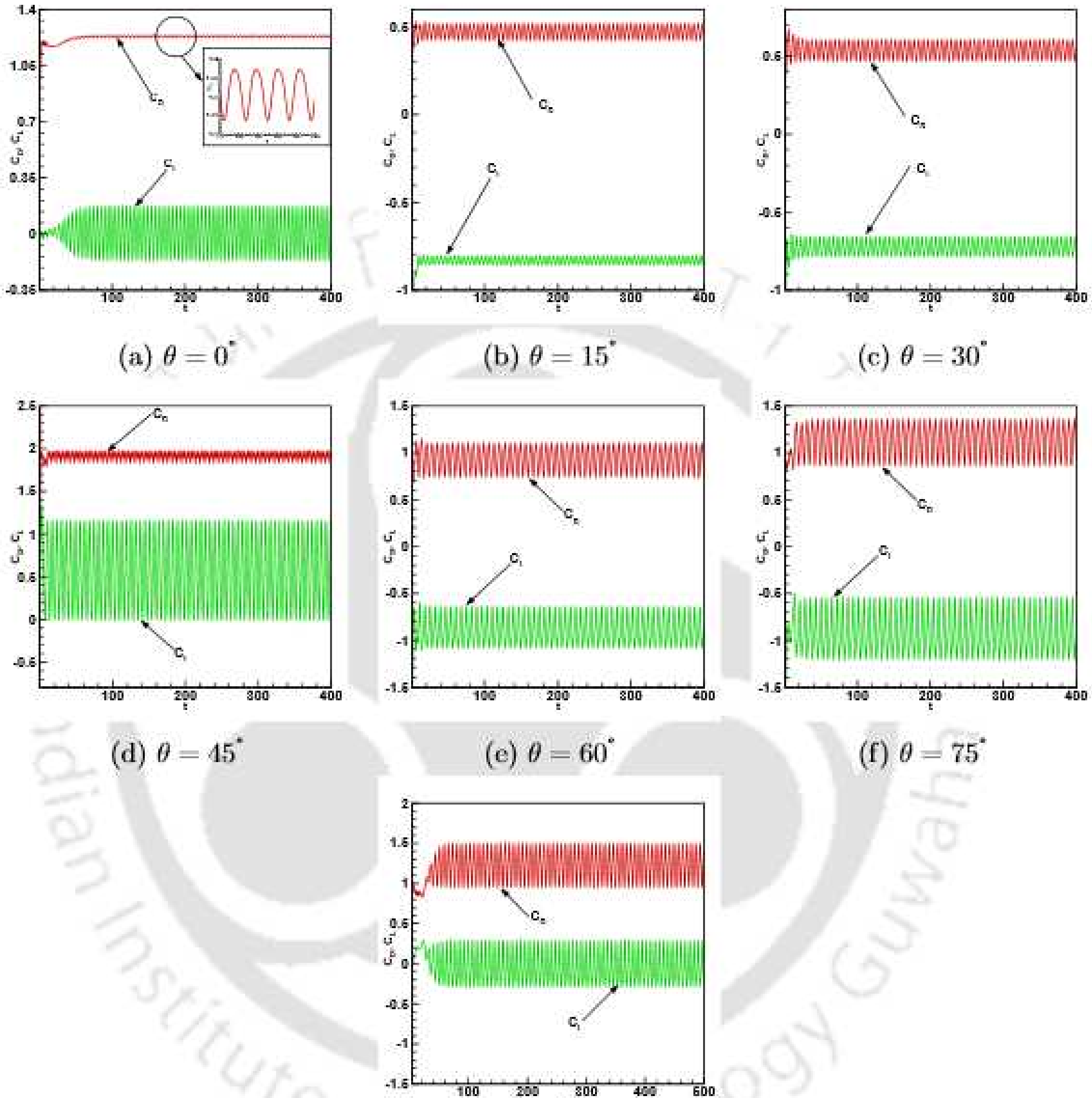

(a) $\theta = 0^{\circ}$ (b) $\theta = 15^{\circ}$ (c) $\theta = 30^{\circ}$

(d) $\theta = 45^{\circ}$ (e) $\theta = 60^{\circ}$ (f) $\theta = 75^{\circ}$

(g) $\theta = 90^{\circ}$

Figure 6.36: Time variation of C_D and C_L for $Re = 100$ and (a) $\theta = 0^{\circ}$, (b) $\theta = 15^{\circ}$, (c) $\theta = 30^{\circ}$, (d) $\theta = 45^{\circ}$, (e) $\theta = 60^{\circ}$, (f) $\theta = 75^{\circ}$, (g) $\theta = 90^{\circ}$.

6.5.2.3 Strouhal Number

The Strouhal number (St) is a measure of the vortex shedding phenomenon, which is defined as

$$St = \frac{fa}{U_0} \tag{6.19}$$

where f is the vortex shedding frequency which is determined as the peak frequency derived from the FFT of the time history of C_L. Note that the FFT is taken after discarding an initial period of at least 300 non-dimensional time units. U_0 is the free stream velocity, and a is the semi-major axis of the ellipse. Figure 6.37 shows the variation of St with θ for two values of Re. We can see that the frequency of vortex shedding decreases as θ is increased. Also, for a particular value of θ, the vortex shedding frequency increases with Re.

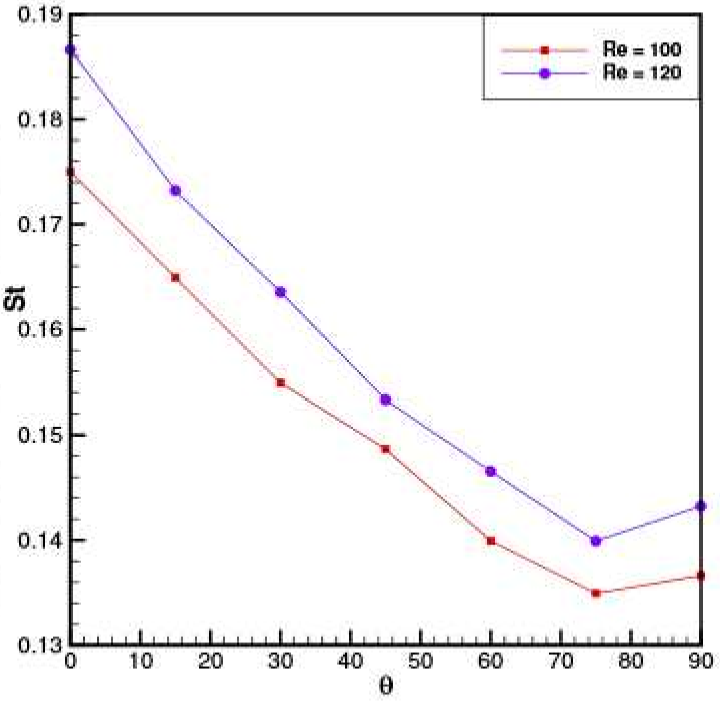

Figure 6.37: variation of the Stouhal number St against the angle of inclination θ for $Re = 100$ and 120.

6.5.2.4 Nusselt number

The surface averaged Nusselt number Nu_{av} is calculated from the equation given by (6.18). Figure 6.38 shows the time history of Nu_{av} for $Re = 100$ and $0^{\circ} \leq \theta \leq 90^{\circ}$. For clarity, the time history is shown only for $t = 350$ to $t = 400$. Similar to C_D and C_L, the surface averaged Nusselt number also exhibits a periodic behaviour w.r.t. time. In figure 6.38 (a) - (g), we have shown the time period T_{Nu} for each of the angles of incidence considered. It is clear that as θ increases, T_{Nu} also increases. Note that this periodicity in the variation of Nu_{av} commences concurrent to vortex shedding, since the vortex shedding phenomena is invariably linked to the heat being convected away from the cylinder. One can also observe a curious co-relation between the vortex shedding phenomena and variation of Nu_{av}. Consider the two angles of incidence viz. $\theta = 0^{\circ}$ and $\theta = 90^{\circ}$. The Strouhal number for these two configurations are 0.175008 and 0.136621 respectively. Now, from figure 6.38 (a) and 6.38 (g), we see that T_{Nu} for $\theta = 0^{\circ}$ and $\theta = 90^{\circ}$ are 2.857 and 3.7049 respectively. Thus, the frequency of oscillation of Nu_{av}, ($f_{\text{Nu}} = 1/T_{\text{Nu}}$) are 0.35001 and 0.269912 respectively. Thus we see that $f_{\text{Nu}} \approx 2\,St$. This relationship is true for all values of θ and all values of Re. As mentioned previously, the isotherms and vorticity contours are struturally similar owing to the fact that the shed vortices convect the heat from the cylinder downstream. Vorticity values alternate between positive and negative, whereas the temperature always remains positive. Thus, it can be expected that the frequency of isotherms being shed would be twice the vortex shedding frequency. The above exercise simply demonstrates this.

The time-varying average Nusselt number can be written as the sum of a mean value $\overline{Nu_{\text{av}}}$ and a fluctuating component Nu'_{av}, i.e., $Nu_{\text{av}} = \overline{Nu_{\text{av}}} + Nu'_{\text{av}}$. The value of Nu'_{av} is nothing but the amplitude of Nu_{av} w.r.t the $\overline{Nu_{\text{av}}}$ value. Table 6.7 shows the breakup of Nu_{av} for $Re = 100$ at different values of θ. We see that for $\theta > 0^{\circ}$ there is an increase in the value of $\overline{Nu_{\text{av}}}$ with θ. At $\theta = 0^{\circ}$, value of the fluctuating component Nu'_{av} is the lowest. It increases gradually with an increase in the angle of incidence. Thus, in general the value of Nu_{av} increases with θ. Also, the amplitude of oscillation increases as θ increases.

Table 6.7: Surface averaged Nusselt number for different values of θ at $Re = 100$.

θ	$Nu_{\text{av}} = \overline{Nu_{\text{av}}} + Nu'_{\text{av}}$
0°	4.709005 ± 0.000965
15°	4.232925 ± 0.002285
30°	4.553334 ± 0.002459
45°	4.625938 ± 0.008026
60°	4.813349 ± 0.012608
75°	4.807956 ± 0.025163
90°	4.892274 ± 0.025311

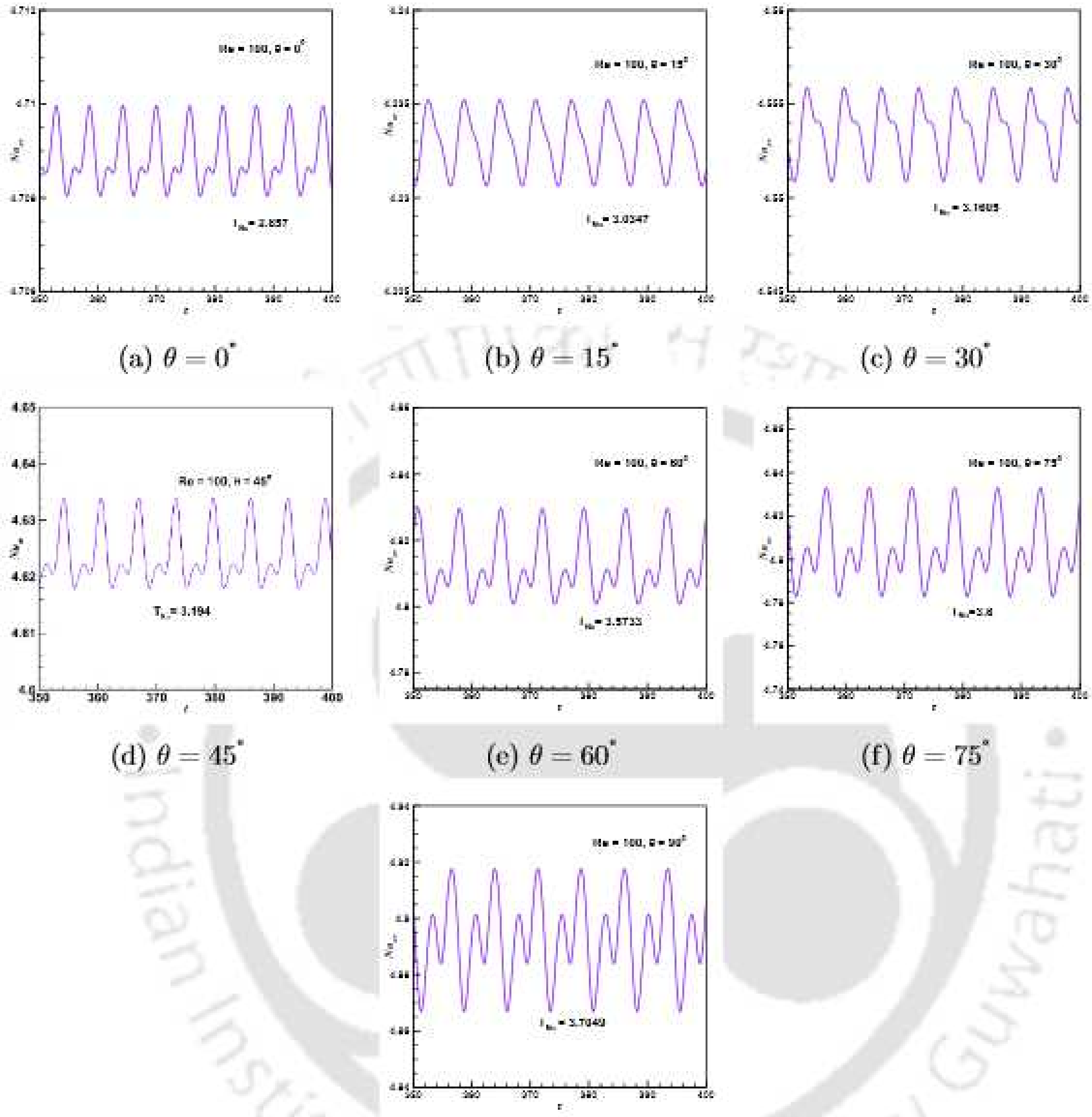

(a) $\theta = 0^{*}$ (b) $\theta = 15^{*}$ (c) $\theta = 30^{*}$

(d) $\theta = 45^{*}$ (e) $\theta = 60^{*}$ (f) $\theta = 75^{*}$

(g) $\theta = 90^{*}$

Figure 6.38: Time variation of surface averaged Nusselt number (Nu_{av}) for $Re = 100$ and (a) $\theta = 0^{*}$, (b) $\theta = 15^{*}$, (c) $\theta = 30^{*}$, (d) $\theta = 45^{*}$, (e) $\theta = 60^{*}$, (f) $\theta = 75^{*}$, (g) $\theta = 90^{*}$.

6.6 Conclusions

In this chapter, we have made a comprehensive investigation of the phenomena of forced convection heat transfer over a heated elliptical cylinder inclined to a uniform free stream of incompressible viscous flows. The Immersed Interface Method developed in chapter 4 has been employed to simulate the flow in conjuction with the strategy of using nonuniform grid of chapter 5. Numerical simulations were carried out for the range of Reynolds number $10 \leq Re \leq 120$, inclination angle $0^{\circ} \leq \theta \leq 180^{\circ}$, with air as the working fluid ($Pr = 0.71$) and the aspect ratio is taken 2 : 3. In the process we also proposed a novel way to calculate the Nusselt number. To the best of our knowledge, no other comprehensive study exists for forced convection heat transfer over an elliptical cylinder where such wide variation of angles of inclination and Reynolds numbers are considered. Hence, code validation is carried out by simulating forced convection over a horizontal circular cylinder at low Reynolds numbers, and excellent match is obtained with well established results in the literature.

Results for both steady and unsteady regimes have been reported in terms of streamlines, vorticity contours, isotherms, drag and lift coefficients, Strouhal number, and Nusselt number. In the process, we have also proposed a novel method of estimating the Nusselt number by showing how the flow variables could be computed along the normal at a point to the ellipse boundary. The flow field for $180^{\circ} - \theta$ was found out to be a mirror image of flow for θ ($0^{\circ} \leq \theta \leq 90^{\circ}$).

For the steady regime, flow in the wake of the cylinder exhibited a symmetry about the x-axis for $\theta = 0^{\circ}, 90^{\circ}$. Thus the streamlines as well as isotherms are symmetric for these two angles of incidence. As the angle of incidence increases, flow separation and formation of recirculation bubble were found to occur at a lower value of Re. Also, the value of the critical Reynolds number Re_c decreases with θ. For $0^{\circ} < \theta < 90^{\circ}$, it was observed that the size and strength of the upper vortex was greater than the lower one. This difference in size and strength was pronounced for lower values of θ, and it was seen to decrease gradually as $\theta \to 90^{\circ}$. As θ increased further, this trend was reversed. Heat transfer phenomena was demonstrated via the local and surface averaged Nusselt number. The variation in the local Nusselt number was plotted along the surface of the cylinder, and the trends observed could be satisfactorily correlated to the flow field. The surface averaged Nusselt number was observed to increase with Re for a given θ. Further, for a particular Re, thee maximum value was seen to attain at $\theta = 0^{\circ}$. On the other hand, the drag force acting on the cylinder decreased with the increase in Re , which however, was seen to increase with θ for a given Re.

Since the unsteady laminar regime is characterized by periodic vortex shedding, results for only a single Re was demonstrated as a representative case. Streamlines, vorticity contours, and isotherms were shown for a vortex shedding cycle at different values of θ. In a shedding cycle, it was seen that the growth of the upper vortex is accompanied by the formation of a lower vortex in the flow field. While the upper vortex begins to decay, the lower vortex grows and attaches itself to the trailing edge. Subsequently, the upper vortex reappears around the leading edge and grows in such a way that it suppresses the lower vortex, which starts to get smaller. As θ increases, the undulations in the streamlines were seen to grow more complicated and vortex shedding occurring at a shorter distance from the trailing edge of the cylinder, becoming much wider as θ is increased. On account of the shed vortices carrying away the heat from the cylinder, the isotherms were also seen to depict vortex shedding as they are structurally similar. The core of the vortex contained most of the heat and it got diffused into the free stream. This diffusion process is demonstrated by the contour plots of temperature and vorticity, as well as a FFT of the y- component of the velocity at different locations in the domain. A plot of the Strouhal number showed that vortex shedding frequency increases with Re, and decreases with θ for a given Re. The surface averaged Nusselt number showed a periodic variation with time, its time period being half the time period of vortex shedding. The mean value of Nu_{av} as well as the amplitude of oscillations were also observed to increase with θ.

7

CONCLUSION

7.1 Observations and remarks

This dissertation is concerned with the development of several HOC numerical formulations in order to solve immersed interface problems on irregular regions in two dimensions on Cartesian grids. The proposed methods were seen to achieve higher-order accuracy, enabled by implementing a modified explicit immersed interface technique on a compact stencil in uniform and non-uniform grids. Jump corrections are incorporated in such a way that a nine point stencil is maintained throughout the computational domain. In order to evaluate their robustness, efficiency and accuracy, the schemes were applied to solve a variety of challenging physical problems, either with or without the presence of heat transfer. The computed results were compared with analytical, numerical, and experimental results, whenever available. In the following, we present a brief description of the work accomplished in this thesis, which paves the way for making some perceptive remarks on them later on.

- We proposed a Hybrid Explicit Jump Immersed Interface Method (HEJIIM) for the elliptic interface problems on uniform grids, where the jump conditions are devoid of any mixed partial derivatives of the solutions. This approach is completely distinct from that of Weigmann [179] approach. For the validation of our approach, we tested it on seven different test cases, some of which possess analytical solutions. Such problems are selected in such a way that the discontinuities in the coefficients, the force function, or the add Dirac delta function vary in conjunction with the problems. The interfaces are chosen from a wide variety of shapes that include both the circular and the five, nine, and twelve-petal stars. In each of the test cases, not only a higher order of accuracy was achieved, but the magnitude of the error also reduced significantly in comparison to the results from other previously known methods.

- Next, we simulated some incompressible viscous fluid flow problems governed by the Navier-Stokes (N-S) equation by using its streamfunction-vorticity (ψ-ζ) formulation. A novel strategy is proposed for approximating the jump corrections for ζ. In this manner, flow past a circular cyclinder as well as flow past two inclined ellipses at different angles of incidence in a uniform flow are simulated. Moreover, we modelled and replicated Taneda's experimental visualizations [174] which accounted for both uniform and the shear layer flow in the Stokes' slow regime of Reynolds numbers. Every aspect of the flow phenomenon has been properly captured, and there are excellent matches between the experimental results and the numerical ones in each instance.

- We then expanded HEJIIM to solve problems involving transient incompressible viscous flows on uniform grids. A new approach has been derived for the jump conditions at the irregular nodes across the interface with the use of Lagrangian interpolation on a Cartesian grid. A detailed description of the computation procedures for drag and lift coefficients in multiple connected domains is also provided. The matrix equations that follow from discretizing the ψ and ζ equations have also been presented in a compact and straightforward form. To determine the spatial rate of convergence of the proposed methodology, first solve a parabolic problem with a known analytical solution. In comparison to other approaches, our method was observed to reduce error magnitude with a substantially faster $O(h^4)$ decay rate, establishing the theoretical rate of convergence in the procedure. After that, it was used to simulate a wide range of complex fluid flow problems past bluff bodies with real-world applications, including flows with multiple and moving bodies. This includes flows past a stationary circular and a twenty-four edge cactus cylinder, as well as flows past two tandem cylinders. In one case, both are fixed; in another situation, one is fixed and the second is transversely oscillating in the flow. To the best of our knowledge, the flow around a cactus cylinder with 24 spikes is analyzed for the first time using a FD setup of the streamfunction vorticity formulation.

- Also in a significant development, we proposed a discrete level set immersed interface method for solving transient incompressible viscous flows on a non-uniform grid to investigate flow involving irregular geometries. This endeavour is specifically designed to serve the situations, when there is no level set function to describe the geometry of the bluff body. An improvement in both the mesh distribution and the computation time in comparison with the uniform one was observed. Computations were carried out for higher Reynolds number flows as well, up to the point where the flow does not become turbulent and continue to maintain its two-dimensionality. In addition, the independence of the computed drag and lift coefficients in terms of the size the control volume was also established. Simulations were performed for flow around a circular cylinder, a cactus-shaped cylinder with eight, sixteen, and twenty-four spikes, the NACA 0012 airfoil, and swimming fish. All of the computed results showed good agreement with both the numerical and experimental results, whenever available.

- Lastly, the immersed interface method developed on nonuniform grid was applied to investigate the heat and fluid flow characteristics of a heated inclined elliptical cylinder with an aspect ratio $2:3$ placed in a uniform free stream. A new approach has been conceived in order to directly compute the Nusselt number using flow data in the normal direction of the ellipse boundary. The flow and heat transfer properties have been closely examined for a wide range of Re and the angle of attack θ, where Re is varied in increments of 10 in the range $10 \leq Re \leq 130$, and θ is varied in increments of 15° in the range $0^{\circ} \leq \theta < 180^{\circ}$. Following are the highlights of our steady and transient state results:

  - **Steady State** - The flow that was left behind by the cylinder showed a symmetric pattern about the x-axis for $\theta = 0^{\circ}$ and 90°. Hence, both the streamlines and the isotherms are symmetrical at these two different angles of incidence. The flow field for θ $(90^0 < \theta < 180^0)$ is a mirror reflection of flow for $180^0 - \theta$ $(0^0 \leq \theta \leq 90^0)$. Flow separation and the development of recirculation bubbles both occur at a lower value of Re when the angle of incidence becomes increasingly acute. Moreover, the value of the critical Reynolds number Re_c gradually decreases when θ increases. The value of Re_c is the same for both θ and $180-\theta$. It was determined that when $0^{\circ} < \theta < 90^{\circ}$, the top vortex had a larger size and stronger force than the lower one did. This disparity in size and strength was most noticeable for smaller values of θ, and it eventually decreased as $\theta \to 90^{\circ}$ was approached. An increase in Re at a given value of θ results in a rise in the surface-averaged Nusselt number (Nu_{av}). The drag force exerted on the cylinder reduces when Re increases. On the other hand, it increases with θ for given Re.

- **Transient State** - The isotherms exhibit vortex shedding since the shed vortices release heat from the cylinder due to their structural similarity. The majority of the heat is concentrated in the vortex's core, where it is dispersed into the free stream. For a given value of Re, the Strouhal number demonstrated that the frequency of vortex shedding increases with increasing Re and decreases with increasing θ. The Nu_{av} observed a periodic fluctuation over time with a half-time period compared to the vortex shedding time period. The amplitude of oscillations and the mean value of Nu_{av} both increased with θ.

As can be seen from the discussions above, all the goals that were outlined at the beginning of this thesis have been successfully accomplished. Along with that, it has also opened up a plethora of other fascinating study opportunities, some of which are summarised in the next section.

7.2 Future work

1. All the schemes proposed in the dissertation were developed on a finite difference framework. However, with some modifications, it might be possible to expand it for the use in the finite volume set-up that work on a similar principle. This would definitely enhance the scope of implementation of such methodologies.

2. Although the transient schemes proposed in this work has been applied on problems involving only laminar flows, its potential to implement on the simulation of turbulent flows through direct numerical simulation has not been explored. It would be interesting to see how these approaches would handle problems involving turbulent flows and also compressible ones.

3. A thorough analysis of shear layer stability and flow instability for different bluff bodies in transition is another area worth exploring.

4. Extension of the HEJIIM to multiphase flow problems and in three dimensions on non-uniform grids could be another important and interesting area of research. Moreover, the proposed schemes have not been implemented to its full potential in tackling problems involving deformed interfaces. This could be another area worth pursuing.

5. It would also be interesting to explore how clubbing of the biharmonic form of the Navier-Stokes equations (both in two and three dimensions), and the EJIIM performs on problems involving irregular interfaces.

A

Procedures for calculating dynamic forces

We have $\vec{x} = x\hat{i} + y\hat{j}$, $\tilde{\mathbf{V}} = u\hat{i} + v\hat{j}$ and $\vec{u_s} = u_s\hat{i} + v_s\hat{j}$. Note that $\vec{\omega} = \zeta\hat{k}$ here so that

$$\{\vec{\omega}(\vec{x} \times \tilde{\mathbf{V}})\}.\hat{n}ds = (\vec{x} \times \tilde{\mathbf{V}})\{\zeta\hat{k}.dy\hat{i} - dx\hat{j}\} = \vec{0}. \tag{A1}$$

Also,

$$\frac{d}{dt}\int_{V(t)} \tilde{\mathbf{V}} dV = \int_{V(t)} \frac{\partial \tilde{\mathbf{V}}}{\partial t} dV + \oint_{S(t)} \hat{n}.\vec{u_s}\tilde{\mathbf{V}}\, ds + \oint_{S_b(t)} \hat{n}.\vec{u_s}\tilde{\mathbf{V}}\, ds. \tag{A2}$$

If the surface is fixed, the surface integral over S reduces to zero. Likewise, for a fixed volume, viz., when $V(t)$ is independent of time, the surface integral over $S_b(t)$ vanishes. A sufficient (although the necessary) condition for this surface integral to vanish is for $\vec{u_s}.\hat{n}$ to be equal to zero. With all these assumptions, (4.52) reduces to

$$\vec{F} = -\frac{d}{dt}\int_{V(t)} \tilde{\mathbf{V}} dV + \oint_{S(t)} \hat{n}.\gamma_{mom}\, ds. \tag{A3}$$

for control volume enclosing solid bodies as the last term in (4.52) vanishes for such bodies, under these assumptions.

$$\gamma_{mom} = \frac{\rho}{2}|\tilde{\mathbf{V}}|^2\mathbf{I} + \rho\left[(\vec{u_s} - \tilde{\mathbf{V}})\tilde{\mathbf{V}} - \tilde{\mathbf{V}}(\vec{x} \times \vec{\omega})\right] - \rho\left[\left(\vec{x}.\frac{\partial \tilde{\mathbf{V}}}{\partial t}\mathbf{I} - \vec{x}\frac{\partial \tilde{\mathbf{V}}}{\partial t}\right)\right] + [\vec{x}.(\nabla.\mathbf{T})\mathbf{I} - \vec{x}(\nabla.\mathbf{T})] + \mathbf{T}. \tag{A4}$$

We will evaluate the second term on the RHS of (A3) using each of terms on the RHS of (A4) (for the cases considered in our study).

$$\frac{1}{2}|\tilde{\mathbf{V}}|^2\mathbf{I}.\hat{n}ds = \frac{1}{2}(u^2+v^2)dy\hat{i} - \frac{1}{2}(u^2+v^2)dx\hat{j}. \tag{A5}$$

$$(\vec{u_s} - \tilde{\mathbf{V}})\tilde{\mathbf{V}}.\hat{n}ds = \{(u_s-u)(udy-vdx)\hat{i} + (v_s-v)(udy-vdx)\hat{j}\}. \tag{A6}$$

$$-\{\tilde{\mathbf{V}}(\vec{x}\times\vec{\omega})\}.\hat{n}ds = (-udy+vdx)(y\zeta\hat{i} - x\zeta\hat{j}). \tag{A7}$$

$$\begin{aligned}\left[\left(\vec{x}.\frac{\partial\tilde{\mathbf{V}}}{\partial t}\mathbf{I} - \vec{x}\frac{\partial\tilde{\mathbf{V}}}{\partial t}\right)\right].\hat{n}ds =& (dy\hat{i} - dx\hat{j})\left(x\frac{\partial u}{\partial t} + y\frac{\partial v}{\partial t}\right) + (xdy - ydx)\left(\frac{\partial u}{\partial t}\hat{i} + \frac{\partial v}{\partial t}\hat{j}\right), \\ =& y\left(dx\frac{\partial u}{\partial t} + dy\frac{\partial v}{\partial t}\right)\hat{i} - x\left(dx\frac{\partial u}{\partial t} + dy\frac{\partial v}{\partial t}\right)\hat{j}. \end{aligned} \tag{A8}$$

Now $\vec{F} = F_D\hat{i} + F_L\hat{j}$, we get

$$\begin{aligned} F_D =& -\iint_V \left(\frac{\partial u}{\partial t} + u\frac{\partial u}{\partial x} + v\frac{\partial v}{\partial y}\right) dx\,dy \\ &+ \oint_{S(t)} \left(-v(u_s-u) + vy\zeta - y\frac{\partial v}{\partial t}\right) dx + \left(\frac{1}{2}(u^2+v^2) + u(u_s-u) - uy\zeta - y\frac{\partial v}{\partial t}\right) dy \end{aligned} \tag{A9}$$

$$\begin{aligned} F_L =& -\iint_V \left(\frac{\partial v}{\partial t} + u\frac{\partial v}{\partial x} + y\frac{\partial v}{\partial y}\right) dx\,dy \\ &+ \oint_{S(t)} \left(-\frac{1}{2}(u^2+v^2) - v(v_s-v) - vx\zeta + x\frac{\partial u}{\partial t}\right) dx + \left(u(v_s-v) + ux\zeta + x\frac{\partial u}{\partial t}\right) dy \end{aligned} \tag{A10}$$

and when the body is stationary then $u_s = 0$. Define $\nabla.\mathbf{T} = \mu(\nabla^2 u\hat{i} + \nabla^2 v\hat{j})$ and

$\mathbf{T} = \mu \left(2\frac{\partial u}{\partial x} + \frac{\partial u}{\partial y} + \frac{\partial v}{\partial x} \right) \hat{i} + \mu \left(\frac{\partial u}{\partial y} + \frac{\partial v}{\partial x} + 2\frac{\partial v}{\partial y} \right) \hat{j}$, then

$$\begin{aligned}
\oint_S \{\vec{x}.(\nabla.\mathbf{T})\mathbf{I} - \vec{x}(\nabla.\mathbf{T}) + \mathbf{T}\}\hat{n}\, ds =& \mu \oint_{S(t)} (x\hat{i} + y\hat{j}).(\nabla^2 u\hat{i} + \nabla^2 v\hat{j})(dy\hat{i} - dx\hat{j}) \\
& -\mu \oint_{S(t)} (xdy - ydx)(\nabla^2 u\hat{i} + \nabla^2 v\hat{j}) \\
& +\mu \oint_{S(t)} \left(2\frac{\partial u}{\partial x} + \frac{\partial u}{\partial y} + \frac{\partial v}{\partial x} \right) dy\hat{i} \\
& -\mu \oint_{S(t)} \left(\frac{\partial u}{\partial y} + \frac{\partial v}{\partial x} + 2\frac{\partial v}{\partial y} \right) dx\hat{j}, \qquad \text{(A11)}
\end{aligned}$$

$$\begin{aligned}
=& \mu \oint_{S(t)} \{(x\nabla^2 u + y\nabla^2 v)dy\}\hat{i} \\
& -\{(x\nabla^2 u + y\nabla^2 v)dx\}\hat{j} - (x\nabla^2 udy - y\nabla^2 udx)\hat{i} - (x\nabla^2 vdy - y\nabla^2 vdx)\hat{j} \\
& + \left(2\frac{\partial u}{\partial x} + \frac{\partial u}{\partial y} + \frac{\partial v}{\partial x} \right) dy\hat{i} - \left(\frac{\partial u}{\partial y} + \frac{\partial v}{\partial x} + 2\frac{\partial v}{\partial y} \right) dx\hat{j}, \qquad \text{(A12)} \\
=& \mu \oint_{S(t)} \left\{ y\nabla^2 udx + \left(y\nabla^2 v + 2\frac{\partial u}{\partial x} + \frac{\partial u}{\partial y} + \frac{\partial v}{\partial x} \right) dy \right\} \hat{i} \\
& - \left\{ x\nabla^2 vdy + \left(x\nabla^2 u + \frac{\partial u}{\partial y} + \frac{\partial v}{\partial x} + 2\frac{\partial v}{\partial y} \right) dx \right\} \hat{j}. \qquad \text{(A13)}
\end{aligned}$$

Bibliography

[1] *Lis: Library of iterative solvers for linear systems*, http://www.ssisc.org/lis/.

[2] L. Adams and Z. Li, *The immersed interface/multigrid methods for interface problems*, SIAM Journal on Scientific Computing, 24 (2002), pp. 463–479.

[3] F. Afroz and M. A. Sharif, *Numerical study of cross-flow around a circular cylinder with differently shaped span-wise surface grooves at low reynolds number*, European Journal of Mechanics-B/Fluids, 91 (2022), pp. 203–218.

[4] C. R. Anderson and M. B. Reider, *A high order explicit method for the computation of flow about a circular cylinder*, Journal of Computational physics, 125 (1996), pp. 207–224.

[5] C. Apelt and M. Ledwich, *Heat transfer in transient and unsteady flows past a heated circular cylinder in the range* $1 \leq R \leq 40$, Journal of Fluid Mechanics, 95 (1979), pp. 761–777.

[6] C. Attanayake and D. Senaratne, *Convergence of an immersed finite element method for semilinear parabolic interface problems*, Appl. Math. Sci.(Ruse), 5 (2011), pp. 135–147.

[7] P. Babu and K. Mahesh, *Aerodynamic loads on cactus-shaped cylinders at low reynolds numbers*, Physics of Fluids, 20 (2008), p. 035112.

[8] H. Bai and M. M. Alam, *Dependence of square cylinder wake on Reynolds number*, Physics of Fluids, 30 (2018), p. 015102.

[9] S. Bailoor, J.-H. Seo, and R. Mittal, *Vortex shedding from a circular cylinder in shear-thinning carreau fluids*, Physics of Fluids, 31 (2019), p. 011703.

[10] R. I. Balam and M. U. Zapata, *A fourth-order compact implicit immersed interface method for 2d poisson interface problems*, Computers & Mathematics with Applications, 119 (2022), pp. 257–277.

[11] S. Behara, V. Chandra, and B. Ravikanth, *Flow-induced oscillations of three tandem circular cylinders in a two-dimensional flow*, Journal of Fluids and Structures, 91 (2019), p. 102711.

[12] P. A. Berthelsen, *A decomposed immersed interface method for variable coefficient elliptic equations with non-smooth and discontinuous solutions*, Journal of Computational Physics, 197 (2004), pp. 364–386.

[13] P. A. Berthelsen and O. M. Faltinsen, *A local directional ghost cell approach for incompressible viscous flow problems with irregular boundaries*, Journal of computational physics, 227 (2008), pp. 4354–4397.

[14] R. P. Bharti, R. Chhabra, and V. Eswaran, *A numerical study of the steady forced convection heat transfer from an unconfined circular cylinder*, Heat and mass transfer, 43 (2007), pp. 639–648.

[15] A. P. S. Bhinder, S. Sarkar, and A. Dalal, *Flow over and forced convection heat transfer around a semi-circular cylinder at incidence*, International Journal of Heat and Mass Transfer, 55 (2012), pp. 5171–5184.

[16] G. Biswas and S. Sarkar, *Effect of thermal buoyancy on vortex shedding past a circular cylinder in cross-flow at low reynolds numbers*, International Journal of Heat and Mass Transfer, 52 (2009), pp. 1897–1912.

[17] S. Biswas and J. C. Kalita, *Moffatt eddies in the driven cavity: a quantification study by an hoc approach*, Computers & Mathematics with Applications, 76 (2018), pp. 471–487.

[18] R. Bouard and M. Coutanceau, *The early stage of development of the wake behind an impulsively started cylinder for $40 <$ re< 104*, Journal of Fluid Mechanics, 101 (1980), pp. 583–607.

[19] F. Bouchon and G. H. Peichl, *The immersed interface technique for parabolic problems with mixed boundary conditions*, SIAM journal on numerical analysis, 48 (2010), pp. 2247–2266.

[20] D. Calhoun, *A cartesian grid method for solving the two-dimensional streamfunction-vorticity equations in irregular regions*, Journal of computational physics, 176 (2002), pp. 231–275.

[21] D. A. Calhoun, *A Cartesian grid method for solving the streamfunction-vorticity equations in irregular geometries*, University of Washington, 1999.

[22] F. Cao, Y. Ge, and H.-W. Sun, *Partial semi-coarsening multigrid method based on the hoc scheme on nonuniform grids for the convection–diffusion problems*, International Journal of Computer Mathematics, 94 (2017), pp. 2356–2372.

[23] S.-L. Cao, X. Sun, J.-Z. Zhang, and Y.-X. Zhang, *Forced convection heat transfer around a circular cylinder in laminar flow: An insight from Lagrangian coherent structures*, Physics of Fluids, 33 (2021), p. 067104.

[24] S. Chamoli, T. Tang, P. Yu, and R. Lu, *Effect of shape modification on heat transfer and drag for fluid flow past a cam-shaped cylinder*, International Journal of Heat and Mass Transfer, 131 (2019), pp. 1147–1163.

[25] A. Chandra and R. Chhabra, *Flow over and forced convection heat transfer in Newtonian fluids from a semi-circular cylinder*, International Journal of Heat and Mass Transfer, 54 (2011), pp. 225–241.

[26] D. Chatterjee, B. Mondal, and P. Halder, *Unsteady forced convection heat transfer over a semicircular cylinder at low Reynolds numbers*, Numerical Heat Transfer, Part A: Applications, 63 (2013), pp. 411–429.

[27] Z. Chen, C. Shu, L. Yang, X. Zhao, and N. Liu, *Immersed boundary–simplified thermal lattice boltzmann method for incompressible thermal flows*, Physics of Fluids, 32 (2020), p. 013605.

[28] Z. Chen and J. Zou, *Finite element methods and their convergence for elliptic and parabolic interface problems*, Numerische Mathematik, 79 (1998), pp. 175–202.

[29] I.-L. Chern and Y.-C. Shu, *A coupling interface method for elliptic interface problems*, Journal of Computational Physics, 225 (2007), pp. 2138–2174.

[30] C. Chi, A. Abdelsamie, and D. Thévenin, *A directional ghost-cell immersed boundary method for incompressible flows*, Journal of Computational Physics, 404 (2020), p. 109122.

[31] T. Chung et al., *Computational fluid dynamics*, Cambridge university press, 2002.

[32] M. Cisternino and L. Weynans, *A parallel second order cartesian method for elliptic interface problems*, Communications in Computational Physics, 12 (2012), pp. 1562–1587.

[33] M. Colnago, W. Casaca, and L. F. de Souza, *A high-order immersed interface method free of derivative jump conditions for poisson equations on irregular domains*, Journal of Computational Physics, 423 (2020), p. 109791.

[34] N. R. Council, *Twenty-First Symposium on Naval Hydrodynamics*, The National Academies Press, Washington, DC, 1997.

[35] M. Coutanceau and R. Bouard, *Experimental determination of the main features of the viscous flow in the wake of a circular cylinder in uniform translation. part 1. steady flow*, Journal of Fluid Mechanics, 79 (1977), pp. 231–256.

[36] A. M. J. Davis and M. E. O'Neill, *Separation in a slow linear shear flow past a cylinder and a plane*, Journal of Fluid Mechanics, 81 (1977), pp. 551–564.

[37] A. M. J. Davis, M. E. O'Neill, J. M. Dorrepaal, and K. B. Ranger, *Separation from the surface of two equal spheres in stokes flow*, Journal of Fluid Mechanics, 77 (1976), pp. 625–644.

[38] S. Deng, K. Ito, and Z. Li, *Three-dimensional elliptic solvers for interface problems and applications*, Journal of Computational Physics, 184 (2003), pp. 215–243.

[39] S. Dennis and G.-Z. Chang, *Numerical solutions for steady flow past a circular cylinder at reynolds numbers up to 100*, Journal of Fluid Mechanics, 42 (1970), pp. 471–489.

[40] S. Dennis and J. Hudson, *Compact h4 finite-difference approximations to operators of navier-stokes type*, Journal of Computational Physics, 85 (1989), pp. 390–416.

[41] S. Dennis and P. Young, *Steady flow past an elliptic cylinder inclined to the stream*, Journal of engineering mathematics, 47 (2003), pp. 101–120.

[42] S. C. R. Dennis, J. D. Hudson, and N. Smith, *Steady laminar forced convection from a circular cylinder at low reynolds numbers*, The Physics of Fluids, 11 (1968), pp. 933–940.

[43] A. Dhiman, R. Chhabra, and V. Eswaran, *Flow and heat transfer across a confined square cylinder in the steady flow regime: effect of Peclet number*, International Journal of Heat and Mass Transfer, 48 (2005), pp. 4598–4614.

[44] A. Dipankar, T. Sengupta, and S. Talla, *Suppression of vortex shedding behind a circular cylinder by another control cylinder at low reynolds numbers*, Journal of Fluid Mechanics, 573 (2007), pp. 171–190.

[45] M. A. DUMETT AND J. P. KEENER, *An immersed interface method for solving anisotropic elliptic boundary value problems in three dimensions*, SIAM Journal on Scientific Computing, 25 (2003), pp. 348–367.

[46] F. DUMOUCHEL, J. LECORDIER, AND P. PARANTHOÃ«N, *The effective reynolds number of a heated cylinder*, International Journal of Heat and Mass Transfer, 41 (1998), pp. 1787–1794.

[47] Z. FARUQUEE, D. S. TING, A. FARTAJ, R. M. BARRON, AND R. CARRIVEAU, *The effects of axis ratio on laminar fluid flow around an elliptical cylinder*, International Journal of Heat and Fluid Flow, 28 (2007), pp. 1178–1189.

[48] R. P. FEDKIW, T. ASLAM, B. MERRIMAN, S. OSHER, ET AL., *A non-oscillatory eulerian approach to interfaces in multimaterial flows (the ghost fluid method)*, Journal of computational physics, 152 (1999), pp. 457–492.

[49] R. P. FEDKIW AND X.-D. LIU, *The ghost fluid method for viscous flows*, in Innovative methods for numerical solution of partial differential equations, World Scientific, 2002, pp. 111–143.

[50] H. FENG, G. LONG, AND S. ZHAO, *An augmented matched interface and boundary (mib) method for solving elliptic interface problem*, Journal of Computational and Applied Mathematics, 361 (2019), pp. 426–443.

[51] ——, *Fft-based high order central difference schemes for poisson's equation with staggered boundaries*, Journal of Scientific Computing, 86 (2021), pp. 1–25.

[52] F. B. FONSECA, S. S. MANSUR, AND E. D. R. VIEIRA, *Flow around elliptical cylinders in moderate reynolds numbers*, in Proceedings of the 22nd international congress of mechanical engineering, November, 2013, pp. 3–7.

[53] B. FORNBERG, *A numerical study of steady viscous flow past a circular cylinder*, Journal of Fluid Mechanics, 98 (1980), pp. 819–855.

[54] R. FRANKE, W. RODI, AND B. SCHÖNUNG, *Numerical calculation of laminar vortex-shedding flow past cylinders*, Journal of Wind Engineering and Industrial Aerodynamics, 35 (1990), pp. 237–257.

[55] P. FREYMUTH, *The vortex patterns of dynamic separation: a parametric and comparative study*, Progress in Aerospace Sciences, 22 (1985), pp. 161–208.

[56] E. GARTLAND, JR, *Discrete weighted mean approximation of a model convection-diffusion equation*, SIAM Journal on Scientific and Statistical Computing, 3 (1982), pp. 460–472.

[57] G. GELLER AND P. NOBEL, *Cactus ribs: influence on par interception and co2 uptake*, Photosynthetica (Praha), 18 (1984), pp. 482–494.

[58] A. S. GHASEMKHEILI AND F. SABETGHADAM, *Applying the immersed boundaries to the incompressible fluid flows using inverse source problem*, Journal of the Brazilian Society of Mechanical Sciences and Engineering, 42 (2020), pp. 1–13.

[59] M. GHOMMEM, G. BOURANTAS, A. WITTEK, K. MILLER, AND M. R. HAJJ, *Hydrodynamic modeling and performance analysis of bio-inspired swimming*, Ocean Engineering, 197 (2020), p. 106897.

[60] P. M. GRESHO, *Incompressible fluid dynamics: some fundamental formulation issues*, Annual review of fluid mechanics, 23 (1991), pp. 413–453.

[61] M. M. GUPTA, *High accuracy solutions of incompressible navier-stokes equations*, Journal of Computational Physics, 93 (1991), pp. 343–359.

[62] M. M. GUPTA, R. P. MANOHAR, AND J. W. STEPHENSON, *A single cell high order scheme for the convection-diffusion equation with variable coefficients*, International Journal for Numerical Methods in Fluids, 4 (1984), pp. 641–651.

[63] ——, *High-order difference schemes for two-dimensional elliptic equations*, Numerical Methods for Partial Differential Equations, 1 (1985), pp. 71–80.

[64] C. HODGE, *All About Saguaros*, Hugh Harelson, Phoenix, 1991.

[65] J. D. HOFFMAN AND S. FRANKEL, *Numerical methods for engineers and scientists*, CRC press, 2018.

[66] N. HOSSEINI, M. GRIFFITH, AND J. LEONTINI, *The flow past large numbers of cylinders in tandem*, Journal of Fluids and Structures, 98 (2020), p. 103103.

[67] H. HUANG AND Z. LI, *Convergence analysis of the immersed interface method*, IMA Journal of Numerical Analysis, 19 (1999), pp. 583–608.

[68] Q. HUANG, Z. LIU, L. WANG, S. RAVI, J. YOUNG, J. LAI, AND F.-B. TIAN, *Streamline penetration, velocity error and consequences of the feedback immersed boundary method*, Physics of Fluids, (2022).

[69] C. JACKSON, *A finite-element study of the onset of vortex shedding in flow past variously shaped bodies*, Journal of fluid Mechanics, 182 (1987), pp. 23–45.

[70] H. JAFROUDI AND H. YANG, *Steady laminar forced convection from a circular cylinder*, Journal of Computational Physics, 65 (1986), pp. 46–56.

[71] D. JAISWAL AND J. C. KALITA, *Novel high-order compact approach for dynamics of spiral waves in excitable media*, Applied Mathematical Modelling, 77 (2020), pp. 341–359.

[72] S. A. Johnson, M. C. Thompson, and K. Hourigan, *Flow past elliptical cylinders at low reynolds numbers*, in 14th Australasian fluid mechanics conference, Elsevier Adelaide, Australia, 2001, pp. 343–346.

[73] J. C. Kalita, *Effect of boundary location on the steady flow past an impulsively started circular cylinder*, International Journal of Computing Science and Mathematics, 5 (2014), pp. 252–279.

[74] J. C. Kalita and P. Chhabra, *An improved (9, 5) higher order compact scheme for the transient two-dimensional convection–diffusion equation*, International journal for numerical methods in fluids, 51 (2006), pp. 703–717.

[75] J. C. Kalita, D. Dalal, and A. K. Dass, *Fully compact higher-order computation of steady-state natural convection in a square cavity*, Physical Review E, 64 (2001), p. 066703.

[76] ——, *A class of higher order compact schemes for the unsteady two-dimensional convection–diffusion equation with variable convection coefficients*, International Journal for Numerical Methods in Fluids, 38 (2002), pp. 1111–1131.

[77] J. C. Kalita, A. K. Dass, and D. Dalal, *A transformation-free hoc scheme for steady convection–diffusion on non-uniform grids*, International journal for numerical methods in fluids, 44 (2004), pp. 33–53.

[78] J. C. Kalita, A. K. Dass, and N. Nidhi, *An efficient transient navier–stokes solver on compact nonuniform space grids*, Journal of Computational and Applied mathematics, 214 (2008), pp. 148–162.

[79] J. C. Kalita and R. K. Ray, *A transformation-free hoc scheme for incompressible viscous flows past an impulsively started circular cylinder*, Journal of computational physics, 228 (2009), pp. 5207–5236.

[80] J. C. Kalita and S. Sen, *Unsteady separation leading to secondary and tertiary vortex dynamics: the sub–phenomena*, Journal of Fluid Mechanics, 730 (2013), pp. 19–51.

[81] ——, *α-, β-phenomena in the post-symmetry break for the flow past a circular cylinder*, Physics of Fluids, 29 (2017), p. 033603.

[82] C. T. Kelley, *Iterative methods for linear and nonlinear equations*, SIAM, 1995.

[83] M. S. U. Khalid, I. Akhtar, and H. Dong, *Hydrodynamics of a tandem fish school with asynchronous undulation of individuals*, Journal of Fluids and Structures, 66 (2016), pp. 19–35.

[84] M. S. U. Khalid, I. Akhtar, H. Imtiaz, H. Dong, and B. Wu, *On the hydrodynamics and nonlinear interaction between fish in tandem configuration*, Ocean Engineering, 157 (2018), pp. 108–120.

[85] R. N. Kieft, C. Rindt, A. Van Steenhoven, and G. Van Heijst, *On the wake structure behind a heated horizontal cylinder in cross-flow*, Journal of Fluid Mechanics, 486 (2003), pp. 189–211.

[86] S. Kim, M. M. Alam, H. Sakamoto, and Y. Zhou, *Flow-induced vibrations of two circular cylinders in tandem arrangement. part 1: Characteristics of vibration*, Journal of Wind Engineering and Industrial Aerodynamics, 97 (2009), pp. 304–311.

[87] W. J. Koning, E. A. Romander, and W. Johnson, *Low reynolds number airfoil evaluation for the mars helicopter rotor*, in Annual Forum and Technology Display, no. ARC-E-DAA-TN53889, 2018.

[88] P. Koumoutsakos and A. Leonard, *High-resolution simulations of the flow around an impulsively started cylinder using vortex methods*, Journal of Fluid Mechanics, 296 (1995), pp. 1–38.

[89] P. Kumar and J. C. Kalita, *A transformation-free ψ-v formulation of the navier–stokes equations on compact nonuniform grids*, Journal of Computational and Applied Mathematics, 353 (2019), pp. 292–317.

[90] ——, *A comprehensive study of secondary and tertiary vortex phenomena of flow past a circular cylinder: A cartesian grid approach*, Physics of Fluids, 33 (2021), p. 053608.

[91] A. Kumar De and A. Dalal, *Numerical simulation of unconfined flow past a triangular cylinder*, International Journal for Numerical Methods in Fluids, 52 (2006), pp. 801–821.

[92] ——, *Numerical Study of Laminar Forced Convection Fluid Flow and Heat Transfer From a Triangular Cylinder Placed in a Channel*, Journal of Heat Transfer, 129 (2006), pp. 646–656.

[93] C. F. Lange, F. Durst, and M. Breuer, *Momentum and heat transfer from cylinders in laminar crossflow at $10^{-4} \leq re \leq 200$*, International Journal of Heat and Mass Transfer, 41 (1998), pp. 3409–3430.

[94] B. W. Lax, *Systems of conservation laws*, Comm. Pure Appl. Math, 13 (1960), p. 217.

[95] D.-V. Le, B. C. Khoo, and J. Peraire, *An immersed interface method for viscous incompressible flows involving rigid and flexible boundaries*, Journal of Computational Physics, 220 (2006), pp. 109–138.

[96] R. J. LeVeque and Z. Li, *The immersed interface method for elliptic equations with discontinuous coefficients and singular sources*, SIAM Journal on Numerical Analysis, 31 (1994), pp. 1019–1044.

[97] C. Li and S. Zhao, *A matched peaceman–rachford adi method for solving parabolic interface problems*, Applied Mathematics and Computation, 299 (2017), pp. 28–44.

[98] Z. Li, *Immersed interface methods for moving interface problems*, Numerical algorithms, 14 (1997), pp. 269–293.

[99] ——, *A fast iterative algorithm for elliptic interface problems*, SIAM Journal on Numerical Analysis, 35 (1998), pp. 230–254.

[100] ——, *The immersed interface method using a finite element formulation*, Applied Numerical Mathematics, 27 (1998), pp. 253–267.

[101] Z. Li, X. Chen, and Z. Zhang, *On multiscale adi methods for parabolic pdes with a discontinuous coefficient*, Multiscale Modeling & Simulation, 16 (2018), pp. 1623–1647.

[102] Z. Li and K. Ito, *Maximum principle preserving schemes for interface problems with discontinuous coefficients*, SIAM Journal on Scientific Computing, 23 (2001), pp. 339–361.

[103] Z. Li, K. Ito, and M.-C. Lai, *An augmented approach for stokes equations with a discontinuous viscosity and singular forces*, Computers & Fluids, 36 (2007), pp. 622–635.

[104] Z. Li, W.-C. Wang, I.-L. Chern, and M.-C. Lai, *New formulations for interface problems in polar coordinates*, SIAM Journal on Scientific Computing, 25 (2003), pp. 224–245.

[105] H.-C. Lim and S.-J. Lee, *Flow control of circular cylinders with longitudinal grooved surfaces*, AIAA journal, 40 (2002), pp. 2027–2036.

[106] M. N. Linnick and H. F. Fasel, *A high-order immersed interface method for simulating unsteady incompressible flows on irregular domains*, Journal of Computational Physics, 204 (2005), pp. 157–192.

[107] X.-D. Liu, R. P. Fedkiw, and M. Kang, *A boundary condition capturing method for poisson's equation on irregular domains*, Journal of computational Physics, 160 (2000), pp. 151–178.

[108] Y. Z. Liu, L. L. Shi, and J. Yu, *Tr-piv measurement of the wake behind a grooved cylinder at low reynolds number*, Journal of Fluids and Structures, 27 (2011), pp. 394–407.

[109] T. P. Loc and R. Bouard, *Numerical solution of the early stage of the unsteady viscous flow around a circular cylinder: a comparison with experimental visualization and measurements*, Journal of Fluid Mechanics, 160 (1985), pp. 93–117.

[110] H. Lugt and H. Haussling, *Laminar flow past an abruptly accelerated elliptic cylinder at 45^0 incidence*, Journal of Fluid Mechanics, 65 (1974), pp. 711–734.

[111] R. J. MacKinnon and R. W. Johnson, *Differential-equation-based representation of truncation errors for accurate numerical simulation*, International Journal for Numerical Methods in Fluids, 13 (1991), pp. 739–757.

[112] A. Mayo, *The fast solution of poissonâ€™s and the biharmonic equations on irregular regions*, SIAM Journal on Numerical Analysis, 21 (1984), pp. 285–299.

[113] U. B. Mehta and Z. Lavan, *Starting vortex, separation bubbles and stall: a numerical study of laminar unsteady flow around an airfoil*, Journal of Fluid Mechanics, 67 (1975), pp. 227–256.

[114] H. Mittal, J. C. Kalita, and R. K. Ray, *A class of finite difference schemes for interface problems with an hoc approach*, International Journal for Numerical Methods in Fluids, 82 (2016), pp. 567–606.

[115] H. Mittal and R. K. Ray, *Solving immersed interface problems using a new interfacial points-based finite difference approach*, SIAM Journal on Scientific Computing, 40 (2018), pp. A1860–A1883.

[116] H. Mittal, R. K. Ray, and Q. M. Al-Mdallal, *A numerical study of initial flow past an impulsively started rotationally oscillating circular cylinder using a transformation-free hoc scheme*, Physics of Fluids, 29 (2017), p. 093603.

[117] K. Morikawa and H. Grönig, *Formation and structure of vortex systems around a translating and oscillating airfoil*, Zeitschrift für Flugwissenschaften und Weltraumforschung, 19 (1995), pp. 391–396.

[118] H. Nakamura and T. Igarashi, *Variation of Nusselt number with flow regimes behind a circular cylinder for Reynolds numbers from 70 to 30000*, International Journal of Heat and Mass Transfer, 47 (2004), pp. 5169–5173.

[119] T. Namshad, M. Shrivastava, A. Agrawal, and A. Sharma, *Effect of wavelength of fish-like undulation of a hydrofoil in a free-stream flow*, Sādhanā, 42 (2017), pp. 585–595.

[120] R. Nepali, H. Ping, Z. Han, D. Zhou, H. Yang, J. Tu, Y. Zhao, and Y. Bao, *Two-degree-of-freedom vortex-induced vibrations of two square cylinders in tandem arrangement at low reynolds numbers*, Journal of Fluids and Structures, 97 (2020), p. 102991.

[121] K. J. Niklas and S. L. Buchman, *The allometry of saguaro height*, American Journal of Botany, 81 (1994), pp. 1161–1168.

[122] F. Noca, D. Shiels, and D. Jeon, *A comparison of methods for evaluating time-dependent fluid dynamic forces on bodies, using only velocity fields and their derivatives*, Journal of Fluids and Structures, 13 (1999), pp. 551–578.

[123] B. Noye and H. Tan, *A third-order semi-implicit finite difference method for solving the one-dimensional convection-diffusion equation*, International journal for numerical methods in engineering, 26 (1988), pp. 1615–1629.

[124] K. Ohmi, M. Coutanceau, O. Daube, and T. P. Loc, *Further experiments on vortex formation around an oscillating and translating airfoil at large incidences*, Journal of Fluid Mechanics, 225 (1991), pp. 607–630.

[125] S. Osher and J. A. Sethian, *Fronts propagating with curvature-dependent speed: Algorithms based on hamilton-jacobi formulations*, Journal of computational physics, 79 (1988), pp. 12–49.

[126] J. Papac, F. Gibou, and C. Ratsch, *Efficient symmetric discretization for the poisson, heat and stefan-type problems with robin boundary conditions*, Journal of Computational Physics, 229 (2010), pp. 875–889.

[127] G. Papaioannou, D. Yue, M. Triantafyllou, and G. Karniadakis, *On the effect of spacing on the vortex-induced vibrations of two tandem cylinders*, Journal of Fluids and Structures, 24 (2008), pp. 833–854.

[128] H. Park, X. Pan, C. Lee, and J.-I. Choi, *A pre-conditioned implicit direct forcing based immersed boundary method for incompressible viscous flows*, Journal of Computational Physics, 314 (2016), pp. 774–799.

[129] J. K. Park, S. O. Park, and J. M. Hyun, *Flow regimes of unsteady laminar flow past a slender elliptic cylinder at incidence*, International Journal of Heat and Fluid Flow, 10 (1989), pp. 311–317.

[130] V. Patel, *Flow around the impulsively started elliptic cylinder at various angles of attack*, Computers & Fluids, 9 (1981), pp. 435–462.

[131] I. Paul, K. A. Prakash, and S. Vengadesan, *Onset of laminar separation and vortex shedding in flow past unconfined elliptic cylinders*, Physics of Fluids, 26 (2014), p. 023601.

[132] A. P. Pawar, S. Sarkar, and S. K. Saha, *Forced convective flow and heat transfer past an unconfined blunt headed cylinder at different angles of incidence*, Applied Mathematical Modelling, 82 (2020), pp. 888–915.

[133] C. S. Peskin, *Flow patterns around heart valves: a numerical method*, Journal of computational physics, 10 (1972), pp. 252–271.

[134] R. H. Pletcher, J. C. Tannehill, and D. Anderson, *Computational fluid mechanics and heat transfer*, CRC press, 2012.

[135] A. Poozesh and M. Mirzaei, *Flow simulation around cambered airfoil by using conformal mapping and intermediate domain in lattice boltzmann method*, Journal of Statistical Physics, 166 (2017), pp. 354–367.

[136] T. Prasanth and S. Mittal, *Vortex-induced vibration of two circular cylinders at low reynolds number*, Journal of fluids and structures, 25 (2009), pp. 731–741.

[137] L. Qian and M. Vezza, *A vorticity-based method for incompressible unsteady viscous flows*, Journal of computational physics, 172 (2001), pp. 515–542.

[138] S. RAMBERG, *The influence of yaw angle upon the vortex wakes of stationary and vibrating cylinders[ph. d. thesis]*, (1978).

[139] R. Ranjan, A. Dalal, and G. Biswas, *A numerical study of fluid flow and heat transfer around a square cylinder at incidence using unstructured grids*, Numerical Heat Transfer, Part A: Applications, 54 (2008), pp. 890–913.

[140] R. K. Ray, *A transformation-free hoc scheme for incompressible viscous flow past a rotating and translating circular cylinder*, Journal of Scientific Computing, 46 (2011), pp. 265–293.

[141] E. Relf and C. Powell, *Tests on Smooth and Stranded Wires Inclined T the Wind Direction, and a Comparison of Results on Stranded Wires in Air and Water*, HM Stationery Office, 1917.

[142] W. Ren, J. Wu, C. Shu, and W. Yang, *A stream function–vorticity formulation-based immersed boundary method and its applications*, International journal for numerical methods in fluids, 70 (2012), pp. 627–645.

[143] A. Roshko, *Perspectives on bluff body aerodynamics*, Journal of Wind Engineering and Industrial Aerodynamics, 49 (1993), pp. 79–100.

[144] D. Russell and Z. J. Wang, *A cartesian grid method for modeling multiple moving objects in 2d incompressible viscous flow*, Journal of Computational Physics, 191 (2003), pp. 177–205.

[145] A. K. Sahu, R. Chhabra, and V. Eswaran, *Effects of reynolds and prandtl numbers on heat transfer from a square cylinder in the unsteady flow regime*, International Journal of Heat and Mass Transfer, 52 (2009), pp. 839–850.

[146] S. Sarkar, A. Dalal, and G. Biswas, *Unsteady wake dynamics and heat transfer in forced and mixed convection past a circular cylinder in cross flow for high Prandtl numbers*, International Journal of Heat and Mass Transfer, 54 (2011), pp. 3536–3551.

[147] S. Sen, *Fourth order compact schemes for variable coefficient parabolic problems with mixed derivatives*, Computers & Fluids, 134 (2016), pp. 81–89.

[148] S. Sen and J. C. Kalita, *A 4oec scheme for the biharmonic steady navier–stokes equations in non-rectangular domains*, Computer Physics Communications, 196 (2015), pp. 113–133.

[149] S. Sen, J. C. Kalita, and M. M. Gupta, *A robust implicit compact scheme for two-dimensional unsteady flows with a biharmonic stream function formulation*, Computers & Fluids, 84 (2013), pp. 141–163.

[150] S. Sen, S. Mittal, and G. Biswas, *Flow past a square cylinder at low Reynolds numbers*, International Journal for Numerical Methods in Fluids, 67 (2011), pp. 1160–1174.

[151] ——, *Steady separated flow past elliptic cylinders using a stabilized finite-element method*, Computer Modeling in Engineering and Sciences, 86 (2012), p. 1.

[152] T. Sengupta, T. Lim, S. V. Sajjan, S. Ganesh, and J. Soria, *Accelerated flow past a symmetric aerofoil: experiments and computations*, Journal of Fluid Mechanics, 591 (2007), pp. 255–288.

[153] M. Shaaban and A. Mohany, *Flow-induced vibration of three unevenly spaced in-line cylinders in cross-flow*, Journal of Fluids and Structures, 76 (2018), pp. 367–383.

[154] J. Shao and T. Li, *Fish-like swimming in oblique flows: A numerical investigation*, Ocean Engineering, 230 (2021), p. 109005.

[155] A. SHARMA AND V. ESWARAN, *Heat and fluid flow across a square cylinder in the two-dimensional laminar flow regime*, Numerical Heat Transfer, Part A: Applications, 45 (2004), pp. 247–269.

[156] B. SHARMA AND R. BARMAN, *Steady laminar flow past a slotted circular cylinder*, Physics of Fluids, 32 (2020), p. 073605.

[157] L. SHEN AND Z. SUN, *Jump phenomena in vortex-induced vibrations of a circular cylinder at a low reynolds number*, Physics of Fluids, 31 (2019), p. 123605.

[158] W.-Z. SHEN AND T. P. LOC, *Simulation of 2d external viscous flows by means of a domain decomposition method using an influence matrix technique*, International journal for numerical methods in fluids, 20 (1995), pp. 1111–1136.

[159] W.-Z. SHEN AND T.-P. LOC, *A coupling finite difference/particle method for the resolution of 2d navier-stokes equations in velocity-vorticity form*, Aerospace science and technology, 1 (1997), pp. 97–109.

[160] J.-M. SHI, D. GERLACH, M. BREUER, G. BISWAS, AND F. DURST, *Heating effect on steady and unsteady horizontal laminar flow of air past a circular cylinder*, Physics of Fluids, 16 (2004), pp. 4331–4345.

[161] R. K. SHUKLA, M. TATINENI, AND X. ZHONG, *Very high-order compact finite difference schemes on non-uniform grids for incompressible navier–stokes equations*, Journal of Computational Physics, 224 (2007), pp. 1064–1094.

[162] R. SINGHAL, S. DUTTA, AND J. C. KALITA, *Comprehensive study of forced convection over a heated elliptical cylinder with varying angle of incidences to uniform free stream*, (Under Review).

[163] R. SINGHAL AND J. C. KALITA, *A discrete level set approach for transient incompressible viscous flows on nonuniform grids*, (Under Preparation).

[164] ——, *A novel higher order compact-immersed interface approach for elliptic problems*, Physics of Fluids, 33 (2021), p. 087112.

[165] ——, *An efficient explicit jump high-order compact immersed interface approach for transient incompressible viscous flows*, Physics of Fluids, 34 (2022), p. 103606.

[166] L. SONG AND S. ZHAO, *Symmetric interior penalty galerkin approaches for two-dimensional parabolic interface problems with low regularity solutions*, Journal of Computational and Applied Mathematics, 330 (2018), pp. 356–379.

[167] J. SORIA, T. H. NEW, T. LIM, AND K. PARKER, *Multigrid ccdpiv measurements of accelerated flow past an airfoil at an angle of attack of 30*, Experimental thermal and fluid science, 27 (2003), pp. 667–676.

[168] W. Spotz and G. Carey, *High-order compact scheme for the steady streamfunction vorticity equations*, International Journal for Numerical Methods in Engineering, 38 (1995), pp. 3497–3512.

[169] J. C. Strikwerda, *High-order-accurate schemes for incompressible viscous flow*, International Journal for Numerical Methods in Fluids, 24 (1997), pp. 715–734.

[170] K. Suzuki, K. Ishizaki, and M. Yoshino, *Local force calculations by an improved stress tensor discontinuity-based immersed boundary–lattice boltzmann method*, Physics of Fluids, 33 (2021), p. 047104.

[171] H. Takami and H. B. Keller, *Steady two-dimensional viscous flow of an incompressible fluid past a circular cylinder*, The Physics of Fluids, 12 (1969), pp. II–51.

[172] S. Tally, G. Iaccarino, G. Mungal, and N. Mansour, *An experimental and computational investigation of flow past cacti. annual research briefs*, Center for Turbulence Research, NASA Ames/Stanford University, (2001), pp. 51–63.

[173] S. Tally and G. Mungal, *Flow around cactus-shaped cylinders. annual research briefs*, Center for Turbulence Research, NASA Ames/Stanford University, (2002), pp. 363–376.

[174] S. Taneda, *Visualization of separating stokes flows*, Journal of the Physical Society of Japan, 46 (1979), pp. 1935–1942.

[175] M. Tatsuno, K. Ishii, and W. Yang, *Flow visualization and force measurements on two cylinders at low reynolds numbers*, Handbook of Flow Visualization, WJ Yang, ed., Hemisphere Publications, Washington DC, (1989).

[176] A.-B. Wang, Z. Trávníček, and K.-C. Chia, *On the relationship of effective Reynolds number and Strouhal number for the laminar vortex shedding of a heated circular cylinder*, Physics of Fluids, 12 (2000), pp. 1401–1410.

[177] Z. Wang, J. Fan, and K. Cen, *Immersed boundary method for the simulation of 2d viscous flow based on vorticity–velocity formulations*, Journal of Computational Physics, 228 (2009), pp. 1504–1520.

[178] Z. Wei, C. Li, and S. Zhao, *A spatially second order alternating direction implicit (adi) method for solving three dimensional parabolic interface problems*, Computers & Mathematics with Applications, 75 (2018), pp. 2173–2192.

[179] A. Wiegmann and K. P. Bube, *The explicit-jump immersed interface method: finite difference methods for PDEs with piecewise smooth solutions*, SIAM Journal on Numerical Analysis, 37 (2000), pp. 827–862.

[180] C. H. WILLIAMSON, *Vortex dynamics in the cylinder wake*, Annual review of fluid mechanics, 28 (1996), pp. 477–539.

[181] ——, *Vortex dynamics in the cylinder wake*, Annual Review of Fluid Mechanics, 28 (1996), pp. 477–539.

[182] Z. WU AND Y. CAO, *Numerical simulation of flow over an airfoil in heavy rain via a two-way coupled eulerian–lagrangian approach*, International Journal of Multiphase Flow, 69 (2015), pp. 81–92.

[183] S. XU AND Z. J. WANG, *An immersed interface method for simulating the interaction of a fluid with moving boundaries*, Journal of Computational Physics, 216 (2006), pp. 454–493.

[184] W. YANG AND M. A. STREMLER, *Critical spacing of stationary tandem circular cylinders at re= 100*, Journal of Fluids and Structures, 89 (2019), pp. 49–60.

[185] H. S. YOON, J. YIN, C. CHOI, S. BALACHANDAR, AND M. Y. HA, *Bifurcation of laminar flow around an elliptic cylinder at incidence for low reynolds numbers*, Progress in Computational Fluid Dynamics, an International Journal, 16 (2016), pp. 163–178.

[186] P. X. YU AND Z. F. TIAN, *Compact computations based on a stream-function–velocity formulation of two-dimensional steady laminar natural convection in a square cavity*, Physical Review E, 85 (2012), p. 036703.

[187] M. M. ZDRAVKOVICH, *Flow around circular cylinders: Volume 1: Fundamentals*, vol. 1, Oxford university press, 1997.

[188] ——, *Flow around circular cylinders: Volume 2: Applications*, vol. 2, Oxford university press, 2003.

[189] M. ZHAO AND L. CHENG, *Two-dimensional numerical study of vortex shedding regimes of oscillatory flow past two circular cylinders in side-by-side and tandem arrangements at low reynolds numbers*, Journal of fluid mechanics, 751 (2014), pp. 1–37.

[190] S. ZHAO, *A matched alternating direction implicit (adi) method for solving the heat equation with interfaces*, Journal of Scientific Computing, 63 (2015), pp. 118–137.

[191] X. ZHONG, *A new high-order immersed interface method for solving elliptic equations with imbedded interface of discontinuity*, Journal of Computational Physics, 225 (2007), pp. 1066–1099.

[192] B. Zhou, X. Wang, W. Guo, W. M. Gho, and S. K. Tan, *Experimental study on flow past a circular cylinder with rough surface*, Ocean Engineering, 109 (2015), pp. 7–13.

[193] Y. Zhou, S. Zhao, M. Feig, and G.-W. Wei, *High order matched interface and boundary method for elliptic equations with discontinuous coefficients and singular sources*, Journal of Computational Physics, 213 (2006), pp. 1–30.

[194] H. Zhu, C. Zhang, and W. Liu, *Wake-induced vibration of a circular cylinder at a low reynolds number of 100*, Physics of Fluids, 31 (2019), p. 073606.